Development of an Adaptive Failure-Detection and Identification System for Detecting Aircraft Control-Element Failures

W. Thomas Bundick

NASA

Development of an Adaptive Failure-Detection and Identification System for Detecting Aircraft Control-Element Failures

W. Thomas Bundick
Langley Research Center
Hampton, Virginia

Contents

Summary

A methodology for designing a failure-detection and identification (FDI) system to detect and isolate control-element failures in aircraft control systems has been developed by Weiss and Hsu (NASA CR-178213), and this methodology has been extended to an adaptive FDI system. In this methodology, the failures are divided into two categories, aircraft path and actuator path, based on failure location, and an FDI subsystem is designed for each path. The actuator path includes those failures that occur between the flight computer output and the measurement of actuator position at the actuator output. The aircraft path includes those failures outboard of the actuator position measurement, such as damage to a control surface. The aircraft-path technique uses a linear model of the aircraft aerodynamics and the nonlinear equations of motion in an analytical redundancy scheme to generate residuals that are processed in decision algorithms to detect and isolate the failures. Hence, the design is for use at a single aircraft operating point. The actuator path similarly uses a separate simplified nonlinear model of the actuator and a decision algorithm for each surface, and thus the system is called a decentralized FDI system. The structure of the decision algorithms is selected by using a simplified design model of the residuals; values for the algorithm parameters, such as thresholds, are then based on a more accurate truth model of the residuals. The decentralized concept and the use of design and truth models are key to the robustness of the methodology.

Using this methodology, a baseline FDI system design for a modified Boeing 737 airplane was produced by Weiss. In this report, the Weiss system, or baseline design, was evaluated in detail by using a six-degree-of-freedom nonlinear simulation of the airplane, including atmospheric turbulence based on the Dryden model. When operated in a no-turbulence environment, the actuator-path subsystem performed very well. All actuator-path failures—stuck at neutral, stuck at current position, and hardover—were detected in a timely manner, and in the no-failure simulation runs, there were no actuator-path false alarms. The aircraft-path subsystem also performed well in zero turbulence. There were no false alarms, and partially missing surface failures of the stabilizer, rudder, elevator, and aileron were all detected when the remaining surface effectiveness was 60 percent. The right-stabilizer failure was isolated to the fictitious right horizontal tail, since the system cannot distinguish between stabilizer and elevator failures because of their identical effects.

When the actuator-path subsystem was evaluated in simulation with model errors in the range of 5 to 15 percent, stuck-at-current-position failures were reliably detected without false alarms. With larger model errors (12.5 to 37.5 percent), the same failures were detected, but some false alarms were experienced. When the aircraft-path subsystem was operated at trim points in the vicinity of the design point, aircraft-path failures were reliably detected with no false alarms, but isolation performance was slightly degraded. At a trim point farther away (cruise instead of terminal area), the system was unusable because of false alarms. When moderate random errors were added to the aircraft-path model, the system was still able to detect failures at 60-percent effectiveness, but two false alarms occurred.

In 10-ft/sec turbulence, the actuator-path subsystem continued to perform well. Again, all actuator-path failures were detected with no false alarms. On the other hand, the baseline aircraft-path subsystem was completely unusable in 10-ft/sec and higher turbulence because of the large number of false alarms. Examination of the residuals indicated that many of the error standard deviations used in the truth model were too small. Thus, new values for the truth model in 10-ft/sec turbulence were obtained, and two new aircraft-path subsystem designs (threshold (TG) and projection vector at 10-ft/sec turbulence (PV10)) were produced. Both of these new designs performed well in 10-ft/sec turbulence, far superior to the baseline design in

false-alarm performance. However, performance of the new designs in zero turbulence was not nearly as good as that of the baseline design, so some type of adaptive design was necessary for operation in atmospheric turbulence.

When a new aircraft-path subsystem (projection vector at 20-ft/sec turbulence (PV20)) was designed for operation in 20-ft/sec turbulence, the standard deviations of the errors for the truth model obtained in 20-ft/sec wind gusts had to be increased to obtain adequate false-alarm performance at that turbulence level. Thus, it appears that, at the higher turbulence levels, the design procedure needs refinement or that the method of obtaining parameter values for the truth model needs improvement. Nevertheless, after the truth model was adjusted, the PV20 design performed very well in 20-ft/sec gusts.

The design procedure was extended to produce an interpolated design for operation over a range of turbulence levels. This was accomplished by linearly interpolating the thresholds, gains, and projection vectors between their baseline, PV10, and PV20 design values based on a priori knowledge of the turbulence level. The interpolated design performed well over the turbulence range of 0 to 20 ft/sec. However, in actual flight, this a priori knowledge of the turbulence level is not available, and an estimate of the turbulence is required.

A turbulence estimator based on the technique used in the NASA F-8 digital fly-by-wire program was developed. This technique estimates the sample standard deviation of the latest 5 sec of turbulence. This estimator was combined with the interpolated design to produce an adaptive aircraft-path subsystem. This adaptive design was evaluated in 0-, 5-, 10-, 15-, and 20-ft/sec turbulence and performed well over the entire range. It successfully detected and isolated all partially missing surface failures at 40-percent effectiveness, and it detected 19 out of 20 failures at 60-percent effectiveness. Only at the smallest failure magnitude (80-percent effectiveness) did performance degrade. Furthermore, in 688 sec of simulation time with no failures, there was only one false alarm.

Although the decentralized FDI technique is robust to small model errors, and the extension of the technique to an adaptive system allows the system to operate in atmospheric turbulence, problems remain to be solved in the development of an operational FDI system. The two most urgent needs are (1) the continuation of work to extend the system from a single operating point to operation over the entire operating envelope of the aircraft and (2) flight testing to provide more realistic noise, or error, values for the truth models and to provide reliable false-alarm evaluation.

Introduction

For certain anticipated failures in the operation of transport aircraft, there are established procedures for the pilot to follow. A typical example is the procedure for handling an engine outage during takeoff. There are, however, unanticipated failure modes for which no appropriate emergency procedures are available. These unanticipated failures must be handled by the pilot and/or the automatic control system in real time to decrease the probability of a tragic accident.

In the case of a hardover (maximum surface deflection) failure in a control element, the pilot may have only a matter of seconds to take corrective action before the aircraft reaches an irrecoverable condition. In the case of a failure of lesser magnitude, the pilot may have more time to take corrective action, but the failure and, hence, the proper corrective action may be difficult to identify. In either case, the pilot may require assistance from the aircraft systems to help determine the appropriate corrective action in a timely manner. A restructurable flight control system (RFCS) is designed to provide such assistance in these emergencies. The RFCS automatically restructures the control system to utilize the remaining useful control

effectors to recover from the emergency and to provide stability and control augmentation when sufficient control power remains. A crucial component of the RFCS is the failure-detection and identification (FDI) system, which detects the occurrence of a control-element failure, identifies the failed elements, and provides needed failure information to the other RFCS components.

A considerable amount of work has been done in the area of failure detection and identification in dynamic systems, and Willsky has provided a well-known survey of many of the available FDI techniques (ref. 1). Chow (ref. 2) and Chow and Willsky (ref. 3) have examined the problem of generating residuals from the system measurement data for use in decision-making processes to detect and identify failures. The detection of failures in sensors has been investigated in references 4 to 7. The generalized likelihood ratio has been investigated for FDI applications in references 8 to 18. This technique has been exercised in a simplified simulation of the F-8 aircraft dynamics (refs. 9 to 12), in a linear simulation of the Boeing 737 aircraft longitudinal dynamics (ref. 18), and in a six-degree-of-freedom nonlinear simulation of the C-130 aircraft (refs. 15 to 17). Another FDI technique is the failure-detection filter. Beard (ref. 19) developed the theory of the failure-detection filter for linear deterministic continuous systems by using a matrix-algebra approach. Jones (ref. 20) extended this theory to stochastic and sampled data systems by using a vector space approach. Meserole (ref. 21) has applied the failure-detection filter to the problem of detecting and identifying failures in an F-100 jet engine. This technique has been applied to the problem of detecting and identifying control-element failures in aircraft in references 15 and 22 for the C-130 and 737, respectively. Early work on restructurable or reconfigurable flight control systems was done by Boudreau and Berman (ref. 23). In a later effort, Caglayan et al. (ref. 24) investigated RFCS design. Their FDI approach was to use a Kalman filter followed by a bank of first-order filters and likelihood-ratio computers and a multiple-hypothesis test.

One of the difficulties with the FDI techniques previously mentioned is their lack of robustness to model errors. Weiss and his colleagues (refs. 25 to 27) have developed an FDI design methodology aimed at improving this robustness to model errors. Like the aforementioned techniques, this approach, which they call decentralized FDI, utilizes analytical redundancy. However, unlike the previous approaches which use a central filter, their technique uses only the most reliable information in these analytical-redundancy relationships, and thus increases robustness with only a small loss in optimality. They have applied this technique to transport aircraft (refs. 25 to 29), high-performance aircraft (refs. 30 and 31), and jet engines (refs. 32 and 33). A forerunner of this approach was used in the NASA F-8 digital fly-by-wire program (ref. 34) to detect sensor failures.

The primary purposes of this report are to present a more thorough evaluation via simulation of the performance of Weiss's FDI design than was contained in reference 25, including the effects of atmospheric turbulence and model errors; to describe an extension to Weiss's design, namely, an adaptive FDI system, for operation in turbulence; and to present a simulation evaluation of this adaptive system. Secondary purposes of this report are to present a review of Weiss's design methodology for completeness and to present additional details concerning a few areas of the design that are not found in reference 25.

The report is organized as follows: The design concept, or methodology, is presented first, followed by numerical results from the design procedure for the baseline system designed by Weiss. Results of a thorough simulation evaluation of the baseline design are next, followed by modifications to the design for operation in turbulence and results of an evaluation of these modifications. A description and an evaluation of an algorithm to estimate the level (standard deviation) of turbulence are then presented, followed by a description of an adaptive FDI design

3

and a presentation of the results of an evaluation of this design. The final section contains a summary of results and conclusions.

Symbols

Some variables are listed with the general subscript ξ. In these cases, specific subscripts are defined under the subheading "Subscripts." Bold capital letters indicate matrices, and bold lower-case letters indicate vectors. A dot over a symbol indicates a derivative with respect to time. An asterisk over a symbol indicates an averaged quantity.

$\mathbf{A}$	system transition matrix
A_{m_ξ}	accelerometer measurement, ft/sec^2
$A_{m_\xi}^c$	accelerometer measurement after compensation for off-center-of-gravity effects, ft/sec^2
$\mathbf{a}$	acceleration, ft/sec^2
$a_{h\ell}$	filter constant for high-pass filter in error model
a_ℓ	filter constant for low-pass filter in error model
$\mathbf{B}$	system input, or control, matrix
$\mathbf{B}_j$	jth column of $\mathbf{B}$ matrix
b	reference wing span, ft
$\widehat{C}_\xi$	nondimensional aerodynamic coefficient
C_{ξ_0}	constant term in series expansion of $\widehat{C}_\xi$ accounting for forces or moments at trim condition
C_{ξ_ζ}	derivative of $\widehat{C}_\xi$ with respect to ζ
$CS(\ )$	failure isolated to confusion set consisting of surfaces listed in parentheses
$\bar{c}$	reference wing chord, ft
d^2	metric defined by equation (36)
E_{wc}	worst-case error, deg
EPR	engine pressure ratio
e_ξ	accelerometer measurement error, ft/sec^2
F_{ξ_i}	pass-fail flag for ith failure test
f_s	effective failure magnitude, deg
$\bar{f}_{s_i}$	minimum failure magnitude to achieve desired value of d^2 metric, deg
G	gain in turbulence estimator
G_A, G_D	SPRT gains
G_E	turbulence estimator gain

$\mathbf{g}, g$	acceleration due to gravity, ft/sec^2
$\mathbf{H}$	system output, or observation, matrix
H_i	hypothesis that the ith component has failed
H_1	hypothesis that a failure has occurred
H_0	hypothesis that no failure has occurred
I_{zx}	product of inertia in zx-plane, ft-lb-sec^2
I_ξ	moment of inertia about ξ-axis, ft-lb-sec^2
K_σ	multiplicative factor used in computing threshold
k	sample number
k_f	sample number (time) when failure occurs
k_T	sample number at which trigger test passes and initiates the verify test
k_t	sample number at which value of equivalent statistic equals or exceeds threshold
L	aerodynamic and propulsive moment about x-axis, ft-lb
LA	left aileron
LE	left elevator
LS	left stabilizer
LT	left thrust
ℓ_ξ	ξ-axis coordinate of sensor relative to center of gravity, ft
M	aerodynamic and propulsive moment about y-axis, ft-lb
m	mass of aircraft, slugs
N	aerodynamic and propulsive moment about z-axis, ft-lb, or number of samples
N_I	maximum number of samples in isolate test
N_T	number of samples in trigger test
N_V	maximum number of samples in verify test
ND	failure not detected
$\mathbf{n}(k), n(k)$	Gaussian noise sequence
P	total roll rate, rad/sec or deg/sec
$\mathbf{P}(k)$	covariance matrix of state in error model
P_D	probability of detection
P_E	probability of error
P_{FA}	probability of false alarm
$\mathbf{P}_i$	trigger, verify projection vector for ith failure

$\mathbf{P}_{i/j}$	isolation projection vector for ith failure more likely than jth failure
P_M	probability of missed detection
p, q, r	body-axis attitude rates, rad/sec or deg/sec
pm	measured perturbed roll rate, rad/sec
$\mathbf{Q}$	covariance matrix of noise input to the error model
Q	total pitch rate, rad/sec or deg/sec
Q_0	pitch rate at trim, rad/sec
$\bar{q}$	dynamic pressure, lb/ft^2
qm	measured perturbed pitch rate, rad/sec
R	total yaw rate, rad/sec or deg/sec
RA	right aileron
RE	right elevator
RS	right stabilizer
RT	right thrust
Ru	rudder
rm	measured perturbed yaw rate, rad/sec
S	reference wing area, ft^2
$\mathbf{S}(N)$, $S(N)$	sum of N residuals
S_I	isolation-test statistic
$S_{I_{i/j}}(k - k_T + 1)$	test statistic in aircraft-path isolation test
S_T	trigger-test statistic in aircraft path
S'_T	trigger-test statistic in actuator path
S_V	verify-test statistic
$S_{\gamma_i}(k - k_T + 1)$, $S_{\gamma_j}(k - k_T + 1)$	sum of $\gamma_i(m)$, $\gamma_j(m)$ from $m = k_T$ to $m = k$
$S_\xi(k)$	equivalent statistic
$\mathbf{s}, s$	failure signal
$\bar{s}$	value of failure signal s that is reliable according to d^2 metric, deg or lb $\times$ 10^3
TURB	specified or estimated value of standard deviation of turbulence, used as independent variable in interpolation, ft/sec
TURBL, TURBM, TURBH	low, medium, and high break points of independent variable in linear interpolation
t_L	lower threshold in sequential probability ratio test

t_T	trigger threshold
t_U	upper threshold in sequential probability ratio test
t_V	verify threshold
t_{ξ_i}	threshold for ith failure test
U	speed in x-direction, ft/sec
$U(\ )$	undetermined failure of one of the surfaces listed in parentheses
U_0	x-velocity at trim, ft/sec
$\mathbf{u}(k)$	vector sequence of control inputs
$\mathbf{V}$	inertial velocity, ft/sec
V	speed in y-direction, ft/sec
$\widehat{\mathbf{V}}(k)$	estimated velocity, ft/sec
V_{cas}	calibrated airspeed, knots
$\mathbf{V}_m(k)$	measured velocity relative to air mass, ft/sec
$\mathbf{V}^P(k)$	predicted velocity, ft/sec
V_T	true airspeed, ft/sec
V_{T_m}	measured true airspeed, ft/sec
V_{T_0}	true airspeed at trim, ft/sec
W	speed in z-direction, ft/sec
$\mathbf{w}(k)$	noise input in state-space model
$w_d(k)$	noise input to high-pass filter in error model
$w_\ell(k)$	white Gaussian noise input to low-frequency error model
W_0	z-velocity at trim, ft/sec
X	total aerodynamic and propulsive force in x-direction, lb
x, y, z	aircraft body axes
$\mathbf{x}(k)$	state vector
$x_h(k)$	output of high-pass-filtered error model
$x_{h\ell}(k)$	output of low-pass filter in high-pass-filtered error model
$x_{S_i}(k)$	state variable in model of error in $S(N)$
Y	total aerodynamic and propulsive force in y-direction, lb
YL, YM, YH	low, medium, and high break points of dependent variable in linear interpolation
$\mathbf{y}(k)$	vector sequence of outputs, or observations
y_m	sensor measurement
Z	total aerodynamic and propulsive force in z-direction, lb

α	angle of attack, deg
α_m	measured total angle of attack, rad or deg
α_m^c	measured perturbed angle of attack after compensation for attitude rate effects, rad or deg
α_0	angle of attack at trim, rad or deg
β	sideslip angle, deg
β_m	measured total sideslip angle, rad or deg
β_m^c	measured perturbed sideslip angle after compensation for attitude rate effects, rad or deg
β_0	sideslip angle at trim, rad or deg
$\gamma_i(m)$, $\gamma_j(m)$	residual sequence after projection and filtering
Δ	total deflection, deg or lb $\times$ 10^3
Δt	sample interval, sec
δ	deflection relative to trim value, deg or lb $\times$ 10^3
δ_a	true actuator position
δ_c	commanded actuator position
δ_m	measured actuator position
δ_{m_i}	measured perturbed deflection of ith control surface, deg
$\epsilon(k)$	measurement error sequence, ft/sec
$\zeta(k)$	sequence of residuals in turbulence estimator
Θ	total pitch angle, deg
θ	total pitch angle, rad or deg
$\Lambda(k)$	log likelihood ratio
ν	residual
$\nu(k)$, $\boldsymbol{\nu}(k)$	sequence of residuals
ν_ξ	force or moment residual, ft/sec^2 or rad/sec
$\boldsymbol{\Sigma}_f$	covariance matrix of $\mathbf{S}(N)$
$\boldsymbol{\Sigma}_\ell$	covariance matrix of low-frequency error sequence $\mathbf{n}_\ell(k)$
$\boldsymbol{\Sigma}_w$	covariance matrix of white-noise sequence $\mathbf{n}_w(k)$
σ	standard deviation, ft/sec
σ^2	variance
σ_f^2	variance of $S(N)$
σ_G	specified standard deviation of simulated turbulence, ft/sec
σ_ℓ^2	variance of scalar low-frequency error sequence $n_\ell(k)$

σ_S^2	variance of $S(k)$
$\sigma_{S_{I_{i/j}}}$	variance of $S_{I_{i/j}}(k - k_T + 1)$
σ_T	sample standard deviation of simulated turbulence, ft/sec
σ_U	sample standard deviation of x-component of simulated turbulence, ft/sec
σ_V	sample standard deviation of y-component of simulated turbulence, ft/sec
σ_W	sample standard deviation of z-component of simulated turbulence, ft/sec
σ_w^2	variance of scalar white-noise sequence $n_w(k)$
Φ	total bank angle, rad or deg
Ψ	total heading angle, rad or deg
ω	attitude rate, rad/sec
ω_a	actuator-model cutoff frequency, rad/sec

Subscripts:

d	component of design model
E	elevator
h	after high-pass filtering
I	isolate test
i	ith component
j	jth component
LA	left aileron
LE	left elevator
LH	left horizontal tail
LS	left stabilizer
LT	left thrust
l	moment about x-axis
ℓ	low-frequency component of error (noise), or moment about x-axis
m	measured quantity, or moment about y-axis
n	moment about z-axis
RA	right aileron
RE	right elevator
RH	right horizontal tail
RS	right stabilizer

RT	right thrust
Ru	rudder
Sp	spoiler
T	trigger test
Th	thrust
Tl	throttle
t	component of truth model
V	verify test
w	white noise
X, Y, Z	force along x-, y-, or z-axis
x, y, z	along or about x-, y-, or z-body axis
δA	aileron deflection about nominal (trim)
δE	elevator deflection about nominal (trim)
δR	rudder deflection about nominal (trim)
δS	stabilizer deflection about nominal (trim)
δSp	spoiler deflection about nominal (trim)
δT	thrust perturbation about nominal (trim)
μ	x-, y-, or z-channel in turbulence estimator

Superscripts:

c	after compensation
p	predicted value
T	transpose of a matrix
$*$	denotes averaged over two successive samples

Operators:

$E\{\ \}$	statistical expected value
$\hat{\ }$	estimate
var ( )	statistical variance

Abbreviations:

BL	baseline
FDI	failure detection and identification
HPF	high-pass filter
LPF	low-pass filter
PV10	projection vector at 10-ft/sec turbulence

PV20	projection vector at 20-ft/sec turbulence
RFCS	restructurable flight control system
SPRT	sequential probability ratio test
TG	threshold

Baseline Design

Design Concept

Failure detection and isolation is the process of detecting abnormal, or out-of-tolerance, behavior in a system and isolating the source of the abnormality to a subsystem or component. One method of accomplishing this is to examine the system outputs, or perhaps the subsystem outputs. For example, the power output of an RF (radio frequency) transmitter could be measured, and if the power were outside of limits established by previous testing, the transmitter could be declared failed. In this way, detection and isolation to the transmitter subsystem level are performed in a single operation. Of course, this procedure is reliable only if the power measurement is more reliable than the transmitter. A common technique for detecting failures in redundant sensors, where three or more sensors measure the same quantity, is a voting scheme whereby the outputs of the sensors are compared with each other. If one of the outputs differs from the others by more than normal tolerance, that sensor is considered failed.

The FDI system for aircraft control elements poses a slightly different problem. Unlike the transmitter, the output (position) of the actuators used to move the control surfaces cannot be compared with a constant, because the output depends on the input. On the other hand, the actuators are not triply replicated, so their outputs cannot be compared with each other. Moreover, the effective outputs of the control surfaces are the aerodynamic forces and moments that are exerted on the aircraft, and these forces and moments are not measured directly. In these cases, some form of analytic redundancy must be used to form a set of normal predicted measurements with which a similar set of actual measurements can be compared. Several such techniques utilize a central filter, which uses a model of the aircraft dynamics to predict aircraft performance, compares this prediction to measured performance, and generates a set of residuals whose behavior is used to detect and isolate failures. Some of these methods, such as the generalized likelihood ratio, failure-detection filter, and a bank of Kalman filters, have been investigated for application to the FDI problem in aircraft control systems. (See refs. 9 to 12, 15 to 18, and 22.) One of the major problems with these techniques is that errors in the models used by the central filter produce abnormalities in the residuals, which are difficult to distinguish from a system failure. Thus, one of the major thrusts of the investigation discussed in this report was to develop an FDI system that was robust to model errors. Weiss and his colleagues conceived such a system, which they call decentralized FDI, developed a design methodology, and used this methodology to design a decentralized FDI system for the 737 aircraft. The remainder of this section presents a review of, and in a few cases an expansion of, the methodology and design from their report.

Subsystems

A major step in the direction of robustness was the division of the FDI system into separate subsystems: the actuator-path subsystem and the aircraft-path subsystem. The actuator-path subsystem was designed to detect and isolate failures that occur between the measurement of actuator input (control system command to the actuator) and the measurement of actuator

output position. (See fig. 1.) The aircraft-path subsystem was designed to detect control-element failures that occur outboard of the actuator position measurement. Such failures include broken linkages or hinges and control surfaces that are damaged or partially missing.
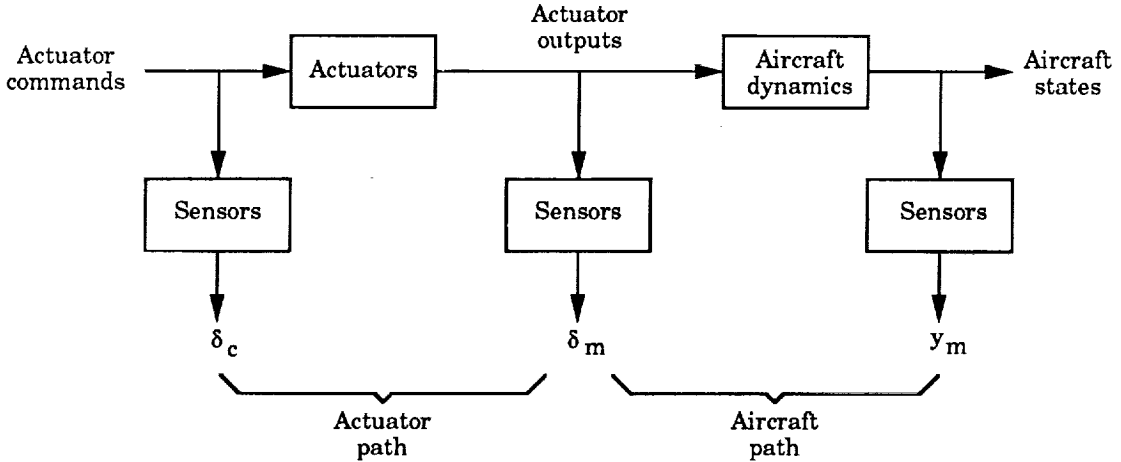

Figure 1. Definition of failure paths.

The actuator-path subsystem consists of a separate FDI element for each actuator. As shown in figure 2, each element operates as follows: The system contains a model of the actuator dynamics, where the complexity of the model depends on the complexity of the actuator dynamics and on the desired sensitivity of the FDI system. The actuator command is input to the model, and a predicted actuator response (output position) is computed. This predicted output is then compared with the measured output of the real actuator, and a residual is generated. During normal operation, this residual would be near zero, since the predicted output would agree with the measured output with an accuracy that depended on the accuracy of the model and the error in the measurement. This residual is then processed by a decision algorithm to detect a failure. Since there is a separate FDI element for each actuator, failure detection also serves as failure isolation, and multiple actuator-path failures are easily accommodated. With this technique, robustness is served because the model is that of the actuator, whose dynamics should be better known than those of the entire aircraft, and because the measurements used should be less noisy than some aircraft performance measurements, such as angular accelerations.
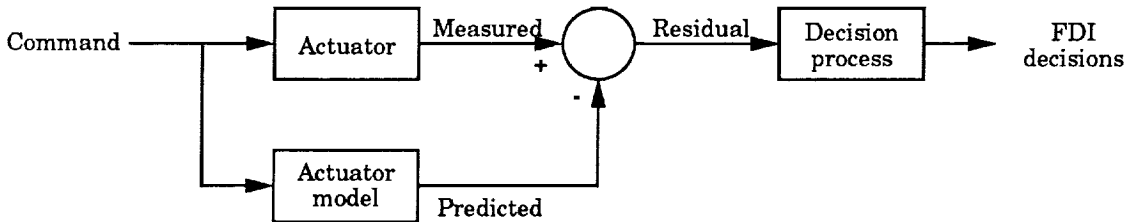

Figure 2. Typical element of actuator-path subsystem.

The design of the aircraft-path subsystem assumes that hinge-moment measurements for each of the control surfaces are not available. Therefore, as shown in figure 3, this subsystem must utilize measurements of the aircraft dynamic response to commanded maneuvers to detect

12

and isolate failures. A linear model of the aerodynamics at the selected operating point, or flight condition, is used to predict the forces and moments acting on the aircraft based on the aircraft state and the measured surface positions. The nonlinear equations of motion and sensor models are then used to predict angular and linear acceleration measurements in body coordinates. These predictions are compared with the measured quantities to form residuals that are processed in a decision algorithm to detect and isolate aircraft-path failures. The current design does not accommodate multiple aircraft-path failures.
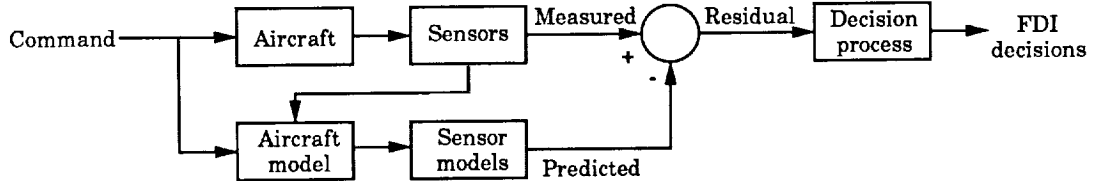

Figure 3. Aircraft-path subsystem.

Decision Process

The general pattern is to make measurements of the response of the system, either the aircraft or an actuator, to compare that measurement with a calculated measurement that was produced by using a model of the system, and to use the residuals that result from this comparison in a decision mechanism. To achieve the desired missed-detection/false-alarm performance in a noisy environment, while providing quick response to a failure when the failure time is unknown, the decision process is structured as a set of trigger-verify-isolate tests as shown in figure 4. All three of the tests are designed as statistical hypotheses tests.
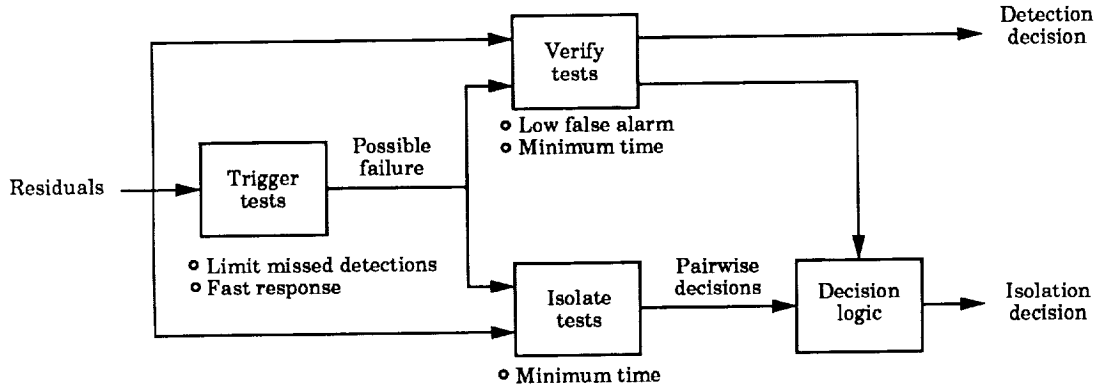

Figure 4. Structure of decision process.

The trigger, verify, and isolate tests each use the vector of residuals as an input. The problem is to determine whether or not the residuals are "normal," that is, whether the residuals result from an unfailed system or from a failed system. The structure of these tests is determined by using a simplified design model for the residuals; this model assumes that the vector sequence of residuals is composed of two parts: (1) a slowly varying signal vector that can be considered constant for the duration of the test and is present only during a failure, and (2) a white Gaussian noise vector that results from sensor noise and quantization noise. Once the test structure is chosen, the parameters of the test are selected by using a more complete truth model for the residuals, a model that includes other sources of error, such as biases and system model errors. This procedure, which uses a design model to determine the algorithm structure and a truth

13

model to determine values for the algorithm parameters, is intended to increase the robustness of the design.

Single Operating Point

The FDI system discussed in this report utilized a linear model of the aircraft aerodynamics in the system design; that is, the aerodynamic forces and moments acting on the aircraft were assumed to be linear functions of the aircraft states and of the control deflections. This assumption is valid only over a limited portion of the aircraft operating envelope. Therefore, the FDI system design presented herein is single-point design. In this case, the operating point for the modified 737 is described in table 1.

Table 1. Aircraft Operating Point for FDI System Design

[Landing gear up]

Altitude, ft	3500
Indicated airspeed, knots	160
Flight-path angle, deg	0
Flap angle, deg	15

Design Methodology

Actuator-Path Subsystem

Residual generation. In the actuator-path subsystem, a sequence of residuals $\nu(k)$ is generated by comparing the measured output position of the actual actuator with the position that was computed by using a nonlinear model of the actuator as shown in figure 5. In general, the actuator model includes a single-pole linear transfer function, a rate limiter, a position limiter, and a cable stretch factor. The model input is the actuator position command generated by the flight control system. The model output (computed actuator position) is compared with a measurement of the actual position, and the measurement includes a bias and additive white Gaussian noise and is assumed to occur somewhere between the actuator rod and the surface hinge, inclusively. The model is single-input/single-output, such that the residual vector is one dimensional, or a scalar sequence. In a flight system, errors would be introduced into the model output, and thus into the residuals, by such things as unmodeled high-frequency dynamics, hysteresis effects, and variations from one set of hardware to another.
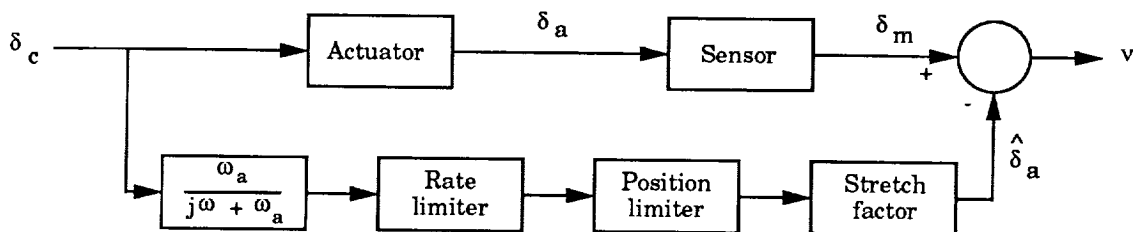

Figure 5. Actuator-path residual generation.

14

The model for the engines is more complex. Commanded thrust is the input, and engine pressure ratio (EPR) is the actual measurement. The EPR is converted to "measured" thrust by using a transformation that is a function of altitude. The rate limit is a function of the current thrust and is different for engine spool-up and spool-down.

Design model. The residuals generated as in the preceding section are assumed to be composed of a zero-mean, white Gaussian random component, which accounts for sensor noise and quantization error, and a low-frequency error component. When a failure has occurred, there is a time-varying component that results from the failure; this component is the signal that must be detected to indicate a failure. For design purposes, it is assumed that this time variation is slow compared with the detection time of 0.5 to 2 sec. Therefore, to determine the structure of the decision tests, the signal s is assumed constant, and the low-frequency error term is ignored. The design model of the residual $\nu_d(k)$ is then

$$\left.\begin{array}{l} H_1\colon \nu_d(k) = s + n_w(k) \\[2mm] H_0\colon \nu_d(k) = n_w(k) \end{array}\right\} \tag{1}$$

where s is the failure signal and $n_w(k)$ is white Gaussian noise. The conditional probability density function for $\nu_d(k)$ is

$$\left.\begin{array}{l} H_1\colon p\left(\nu_d(k)|H_1\right) = \dfrac{1}{\sqrt{2\pi\sigma_w^2}} \exp\left[-\left(\nu_d - s\right)^2 / 2\sigma_w^2\right] \\[4mm] H_0\colon p\left(\nu_d(k)|H_0\right) = \dfrac{1}{\sqrt{2\pi\sigma_w^2}} \exp\left[-\nu_d^2 / 2\sigma_w^2\right] \end{array}\right\} \tag{2}$$

where σ_w^2 is the variance of $n_w(k)$.

Truth model. The truth model for the residuals used in determining the parameters of the tests includes a low-frequency noise term $n_{\ell H}(k)$ to account for sensor biases and other model errors. As noted previously, the decision process assumes that the random component of the residual is white. Therefore, a high-pass whitening prefilter is used between the residual generator and the decision algorithm to decorrelate the residual noise. The filter cutoff frequency is chosen to be less than the inverse of the detection time to preserve the coherence of the signal. The truth model for the residuals then becomes

$$\left.\begin{array}{l} H_1\colon \nu_t(k) = s_h + n_{\ell h}(k) + n_{wh}(k) \\[2mm] H_0\colon \nu_t(k) = n_{\ell h}(k) + n_{wh}(k) \end{array}\right\} \tag{3}$$

where the subscript h denotes the quantity after high-pass filtering, and σ_ℓ^2 is the variance of the low-frequency noise $n_\ell(k)$ before high-pass filtering.

To improve detection performance, the decision process utilizes a signal $S(N)$ that is the sum of the residuals over N samples; that is,

$$S(N) = \sum_{k=1}^{N} \nu_t(k) \tag{4}$$

The variance σ_f^2 of $S(N)$ can be approximated as $\sigma_f^2 = N^2\sigma_\ell^2 + N\sigma_w^2$. To determine the variance σ_f^2 more accurately, first express the random portion of the process $\nu_t(k)$ as the output of a linear system. Let the linear system be expressed in state-space form as follows:

$$\left. \begin{array}{l} \mathbf{x}(k+1) = \mathbf{A}\,\mathbf{x}(k) + \mathbf{B}\,\mathbf{w}(k) \\[2mm] \mathbf{y}(k) = \mathbf{H}\,\mathbf{x}(k) \end{array} \right\} \tag{5}$$

With reference to figure 6, the low-pass noise $n_\ell(k)$ can be expressed as the output of a low-pass filter driven by zero-mean, white Gaussian noise $w_\ell(k)$ as follows:

$$n_\ell(k+1) = a_\ell n_\ell(k) + (1 - a_\ell)w_\ell(k) \tag{6}$$
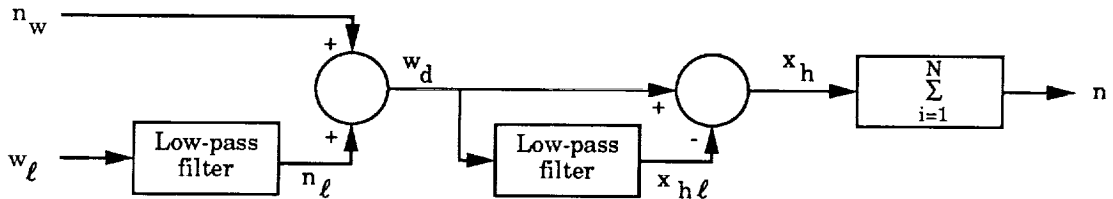
Figure 6. Truth model of residual noise process.

Let $w_d(k)$ be the sum of $n_\ell(k)$ and $n_w(k)$. The high-pass-filtered noise $x_h(k)$ can be modeled as the difference between noise $w_d(k)$ and the output $x_{h\ell}(k)$ of a low-pass filter driven by $w_d(k)$; that is

$$w_d(k) = n_\ell(k) + n_w(k) \tag{7}$$

and

$$x_{h\ell}(k+1) = a_{h\ell}x_{h\ell}(k) + (1 - a_{h\ell})\,w_d(k) \tag{8}$$

Combining equations (7) and (8) gives

$$x_{h\ell}(k+1) = a_{h\ell}x_{h\ell}(k) + (1 - a_{h\ell})n_\ell(k) + (1 - a_{h\ell})n_w(k) \tag{9}$$

and

$$x_h(k) = w_d(k) - x_{h\ell}(k) \tag{10}$$

The output $x_h(k)$ of the high-pass filter is the input to the summation function, which sums the input over N samples as follows:

$$n(k) = \sum_{i=k-N+1}^{k} x_h(i) \tag{11}$$

The summation function can be modeled as an N-state linear system, where each state $x_{S_i}(k)$ only provides a one-sample delay and the output matrix provides the summation.

16

We now combine equations (6) to (11) into the state-space system described by equations (5). The resulting system is described by the following system of equations:

$$x(k) = \begin{bmatrix} x_1(k) \\ x_2(k) \\ x_3(k) \\ x_4(k) \\ \vdots \\ x_{N+2}(k) \end{bmatrix} = \begin{bmatrix} n_\ell(k) \\ x_{h\ell}(k) \\ x_{S_1}(k) \\ x_{S_2}(k) \\ \vdots \\ x_{S_N}(k) \end{bmatrix} \tag{12}$$

$$\mathbf{w}(k) = \begin{bmatrix} w_1(k) \\ w_2(k) \end{bmatrix} = \begin{bmatrix} n_w(k) \\ w_\ell(k) \end{bmatrix} \tag{13}$$

$$\mathbf{A} = \begin{bmatrix} a_\ell & 0 & 0 & 0 & \cdots & 0 & 0 \\ (1-a_{h\ell}) & a_{h\ell} & 0 & 0 & \cdots & 0 & 0 \\ 1 & -1 & 0 & 0 & \cdots & 0 & 0 \\ 0 & 0 & 1 & 0 & \cdots & 0 & 0 \\ 0 & 0 & 0 & 1 & \cdots & 0 & 0 \\ & & \vdots & & & \vdots & \\ 0 & 0 & 0 & 0 & \cdots & 1 & 0 \end{bmatrix} \tag{14}$$

$$\mathbf{B} = \begin{bmatrix} 0 & (1-a_\ell) \\ (1-a_{h\ell}) & 0 \\ 1 & 0 \\ 0 & 0 \\ & \vdots \\ 0 & 0 \end{bmatrix} \tag{15}$$

$$\mathbf{H} = \begin{bmatrix} 0 & 0 & 1 & 1 & \cdots & 1 \end{bmatrix} \tag{16}$$

where
$$\mathbf{A} = N+2 \times N+2, \mathbf{B} = N+2 \times 2, \text{ and } \mathbf{H} = 1 \times N+2$$

The system output $y(k)$ is the noise sequence $n(k)$ in the truth model after summing over N samples; that is
$$n(k) = y(k) \tag{17}$$

The covariance matrix $\mathbf{P}(k)$ of the system state $\mathbf{x}(k)$ can be found by solving the Lyapunov equation as follows:

$$E\{\mathbf{x}(k+1)\mathbf{x}^T(k+1)\} = \mathbf{A}E\{\mathbf{x}(k)\mathbf{x}^T(k)\}\mathbf{A}^T + \mathbf{A}E\{\mathbf{x}(k)\mathbf{w}^T(k)\}\mathbf{B}^T$$
$$+ \mathbf{B}E\{\mathbf{w}(k)\mathbf{x}^T(k)\}\mathbf{A}^T + \mathbf{B}E\{\mathbf{w}(k)\mathbf{w}^T(k)\}\mathbf{B}^T$$

17

or

$$\mathbf{P}(k+1) = \mathbf{AP}(k)\mathbf{A}^T + \mathbf{BQB}^T \tag{18}$$

where

$$\mathbf{Q} = \begin{bmatrix} \sigma_w^2 & 0 \\ 0 & \sigma_\ell^2 \end{bmatrix} \tag{19}$$

In the steady state as k approaches infinity, equation (18) becomes

$$\mathbf{P} = \mathbf{APA}^T + \mathbf{BQB}^T \tag{20}$$

The solution for the variance σ_f^2 of the noise $n(k)$ in the truth model can then be found from

$$\sigma_f^2 = \mathbf{HPH}^T \tag{21}$$

This value is then used in the statistical hypotheses tests.

Trigger test. To detect the potential presence of a failure that, according to the design model, results in a constant of unknown magnitude and sign in white Gaussian noise, the trigger test is designed to perform a Bayesian hypothesis test on a fixed sample length of residuals. This is accomplished by computing the log likelihood ratio $\Lambda_T(k)$ of the most recent N_T residuals, taking the absolute value of $\Lambda_T(k)$, and comparing the result to a threshold. A window of N_T residuals is used rather than a single sample to increase the signal-to-noise ratio, and the window of fixed sample length is updated every iteration to account for the unknown onset time of the failure.

Since the $\nu(k)$'s are independent according to the design model, the log likelihood ratio based on the probability density function in equations (2) is given by

$$\Lambda_T(k) = \ln\left\{ \frac{p\left[\nu\left(k-N_T+1\right),\ \nu\left(k-N_T+2\right),\ \cdots,\ \nu(k)|H_1\right]}{p\left[\nu\left(k-N_T+1\right),\ \nu\left(k-N_T+2\right),\ \cdots,\ \nu(k)|H_0\right]} \right\}$$

$$= \sum_{i=k-N_T+1}^{k} \frac{s\nu(i)}{\sigma_w^2} - \frac{s^2}{2\sigma_w^2} \tag{22}$$

where $p\left[\nu(k-N_T+1),\ \nu(k-N_T+2),\ \cdots,\ \nu(k)|H_i\right]$ is the joint conditional probability density function of the most recent N_T residuals (given H_i). Instead of using $\Lambda_T(k)$, the trigger test utilizes an equivalent statistic $S_T(k)$ given by

$$S_T(k) = (1/N_T) \sum_{i=k-N_T+1}^{k} \nu(i) \tag{23}$$

Since the $\nu(k)$'s are independent, $S_T(k)$ is Gaussian with variance $\sigma_{S_T}^2 = \sigma_w^2/N_T$ and mean zero under H_0 and mean s under H_1. The trigger test becomes

$$|S_T(k)| \begin{cases} \geq t_T, \text{ then } H_1 \\ < t_T, \text{ then } H_0 \end{cases} \tag{24}$$

To determine the threshold t_T, first consider the design model for the residuals. The probability of false alarm (choosing the hypothesis H_1 when H_0 is true) is given by the integral

$$
\begin{aligned}
P_{FA} &= 2 \int_{t_T}^{\infty} p\left(S_T | H_0\right) \, dS_T \\
&= 2 \int_{t_T}^{\infty} \frac{1}{\sqrt{2\pi\sigma_{S_T}^2}} \exp\left(-S_T^2/2\sigma_{S_T}^2\right) dS_T
\end{aligned}
\tag{25}
$$

The threshold t_T is chosen to achieve the desired false-alarm rate; that is

$$
t_T = K_\sigma \sigma_{S_T}
\tag{26}
$$

For example, a P_{FA} of 1×10^{-3} results in $K_\sigma = 3.3$, or $t_T = 3.3\sigma_{S_T}$.

Now that the structure of the trigger test has been chosen, the whitening prefilter is inserted, and equations (5) to (21) are used to compute the variance $\sigma_{S_T}^2$ of the test statistic $S_T(k)$ using the truth model. The truth-model variance is then used in equation (26) to determine the threshold t_T. The resulting trigger test is shown in figure 7.
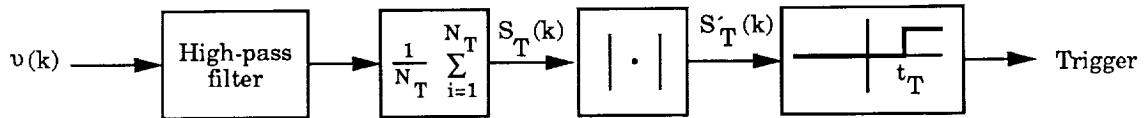

Figure 7. Actuator-path trigger test.

Verify test. The output of the trigger test is used to initiate the verify test, which is structured as a sequential probability ratio test (SPRT) as shown in figure 8. It has been shown (ref. 35) that, on the average, the SPRT decides between two hypotheses in a shorter time than a fixed-length test. If, in the design model (eqs. (1)), the signal s is a known constant, then at each sample time k after initiation of the test, the standard SPRT computes the likelihood ratio $\Lambda_V(k)$ as in equation (22). The likelihood ratio is then compared with two thresholds. If the ratio exceeds the upper threshold, hypothesis H_1 is accepted, and if the ratio is less than the lower threshold, hypothesis H_0 is accepted (or H_1 rejected). If the ratio is between the two thresholds, another sample is taken and the test is repeated. Mathematically, this procedure is expressed as follows:

$$
\left.
\begin{aligned}
\Lambda_V(k) &= \frac{p\left[\nu(k_T), \nu(k_T+1), \cdots, \nu(k)|H_1\right]}{p\left[\nu(k_T), \nu(k_T+1), \cdots, \nu(k)|H_0\right]} \\
&= \exp\left[\sum_{i=k_T}^{k} \frac{s\nu(i)}{\sigma_w^2} - \frac{s^2}{2\sigma_w^2}\right]
\end{aligned}
\right\}
\tag{27}
$$

If $\Lambda_V(k) \geq t_U$,   then decide H_1

If $t_L < \Lambda_V(k) < t_U$,   then take another sample

If $\Lambda_V(k) \leq t_L$,   then decide H_0

19
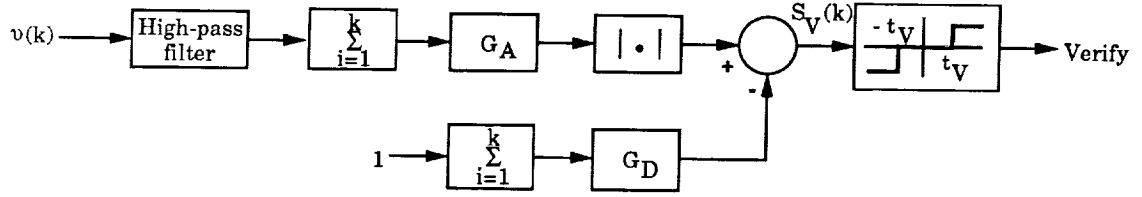
Figure 8. Actuator-path verify test.

It has been shown (ref. 35) that if P_M and P_{FA} are the desired missed-detection and false-alarm probabilities, then the thresholds should be set to

$$t_U = \frac{1 - P_M}{P_{FA}} \tag{28}$$

and

$$t_L = \frac{P_M}{1 - P_{FA}} \tag{29}$$

If the desired missed-detection and false-alarm probabilities are equal, then the test is symmetrical, and the thresholds become

$$t_U = -t_L = t_V \tag{30}$$

Instead of the likelihood ratio $\Lambda_V(k)$, the sufficient statistic $S_V(k)$ can be used, where (for notational simplicity k is redefined to begin when the trigger test passes)

$$S_V(k) = \sum_{i=1}^{k} \left[\nu(i) - \frac{s}{2} \right] \tag{31}$$

If $S_V(k) \geq t_V$,   then decide H_1

If $-t_V < S_V(k) < t_V$,   then take another sample

If $S_V(k) \leq -t_V$,   then decide H_0

From equations (27) and (31),

$$t_V = \left(\sigma_w^2 / s \right) \ln \left(t_U \right) \tag{32}$$

As a preface to designing the verify test with the truth model, a few characteristics of the design-model verify test should be discussed. First, the conditional expected values of the test statistic $S_V(k)$ are

$$E\{S_V(k)|H_1\} = \frac{ks}{2} \tag{33}$$

and

$$E\{S_V(k)|H_0\} = -\frac{ks}{2} \tag{34}$$

Also, the variance of the test statistic, independent of the hypothesis, is given by

$$\sigma_{S_V}^2(k) = k\sigma_w^2 \tag{35}$$

20

Consider a measure d^2 of the ability of a signal y to distinguish between two hypotheses H_0 and H_1, where the d^2 metric is defined by (ref. 25)

$$d^2 = \frac{(E\{y|H_1\} - E\{y|H_0\})^2}{\text{var}(y)} \tag{36}$$

The d^2 metric is then a measure of the distance between the means of the signal under the two hypotheses normalized by the standard deviation of the signal. For the test statistic $S_V(k)$, d^2 can be determined by using equations (33) to (36) as follows:

$$d^2(k) = \frac{ks^2}{\sigma_w^2} \tag{37}$$

Furthermore, at sample k_t when the expected value of the test signal equals the threshold, that is, when

$$E\{S_V(k_t)|H_1\} = t_V \tag{38}$$

then $d^2(k_t)$ is given by

$$d^2(k_t) = \frac{2st_V}{\sigma_w^2} = 2\ln\left(\frac{1 - P_M}{P_{FA}}\right) \tag{39}$$

These relationships will be used subsequently.

Thus far we have structured the verify test as an SPRT and have seen how the parameters can be chosen for the design model, that is, for the case of a constant in white Gaussian noise. Selecting the parameter values for the truth model is more difficult than for the trigger test. First of all, provisions must be made to assure that the test does not continue indefinitely without making a decision. Thus, if the test has not made a decision after N_V samples, the test will be terminated and a false trigger will be declared.

Following the procedure developed by Weiss (ref. 25), the gains G_A and G_D and the threshold t_V will be selected. The procedure is as follows:

1. Determine what value $\bar{s}$ of the failure signal s will produce a verify test at sample N_V that is reliable according to the d^2 metric; that is, solve the following equation for $\bar{s}$:

$$d^2(N_V) = \frac{N_V^2 \bar{s}^2}{\sigma_{S_V}^2(N_V)} = (2K_\sigma)^2 \tag{40}$$

where $2K_\sigma$ is the desired normalized distance between the means of $S_V(N_V)$ for reliable detection, and $\sigma_{S_V}^2(N_V)$ is the variance of $S_V(N_V)$, which is calculated as presented previously by using the model for $S_V(N_V)$ and solving the appropriate Lyapunov equation.

2. From figure 8, let

$$\left.\begin{array}{l} G_A = 1 \\[2mm] G_D = \dfrac{\bar{s}}{2} \end{array}\right\} \tag{41}$$

3. Determine the value k_t of k for which the d^2 metric equals or exceeds $2\ln[(1 - P_E)/P_E]$; that is, from equations (36) and (39) solve the following for k_t:

$$d^2(S_V(k_t)) = \frac{k_t^2 \bar{s}^2}{\sigma_{S_V}^2(k_t)} \geq 2\ln\left(\frac{1 - P_E}{P_E}\right) \tag{42}$$

21

4. Set the threshold t_V equal to the mean value of $S(k)$ at $k = k_t$ as follows:

$$t_V = E\{S_V(k_t)|H_1\} \tag{43}$$

This completes the design of the verify test with one exception. Since the sign of the failure signal s is unknown, take the absolute value of the sum of the residuals to form $S_V(k)$. The resulting configuration of the verify test is shown in figure 8.

Aircraft-Path Subsystem

Residual generation. The design of the aircraft-path subsystem must detect failures that occur outboard of the measurements of the actuator positions, failures such as a partially missing surface. When a failure of this type occurs, the response of the aircraft is different from the response that would normally be produced by the commands or controls. If this response is measured, and if a model could be used to predict the normal (unfailed) response to the commands in effect, then perhaps these responses could be compared to detect and isolate the failure. Thus, the first element in the aircraft-path subsystem is a residual generator, which utilizes measurements related to the aircraft state, measurements of the actuator positions, a linear model of the aircraft aerodynamics, and the nonlinear equations of motion in the residual-generation process.

To understand this residual-generation process in more detail, assume a rigid-body aircraft that is symmetrical with respect to the xz-plane, and neglect the rotation of the Earth. The equations of motion in body axes are (ref. 36)

$$\left.\begin{aligned}
X - mg\sin\theta &= m\left(\dot{U} + QW - RV\right) \\
Y + mg\cos\theta\sin\Phi &= m\left(\dot{V} + RU - PW\right) \\
Z + mg\cos\theta\cos\Phi &= m\left(\dot{W} + PV - QU\right) \\
L &= I_x\dot{P} - I_{zx}\left(\dot{R} + PQ\right) - \left(I_y - I_z\right)QR \\
M &= I_y\dot{Q} - I_{zx}\left(R^2 - P^2\right) - \left(I_z - I_x\right)RP \\
N &= I_z\dot{R} - I_{zx}\left(\dot{P} - QR\right) - \left(I_x - I_y\right)PQ
\end{aligned}\right\} \tag{44}$$

Uppercase symbols have been used to denote total quantities rather than perturbed quantities. Consider the first three equations of equations (44), which describe the translational dynamics of the aircraft. These can be arranged in units of linear acceleration as follows:

$$\left.\begin{aligned}
X/m &= \dot{U} + QW - RV + g\sin\theta \\
Y/m &= \dot{V} + RU - PW - g\cos\theta\sin\Phi \\
Z/m &= \dot{W} + PV - QU - g\cos\theta\cos\Phi
\end{aligned}\right\} \tag{45}$$

22

The quantities on the right side of equations (45) are the specific forces that are measured by the body-mounted accelerometers; that is, the accelerometer measurements at the center of gravity are

$$
\left.
\begin{aligned}
A_{m_x}^c &= \dot{U} + QW - RV + g\sin\theta + e_x \\
A_{m_y}^c &= \dot{V} + RU - PW - g\cos\theta\sin\Phi + e_y \\
A_{m_z}^c &= \dot{W} + PV - QU - g\cos\theta\cos\Phi + e_z
\end{aligned}
\right\}
\tag{46}
$$

where e_i is the measurement error.

If a model of the aircraft aerodynamics could be used to compute predicted values for the forces X, Y, and Z as functions of the aircraft state and the control-surface positions, we could compare these predictions with the accelerometer measurements to form residuals. These residuals would normally (no failures) be zero except for noise and model errors. To compute these predicted values, consider that estimates $\widehat{X}$, $\widehat{Y}$, and $\widehat{Z}$ of the forces can be expressed as functions of the nondimensional coefficients as follows:

$$
\left.
\begin{aligned}
\widehat{X} &= \bar{q}S\widehat{C}_x \\
\widehat{Y} &= \bar{q}S\widehat{C}_y \\
\widehat{Z} &= \bar{q}S\widehat{C}_z
\end{aligned}
\right\}
\tag{47}
$$

where $\bar{q}$ is the dynamic pressure and S is the reference wing area. In the vicinity of a single-aircraft operating point, such as the one given in table 1, the coefficients can be approximated as a truncated Taylor series that retains only the first derivatives as follows:

$$
\left.
\begin{aligned}
\widehat{C}_x &= C_{x0} + C_{x_\alpha}\alpha_m^c + \frac{\bar{c}}{2V_{T_0}}C_{x_q}qm + \sum_i C_{x_{\delta_i}}\delta m_i \\
\widehat{C}_y &= C_{y0} + C_{y_\beta}\beta_m^c + \frac{b}{2V_{T_0}}\left(C_{y_p}pm + C_{y_r}rm\right) + \sum_i C_{y_{\delta_i}}\delta m_i \\
\widehat{C}_z &= C_{z0} + C_{z_\alpha}\alpha_m^c + \frac{\bar{c}}{2V_{T_0}}C_{z_q}qm + \sum_i C_{z_{\delta_i}}\delta m_i
\end{aligned}
\right\}
\tag{48}
$$

In equations (48) the air-data variables α_m^c and β_m^c, the body-axis angular rates p_m, q_m, and r_m, and the surface deflections δ_{m_i} are perturbed quantities relative to the operating point, or trim values. Effects of the trim values are contained in the constants C_{x0}, C_{y0}, and C_{z0}. Predicted, or estimated, values of the forces can now be computed by using equations (47) and (48), and the following residuals can be formed for the linear accelerations:

$$
\left.
\begin{aligned}
\nu_x &= A_{m_x}^c - \widehat{X}/m \\
\nu_y &= A_{m_y}^c - \widehat{Y}/m \\
\nu_z &= A_{m_z}^c - \widehat{Z}/m
\end{aligned}
\right\}
\tag{49}
$$

23

The last three equations of equations (44) can be rearranged as follows, neglecting cross products of inertia:

$$\left.\begin{aligned}
\dot{P} &= \frac{1}{I_x}L + \frac{I_y - I_z}{I_x}QR \\[2mm]
\dot{Q} &= \frac{1}{I_y}M + \frac{I_z - I_x}{I_y}RP \\[2mm]
\dot{R} &= \frac{1}{I_z}N + \frac{I_x - I_y}{I_z}PQ
\end{aligned}\right\} \tag{50}$$

For the purpose of forming residuals, predicted values of the right-hand sides of equations (50) can be obtained by using measured quantities for the angular rates P, Q, and R and by using estimates of the moments L, M, and N as with the previous forces. In particular, let the moments be expressed as

$$\left.\begin{aligned}
\widehat{L} &= \bar{q}Sb\widehat{C}_\ell \\[2mm]
\widehat{M} &= \bar{q}S\bar{c}\widehat{C}_m \\[2mm]
\widehat{N} &= \bar{q}Sb\widehat{C}_n
\end{aligned}\right\} \tag{51}$$

Now approximate the coefficients $\widehat{C}_i$ as the linear terms of a Taylor series expansion as follows:

$$\left.\begin{aligned}
\widehat{C}_\ell &= C_{\ell_0} + C_{\ell_\beta}\beta_m^c + \frac{b}{2V_{T_0}}\left(C_{\ell_p}p_m + C_{\ell_r}r_m\right) + \sum_i C_{\ell_{\delta_i}}\delta_{m_i} \\[3mm]
\widehat{C}_m &= C_{m_0} + C_{m_\alpha}\alpha_m^c + \frac{\bar{c}}{2V_{T_0}}C_{m_q}q_m + \sum_i C_{m_{\delta_i}}\delta_{m_i} \\[3mm]
\widehat{C}_n &= C_{n_0} + C_{n_\beta}\beta_m^c + \frac{b}{2V_{T_0}}\left(C_{n_p}p_m + C_{n_r}r_m\right) + \sum_i C_{n_{\delta_i}}\delta_{m_i}
\end{aligned}\right\} \tag{52}$$

As in equations (48), the air-data variables, the body-axis angular rates, and the surface deflections are perturbed values relative to the operating point. Equations (50), (51), and (52) can now be combined to obtain predicted values for the angular accelerations as follows:

$$\left.\begin{aligned}
\widehat{\dot{P}} &= \frac{1}{I_x}\widehat{L} + \frac{I_y - I_z}{I_x}Q_m R_m \\[2mm]
\widehat{\dot{Q}} &= \frac{1}{I_y}\widehat{M} + \frac{I_z - I_x}{I_y}R_m P_m \\[2mm]
\widehat{\dot{R}} &= \frac{1}{I_z}\widehat{N} + \frac{I_x - I_y}{I_z}P_m Q_m
\end{aligned}\right\} \tag{53}$$

These predicted quantities could now be compared with the measured values $\dot{P}_m$, $\dot{Q}_m$, and $\dot{R}_m$ of the angular accelerations if they were available; however, angular accelerations normally are not measured. Therefore, residuals are formed by comparing the predicted change in angular rate in one sample period with the change obtained from differencing successive measurements

of angular rate. Let

$$
\left.\begin{array}{l}
\Delta\widehat{P}(k) = \dfrac{\Delta t}{2}\left[\widehat{P}(k) + \widehat{P}(k-1)\right] \\[2mm]
\Delta\widehat{Q}(k) = \dfrac{\Delta t}{2}\left[\widehat{Q}(k) + \widehat{Q}(k-1)\right] \\[2mm]
\Delta\widehat{R}(k) = \dfrac{\Delta t}{2}\left[\widehat{R}(k) + \widehat{R}(k-1)\right]
\end{array}\right\}
\tag{54}
$$

Also, let

$$
\left.\begin{array}{l}
\Delta P_m(k) = P_m(k) - P_m(k-1) \\[2mm]
\Delta Q_m(k) = Q_m(k) - Q_m(k-1) \\[2mm]
\Delta R_m(k) = R_m(k) - R_m(k-1)
\end{array}\right\}
\tag{55}
$$

The residuals can now be formed as follows:

$$
\left.\begin{array}{l}
\nu_P(k) = \Delta P_m(k) - \Delta\widehat{P}(k) \\[2mm]
\nu_Q(k) = \Delta Q_m(k) - \Delta\widehat{Q}(k) \\[2mm]
\nu_R(k) = \Delta R_m(k) - \Delta\widehat{R}(k)
\end{array}\right\}
\tag{56}
$$

In equations (48), (52), (53), and (55), measured values of the attitude rates are used. Although perturbed values of these rates are used in equations (48) and (52), these will usually be the same as the total values, since the attitude rates are normally zero at trim. The angles of attack and sideslip in equations (48) and (52) are perturbed, measured quantities that have compensated for lever-arm effects if the α and β sensors are not at the center of gravity; that is,

$$
\left.\begin{array}{l}
\alpha_m^c = \alpha_m + \ell_x\left(Q_m/V_{T_m}\right) - \ell_y\left(P_m/V_{T_m}\right) - \alpha_0 \\[2mm]
\beta_m^c = \beta_m - \ell_x\left(R_m/V_{T_m}\right) + \ell_z\left(P_m/V_{T_m}\right) - \beta_0
\end{array}\right\}
\tag{57}
$$

Also, the accelerations in equations (46) and (49) are measured quantities that include compensation for a location other than the center of gravity; that is,

$$
\left.\begin{array}{l}
A_{m_x}^c = A_{m_x} - \left[-\ell_x\left(R_m^2 + Q_m^2\right) + \ell_y\left(P_m Q_m - \dot{R}_m\right) + \ell_z\left(P_m R_m + \dot{Q}_m\right)\right] \\[2mm]
A_{m_y}^c = A_{m_y} - \left[\ell_x\left(P_m Q_m + \dot{R}_m\right) - \ell_y\left(P_m^2 + R_m^2\right) + \ell_z\left(R_m Q_m - \dot{P}_m\right)\right] \\[2mm]
A_{m_z}^c = A_{m_z} - \left[\ell_x\left(R_m P_m - \dot{Q}_m\right) + \ell_y\left(R_m Q_m + \dot{P}_m\right) - \ell_z\left(Q_m^2 + P_m^2\right)\right]
\end{array}\right\}
\tag{58}
$$

The residuals from equations (49) and (56) form a six-dimensional vector sequence of residuals $\boldsymbol{\nu}(k)$ as follows:

$$
\boldsymbol{\nu}(k) =
\begin{bmatrix}
\nu_1(k) \\
\nu_2(k) \\
\nu_3(k) \\
\nu_4(k) \\
\nu_5(k) \\
\nu_6(k)
\end{bmatrix}
=
\begin{bmatrix}
\nu_x(k) \\
\nu_y(k) \\
\nu_z(k) \\
\nu_P(k) \\
\nu_Q(k) \\
\nu_R(k)
\end{bmatrix}
\tag{59}
$$

25

To see what happens to the residual $\boldsymbol{\nu}(k)$ in the event of a failure, consider the first component $\nu_x(k)$ when a portion of the jth control surface is lost at time $k = k_f$. From equations (47), (48), and (49)

$$\nu_x(k) = A^c_{m_x} - \frac{\widehat{X}}{m} = A^c_{m_x} - \frac{\bar{q}S}{m}\widehat{C}_x$$

$$= A^c_{m_x} - \frac{\bar{q}S}{m}\left[C_{x_0} + C_{x_\alpha}\alpha^c_m(k) + \frac{\bar{c}}{2V_{T_0}}C_{x_q}qm(k) + \sum_i C_{x_{\delta_i}}\delta_{m_i}(k)\right] \qquad (60)$$

As shown by Weiss (ref. 25), the aerodynamic coefficients can be expressed in terms of elements of the $\mathbf{A}$ and $\mathbf{B}$ matrices. Equation (60) can then be written as

$$\nu_x(k) = A^c_{m_x} - \frac{\bar{q}S}{m}C_{x_0} - \left[-A_{11}W_0 + (Q_0 + A_{12})U_0\right]\alpha^c_m(k)$$

$$- (W_0 + A_{13})qm(k) - \sum_i B_{1i}\delta_{m_i}(k) \qquad (61)$$

If there were no noise, no model errors, and no failures, then $\nu_x(k)$ would be zero. Suppose that at $k = k_f$, a portion of control surface j is lost, such that a fraction ϵ of its effectiveness is lost. Then the residual is described by .

$$\nu_x(k) = B_{1j}\epsilon\delta_{m_j}(k) \qquad\qquad (k \geq k_f) \qquad (62)$$

Similar results hold for the other components of the residual vector, so that $\boldsymbol{\nu}(k)$ can be expressed as

$$\boldsymbol{\nu}(k) = \mathbf{B}_j\epsilon\delta_{m_j} = \mathbf{B}_j f_s = \mathbf{s} \qquad\qquad (k \geq k_f) \qquad (63)$$

where $\mathbf{B}_j$ is the jth column of the $\mathbf{B}$ matrix, and f_s is the effective failure magnitude.

Design model. In a realistic system, there is sensor noise and quantization noise, and there are errors due to modeling inaccuracies; these add a random component $\mathbf{n}(k)$ to the residual sequence $\boldsymbol{\nu}(k)$. When a failure of the ith surface has occurred, a time-varying component $\mathbf{B}_i f_s(k)$ results from the failure; this component is the signal that must be detected to detect a failure. As in the actuator-path subsystem, it is assumed for design purposes that this time variation is slow compared with the detection time of 0.5 to 2 sec. Furthermore, it is assumed that the random component is a zero-mean, white Gaussian vector sequence with uncorrelated components. The design model $\boldsymbol{\nu}(k)$ of the residual is then

$$\left.\begin{array}{l} H_i: \; \boldsymbol{\nu}_d(k) = \mathbf{s}_i + \mathbf{n}_w(k) \\[2mm] H_0: \; \boldsymbol{\nu}_d(k) = \mathbf{n}_w(k) \end{array}\right\} \qquad (64)$$

where $\mathbf{s}_i$ is the failure signal and $\mathbf{n}_w(k)$ is white Gaussian noise. The conditional probability density functions for $\boldsymbol{\nu}_d(k)$ are

$$\left.\begin{array}{l} H_i: \; p\left(\boldsymbol{\nu}_d(k)|H_i\right) = \dfrac{1}{(2\pi)^3\left[\det\left(\boldsymbol{\Sigma}_w\right)\right]^{1/2}}\exp\left\{-\dfrac{1}{2}\left[\boldsymbol{\nu}_d(k) - \mathbf{s}_i\right]^T\boldsymbol{\Sigma}_w^{-1}\left[\boldsymbol{\nu}_d(k) - \mathbf{s}_i\right]\right\} \\[5mm] H_0: \; p\left(\boldsymbol{\nu}_d(k)|H_0\right) = \dfrac{1}{(2\pi)^3\left[\det\left(\boldsymbol{\Sigma}_w\right)\right]^{1/2}}\exp\left\{-\dfrac{1}{2}\boldsymbol{\nu}_d^T(k)\boldsymbol{\Sigma}_w^{-1}\boldsymbol{\nu}_d(k)\right\} \end{array}\right\} \qquad (65)$$

where the covariance matrix $\mathbf{\Sigma}_w$ of $\mathbf{n}_w(k)$ is diagonal. The decision process is structured according to this design model.

Truth model. As in the case of the actuator-path subsystem, the truth model for the residuals used in determining the parameters of the decision process includes a low-frequency noise term $\mathbf{n}_{\ell h}(k)$ to account for sensor biases and other model errors. As noted previously, the decision process assumes that the random component of the residual is white. Therefore, a high-pass whitening prefilter is used between the residual generator and the decision algorithm to decorrelate the residual noise. The filter cutoff frequency is chosen to be less than the inverse of the detection time to preserve the coherence of the signal. The truth model for the residuals then becomes

$$
\left.
\begin{aligned}
H_i &: \quad \nu_t(k) = \mathbf{s}_{ih} + \mathbf{n}_{\ell h}(k) + \mathbf{n}_{wh}(k) \\
H_0 &: \quad \nu_t(k) = \mathbf{n}_{\ell h}(k) + \mathbf{n}_{wh}(k)
\end{aligned}
\right\}
\tag{66}
$$

where the subscript h denotes the quantity after high-pass filtering and $\mathbf{\Sigma}_\ell$ is the variance of the low-frequency noise $\mathbf{n}_\ell(k)$ before high-pass filtering; $\mathbf{\Sigma}_\ell$ is assumed to be diagonal.

To improve detection performance, the decision process again utilizes a signal $\mathbf{S}(N)$ that is the sum of the residuals over N samples; that is,

$$
\mathbf{S}(N) = \sum_{k=1}^{N} \nu_t(k)
\tag{67}
$$

The covariance $\mathbf{\Sigma}_f$ of $\mathbf{S}(N)$ can be approximated as $\mathbf{\Sigma}_f = N^2 \mathbf{\Sigma}_\ell + N \mathbf{\Sigma}_w$. Since $\mathbf{\Sigma}_f$ is diagonal, each element σ_{ii}^2 of $\mathbf{\Sigma}_f$ can be determined separately. Express each component of the noise vector $\mathbf{n}(k) = \mathbf{n}_{\ell h}(k) + \mathbf{n}_{wh}(k)$ in state space as the output of a linear system, as was done with the scalar noise $n(k)$ in the actuator path, and then solve the Lyapunov equation.

Trigger tests. Based on the design model, the trigger test for the ith surface must decide whether a constant vector signal $\mathbf{s}_i$ is present (hypothesis H_i) or not (hypothesis H_0), where the signal is corrupted by additive white Gaussian noise. The resulting trigger test for the ith failure in the aircraft path, as with the actuator path, is based on computing the log likelihood ratio $\Lambda_{T_i}(k)$ of a window of the most recent N_T residuals. That ratio is

$$
\Lambda_{T_i}(k) = \sum_{j=k-N_T+1}^{k} \left\{ \mathbf{s}_i^T \mathbf{\Sigma}_w^{-1} \nu(j) - \frac{1}{2} \mathbf{s}_i^T \mathbf{\Sigma}_w^{-1} \mathbf{s}_i \right\}
\tag{68}
$$

An equivalent statistic is

$$
S_{T_i}(k) = \sum_{j=k-N_T+1}^{k} \mathbf{P}_i^T \nu(j)
\tag{69}
$$

where the projection vector $\mathbf{P}_i$ is used to produce a scalar metric for the test, and the residuals are computed as in equations (49), (56), and (59). Since the $\nu(k)$'s are independent, $S_{T_i}(k)$ is

27

Gaussian with conditional means and variance as follows:

$$E\left\{S_{T_i}(k)|H_i\right\} = N_T \mathbf{P}_i^T \mathbf{s}$$

$$E\left\{S_{T_i}(k)|H_0\right\} = 0$$

$$\text{var}\left(S_{T_i}(k)|H_i\right) = \text{var}\left(S_{T_i}(k)|H_0\right) = \sigma_d^2 = N_T \mathbf{P}_i^T \mathbf{\Sigma}_w \mathbf{P}_i \qquad (70)$$

The trigger test becomes

$$S_{T_i}(k)\begin{cases} \geq t_{T_i}, & \text{then } H_1 \\ < t_{T_i}, & \text{then } H_0 \end{cases} \qquad (71)$$

where the threshold t_{T_i} is determined as in the actuator-path subsystem. First, for the design model, the probability of false alarm is given by equation (25). In equation (26), K_σ is chosen to achieve the desired false-alarm rate. The number of samples N_T to use in the tests is chosen to minimize the trigger time while maintaining reliable tests. If any of these tests pass (H_i accepted), a trigger flag F_{T_i} is set to TRUE.

Now that the basic structure of the trigger test has been chosen, the whitening prefilter is inserted. To choose the threshold, consider the test statistic $S_{T_i}(k)$ under the truth model. Equations (5) to (21), (66), and (67) are used to compute the variance $\mathbf{\Sigma}_f$ of the sum of N_T residuals by using the truth model as previously described. The conditional means and variance of the test statistic are

$$E\left\{S_{T_i}(k)|H_i\right\} = N_T \mathbf{P}_i^T \mathbf{B}_i f_s$$

$$E\left\{S_{T_i}(k)|H_0\right\} = 0$$

$$\text{var}\left(S_{T_i}(k)\right) = \sigma_{S_{T_i}}^2 = \mathbf{P}_i^T \mathbf{\Sigma}_f \mathbf{P}_i \qquad (72)$$

The variance $\sigma_{S_{T_i}}^2$ is then used in equation (26) to determine the threshold t_{T_i}, as was done previously for the actuator-path trigger test.

The remaining step in the design of the trigger test is the computation of the projection vector $\mathbf{P}_i$. The projection vector is chosen to optimize the d^2 metric for the test statistic $S_{T_i}(k)$; the signal-to-noise ratio for the given values of the failure signal $\mathbf{s}_i = \mathbf{B}_i f_s$ and noise $\mathbf{\Sigma}_f$ is thus maximized, and the probabilities of detection and false alarm are improved. For the truth model

$$d^2\left(S_{T_i}\right) = \frac{\left(N_T \mathbf{P}_i^T \mathbf{B}_i f_s\right)^2}{\mathbf{P}_i^T \mathbf{\Sigma}_f \mathbf{P}_i} \qquad (73)$$

from equations (36) and (72). Weiss (ref. 25) has shown that d^2 is maximized by choosing $\mathbf{P}_i$ such that

$$\mathbf{P}_i = K \mathbf{\Sigma}_f^{-1} \mathbf{B}_i f_s \qquad (74)$$

where K is any scalar constant. Normally, K is chosen to normalize the projection vector to unity magnitude, such that $\mathbf{P}_i$ becomes

$$\mathbf{P}_i = \frac{\mathbf{\Sigma}_f^{-1} \mathbf{B}_i}{\left[\left(\mathbf{\Sigma}_f^{-1} \mathbf{B}_i\right)^T \left(\mathbf{\Sigma}_f^{-1} \mathbf{B}_i\right)\right]^{1/2}} \qquad (75)$$

The minimum signal magnitude $\bar{f}_{s_i}$ required to achieve the desired value $(2K_\sigma)^2$ of d^2 can now be computed from equations (72) and (73) as follows:

$$\bar{f}_{s_i} = \left(2K_\sigma \sigma_{S_{T_i}}\right) / \left(N_T \mathbf{P}_i^T \mathbf{B}_i\right) \tag{76}$$

In quest of robustness to modeling errors, the projection vectors are examined to determine if any components can be eliminated (set to zero). The criteria are as follows: eliminate the jth component of $\mathbf{P}_i$ and recompute $\sigma_{S_{T_i}}^2$, t_{T_i}, and $\bar{f}_{s_i}$. If $\bar{f}_{s_i}$ changes insignificantly (e.g., less than 5 percent) from its previous value, then the jth component of $\mathbf{P}_i$ is set to zero, and modeling errors in the corresponding component of the residual are not reflected into the test statistic. Otherwise it is restored to its original value. This procedure is repeated for each component of the projection vector. To account for the unknown sign of f_s, the absolute value of $S_{T_i}(k)$ is taken before comparing it with the threshold. With this addition, the design of the trigger test is complete, and the final test is shown in figure 9.
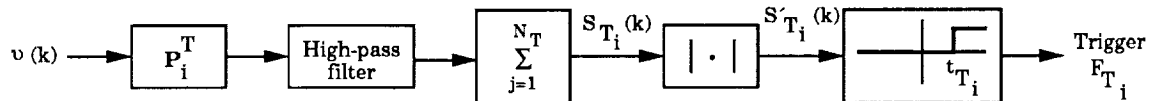

Figure 9. Aircraft-path trigger test.

Verify tests. The verify tests in the aircraft path are SPRT's similar to those in the actuator path. The difference is that, since the aircraft-path residual sequence $\nu(k)$ is a vector sequence, a projection vector $\mathbf{P}_i$ must be incorporated, as in the trigger tests, and this vector results in the verify test shown in figure 10. Before proceeding with the design, note that when using the truth model, the statistics of $S_{V_i}(k)$ are

$$
\begin{aligned}
E\left\{S_{V_i}(k)|H_i\right\} &= kG_A \mathbf{P}_i^T \mathbf{B}_i f_s - kG_D \\
E\left\{S_{V_i}(k)|H_0\right\} &= -kG_D \\
\text{var}\left[S_{V_i}(k)\right] &= \sigma_{S_{V_i}}^2 = G_A^2 \mathbf{P}_i^T \Sigma_f(k)\mathbf{P}_i
\end{aligned}
\right\} \tag{77}
$$
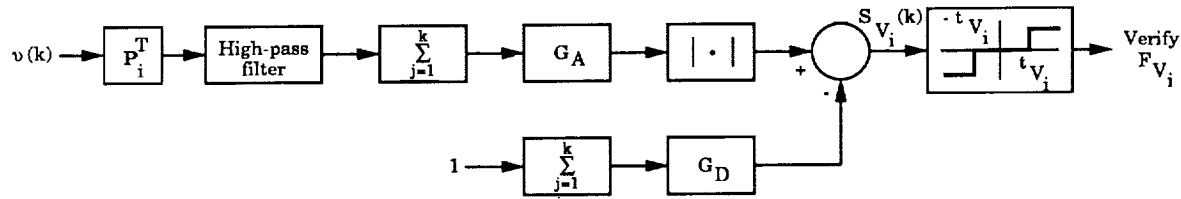
Figure 10. Aircraft-path verify test.

After the maximum test length N_V is selected, the projection vector is chosen to maximize the d^2 metric at the end of the maximal length test $(k = N_V)$.

$$d^2 \left(S_{V_i} (N_V) \right) = \frac{\left(N_V \mathbf{P}_i^T \mathbf{B}_i f_s \right)^2}{\mathbf{P}_i^T \Sigma_f (N_V) \mathbf{P}_i} \qquad (78)$$

As with the trigger test, the result is that $\mathbf{P}_i$ is given by equation (74) as

$$\mathbf{P}_i = K \Sigma_f^{-1} (N_V) \mathbf{B}_i f_s$$

If $N_V = N_T$, then the projection vectors for the verify tests are identical to those in the trigger tests.

The remaining parameters $(G_{A_i}, G_{D_i}, \text{and } t_{V_i})$ are chosen by using the following four-step procedure described for the actuator-verify tests:

1. Determine what value of the failure signal $\bar{f}_{s_i}$ produces a verify test at sample N_V that is reliable according to the d^2 metric; that is,

$$\bar{s}_i = \mathbf{P}_i^T \mathbf{B}_i \bar{f}_{s_i} = \left[2 K_\sigma \sigma_{S_{V_i}} (N_V) \right] \Big/ (N_V G_A)$$

$$= 2 K_\sigma \left[\mathbf{P}_i^T \Sigma_f (N_V) \mathbf{P}_i \right]^{1/2} \Big/ N_V \qquad (79)$$

where $2 K_\sigma$ is the desired value of d.

2. Let

$$\left. \begin{aligned} G_{A_i} &= \mathbf{P}_i^T \mathbf{B}_i \bar{f}_{s_i} = \bar{s}_i \\ G_{D_i} &= \left(\mathbf{P}_i^T \mathbf{B}_i \bar{f}_{s_i} \right)^2 \Big/ 2 = \bar{s}_i^2 / 2 \end{aligned} \right\} \qquad (80)$$

3. Determine the value k_{t_i} of k for which the d^2 metric equals or exceeds $2 \ln \left[(1 - P_E) / P_E \right]$; that is, solve the following for k_{t_i}:

$$d^2 \left(S_{V_i} (k_{t_i}) \right) = \left[k_{t_i} \mathbf{P}_i^T \mathbf{B}_i \bar{f}_{s_i} \right]^2 \Big/ \left[\mathbf{P}_i^T \Sigma_f (k_{t_i}) \mathbf{P}_i \right]$$

$$\geq 2 \ln \left[(1 - P_E) / P_E \right] \qquad (81)$$

4. Set the threshold t_{V_i} equal to the mean value of $S_{V_i} (k_{t_i})$ as follows:

$$t_{V_i} = E \left\{ S_{V_i} (k_{t_i}) | H_i \right\} = \frac{k_t \bar{s}_i^2}{2} \qquad (82)$$

Whenever the ith verify-test statistic exceeds this threshold, the ith verify flag F_{V_i} is set to TRUE (1). If the test statistic becomes less than $-t_{V_i}$, F_{V_i} is set to FALSE (0). Otherwise, F_{V_i} remains undecided (2). This completes the design of the verify tests.

Isolate tests. The purpose of the isolate tests is to help decide which surface failed when a trigger test and a verify test have passed. The isolate tests are initiated by the trigger tests and operate in parallel with the verify tests. The isolate tests are designed to decide between two hypotheses, H_i and H_j, which represent failures in the ith and jth surfaces, respectively. In reality, of course, both of these may be false. Ambiguities that result from these tests are resolved by a subsequent algorithm.

30

As a design model, assume that the residual vector sequence $\nu(k)$ is composed of either of two constants $\mathbf{B}_i f_s$ or $\mathbf{B}_j f_s$, plus additive white Gaussian noise $\mathbf{n}_w(k)$:

$$\left.\begin{aligned} H_i: \quad \nu_d(k) &= \mathbf{B}_i f_s + \mathbf{n}_w(k) \\ H_j: \quad \nu_d(k) &= \mathbf{B}_j f_s + \mathbf{n}_w(k) \end{aligned}\right\} \tag{83}$$

The conditional probability density functions for $\nu_d(k)$ are

$$\left.\begin{aligned} H_i: \quad p\left(\nu_d(k)|H_i\right) &= \frac{1}{(2\pi)^{6/2}\left[\det\left(\mathbf{\Sigma}_w\right)\right]^{1/2}} \\ &\quad \times \exp\left\{-\frac{1}{2}\left[\nu_d(k) - \mathbf{B}_i f_s\right]^T \mathbf{\Sigma}_w^{-1} \left[\nu_d(k) - \mathbf{B}_i f_s\right]\right\} \\ H_j: \quad p\left(\nu_d(k)|H_j\right) &= \frac{1}{(2\pi)^{6/2}\left[\det\left(\mathbf{\Sigma}_w\right)\right]^{1/2}} \\ &\quad \times \exp\left\{-\frac{1}{2}\left[\nu_d(k) - \mathbf{B}_j f_s\right]^T \mathbf{\Sigma}_w^{-1} \left[\nu_d(k) - \mathbf{B}_j f_s\right]\right\} \end{aligned}\right\} \tag{84}$$

where the covariance matrix $\mathbf{\Sigma}_w$ of $\mathbf{n}_w(k)$ is diagonal.

One test for deciding between H_i and H_j is the sequential probability ratio test shown in figure 11 and described by

$$\begin{aligned} S_{I_{i/j}}\left(k - k_T + 1\right) &= \left|S_{\gamma_j}\left(k - k_T + 1\right)\right| - \left|S_{\gamma_i}\left(k - k_T + 1\right)\right| \\ &= \left|\sum_{m=k_T}^{k} \gamma_j(m)\right| - \left|\sum_{m=k_T}^{k} \gamma_i(m)\right| \end{aligned} \tag{85}$$

If $S_{I_{i/j}}(k - k_T - 1) \geq t_{I_{i/j}}$, then decide H_j $\left(F_{I_{i/j}} = 0\right)$

If $-t_{I_{i/j}} < S_{I_{i/j}}(k - k_T + 1) < t_{I_{i/j}}$, then take another sample $\left(F_{I_{i/j}} = 2\right)$

If $S_{I_{i/j}}(k - k_T - 1) \leq -t_{I_{i/j}}$, then decide H_i $\left(F_{I_{i/j}} = 1\right)$

where k_T is the trigger time. The absolute values have been used because the signs of the failure signals $\mathbf{B}_i f_s$ and $\mathbf{B}_j f_s$ are unknown. As with the verify tests, a maximum test length N_I is selected. The other parameters of the test $(\mathbf{P}_{i/j}, \mathbf{P}_{j/i},$ and $t_{I_{i/j}})$ are chosen using the truth model. The random component of the residuals in the truth model is the same as that used in the aircraft-path verify tests. The signals, or mean values, under the two hypotheses are the same as in the design model discussed previously.

With this truth model and this test structure, and if the absolute-value functions are neglected, the relevant statistics for the isolate test are (where k is the number of samples from trigger time to simplify notation)

$$\left.\begin{aligned} E\left\{S_{\gamma_i}(k)|H_i\right\} &= k\mathbf{P}_{i/j}^T \mathbf{B}_i f_s \\ E\left\{S_{\gamma_i}(k)|H_j\right\} &= 0 \end{aligned}\right\} \tag{86}$$

31
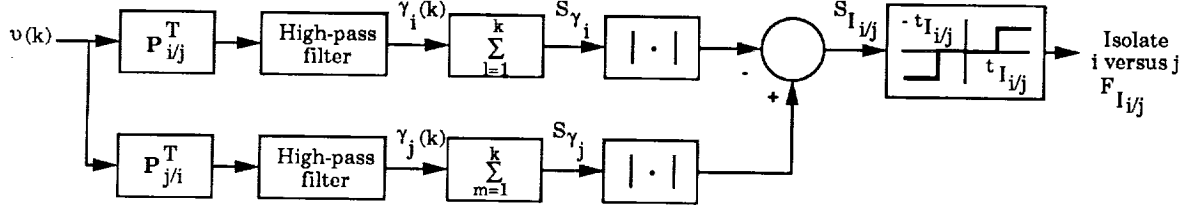
Figure 11. Aircraft-path isolation test.

$$\text{var}\left[S_{\gamma_i}(k)|H_i, H_j\right] = \mathbf{P}_{i/j}^T \boldsymbol{\Sigma}_f(k)\mathbf{P}_{i/j} \tag{87}$$

$$d^2\left(S_{\gamma_i}(k)\right) = \frac{k^2\left(\mathbf{P}_{i/j}^T \mathbf{B}_i\right)^2 f_s^2}{\mathbf{P}_{i/j}^T \boldsymbol{\Sigma}_f(k)\mathbf{P}_{i/j}} \tag{88}$$

$$\left.\begin{aligned} E\left\{S_{I_{i/j}}(k)|H_i\right\} &= k\mathbf{P}_{i/j}^T \mathbf{B}_i f_s \\ E\left\{S_{I_{i/j}}(k)|H_j\right\} &= -k\mathbf{P}_{j/i}^T \mathbf{B}_j f_s \end{aligned}\right\} \tag{89}$$

$$\begin{aligned} \sigma_{S_{I_{i/j}}}^2 &= \text{var}\left[S_{I_{i/j}}(k)|H_i, H_j\right] \\ &= \left(\mathbf{P}_{i/j}^T - \mathbf{P}_{j/i}^T\right)\boldsymbol{\Sigma}_f\left(\mathbf{P}_{i/j} - \mathbf{P}_{j/i}\right) \\ &\le \mathbf{P}_{i/j}^T \boldsymbol{\Sigma}_f(k)\mathbf{P}_{i/j} + \mathbf{P}_{j/i}^T \boldsymbol{\Sigma}_f(k)\mathbf{P}_{j/i} \end{aligned} \tag{90}$$

$$d^2\left(S_{I_{i/j}}(k)\right) \ge \frac{k^2\left(\mathbf{P}_{i/j}\mathbf{B}_i + \mathbf{P}_{j/i}\mathbf{B}_j\right)^2 f_s^2}{\mathbf{P}_{i/j}^T \boldsymbol{\Sigma}_f(k)\mathbf{P}_{i/j} + \mathbf{P}_{j/i}^T \boldsymbol{\Sigma}_f(k)\mathbf{P}_{j/i}} \tag{91}$$

The following procedure, which is similar to that used for the verify tests, is used to choose the parameters for the isolate tests:

1. Choose the projection operator $\mathbf{P}_{i/j}$ to maximize the sensitivity of the test to the ith failure while making it minimally sensitive to the jth failure. This is done by selecting $\mathbf{P}_{i/j}$ to maximize $d^2\left(S_{\gamma_i}(N_I)\right)$, subject to the constraint

$$\mathbf{P}_{i/j}^T \mathbf{B}_j = 0 \tag{92}$$

Weiss (ref. 25) has shown that the solution is given by

$$\mathbf{P}_{i/j} = K\boldsymbol{\Sigma}_f^{-1}(N_I)\left[\mathbf{B}_i - \frac{\mathbf{B}_i^T \boldsymbol{\Sigma}_f^{-1}(N_I)\mathbf{B}_j}{\mathbf{B}_j^T \boldsymbol{\Sigma}_f^{-1}(N_I)\mathbf{B}_j}\mathbf{B}_j\right] \tag{93}$$

where K is chosen to normalize $\mathbf{P}_{i/j}$ to unit length; $\mathbf{P}_{j/i}$ is similarly computed.

2. Determine the minimum failure-signal amplitude $\bar{f}s_{i/j}$ that produces the desired value of $d^2\left(S_{I_{i/j}}(N_I)\right)$ for the maximal length test (eq. (91)):

$$\bar{s}_{i/j} = \frac{K_\sigma \sigma_{S_{I_{i/j}}}}{N_I} \tag{94}$$

$$\left.\begin{array}{l} \bar{f}s_{i/j} = \bar{s}_{i/j} / \left(\mathbf{P}_{i/j}^T \mathbf{B}_i\right) \\[2mm] \bar{f}s_{j/i} = \bar{s}_{i/j} / \left(\mathbf{P}_{j/i}^T \mathbf{B}_j\right) \end{array}\right\} \tag{95}$$

3. Determine the threshold $t_{I_{i/j}}$ by setting it equal to the expected value of the test statistic at the same stage (sample number) $k_{t_{i/j}}$ in the test at which the d^2 metric is $2\ln\left[(1-P_E)/P_E\right]$; P_E is the desired minimum probability of error in the test. This is done by using the minimum signal amplitude $\bar{s}_{i/j}$ from step 2 and solving

$$\frac{4k^2\bar{s}_{i/j}^2}{\sigma_{S_{I_{i/j}}}^2(k)} \geq 2\ln\left[(1-P_E)/P_E\right] \tag{96}$$

for the minimum value $k_{I_{i/j}}$ of k that satisfies equation (96). Then, the threshold $t_{I_{i/j}}$ is given by

$$\begin{aligned} t_{I_{i/j}} &= E\left[S_{I_{i/j}}\left(k_{I_{i/j}}\right)\Big|H_i\right] \\[2mm] &= k_{I_{i/j}}\mathbf{P}_{i/j}^T\mathbf{B}_i\bar{f}s_{i/j} \end{aligned} \tag{97}$$

4. As with the trigger-verify projection vectors, examine each component of the $\mathbf{P}_{i/j}$ to determine whether that component can be eliminated without severely affecting nominal performance. The criterion is as follows: eliminate the mth components of $\mathbf{P}_{i/j}$ and $\mathbf{P}_{j/i}$ by eliminating the mth components of $\mathbf{B}_i$ and $\mathbf{B}_j$ and recomputing $\mathbf{P}_{i/j}$ and $\mathbf{P}_{j/i}$ by using equation (93). Recompute $\bar{f}s_{i/j}$ and $\bar{f}s_{j/i}$. If $\bar{f}s_{i/j} + \bar{f}s_{j/i}$ changes insignificantly (e.g., less than 5 percent) from its previous value, use the new values of $\mathbf{P}_{i/j}$ and $\mathbf{P}_{j/i}$ with zero mth components. Otherwise, return to the previous vectors $\mathbf{P}_{i/j}$ and $\mathbf{P}_{j/i}$. This procedure is repeated for each component of the projection vectors. New thresholds $t_{I_{i/j}}$ are then computed by using equation (97) and thus completing the design of the isolation tests.

Ambiguity resolution. The isolation test is performed for each pair of potential failures, and the result of each test is a decision that the ith failure is more likely than the jth, that the jth failure is more likely than the ith, or that more data are needed (take another sample). For an aircraft with n actuators, there are $n(n-1)/2$ of these decisions. Further processing is required to isolate the failure to a particular surface, if possible, based on the results of these pairwise decisions.

During the FDI process, several flags are set. As previously noted, the trigger flag F_T, verify flags F_{V_i}, and isolate flags $F_{I_{i/j}}$ are set by the trigger, verify, and isolate tests, respectively. On

succeeding samples, if a flag is undecided, the test is performed again. Once a verify or isolate decision is made and the corresponding flag is set to 1 or 0, that test is not repeated and the flag is not changed unless a false trigger is declared. The flags are then reinitialized, and the FDI process restarts.

During the ambiguity resolution process a failure flag F_F is set to TRUE to indicate that an aircraft-path failure has been detected and isolated, and a confusion flag F_C is set to TRUE to indicate that the isolation process has not isolated the failure to a particular surface but only to a group of surfaces called the confusion set.

Because stabilizer and elevator failure effects are so similar, the FDI system cannot distinguish between these failures. Therefore, the system attempts to isolate a failure in one of these surfaces only to the left horizontal tail or the right horizontal tail. In this case, the confusion flag is set to TRUE, and the confusion set is compiled. Once an aircraft-path failure has been isolated, including isolation to the left or right horizontal tail, the aircraft-path subsystem ceases to process data. (The current FDI system cannot accommodate multiple aircraft-path failures.) In some cases, results of the verify and isolate tests lead to detection of a failure that cannot be isolated. In these cases, an undetermined aircraft-path failure is declared, the confusion flag is set to TRUE, and the confusion set is compiled. However, the false-trigger flag is set to TRUE, and on the next sample the system reinitializes the flags and continues to search for a failure.

The ambiguity resolution procedure is illustrated in flowchart form in figure 12. The salient features of the procedure are as follows:

1. If all verify tests fail, a false trigger is declared and the FDI process is reinitialized
2. If the verify test for the ith surface passes and all pairwise isolation tests pass in favor of the ith surface, the ith surface is declared failed; if this surface is either the left or right horizontal tail, the confusion flag is set and the confusion set is compiled
3. If each of the surfaces satisfies one of the following:

   a. The verify test fails
   b. The verify test is undecided and the surface fails all of its pairwise isolation tests
   c. The verify test passes and there are no undecided isolation tests for this surface

   then an undetermined failure is declared, the confusion flag is set to TRUE, and a confusion set is compiled that consists of the potential failed surfaces; if the confusion set is empty, a false trigger is declared, and the aircraft path is reinitialized to continue processing
4. Otherwise, another sample is taken, and the process continues

Design Results

Using the methodology described in the section "Design Concept," a baseline FDI system was designed (ref. 25) for the modified 737 aircraft for subsequent evaluation via nonlinear simulation. This section contains the results of this design process for the baseline design.

Actuator-Path Subsystem

Application of the design methodology requires knowledge of the parameters for the actuator models. Values used in the baseline design for the actuator dynamics, namely cutoff frequency, position limits, rate limits, and cable stretch factor, are shown in table 2. Some engine parameters are not shown since, as previously noted, the model used for the engines is more complicated than the generic first-order system with position and rate limits used for the other
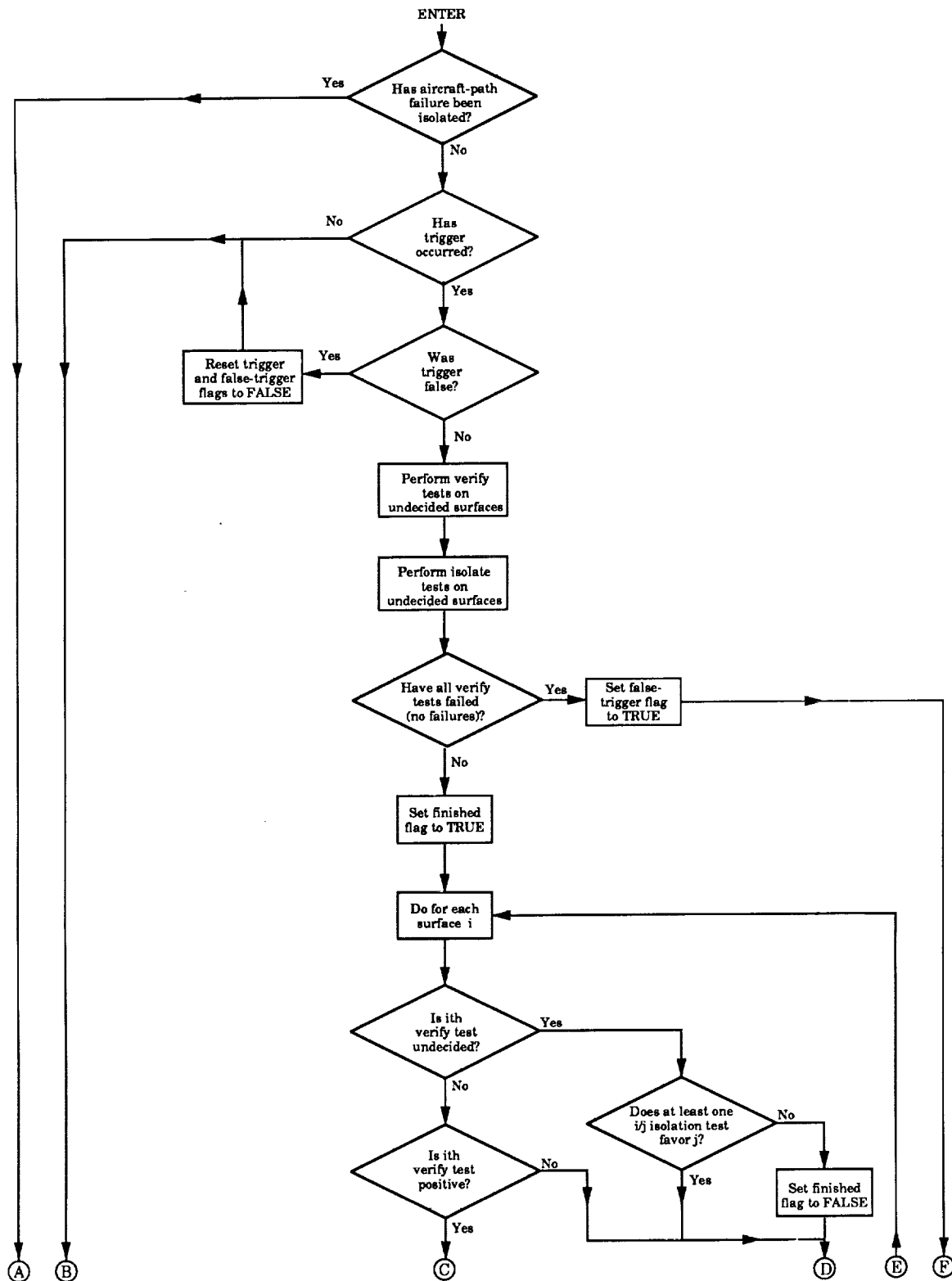
Figure 12. Aircraft-path subsystem logic flowchart.
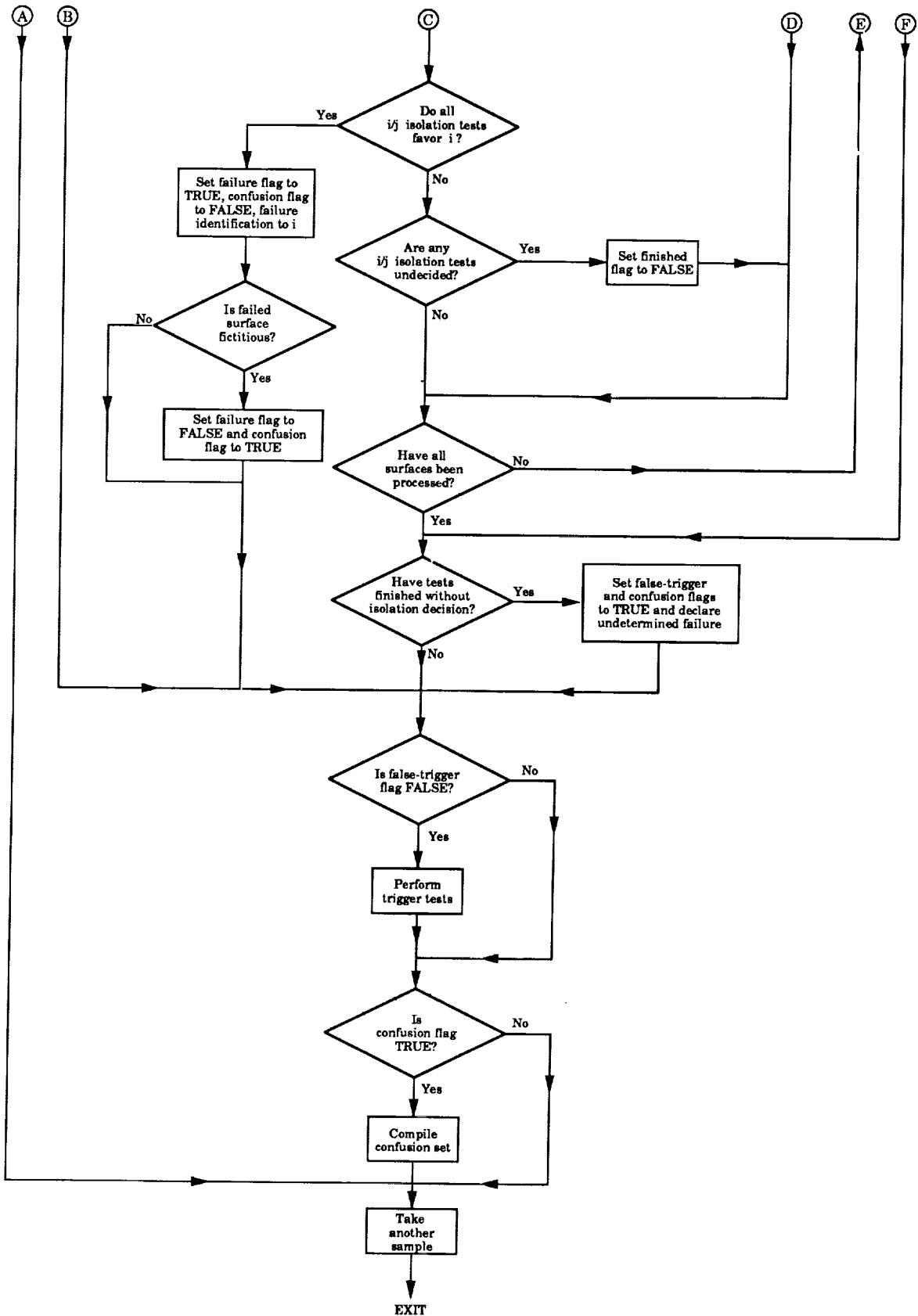
Figure 12. Concluded.

36

Table 2. Actuator-Model Parameter Values

Surface	Cutoff frequency, ω_a, rad/sec	Position limits, deg		Rate limits, deg/sec	Stretch factor	HPF cutoff frequency, rad/sec
Thrust	[a]	[b]1.54	[b]13.77	[a]	0	0.01
Stabilizers	1.5	−14	3	±10	0	
Rudder	22	−10.3	10.3	±18	0	↓
Elevators	22	−10	10	±20	.0023	
Ailerons	20	−20	20	±20	.0016	

[a]Throttle-EPR-thrust relationship in actuator model is nonlinear.
[b]Thrust in lb $\times 10^3$, corresponds to limits of 0° and 40° on throttle.

actuators. Values for the noise, or error, terms in the model are shown in table 3. The low-frequency error terms were determined by the following procedure. The nonlinear simulation (described subsequently) was run for doublet maneuvers in roll, pitch, and sideslip. For each actuator, the residuals $\nu(k)$ that resulted from comparison of the measurement of surface position with the position predicted by the actuator model were examined, and the maximum error (residual) magnitudes were determined. These worst-case errors E_{wc} were assumed to approximate the three-standard-deviation $(3\sigma_\ell)$ values for the low-frequency noise. The values for the white noise σ_w were twice the standard deviation of the white noise assumed for the sensors that measure the actuator positions. These values were then used to design trigger and verify tests for each actuator.

Table 3. Errors for Actuator-Path Truth Model

Actuator	Standard deviation of white noise, σ_w, deg	Worst-case low-frequency noise, E_{wc}, deg	Standard deviation of low-frequency noise, σ_ℓ, deg
Thrust	[a]0.02	[a]1.5	[a]0.5
Stabilizers	.2	.5	.167
Rudder	.2	3.0	1.0
Elevators	.2	.75	.25
Ailerons	.2	.50	.167

[a]Thrust in lb $\times 10^3$.

One-half second was selected as the window of samples for the fixed-sample trigger test, and similarly one-half second was chosen as the maximum time for the verify SPRT. At 20 samples/sec, this window corresponds to 10 samples for N_T and N_V. The low-frequency cutoff for the high-pass filters was selected to be 0.01 rad/sec.

Trigger tests. To determine the trigger thresholds using equation (26), we need to know the factor K_σ that corresponds to the desired probability of error and σ_{S_T}, the standard deviation of the trigger-test statistic. It was assumed that the low-frequency noise in the residuals was nearly constant over the 0.5-sec trigger-test window. The variance of S_T was then approximated as

$$\sigma_{S_T}^2 \approx \sigma_\ell^2 + \frac{\sigma_w^2}{N_T} \tag{98}$$

or

$$\sigma_{S_T} \approx \sigma_\ell + \frac{\sigma_w}{2\sqrt{N_T}} \tag{99}$$

A probability of error of 2.7×10^{-3} corresponds to $K_\sigma = 3$. These values were then used to calculate the trigger thresholds according to equation (26), or

$$t_T = K_\sigma \sigma_{S_T}$$

Results are listed in table 4. Equation (26) produced a threshold of 3.1° for the rudder. However, because of a problem with false alarms in the rudder test during simulation, the threshold was increased to 4.1° for the baseline design.

Table 4. Baseline-Design Results for Actuator-Path Subsystem

Surface	N_T	t_T, deg	N_V	t_V, deg	$\bar{s}$, deg	G_A	G_D
Thrust	10	[a]1.6	10	[a]7.5	[a]3.0	1.0	1.5
Stabilizers		.6		2.5	1.0		.5
Rudder		4.1		20	6.0		3.0
Elevators		.85		3.75	1.5		.75
Ailerons		.6		2.5	1.0		.5

[a]Thrust in lb $\times 10^3$.

Verify tests. The first step in the design of the verify test is to determine the minimally detectable signal $\bar{s}$ by using equation (40) as follows:

$$d^2(N_V) = \frac{N_V^2 \bar{s}^2}{\sigma_{S_V}^2(N_V)} = (2K_\sigma)^2$$

The number of samples has been chosen to be 10, and $K_\sigma = 3$ as in the trigger test. The variance of the verify statistic is approximated as

$$\sigma_{S_V}^2(N_V) \approx N_V^2 \sigma_\ell^2 \tag{100}$$

Therefore,

$$\bar{s} = 2K_\sigma \sigma_\ell = 2E_{wc} \tag{101}$$

With this approximation for the variance of S_T, the minimally detectable signal $\bar{s}$ and the metric d^2 are independent of N_V (and k). The gains G_A and G_D can now be determined from equations (41). The next step in the design is to determine the value k_t at which $d^2(S_V(k_t)) \geq 2\ln[(1 - P_E)/P_E]$. Since d^2 is independent of k, this step is omitted, and the verify threshold is set equal to the expected value of the verify statistic at sample $N_V/2$ as follows:

$$t_V = E\{S_V(N_V/2)\} = \frac{N_V \bar{s}}{4} = 5E_{wc} \tag{102}$$

Results are shown in table 4. Because of the false-alarm problems with the rudder, the computed value of 15.0 for the rudder-verify threshold was increased to 20.0 for the baseline design.

Aircraft-Path Subsystem

Design of the aircraft-path subsystem requires that the variances $\boldsymbol{\Sigma}_w$ and $\boldsymbol{\Sigma}_\ell$ of the white and low-frequency errors in the truth model of the residuals (eqs. (66)) be determined. In this case, the residuals and, thus, the error terms are six-component vectors, but the covariance matrices are assumed to be diagonal.

The white-noise term is produced by the noise on the various sensor outputs and propagated into the residuals in the following manner. Consider, for example, the x-acceleration component $\nu_x(k)$ of the residuals. From equations (60) and (61),

$$\nu_x(k) = A^c_{m_x} - \widehat{X}/m$$

$$= A^c_{m_x} - \frac{\bar{q}S}{m}\left[C_{x_0} + C_{x_\alpha}\alpha^c_m(k) + \frac{\bar{c}}{2V_{T_0}}C_{x_q}q_m(k) + \sum_i C_{x_{\delta_i}}\delta_{m_i}(k)\right]$$

$$= A^c_{m_x} - \frac{\bar{q}S}{m}C_{x_0} - [-A_{11}W_0 + (Q_0 + A_{12})U_0]\,\alpha^c_m(k)$$

$$- [W_0 + A_{13}]\,q_m(k) - \sum_i B_{1i}\delta_{m_i}(k)$$

$$= A^c_{m_x}(k) - \frac{\bar{q}S}{m}C_{x_0} - \sum_j C_{x_j}\delta_{m_j}(k) \tag{103}$$

where the C_{x_j}'s are the dimensional stability and control derivatives listed in table 5, and the $\delta_{m_j}(k)$'s are the measurements from the aircraft sensors. The variance $\sigma^2_{w_x}$ of the white-noise component of the error in $\nu_x(k)$ can be determined from

$$\sigma^2_{w_x} = \sigma^2_{a_x} + \sum_j C^2_{x_j}\sigma^2_j \tag{104}$$

Table 5. Dimensional Stability and Control Derivatives

Force or moment axis	α, deg	β, deg	p, deg/sec	q, deg/sec	r, deg/sec	Thrust, lb $\times 10^3$	Stabilizer, deg	Rudder, deg	Elevator, deg	Aileron, deg	Spoiler, deg
$\ddot{x}$, ft/sec^2	0.576	0	0	0.000309	0	0.342	0.0211	0	0.00989	0.0113	-0.0181
$\ddot{y}$, ft/sec^2	0	$-.663$	.0131	0	.0372	0	0	.202	0	$\pm.00179$	$\pm.0185$
$\ddot{z}$, ft/sec^2	-3.60	0	0	$-.00355$	0	$-.00474$	$-.248$	0	$-.116$	$-.133$	.133
$\dot{P}$, rad/sec^2	0	$-.0829$	$-.0347$	0	.0124	$\pm.0021$	$\pm.0119$	.0147	$\pm.00556$	$\pm.0118$	$\pm.013$
$\dot{Q}$, rad/sec^2	$-.0327$	0	0	$-.0113$	0	.00620	$-.036$	0	$-.0167$	$-.00473$	.00197
$\dot{R}$, rad/sec^2	0	.0159	$-.00267$	0	$-.00300$	$\pm.0124$	$\pm.000883$	$-.0174$	$\pm.000506$	$\pm.000959$	$\pm.002$

where $\sigma^2_{a_x}$ is the variance of the noise on the x-accelerometer output, and σ^2_j is the variance of the white noise on the jth measurement. The values for σ_j are the same as the values used in

the simulation. The other five diagonal terms of Σ_w are computed in a similar manner, and the results are shown in table 6.

A dominant component of the low-frequency error in the residuals is produced when errors in the aircraft model (the derivatives) are excited by aircraft motion and surface deflections. The magnitudes of the low-frequency errors can be estimated as shown in reference 25. One technique is to estimate the maximum error in the stability and control derivatives, estimate the variance of the measured parameters (such as angle of attack and surface deflections) that multiply these derivatives, and compute the variances of the low-frequency errors, much like the computation of the white-noise variances in equation (103). For the baseline design, however, the variance of the low-frequency error was determined another way, much like it was done for the actuator-path subsystem. The aircraft was flown in simulation in a climbing turn with no turbulence. Residuals $\nu(k)$ were calculated, and the worst-case errors were determined. The error standard deviations σ_ℓ were then set equal to two-thirds of the worst-case errors. The resulting values are shown in table 6. The cutoff frequency of the low-frequency error model was selected to be 2 rad/sec ($a_\ell = 0.905$ in eq. (6)). The values of $\sigma_f(20)$ are the square roots of the diagonal terms of $\Sigma_f(N)$ for $N = 20$.

The cutoff frequency of the high-pass filter was chosen to be 0.5 rad/sec. The window length for the trigger tests was chosen to be 1 sec, or 20 samples. The maximum length for the verify and isolate SPRT's was similarly selected to be 20 samples. Using these data in the truth model, the Lyapunov equation was solved for each of the six components of the residual as previously described to compute the diagonal terms of $\Sigma_f(20)$. Results are listed in table 6.

Trigger tests. The projection vector $\mathbf{P}_i$, which will operate upon the residuals $\nu(k)$ in the trigger test for the ith surface, was computed from equation (75), and the resulting vectors are shown in table 7. The test statistic for the ith trigger test is given by equation (69). The variance $\sigma_{S_{T_i}}^2$ of the test statistic was computed by using equation (72). By using equation (26) and a value of 3.1 for K_σ, which corresponds to a probability of error of 2×10^{-3}, the thresholds for the trigger tests were computed, and the results are listed in table 7. For the test statistic, the software used in the simulation actually uses

$$S_{T_i}(k) = \left| \sum_{j=k-N_T+1}^{k} \mathbf{P}_i^T \nu(j) \right| - \sum_{j=k-N_T+1}^{k} \frac{1}{2} \mathbf{P}_i^T \mathbf{P}_i \tag{105}$$

Since $E\left\{ S_{T_i} \middle| H_0 \right\} = N_T/2$, the trigger thresholds actually used in the simulation were calculated using

$$t_{T_i} = K_\sigma \sigma_{S_{T_i}} - \frac{N_T}{2} \tag{106}$$

The minimum value $\bar{f}_{s_i}$ of the failure that will produce a reliable test at sample N_T according to the d^2 metric was calculated from equation (76) with $K_\sigma = 3.1$.

Each projection vector $\mathbf{P}_i$ was then examined to determine which components contributed significantly to the reliability of the detection process. Each of the six components of $\mathbf{P}_i$ were set to zero one at a time, and a new value for the minimum signal $\bar{f}_{s_i}$ was computed. If the ratio of the new value to the previous value was less than 1.05, the component of $\mathbf{P}_i$ being examined was kept at zero. Otherwise, it was restored to its original value. Using this procedure, new projection vectors were computed with new thresholds and new values for the minimal detectable failures. Results are shown in table 8.

Table 6. Errors for Aircraft-Path Truth Model

Residual	Standard deviation of white noise, $^a\sigma_w$	Low-frequency noise cutoff, rad/sec	Standard deviation of low-frequency noise, $^b\sigma_\ell$	HPF cutoff frequency, rad/sec	Standard deviation of total noise, $^c\sigma_f(20)$
x-acceleration, ν_x	0.39 ft/sec^2	2.0	0.20 ft/sec^2	0.5	2.94 ft/sec^2
y-acceleration, ν_y	.42 ft/sec^2		.033 ft/sec^2		1.74 ft/sec^2
z-acceleration, ν_z	1.50 ft/sec^2		.20 ft/sec^2		6.52 ft/sec^2
P-acceleration, ν_P	.035 rad/sec^2		.020 rad/sec^2		.286 rad/sec^2
Q-acceleration, ν_Q	.017 rad/sec^2		.0050 rad/sec^2		.0925 rad/sec^2
R-acceleration, ν_R	.012 rad/sec^2		.0034 rad/sec^2		.0642 rad/sec^2

^{a}Square root of diagonal terms of Σ_w.

^{b}Square root of diagonal terms of Σ_ℓ.

^{c}Square root of diagonal terms of Σ_f.

Table 7. Baseline-Design Results for Aircraft-Path Trigger Test Before Projection-Vector Optimization

Design parameter	Left thrust	Right thrust	Left horizontal tail	Right horizontal tail	Rudder	Left aileron	Right aileron
P:							
(ν_x)	0.0127	0.0127	0.00055	0.000577	0	0.00211	0.00211
(ν_y)	0	0	0	0	.0158	.000962	.000962
(ν_z)	−.0000360	−.0000360	−.00138	−.00138	0	−.00507	−.00507
(ν_p)	.00828	−.00828	.0344	−.0344	.0424	.233	−.233
(ν_q)	.234	.234	−.998	−.998	0	−.896	−.896
(ν_r)	.972	−.972	.0508	−.0508	−.9990	.377	−.377
σ_{S_T}	.0760	.0760	.0933	.0933	.0709	.114	.114
t_T	−9.764	−9.764	−9.711	−9.711	−9.780	−9.646	−9.646
$\bar{f}_{S_T}$	1.32	1.32	.787	.787	1.04	4.40	4.40

Verify tests. Since the maximum length of the verify SPRT is the same as the length of the trigger tests ($N_V = N_T = 20$), the projection vectors for the verify tests are the same as those for the trigger tests. The minimum value $\bar{s}_i$ of the failure that produces a reliable test at sample N_V according to the d^2 metric was calculated from equation (79) by using $K_\sigma = 3.1$. Since $N_V = N_T$, and the same value of K_σ was used for the trigger and verify tests, the values of $\bar{f}_{s_i}$ are the same as the final values from the trigger tests (after the insignificant components of $\mathbf{P}_i$ were set to zero). The gains G_{A_i} and G_{D_i} were then determined from equations (80). Using $P_E = 1 \times 10^{-3}$, the verify thresholds were then computed with equation (82) after determining k_{t_i} from equation (81). Results are shown in table 9.

Isolate tests. The maximum length of the isolate SPRT's was chosen to be 1 sec ($N_I = 20$), and the projection vectors $\mathbf{P}_{i/j}$ were computed from equation (93). Minimum-failure signal amplitudes for reliable detection were computed from equations (94) and (95) by using $K_\sigma = 3.1$

Table 8. Baseline-Design Results for Aircraft-Path Trigger Test After
Projection-Vector Optimization

Design parameter	Left thrust	Right thrust	Left horizontal tail	Right horizontal tail	Rudder	Left aileron	Right aileron
P:							
(ν_x)	0.0131	0.0131	0	0	0	0	0
(ν_y)	0	0	0	0	.0159	0	0
(ν_z)	0	0	0	0	0	0	0
(ν_p)	0	0	0	0	0	.252	−.252
(ν_q)	0	0	−1.0	−1.0	0	−.968	−.968
(ν_r)	.9999	−.9999	0	0	−.9999	0	0
σ_{S_T}	.0749	.0749	.0925	.0925	.0699	.115	.115
t_T	−9.768	−9.768	−9.713	−9.713	−9.783	−9.644	−9.644
$\bar{f}_{S_T}$	1.38	1.38	.796	.796	1.05	4.72	4.72

Table 9. Baseline-Design Results for Aircraft-Path Verify Test After
Projection-Vector Optimization

Design parameter	Left thrust	Right thrust	Left horizontal tail	Right horizontal tail	Rudder	Left aileron	Right aileron
$\bar{s}$	0.0232 lb × 10³	0.0232 lb × 10³	0.0287°	0.0287°	0.0217°	0.0356°	0.0356°
G_A	.0232	.0232	.0287	.0287	.0217	.0356	.0356
G_D	.00027	.00027	.00041	.00041	.00023	.00063	.00063
k_T	6	6	7	7	7	6	6
t_V	.00162	.00162	.00288	.00288	.00164	.00381	.00381

and $P_E = 1 \times 10^{-3}$. Thresholds for the isolate test were then computed by using equation (96) to find $k_{I_{i/j}}$ and equation (97) to find $t_{I_{i/j}}$.

As with the trigger-verify projection vectors, the isolate projection vectors $\mathbf{P}_{i/j}$ were examined to set to zero any vector component that contributed insignificantly to the isolate process. In this case, a value of 1.2 was used as the test of significance for the ratio of minimum signal amplitudes $\left(\bar{f}_{i/j} + \bar{f}_{j/i}\right)_{\text{new}} / \left(\bar{f}_{i/j} + \bar{f}_{j/i}\right)_{\text{old}}$. Results are listed in table 10.

Baseline-Design Simulation Results

Simulation Description

The simulation used to evaluate the baseline FDI system was a six-degree-of-freedom nonlinear digital simulation of a transport airplane. The airplane model was a modified 737. The aerodynamics and controls were changed to allow for separate surface operation of the right and left ailerons, elevator, and stabilizer; that is, the right and left surfaces could be controlled individually. Also, the speed of response of the stabilizer was improved by modeling the actuator as a first-order system with a time constant of 1.5 sec. This change was made

42

so that the stabilizer would be a more useful redundant surface in the restructurable-controls studies. Position and rate limits were included in the model.

Table 10. Baseline-Design Results for Aircraft-Path Isolate Test After Projection-Vector Optimization

Design parameter	Left thrust	Right thrust	Left horizontal tail	Right horizontal tail	Rudder	Left aileron	Right aileron
$\sigma_{S_{i/j}}$:							
(LT)		0.176	0.109	0.109	0.336	0.110	0.132
(RT)			.109	.109	.336	.132	.110
(LH)				.387	.113	.306	.306
(RH)					.113	.306	.306
(Ru)						.132	.132
(LA)							.193
(RA)							
$\bar{s}_{i/j}$:							
(LT)		0.0273	0.0168	0.0168	0.0521	0.0170	0.0204
(RT)			.0168	.0168	.0521	.0204	.0170
(LH)				.0599	.0175	.0474	.0474
(RH)					.0175	.0474	.0474
(Ru)						.0205	.0205
(LA)							.0300
(RA)							
$k_{i/j}$:							
(LT)		6	7	7	7	7	6
(RT)			7	7	7	6	7
(LH)				5	7	5	5
(RH)					7	5	5
(Ru)						6	6
(LA)							6
(RA)							
$t_{I_{i/j}}$:							
(LT)		0.164	0.118	0.118	0.365	0.119	0.123
(RT)			.118	.118	.365	.123	.119
(LH)				.300	.122	.237	.237
(RH)					.122	.237	.237
(Ru)						.123	.123
(LA)							.180
(RA)							

The simulation included provisions for simulating failures in each of the controls: left throttle, right throttle, left stabilizer, right stabilizer, rudder, left elevator, right elevator, left aileron, and right aileron. Each surface could be failed to stick at its current position, to stick at a neutral (trim) position, to stick at hardover position, or to lose part of its effectiveness. In the neutral and hardover failures, the actuator command was set to the failed position at the time of failure, and this command was then propagated through the actuator dynamics to determine the surface position as a function of time. For the partial-surface loss, the command to the actuator was set at the time of failure to the commanded (desired) position multiplied by the percent effectiveness due to the failure.

43

The simulation included the capability to simulate atmospheric turbulence and steady-state winds. Turbulence was modeled according to the Dryden spectra.

Aircraft sensors modeled in the simulation included attitude gyros, rate gyros, body-mounted accelerometers, an inertial navigation system, an air-data system, alpha and beta vanes, actuator position sensors, engine pressure ratio (EPR) sensors, and a microwave landing system. The models provided for white Gaussian noise, bias, scale factor, and alignment errors in the sensor measurements as appropriate. Sensor dynamics were not included. Values for the errors can be found in table 11.

Table 11. Sensor Errors Used in Simulation

Sensor	White-noise error, 1σ	Bias error	Scale-factor error	Misalignment error
Altitude gyros:				
Φ	$0.23°$	$-0.23°$	0	0
Θ	$.23°$	$.23°$	0	0
Ψ	$.23°$	$-.23°$	0	0
Attitude rates:				
P	0.02 deg/sec	0	0	0
Q	.02 deg/sec	0	0	0
R	.02 deg/sec	0	0	0
Angle of attack, α	$0.4°$	$0.25°$	0	0
Sideslip, β	$0.4°$	$0.25°$	0	0
Accelerometers:				
a_x	0.32 ft/sec^2	0.32 ft/sec^2	0.0025	[a]0.2, $-.2$, .25
a_y	.32 ft/sec^2	.32 ft/sec^2	.0025	[a].2, $-.2$, .25
a_z	.32 ft/sec^2	.32 ft/sec^2	.0025	[a].2, $-.2$, .25
True airspeed, V_T	2.5 ft/sec	4.0 ft/sec	0	0
Thrust	0.01 lb $\times$ 10^3	0.02 lb $\times$ 10^3	0	0
Surface positions	$0.1°$	$0.1°$	0	0

[a]Misalignment in degrees for Φ, Θ, and Ψ, respectively.

The control laws and the FDI algorithms implemented in the simulation were developed by Alphatech (refs. 25, 26, 37, and 38) in their restructurable-controls studies. This implementation was accomplished by integrating into the Langley simulation the software produced by Alphatech to simulate a restructurable flight control system. The control laws were the baseline linear quadratic (LQ) control system described in reference 38. Input commands to the control system to perform simulated maneuvers were perturbations in pitch θ, x-velocity u, roll ϕ, and y-velocity v. The maneuver used for most of the evaluation runs was a climbing turn beginning at 10 sec into the run. This maneuver, denoted CT4 and illustrated in figure 13, consists of a 15-sec bank right and a 34-sec pitch-up. Most runs lasted 60 sec, with failures at 5 sec.

The FDI system was the baseline design described in the previous section. Values for the actuator subsystem design parameters were the same as those in reference 25, except for the rudder as previously noted. The aircraft-path subsystem design parameters were similar to, but slightly different than, those presented in reference 25.
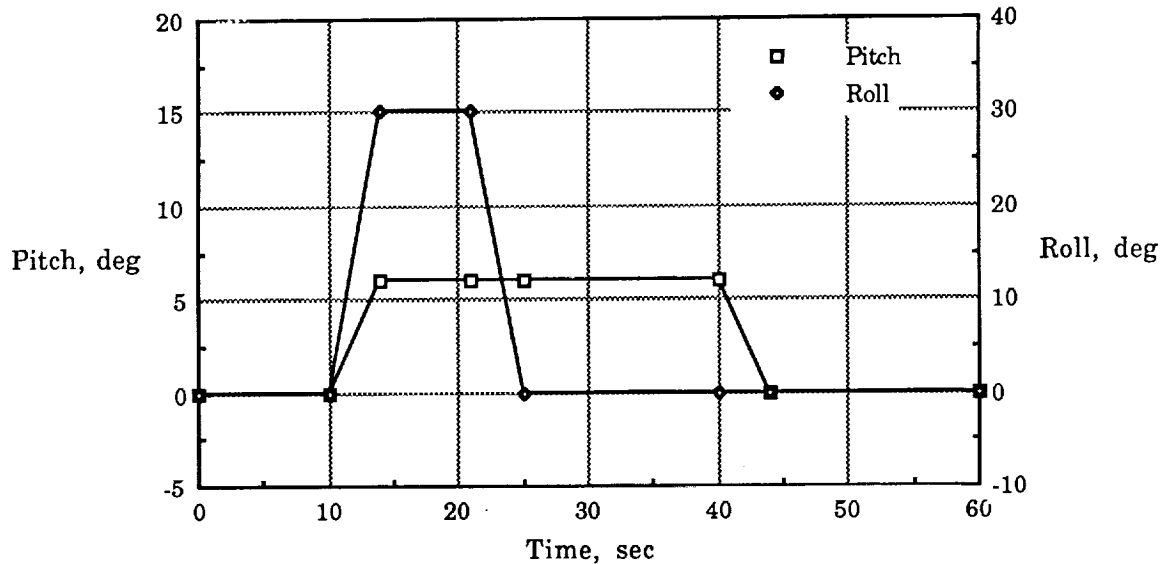
Figure 13. Climbing-turn maneuver CT4.

No-Turbulence Results

Actuator-Path Subsystem

The performance of the FDI system in detecting and isolating actuator-path failures under zero atmospheric turbulence conditions was evaluated by simulating three different types of failures for each of five actuators. These were single-point failures; that is, the failures occurred one at a time, and there was a separate simulation run for each failure. The three types of failures were current position—at the failure time, the failed actuator stuck at its last calculated position; neutral—at the failure time, the actuator was driven to its trim position through the actuator dynamics; and hardover—at the failure time, the actuator was driven to a hardover position through the actuator dynamics. Each failure occurred at $t = 5$ sec, and the climbing-turn maneuver was initiated at $t = 10$ sec.

As can be seen from the results shown in table 12, all the failures were detected and correctly isolated; this was accomplished with only one false alarm. Except for the rudder, the current position and neutral failures were not detected until the maneuver began, because in nonmaneuvering flight in zero turbulence, there is little actuator activity. Also, the detection times for the current position and neutral failures are similar. Because of the small actuator excursions prior to the maneuver, the current position failures caused the actuator to be stuck in a position not far from neutral (trim). All current position and neutral failures except the throttle were detected and correctly isolated within 1 sec after maneuver initiation. The longer time needed to detect the throttle failure was due in large part to the slower change in commanded throttle position and the considerably slower throttle-thrust dynamic response. As would be expected, the hardover failures were detected much more quickly than the current position and neutral failures; all hardover failures except throttle were detected in less than 0.5 sec. While the quicker detection of hardover failures was anticipated, it was also necessary, since a hardover failure can place the aircraft in danger more quickly. The one false alarm was a rudder false alarm in the aircraft-path subsystem; this false alarm occurred after the actuator-path subsystem had correctly detected a hardover rudder failure.

45

Table 12. Simulation Results for Actuator-Path Failures, No Turbulence

Failure	Detection/isolation times,[a] sec			Failed actuator position,[b] deg			False alarms[c]		
	Current	Neutral	Hardover	Current	Neutral	Hardover	Current	Neutral	Hardover
Right throttle	12.60		3.25	−1.10		0	0		0
Right stabilizer	6.00	5.95	.30	−0.07	0	[d] −14	↓	0	0
Rudder	.70	1.10	.45	−1.80	↓	10	↓	↓	1
Right elevator	5.60	5.60	.25	−0.44		−10	↓		0
Right aileron	5.40	5.50	.25	1.30	↓	−10	↓	↓	0

[a]Verify time relative to failure time.
[b]Relative to trim.
[c]Includes both actuator-path and aircraft-path false alarms.
[d]Absolute, not relative to trim.

Illustrations of the data produced by the FDI actuator-path subsystem are shown in figures A1 and A2 in the appendix for a failure of the right aileron stuck at its current position at $t = 5$ sec. For each of the nine actuators, figure A1 contains plots of the commanded actuator position, the measured position, and the position estimated by the actuator model. Figure A1 also contains plots of the residual for each actuator before and after high-pass filtering. Figure A2 contains plots of the trigger statistic and the trigger threshold and plots of the verify statistic and verify thresholds for each actuator. For the convenience of the reader, those time histories pertaining to the right aileron are repeated in figure 14. At $t = 5$ sec the measured right-aileron position sticks at about $1.3°$ and the right-aileron residual increases at this point. The residual becomes much larger when the maneuver begins ($t = 10$ sec). The squared-off appearance of the residual is the result of limiting in the plotting program to prevent the plot from going off scale. There is no noticeable change in the other actuator residuals as a result of the failure. Also, the right-aileron trigger statistic crosses its threshold at least three times, twice prior to the maneuver. It can be seen from the plot that, in response to the triggers before the maneuver, the verify statistic begins to accumulate but the time limit is exceeded before reaching either threshold. When the maneuver begins and the residuals are larger, the verify statistic crosses the threshold and correctly detects and isolates a right-aileron failure 0.1 sec after the trigger. The trigger and verify statistics are limited by the plotting program. There were no triggers in any of the other actuator tests. After the failure is detected and isolated (fig. 14), the control system continues to command the right aileron. A restructurable control system would at that point cease commanding the right aileron and distribute control among the remaining effectors.

Aircraft-Path Subsystem

The performance of the baseline FDI system in detecting and isolating aircraft-path failures under zero atmospheric turbulence conditions was evaluated by simulating a loss of surface effectiveness, or a partially missing surface, for each of the four types of surfaces: stabilizer, rudder, elevator, and aileron. Aircraft-path failures of the throttle-engine combination were not implemented in the simulation. These were single-point failures; that is, the failures occurred one at a time, and there was a separate simulation run for each failure. The aircraft-path subsystem was not designed to detect multiple failures. Each failure occurred at $t = 5$ sec, and the climbing-turn maneuver CT4 was initiated at $t = 10$ sec.

Results of the simulation that demonstrates the performance of the aircraft-path subsystem are shown in table 13 as a function of the percent effectiveness of the failed surface. To a

46
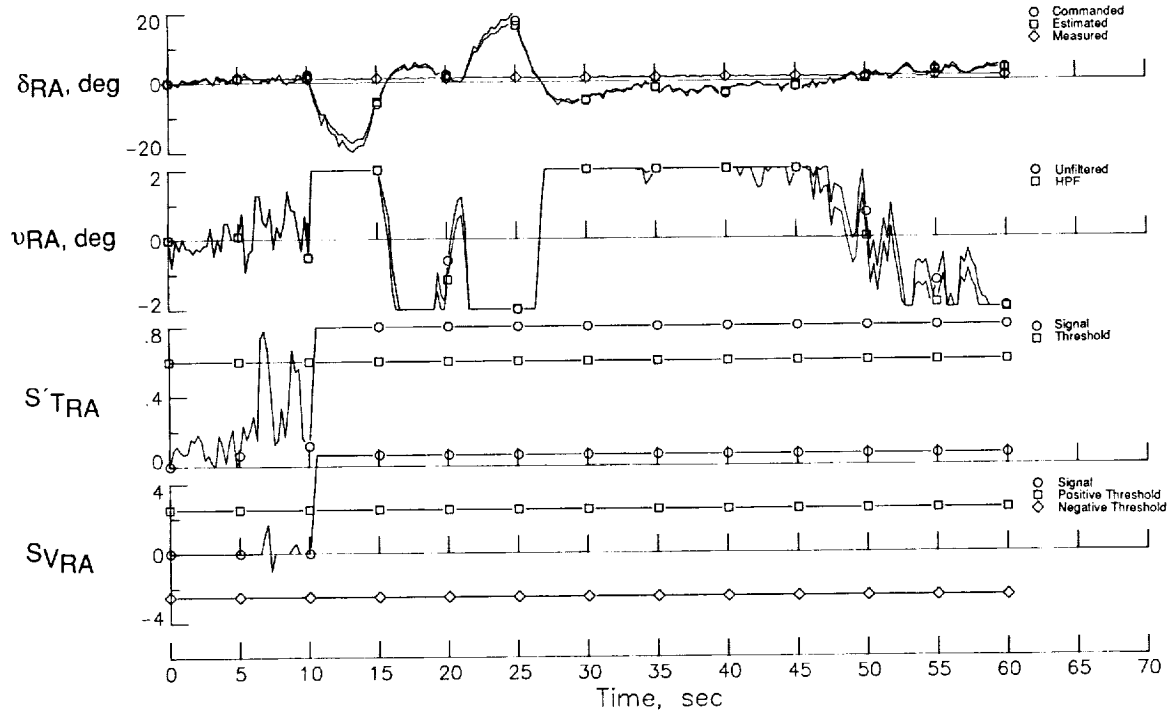
Figure 14. Right-aileron position, residual, trigger statistic, and verify statistic for stuck-at-current-position failure with no turbulence.

first-order approximation the percent of the surface that is missing equals 100 minus the percent effectiveness. All four failures, right stabilizer, rudder, right elevator, and right aileron, were detected with the surface at 60-percent effectiveness. Failures of lesser effectiveness were not simulated, because they would be easier to detect and isolate. The stabilizer and rudder failures were detected in less than 2 sec, while the elevator and aileron failures were detected after the maneuver began. When the rudder was failed at 80-percent effectiveness, the failure was detected, but only after a delay of slightly more than 48 sec. Failures of the stabilizer, elevator, and aileron at 80 percent were not detected. As can be seen in table 13(b), all the failures at 60-percent effectiveness, except the right elevator, were isolated at least to a confusion set containing the failed surface. The isolation times were comparable with those with the actuator-path stuck-at-neutral and stuck-at-current-position failures, but as expected, detection and isolation were not as quick as with the hardover failures. The stabilizer failure was isolated to a confusion set containing the failed surface, since the system was not designed to discriminate between stabilizer and elevator failures. When the elevator failed, it was not isolated, but an undetermined failure was declared with the confusion set containing the failed surface. Similarly, when the rudder was failed at 80-percent effectiveness, the failure was not isolated to the rudder, but an undetermined failure was declared with the confusion set containing the rudder and the left throttle. No false alarms were experienced in these simulation runs in either the aircraft-path or actuator-path subsystems. In fact, no actuator-path triggers were experienced during these runs. A run with no failures was also made, and no false alarms and only one false trigger were experienced (table 13(c)).

To illustrate the type of data produced by the aircraft-path subsystem, figures A3 to A6 contain time-history plots of data produced during a simulation run with a partial right-aileron failure—in particular, a reduction of the aileron effectiveness to 60 percent at $t = 5$ sec. Figure A3 shows how the aircraft responds to the failure at $t = 5$ sec and to the climbing-turn maneuver $CT4$ at $t = 10$ sec. Application of the commanded maneuver illustrated in

47

figure 13 produces the elevator, stabilizer, and aileron activity shown in figure A3; as a result, the aircraft pitches up and rolls right between $t = 10$ and $t = 15$ sec. Between 20 and 30 sec, the aircraft rolls back to where the wings are level, and between 40 and 45 sec it pitches back down. This maneuver results in a heading change of approximately 45° and an altitude increase of nearly 600 ft, as seen in figure A3.

Table 13. Failure-Detection and Isolation Performance of Aircraft-Path Subsystem
Baseline Design With No Turbulence

(a) Detection performance

Failed surface	Failure-detection time[a] as a function of percent surface effectiveness				
	0%	20%	40%	60%	80%
Right stabilizer				1.15	[b]ND
Rudder				1.95	48.20
Right elevator				7.05	[b]ND
Right aileron				11.70	[b]ND

[a]Time of failure declaration relative to time of failure.
[b]See symbol list for definition.

(b) Isolation performance

Failed surface	Failure isolation as a function of percent surface effectiveness				
	0%	20%	40%	60%	80%
Right stabilizer				[a]$CS\,(RS,RE)$	[a]ND
Rudder				Yes	[a]$U\,(LT,Ru)$
Right elevator				[a]$U\,(LS,RS,RE)$	[a]ND
Right aileron				Yes	[a]ND

[a]See symbol list for definition.

(c) False-alarm performance

Run	Random-sequence set	Number of triggers	Number of false alarms	Isolated surface	FDI active time,[a] sec
1	1	1	0		56.00

[a]Time aircraft-path subsystem is operational before being inhibited by a failure isolation.

Figure A4 shows the measured and predicted linear and angular accelerations and the residuals, which are the differences between the measured and predicted values. The plots for the $\dot{p}$ channel are repeated in figure 15. Changes in the accelerations $\ddot{x}$, $\ddot{z}$, and $\dot{p}$ are noticeable during the maneuver. However, the measured and predicted values track well, so that the residuals, though noisy, do not change significantly as a result of the maneuver. Neither changes in the accelerations nor in the residuals at the time of the failure are obvious in the plots. The
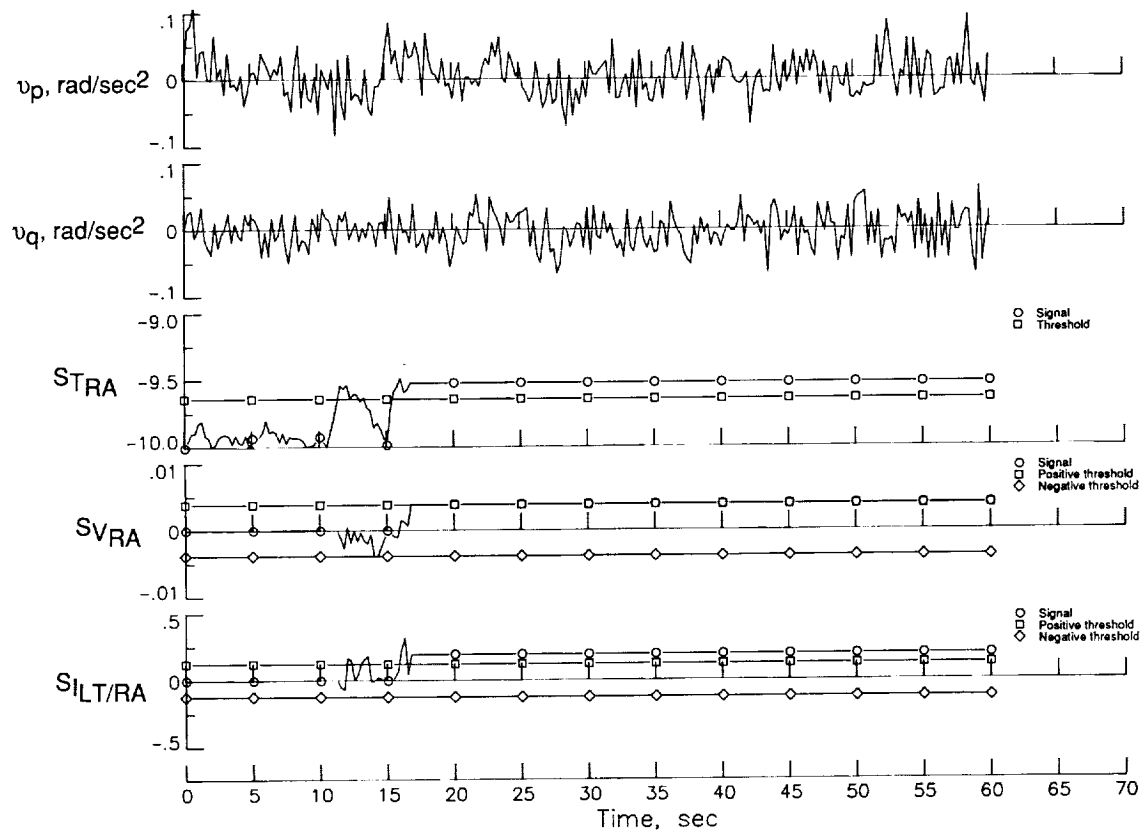
Figure 15. Residuals, trigger statistic, verify statistic, and isolate statistic for right-aileron partially missing surface failure (60-percent effectiveness). Baseline design; no turbulence.
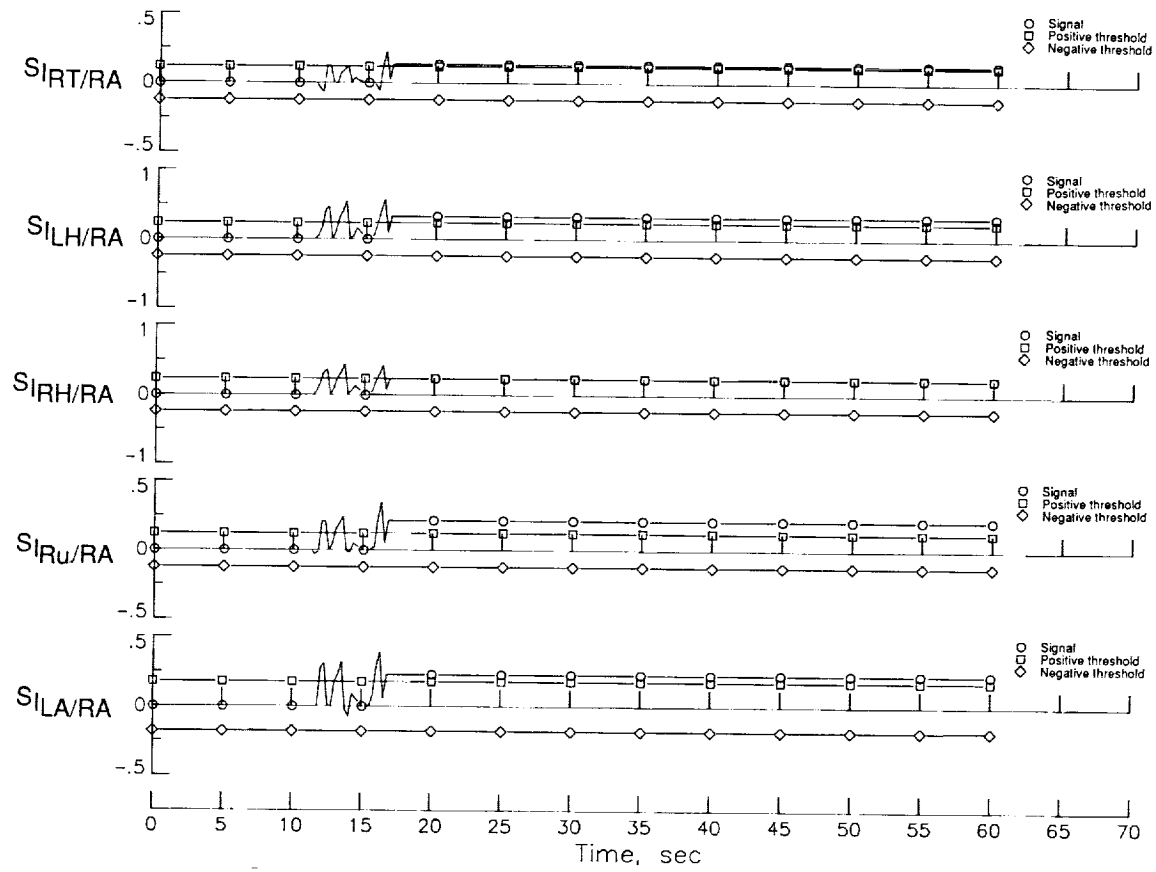
Figure 15. Concluded.

projection vectors in table 8 show that the right-aileron trigger and verify tests only utilize the $\dot{p}$ and $\dot{q}$ residuals, ν_p and ν_q, respectively. Residual errors are weighted sums of band-pass-filtered measurements and were not used in the designs evaluated in this report.

Figure A5 contains plots of the trigger statistics and thresholds and the verify statistics and thresholds for each of the seven surfaces; the plots for the right aileron are also shown in figure 15. (The left stabilizer and elevator and the right stabilizer and elevator are combined into the fictitious left and right horizontal tails.) Because of the relatively small aircraft accelerations in the no-turbulence environment, there are no triggers before the maneuver begins, even though the failure has already occurred. (The apparent left-aileron trigger at about $t = 1$ sec is not a true trigger, because it occurs during the 4-sec initialization period, when the FDI system is inhibited.) The first trigger occurs at $t = 11.35$ sec in the right-aileron channel (fig. 15), but the time limit on the right-aileron verify test is exceeded without making a decision, and the other six surfaces verify negatively (no failure) (fig. A5). Additional triggers occur in the right aileron, right throttle, and left horizontal tail at $t = 12.50$, 13.70, and 15.35 sec, respectively, without a failure being declared. Finally, as a result of a right-aileron trigger at $t = 16.40$ sec, the right-aileron verify test passes, all right-aileron isolation tests pass, and a right-aileron failure is correctly declared at $t = 16.70$ sec (11.70 sec after the failure). The isolate statistics and thresholds are shown in figure A6 and in figure 15 for the right aileron. All the pairwise isolation tests involving the right aileron indicate a right-aileron failure. Figures A5 and A6 show that, after the failure is declared, the trigger, verify, and isolate tests cease to function, because the aircraft-path subsystem is designed to detect only single-point failures.

Results With Turbulence

Actuator-Path Subsystem

As done with no turbulence the performance of the FDI system in detecting and isolating actuator-path failures while flying in atmospheric turbulence was evaluated by simulating three different types of failures for each of five actuators. Again, the three types of failures were as follows: current position—at the failure time, the failed actuator stuck at its last calculated position; neutral—at the failure time, the actuator was driven to its trim position through the actuator dynamics; and hardover—at the failure time, the actuator was driven to a hardover position through the actuator dynamics. As in previous runs, each failure occurred at $t = 5$ sec, and the climbing-turn maneuver was initiated at $t = 10$ sec.

As can be seen from the results shown in table 14, all the failures were detected and correctly isolated. In general, the current position and neutral failures were detected significantly faster than in the no-turbulence case because of the increased actuator activity due to the turbulence. In fact, all the failures except the right-throttle stuck-at-current-position failure were detected before the maneuver began, and 11 failures out of 14 were detected in 1 sec or less. The most significant result from these runs, however, was the occurrence of false alarms. There was one false alarm in the aircraft-path subsystem in each failure run. In each case, it was a false detection and isolation of a right-throttle failure soon after the actual failure occurred; the first trigger occurred before the actual failure. When the aircraft-path failure was isolated, the aircraft-path subsystem was inhibited, and no further aircraft-path false alarms were possible.

Three 60-sec runs were made, with no failures, and different sample sequences were used for the turbulence in each run. In the three runs, there were a total of seven false alarms, all in the aircraft path. Since there were no actuator-path false alarms, these no-failure runs are discussed in the next subsection.

51

Table 14. Simulation Results for Actuator-Path Failures, 10-ft/sec Turbulence

Failure	Detection/isolation times,[a] sec			Failed actuator position,[b] deg			False alarms[c]		
	Current	Neutral	Hardover	Current	Neutral	Hardover	Current	Neutral	Hardover
None[d]							[d]7		
Right throttle	5.55		4.40	−5.6		0	1		1
Right stabilizer	1.15	1.00	.35	.32	0	[e] −14	↓	1	↓
Rudder	.70	.80	.95	2.3	↓	10		↓	
Right elevator	.80	.85	.30	.27		−10			
Right aileron	.25	1.00	.40	1.3	↓	−10	↓	↓	↓

[a]Verify time relative to failure time.
[b]Relative to trim.
[c]Includes both actuator-path and aircraft-path false alarms.
[d]Three simulation runs with different sample sequences for random noises and turbulence.
[e]Absolute, not relative to trim.

Figures A7 and A8 and figure 16 show the data produced by the FDI actuator-path subsystem for a failure of the right aileron stuck at its current position at $t = 5$ sec. Comparison of the plots in figure A7 with those in figure A1 reveals the increased actuator activity and increased noise on the residuals in the turbulence case, especially in the rudder channel. The residuals are
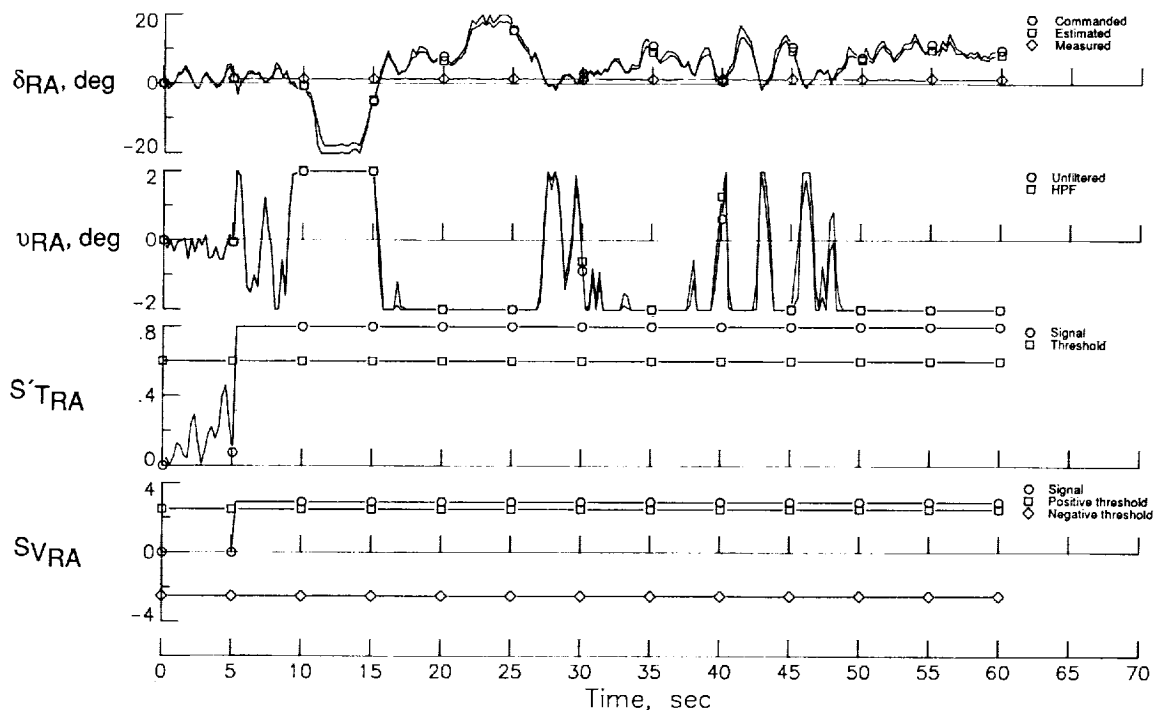

Figure 16. Right-aileron position, residual, trigger statistic, and verify statistic for stuck-at-current-position failure with 10-ft/sec turbulence.

larger in the thrust and rudder channels than in the others because the rudder is more active than the other surfaces and because the thrust and rudder FDI model errors are larger than the others. The rudder model in the simulation contains hysteresis and nonlinear rate limits. The

FDI engine model, while more complex than the other FDI actuator models, is considerably simpler than the engine model in the simulation. In spite of the increased noise on the residuals, there are no false alarms in the actuator path, and there is only one false trigger, namely, a left-throttle trigger shortly after $t = 10$ sec. (See fig. A8.) As a result of this trigger, the left-thrust verify test is activated, and the time is exceeded without making a decision. Comparison of figure 16 with figure 14 shows that the right-aileron verify test passes much more quickly in the presence of turbulence.

The ability of the actuator-path subsystem to correctly detect failures without false alarms indicates that this subsystem is performing as anticipated. Although the limited amount of testing via simulation to this point has not revealed any design deficiencies or any need for redesign of the actuator-path subsystem, operation in higher turbulence reveals some deficiencies, as shown subsequently.

Aircraft-Path Subsystem

As stated in the previous section, three simulation runs with no failures were made with 10-ft/sec turbulence and with the aircraft performing the CT4 climbing-turn maneuver. Each run utilized a different sample sequence for the turbulence. As can be seen in table 15, in the three runs there were a total of 11 false triggers and 7 false alarms in the aircraft path. Two of these were right-throttle false failures, and five were classified as undetermined failures, which allowed the aircraft-path subsystem to continue functioning. To help separate turbulence and maneuver effects on the false-alarm performance, another run was made in 10-ft/sec turbulence with no failures and no maneuver. Two aircraft-path false alarms were experienced in this run, an undetermined failure and a right-throttle failure. One more no-failure run was made with the CT4 maneuver with less turbulence (4 ft/sec). One false alarm, an undetermined failure, occurred at $t = 42.25$ sec. There were seven false triggers at this lower level of turbulence, because the aircraft-path subsystem operated for a longer period of time.

Table 15. False-Alarm Performance of Baseline Design With 10-ft/sec Turbulence

Run	Random-sequence set	Maneuver	Number of triggers	Number of false alarms	Isolated surface	FDI active time,[a] sec
1	1	CT4	1	1	[b]RT	1.50
2	2	CT4	1	1	[b]U	2.50
3	3	CT4	9	5	[b]RT,[b]U	18.50
4	3	None	6	2	[b]RT,[b]U	6.95
[c]5	1	CT4	7	1	[b]U	56.00

[a]Time aircraft-path subsystem is operational before being inhibited by a failure isolation.
[b]See symbol list for definition.
[c]4-ft/sec turbulence.

Figure A9 shows the measured and predicted accelerations and the residuals for the no-failure, no-maneuver run in 10-ft/sec turbulence, and figure A10 shows the corresponding trigger and verify statistics. The accelerations are considerably larger and more volatile than those in figure A4 for the no-turbulence, CT4 maneuver case. Though differences in the residuals are not as obvious, the trigger statistics in figure A10 are significantly larger than those in figure A5 for the no-turbulence case. In the first 11 sec of the run, there were six false triggers, two false verifies, one false undetermined failure declaration, and one false right-throttle failure isolation.

The level of false alarms observed in these runs is obviously unacceptable and indicates that the truth model for the trigger, verify, and isolate statistics does not account for all the noises, or errors, introduced by the actuator activity and aircraft motion caused by the turbulence. Some modification must be made to the design to allow the system to operate in atmospheric turbulence.

Results With Model Errors

Previous studies (refs. 15, 18, and 22) indicate that one of the biggest problems to be overcome in FDI systems is the degradation in FDI performance caused by errors in the model of the plant. As mentioned previously, a primary reason for selecting a decentralized design for the current FDI system was to improve the robustness to aircraft model errors. These errors can be caused by the simplicity of the model, by the errors in measuring the basic parameters such as the aerodynamic coefficients, by variation from component to component, and by departing from the flight condition for which the FDI system was designed. To evaluate the robustness of the system, model errors were introduced; a number of simulation runs were completed to evaluate system performance. The types of model errors and the simulation results are discussed in the next two subsections.

Actuator-Path Subsystem

Errors were introduced into the actuator-path subsystem by changing the cutoff frequency, rate limit, position limits, and stretch factor of each of the actuator models for the stabilizers, rudder, elevators, and ailerons. The amount of error was based on a percentage of the nominal value, and the percentages for two different cases are tabulated in table 16. No model errors were introduced into the aircraft-path subsystem in either of these cases.

Table 16. Actuator-Path Model Errors

	Model error, percent of nominal			
	Case 1		Case 2	
Model parameter	Left surfaces	Right surfaces and rudder	Left surfaces	Right surfaces and rudder
Cutoff frequency	-10	10	-25	25
Rate limit	-10	10	-25	25
Upper position limit	5	-5	12.5	-12.5
Lower position limit	-5	5	-12.5	12.5
Stretch factor	-15	15	-37.5	37.5

Simulation runs were made to evaluate actuator-path subsystem performance with errors in the actuator models according to the two cases in table 16. Runs were made with no failures and with a right-stabilizer failure, a rudder failure, a right-elevator failure, and a right-aileron failure, all without turbulence. One no-failure run with 10-ft/sec turbulence was made for each of the model-error cases. The failures were identical to the stuck-at-current-position failures reported in table 12.

Results of the 12 simulation runs are shown in table 17. The table shows that all the failures were detected and isolated for both cases of model errors. Comparison with table 12 shows that the detection-isolation times were equal to or less than those with no model error. For case 1, the case with the smaller model errors, there were no actuator-path false alarms. The one false

alarm for this case was the previously experienced aircraft-path subsystem right-throttle false failure in the run with atmospheric turbulence. For the larger model errors of case 2, however, the results were different. There were two false alarms in the actuator-path subsystem for each of the no-failure runs; these two false alarms were false failures of the left and right ailerons in both runs. Two false alarms were also experienced in each of the runs; these false alarms simulated a rudder failure, a right-elevator failure, and a right-aileron failure. Three false alarms occurred in the right-stabilizer-failure run. All the false alarms were either left-aileron, right-aileron, or right-elevator failures. From these data, it seems that failure detection in the actuator-path subsystem is not a problem with small or moderate model errors, and small model errors can be tolerated without false alarms. However, as would be expected, false alarms become a problem as the model errors increase.

Table 17. Simulation Results for Actuator-Path Stuck-at-Current-Position Failures
With No Turbulence and With Model Errors

Failed surface	Failed actuator position,[a] deg	Model-error case 1		Model-error case 2	
		Detection/ isolation times,[b] sec	False alarms[c]	Detection/ isolation times,[b] sec	False alarms[c]
None			0		2
None[d]			[e]1		[f]3
Right stabilizer	−0.07	5.95	0	5.95	3
Rudder	−1.80	.70		.70	2
Right elevator	−.44	5.60		5.60	2
Right aileron	1.30	1.90		1.90	2

[a]Relative to trim.
[b]Verify time relative to failure time.
[c]Includes both actuator-path and aircraft-path false alarms.
[d]With 10-ft/sec turbulence.
[e]Aircraft-path right-throttle false alarm.
[f]Includes one aircraft-path right-throttle false alarm.

Aircraft-Path Subsystem

To evaluate aircraft-path subsystem performance with respect to errors in the aircraft model, errors were introduced into the aircraft-path subsystem model in two ways. The FDI system design is based on a linear aircraft model at a single operating point described in table 1, and results previously discussed have been produced with the aircraft operating at that point. The first method of introducing model errors was to fly the aircraft (in simulation) at operating points different from that in table 1. Obviously, this technique simulates the performance of the FDI system as the aircraft departs from the design point, as it would always do during any flight. The second method of incorporating model errors was to inject random errors into the values for the aerodynamic and control derivatives that are used in the aircraft-path subsystem. These errors simulate the inaccuracies in the knowledge of the aircraft parameters, even at the design operating point. These procedures and the results of the simulation are discussed in the following two subsections.

Other operating points. When the aircraft was flown at trim case A (see table 18) and the climbing-turn maneuver CT4 was performed, there was one false trigger in the aircraft-path

subsystem, but no false alarms, as summarized in table 19. When this run was repeated with 10-ft/sec turbulence, the same right-throttle false alarm occurred that was experienced in the nominal trim case.

Table 18. Aircraft Operating Points for Evaluation of Effects of Aircraft-Path Model Errors

Parameter	Nominal trim	Trim case A	Trim case B	Trim case C
Altitude, ft	3500	5000	1500	20 000
Indicated airspeed, knots	160	175	140	325
Flight-path angle, deg	0	0	-3	0
Flaps, deg	15	15	30	0
Landing gear	Up	Up	Down	Up

Table 19. False-Alarm Performance of Aircraft-Path Subsystem at Off-Nominal Trim Points

Run	Trim case	Turbulence, ft/sec	Number of triggers	Number of false alarms	Isolated surface	FDI active time,[a] sec
1	A	None	1	0		56.00
2	A	10	1	1	^bRT	.50
3	B	None	0	0		56.00
4	C	None	1	$^c4$	$^bLT,^bRT,^bRA$	.40

[a]Time aircraft-path subsystem is operational before being inhibited by a failure isolation.
[b]See symbol list for definition.
[c]Includes three actuator-path false alarms.

When the aircraft was initialized at trim case B (final approach on a 3° glideslope) and the climbing-turn maneuver was flown, there were no false triggers. Eight simulation runs were then executed at trim case B, each with an aircraft-path failure, and the results are shown in table 20. All the failures were detected. At 60-percent effectiveness, detection was a little slower than at nominal trim for the rudder failure and a little faster for the elevator failure. Although all failures were detected, isolation was a little more difficult than at nominal trim. Of the four failures at 60-percent effectiveness, only the stabilizer failure was isolated, and that to a confusion set (right horizontal tail) containing the right stabilizer as expected. Undetermined failures were declared as a result of the other three failures. The resulting confusion set contained the failed surface, except for the aileron failure. For the failures at 40-percent effectiveness, the rudder and aileron failures were isolated to the correct surfaces, and the stabilizer and elevator failures were isolated to confusion sets that contained the failed surface. (The right-stabilizer failure was correctly isolated to the right horizontal tail.)

The aircraft was then initialized at trim case C, which represented a cruise condition at an altitude of 20,000 ft. Obviously, this condition was a large departure from the nominal trim for which the system was designed. A false failure of the right aileron was declared by the aircraft-path subsystem less than 1 sec after the FDI system was activated. It was expected that false alarms would occur in this case because of the model errors produced by the large departure from the design point.

Table 20. Failure-Detection and Isolation Performance for Aircraft-Path Failures With
No Turbulence and Trim Case B

(a) Detection performance

Failed surface	Failure-detection time[a] as a function of percent surface effectiveness				
	0%	20%	40%	60%	80%
Right stabilizer			0.60	1.15	
Rudder			2.30	8.70	
Right elevator			6.95	7.10	
Right aileron			6.70	7.40	

[a]Time of failure declaration relative to time of failure.

(b) Isolation performance

Failed surface	Failure isolation as a function of percent surface effectiveness				
	0%	20%	40%	60%	80%
Right stabilizer			[a]$CS\,(RS,RE)$	[a]$CS\,(RS,RE)$	
Rudder			Yes	[a]$U\,(RT,R_u)$	
Right elevator			[a]$CS\,(LS,RS,LE,RE)$	[a]$U\,(LS,RS,LE,RE)$	
Right aileron			Yes	[a]$U\,(LS,RS,LE,RE)$	

[a]See symbol list for definition.

Random errors. To evaluate the effect of uncertainties in the aircraft model at the design point on the performance of the aircraft-path subsystem, simulation runs were made at the nominal trim point with random errors added to the model parameters. The random errors were generated by using a sequence of zero-mean, unit-variance, Gaussian, random numbers that were then multiplied by the desired standard deviation of the error in the model parameter. If the resulting error exceeded three standard deviations, a new random error was generated for that parameter. The standard deviations of the errors for the various parameters in the model are tabulated in table 21 in terms of percent of the nominal value. These percentages were based on data in reference 39 and on parameter estimation experience at Langley Research Center.

Three no-failure runs were made that simulated the CT4 maneuver with no turbulence. Each run utilized a different seed for the random-number generator, so that different random errors were added to the model parameters for each run. In the first run, there were two aircraft-path false alarms; one was an undetermined (not isolated) failure, and the other was a false failure of the left throttle. In the second run, there were five false triggers, but no verifies and, thus, no false alarms. In the third run, there was one false trigger, but no false alarms. These results are summarized in table 22.

Four additional runs, each with a different surface failed at 60-percent effectiveness, were made with random-error set C. As can be seen from table 22, the failure was detected in each case. The stabilizer failure was correctly isolated to the right horizontal tail, but the elevator failure was incorrectly isolated to the left horizontal tail. Comparisons with similar runs without model errors in table 13 show that the detection time was the same for the stabilizer failure, but

Table 21. Standard Deviations of Random Errors Added to Aerodynamic and Control
Derivatives and to Other Model Parameters To Evaluate Model-Error Effects

Parameter	Standard deviation, percent	Parameter	Standard deviation, percent	Parameter	Standard deviation, percent
C_{X_α}	10	C_{Y_β}	10	C_{Z_α}	5
C_{X_q}	30	C_{Y_p}	50	C_{Z_q}	20
		C_{Y_r}	30		
$C_{X_{\delta T}}$	5	$C_{Y_{\delta T}}$	20	$C_{Z_{\delta T}}$	5
$C_{X_{\delta S}}$	10	$C_{Y_{\delta S}}$	20	$C_{Z_{\delta S}}$	10
$C_{X_{\delta R}}$	20	$C_{Y_{\delta R}}$	5	$C_{Z_{\delta R}}$	20
$C_{X_{\delta E}}$	10	$C_{Y_{\delta E}}$	20	$C_{Z_{\delta E}}$	10
$C_{X_{\delta A}}$	20	$C_{Y_{\delta A}}$	20	$C_{Z_{\delta A}}$	20
$C_{X_{\delta Sp}}$	10	$C_{Y_{\delta Sp}}$	20	$C_{Z_{\delta Sp}}$	10
C_{X_0}	5	C_{Y_0}	5	C_{Z_0}	5
C_{l_β}	10	C_{m_α}	5	C_{n_β}	5
C_{l_p}	10	C_{m_q}	10	C_{n_p}	90
C_{l_r}	40			C_{n_r}	10
$C_{l_{\delta T}}$	20	$C_{m_{\delta T}}$	5	$C_{n_{\delta T}}$	5
$C_{l_{\delta S}}$	10	$C_{m_{\delta S}}$	5	$C_{n_{\delta S}}$	10
$C_{l_{\delta R}}$	10	$C_{m_{\delta R}}$	10	$C_{n_{\delta R}}$	5
$C_{l_{\delta E}}$	10	$C_{m_{\delta E}}$	5	$C_{n_{\delta E}}$	10
$C_{l_{\delta A}}$	5	$C_{m_{\delta A}}$	10	$C_{n_{\delta A}}$	10
$C_{l_{\delta Sp}}$	10	$C_{m_{\delta Sp}}$	10	$C_{n_{\delta Sp}}$	10
C_{l_0}	5	C_{m_0}	5	C_{n_0}	5
I_X	1	I_Y	1	I_Z	1
Mass	0.5				
b	0.5	$\bar{c}$	0.5	S	0.5

detection and isolation of the rudder failure took much longer in the presence of model errors. Detection and isolation of the aileron failure were somewhat faster with model errors, presumably because the model errors in this case increased the residuals used to detect and isolate a right-aileron failure. For the elevator failure, isolation (to a confusion set) was incorrectly declared with model errors present, but only an undetermined (not isolated) failure was declared in the simulation run without model errors.

Summarizing the effects of model errors, it has been shown that small errors on the order of 10 percent in the model parameters have little effect on the actuator-path subsystem performance, although larger errors cause some false alarms. Performance of the aircraft-path subsystem is not severely affected by moderate departures from the design operating point. As expected, large departures from the design point produce unacceptable false alarms. At the design point, nominal errors in the model parameters affected the aircraft-path subsystem performance, but the effect was not extreme.

Aircraft-Path Subsystem Designs for Operation in Turbulence

As noted previously (see table 15), the baseline (BL) design produced unacceptable performance when operating in 10-ft/sec turbulence ($\sigma_G = 10$) because of the false alarms experienced

Table 22. Failure-Detection and Isolation Performance for Aircraft-Path Failures With Random-Model Errors and No Turbulence

(a) Detection performance

Failed surface	Failure-detection time[a] as a function of percent surface effectiveness				
	0%	20%	40%	60%	80%
Right stabilizer				1.15	
Rudder				47.65	
Right elevator				7.90	
Right aileron				6.50	

[a]Time of failure declaration relative to time of failure.

(b) Isolation performance

Failed surface	Failure isolation as a function of percent surface effectiveness				
	0%	20%	40%	60%	80%
Right stabilizer				$^aCS(RS,RE)$	
Rudder				Yes	
Right elevator				$^aCS(LS,LE)$	
Right aileron				Yes	

[a]See symbol list for definition.

(c) False-alarm performance

Run	Random-error set	Number of triggers	Number of false alarms	Isolated surface	FDI active time,[a] sec
1	A	4	2	$^bLT,^bU$	12.70
2	B	5	0		56.00
3	C	1	0		56.00

[a]Time aircraft-path subsystem is operational before being inhibited by a failure isolation.
[b]See symbol list for definition.

by the aircraft-path subsystem. One way to improve false-alarm performance is to increase the thresholds in the trigger, verify, and isolate tests. Of course, increasing the thresholds affects the missed-detection and false-alarm performances, and a compromise solution may be required. An adaptive system may be required in which the thresholds and other parameters are adjusted as functions of the turbulence level.

Recall that computation of the thresholds utilizes the covariance matrices $\Sigma_f(k)$ of the sum of k residuals $\nu(j)$, and that the values of $\Sigma_f(k)$ depend on the white-noise and low-pass-noise covariances, Σ_w and Σ_ℓ, respectively, of the residuals as determined by the truth model. For the BL design, Σ_w was determined by propagating the sensor noise into the residuals, and Σ_ℓ was computed from the worst-case residuals experienced during a simulated climbing-turn maneuver (CT4) without sensor noise or turbulence.

When the CT4 maneuver was flown in 10-ft/sec turbulence without failures (three runs with different random-number seeds), the aircraft-path residuals were examined, and it was

found that the sample variances of some residual components were significantly larger than the variances in the truth model, particularly for the $\dot{q}$ component. Furthermore, when the simulation was flown with sensor noise but without maneuvers, turbulence, or failures, the sample variances of the residuals were larger than the white-noise variances in the truth model for the A_z, $\dot{q}$, and $\dot{r}$ components. Thus, it appears that the noise variances in the truth model for the BL design were too small for the turbulence case, and as a result, the covariance matrices $\boldsymbol{\Sigma}_f(k)$ were incorrect and the thresholds were too low.

Nonadaptive Designs for 10-ft/sec Turbulence

Based on the preceding results, the variances σ_w^2 of the white noise on the A_z, $\dot{q}$, and $\dot{r}$ residuals were increased, and the new values (diagonals of $\boldsymbol{\Sigma}_w$) are shown in table 23. Also, the variances of the low-pass noise (diagonals of $\boldsymbol{\Sigma}_\ell$) were increased for the turbulence case in accordance with the simulation results for the climbing turn with and without sensor noise in 10-ft/sec turbulence; these new values are likewise shown in table 23. Also shown in the table are values for the diagonals $\sigma_f(N)$ of the covariance matrix $\boldsymbol{\Sigma}_f(N)$ of the sum $S(k)$ of the N latest residuals for $N = 20$.

Table 23. Errors for Aircraft-Path Truth Model for New-Threshold Design

Residual	Standard deviation of white noise, $^a\sigma_w$	Low-frequency noise cutoff, rad/sec	Standard deviation of low-frequency noise, $^b\sigma_\ell$	HPF cutoff frequency, rad/sec	Standard deviation of total noise, $^c\sigma_f(20)$
x-acceleration, ν_x	0.39 ft/sec^2	2.0	0.419 ft/sec^2	0.5	5.46 ft/sec^2
y-acceleration, ν_y	.42 ft/sec^2		.233 ft/sec^2		3.36 ft/sec^2
z-acceleration, ν_z	1.60 ft/sec^2		1.09 ft/sec^2		15.04 ft/sec^2
P-acceleration, ν_P	.035 rad/sec^2		.020 rad/sec^2		.286 rad/sec^2
Q-acceleration, ν_Q	.026 rad/sec^2		.0130 rad/sec^2		.193 rad/sec^2
R-acceleration, ν_R	.0157 rad/sec^2		.0169 rad/sec^2		.220 rad/sec^2

^{a}Square root of diagonal terms of $\boldsymbol{\Sigma}_w$.
^{b}Square root of diagonal terms of $\boldsymbol{\Sigma}_\ell$.
^{c}Square root of diagonal terms of $\boldsymbol{\Sigma}_f$.

Using these new values for noise variances in the truth model, two new aircraft-path subsystem designs for operation in 10-ft/sec turbulence were produced. These two designs, new-threshold (TG) design and new-projection-vector (PV10) design, and the results of their evaluation via simulation are discussed in the next two subsections.

New-Threshold Design

When new values for the covariance matrices $\boldsymbol{\Sigma}_f(k)$ are used in the design procedure discussed in previous sections to design a new aircraft-path subsystem, the trigger thresholds, projection vectors, verify gains, verify thresholds, and isolate thresholds are all affected. If an adaptive system is required in order to achieve an acceptable false-alarm/missed-detection performance, then some of these parameters must be adjusted as functions of turbulence. Adjusting the projection vectors would be more complex computationally than adjusting the gains and thresholds, which are scalar quantities. Therefore, in the first of the two new designs, the new TG design, the projection vectors obtained in the BL design were retained. New

gains G_{A_i} and G_{D_i} and new thresholds t_{T_i}, t_{V_i}, and $t_{I_{i/j}}$ were computed by using the design procedure with the new covariance matrices Σ_f but retaining the old projection vectors $\mathbf{P}_i$ and $\mathbf{P}_{i/j}$. Values for the gains and thresholds for the new TG design are shown in table 24. The trigger and verify thresholds have increased for each of the surfaces. Also, the minimum detectable trigger and verify signals, $\bar{f}_{S_{T_i}}$ and $\bar{s}_i$, have increased; this increase indicates that a larger signal (failure magnitude) is required for reliable detection, as would be expected with the larger noise variances.

Table 24. Design Results for Aircraft-Path Subsystem for New-Threshold Design

Design parameter	Left thrust	Right thrust	Left horizontal tail	Right horizontal tail	Rudder	Left aileron	Right aileron
$\bar{f}_{s_T}$	4.25	4.25	1.66	1.66	3.41	8.22	8.22
t_T	−9.283	−9.283	−9.402	−9.402	−9.298	−9.380	−9.380
$\bar{s}$	0.0717	0.0717	0.0598	0.0598	0.0702	0.0620	0.0620
G_A	0.0717	0.0717	0.0598	0.0598	0.0702	0.0620	0.0620
G_D	0.00257	0.00257	0.00179	0.00179	0.00246	0.00192	0.00192
t_V	0.00771	0.00771	0.00894	0.00894	0.00738	0.00962	0.00962
$\bar{s}_{i/j}$: (LT)		0.0648	0.0459	0.0459	0.1058	0.0458	0.0469
(RT)			.0459	.0459	.1058	.0469	.0458
(LH)			.0611		.0453	.0539	.0539
(RH)					.0453	.0539	.0539
(Ru)						.0463	.0463
(LA)							.0457
(RA)							
$t_{I_{i/j}}$: (LT)		0.194	0.184	0.184	0.317	0.183	0.188
(RT)			.184	.184	.317	.188	.183
(LH)			.305		.181	.270	.270
(RH)					.181	.270	.270
(Ru)						.185	.185
(LA)							.228
(RA)							

To evaluate the false-alarm performance of the new TG design, three runs with the CT4 climbing-turn maneuver were made in 10-ft/sec turbulence; each run utilized different random sequences for the turbulence. Results are summarized in table 25. No false alarms and only two false triggers were experienced in the three runs for a total of 168 sec of aircraft-path subsystem operating time, compared with seven false alarms in 22.5 sec for the BL system under the same conditions.

The performance of the new TG design in detecting and isolating aircraft-path failures under turbulent conditions ($\sigma_G = 10$ ft/sec) was evaluated by simulating a loss of surface effectiveness, or a partially missing surface, for each of the four types of surfaces: stabilizer, rudder, elevator, and aileron. Each failure occurred at $t = 5$ sec, and the climbing-turn maneuver CT4 was initiated at $t = 10$ sec.

Results of the simulation are shown in table 25 as a function of the percent effectiveness of the failed surface. With the surface at 60-percent effectiveness, the stabilizer, rudder, and

61

elevator failures were detected, but the aileron failure was not. The aileron failure at 40-percent effectiveness was detected. With no atmospheric turbulence, the BL system detected all four failures at 60-percent effectiveness (table 13). Also, the new TG design took slightly longer to detect the failures in turbulence than the BL system did with no turbulence. At 40-percent effectiveness, the stabilizer and elevator failures were detected more quickly by the TG design than at 60-percent effectiveness, but the stabilizer, rudder, and elevator failures at 80-percent effectiveness were not detected.

Table 25. Failure-Detection and Isolation Performance for New-Threshold Design
With 10-ft/sec Turbulence

(a) Detection performance

Failed surface	Failure-detection time[a] as a function of percent surface effectiveness				
	0%	20%	40%	60%	80%
Right stabilizer			1.15	2.10	[b]ND
Rudder				3.45	[b]ND
Right elevator			7.10	7.35	[b]ND
Right aileron			6.50	[b]ND	

[a]Time of failure declaration relative to time of failure.
[b]See symbol list for definition.

(b) Isolation performance

Failed surface	Failure isolation as a function of percent surface effectiveness				
	0%	20%	40%	60%	80%
Right stabilizer			[a]$CS(RS,RE)$	[a]$U(LS,RS,LE,RE)$	[a]ND
Rudder				Yes	[a]ND
Right elevator			[a]$CS(RS,RE)$	[a]$U(RA)$	[a]ND
Right aileron			Yes	[a]ND	

[a]See symbol list for definition.

(c) False-alarm performance

Run	Random-sequence set	Number of triggers	Number of false alarms	Isolated surface	FDI active time,[a] sec
1	1	1	0		56.00
2	2	1	0		56.00
3	3	0	0		56.00

[a]Time aircraft-path subsystem is operational before being inhibited by a failure isolation.

In terms of isolation performance, at 60-percent effectiveness the rudder failure was isolated correctly, but the stabilizer and elevator failures resulted in undetermined failure declarations.

In the stabilizer case, the confusion set contained the failed surface, but in the elevator case it did not. At 40-percent effectiveness, the stabilizer and elevator failures were isolated to the correct confusion sets. Although there were a few actuator-path triggers, no actuator-path false alarms were experienced during these runs. In general, the new TG design performed almost as well in detecting and isolating failures in turbulence as the BL system did in a zero-turbulence environment, and the false-alarm performance of the new TG design was vastly superior to that of the BL system in turbulence.

As mentioned previously, it is to be expected that the detection performance of the new TG design with no turbulence would be degraded from the BL system because the thresholds have been increased. To evaluate this performance, 15 runs were made with the new TG design in a no-turbulence environment with various simulated failures. The results are summarized in table 26. For failed-surface effectivenesses of 0 and 20 percent, failures were detected and isolated correctly. At 40-percent effectiveness, the aileron failure was not detected, and only the stabilizer failure was correctly isolated. Detection was quicker for the larger failures. Failures of the stabilizer, rudder, and elevator at 60-percent effectiveness were not detected. Detection/isolation performance was not quite as good as in turbulence (table 25), where failures were detected with smaller failure magnitudes (with 20 percent more effectiveness). Thus, the new TG design performed well. It did not perform quite as well as the BL system with no turbulence, but much better than the BL system in 10-ft/sec turbulence.

Table 26. Failure-Detection and Isolation Performance for New-Threshold Design
With No Turbulence

(a) Detection performance

Failed surface	Failure-detection time[a] as a function of percent surface effectiveness				
	0%	20%	40%	60%	80%
Right stabilizer	0.70	0.85	1.15	[b]ND	
Rudder	1.25	2.65	48.30	[b]ND	
Right elevator	0.65	1.20	7.25	[b]ND	
Right aileron	6.35	6.60	[b]ND		

[a]Time of failure declaration relative to time of failure.
[b]See symbol list for definition.

(b) Isolation performance

Failed surface	Failure isolation as a function of percent surface effectiveness				
	0%	20%	40%	60%	80%
Right stabilizer	[a]$CS\,(RS,RE)$	[a]$CS\,(RS,RE)$	[a]$CS\,(RS,RE)$	[a]ND	
Rudder	Yes	Yes	[a]$U\,(LT)$	[a]ND	
Right elevator	[a]$CS\,(RS,RE)$	[a]$CS\,(RS,RE)$	[a]$U\,(RA)$	[a]ND	
Right aileron	Yes	Yes	[a]ND		

[a]See symbol list for definition.

While the new-threshold design was intended for operation in 10-ft/sec turbulence, in terms of thresholds and gains, it was not completely designed for turbulence, in that the projection vectors from the BL design were retained. The optimum system for use in 10-ft/sec turbulence, in terms of the design procedure previously described, would be a system completely redesigned by using the noise standard deviations for the turbulence truth model in table 23. Such an aircraft-path subsystem, referred to herein as the new-projection-vector (PV10) design, was designed and evaluated for comparison with the new TG design. Results of the design process are shown in tables 27 to 29. It is interesting to note the projection vectors (table 27) for the trigger and verify tests and to compare them with those in the baseline design (table 8). In the BL design, the tests for thrust failures depended almost entirely on the yaw-rate residual (the ν_r-component of the projection vector is 0.9999) and not at all on the pitch-rate residual. In the new PV10 design, however, the thrust-failure tests depend significantly on the pitch-rate residual. A similar change occurred in the vector for the rudder-failure tests. On the other hand, the projection vectors for the horizontal tail failures remain unchanged. Also, while the minimum detectable failure magnitudes $\bar{f}_{S_{T_i}}$ for the new PV10 design are considerably larger than for the BL system, they are smaller than those for the new TG design.

Table 27. New-Projection-Vector Design Results for Aircraft-Path Trigger Test
After Projection-Vector Optimization

Design parameter	Left thrust	Right thrust	Left horizontal tail	Right horizontal tail	Rudder	Left aileron	Right aileron
P:							
(ν_x)	0.0376	0.0376	0	0	0	0	0
(ν_y)	0	0	0	0	.0445	0	0
(ν_z)	0	0	0	0	0	0	0
(ν_p)	0	0	0	0	.446	.749	−.749
(ν_q)	.545	.545	−1.0	−1.0	0	−.662	−.662
(ν_r)	.838	−.838	0	0	−.894	0	0
σ_{S_T}	.295	.295	.193	.193	.278	.250	.250
t_T	−9.086	−9.086	−9.402	−9.402	−9.138	−9.226	−9.226
$\bar{f}_{S_T}$	3.44	3.44	1.66	1.66	2.77	6.46	6.46

Table 28. New-Projection-Vector Design Results for Aircraft-Path Verify Test
After Projection-Vector Optimization

Design parameter	Left thrust	Right thrust	Left horizontal tail	Right horizontal tail	Rudder	Left aileron	Right aileron
$\bar{s}$	0.0914 lb × 10^3	0.0914 lb × 10^3	0.0598°	0.0598°	0.0862°	0.0774°	0.0774°
G_A	.0914	.0914	.0598	.0598	.0862	.0774	.0774
G_D	.00418	.00418	.00179	.00179	.00372	.00300	.00300
k_T	3	3	5	5	4	5	5
t_V	.01254	.01254	.00894	.00894	.01486	.01498	.01498

Table 29. New-Projection-Vector Design Results for Aircraft-Path Isolate Test
After Projection-Vector Optimization

Design parameter	Left thrust	Right thrust	Left horizontal tail	Right horizontal tail	Rudder	Left aileron	Right aileron
$\sigma_{S_{I_{i/j}}}$:							
(LT)		0.418	0.385	0.390	0.585	0.360	0.360
(RT)			.390	.385	.585	.360	.360
(LH)				.394	.293	.348	.348
(RH)					.293	.348	.348
(Ru)						.341	.341
(LA)							.295
(RA)							
$\bar{s}_{i/j}$:							
(LT)		0.0648	0.0597	0.0604	0.0907	0.0558	0.0558
(RT)			.0604	.0597	.0907	.0558	.0558
(LH)				.0611	.0453	.0539	.0539
(RH)					.0453	.0539	.0539
(Ru)						.0529	.0529
(LA)							.0457
(RA)							
$k_{i/j}$:							
(LT)		3	3	3	3	4	4
(RT)			3	3	3	4	4
(LH)				5	4	5	5
(RH)					4	5	5
(Ru)						4	4
(LA)							5
(RA)							
$t_{I_{i/j}}$:							
(LT)		0.194	0.179	0.181	0.272	0.223	0.223
(RT)			.181	.179	.272	.223	.223
(LH)				.305	.181	.270	.270
(RH)					.181	.270	.270
(Ru)						.212	.212
(LA)							.228
(RA)							

To evaluate the false-alarm performance of the new PV10 design, three runs with the CT4 climbing-turn maneuver were made with $\sigma_G = 10$ ft/sec; each run used different random sequences for the turbulence. Results are summarized in table 30. One false alarm (false detection) and five false triggers were experienced in the three runs, for a total of 168 sec of aircraft-path subsystem operating time, compared with no false alarms and only two false triggers for the new TG design under the same conditions and compared with seven false alarms in 22.5 sec for the BL system. Thus, in terms of false-alarm performance in turbulence, the new PV10 design was far superior to the BL design, but not quite as good as the new TG design. It is not known why the new PV10 design exhibited slightly poorer false-alarm performance, contrary to expectations, than the new TG design.

Table 30. Failure-Detection and Isolation Performance for New-Projection-Vector Design With 10-ft/sec Turbulence

(a) Detection performance

Failed surface	Failure-detection time[a] as a function of percent surface effectiveness				
	0%	20%	40%	60%	80%
Right stabilizer			1.15	13.30	14.30
Rudder				3.45	38.35
Right elevator			7.10	7.35	[b]ND
Right aileron				6.55	13.05

[a]Time of failure declaration relative to time of failure.
[b]See symbol list for definition.

(b) Isolation performance

Failed surface	Failure isolation as a function of percent surface effectiveness				
	0%	20%	40%	60%	80%
Right stabilizer			[a]$CS(RS, RE)$	[a]RA	[a]$U(LT)$
Rudder				Yes	Yes
Right elevator			[a]$CS(RS, RE)$	[a]$U(RA)$	[a]ND
Right aileron				Yes	Yes

[a]See symbol list for definition.

(c) False-alarm performance

Run	Random-sequence set	Number of triggers	Number of false alarms	Isolated surface	FDI active time,[a] sec
1	1	3	0		56.00
2	2	2	1	[b]LT	56.00
3	3	0	0		56.00

[a]Time aircraft-path subsystem is operational before being inhibited by a failure isolation.
[b]See symbol list for definition.

The performance of the new PV10 design in detecting and isolating aircraft-path failures under turbulent conditions ($\sigma_G = 10$ ft/sec) was evaluated by simulating a loss of surface effectiveness during the climbing-turn maneuver CT4, and results are shown in table 30 as a function of the percent effectiveness of the failed surface. With the surface at 60-percent effectiveness, all failures were detected, and at 80 percent, all failures but the elevator were detected. This performance is somewhat better than that of the new TG design (table 25), which failed to detect failures at 80-percent effectiveness. With respect to isolation performance, the new PV10 design was able to correctly isolate rudder and aileron failures even at 80-percent effectiveness, an improvement over the new TG design. However, the two designs were nearly equal in their ability to isolate stabilizer and elevator failures in 10-ft/sec turbulence.

Results of nine simulation runs to evaluate the performance of the new PV10 design with no turbulence are tabulated in table 31. In this environment, failure-detection performance of the new TG and new PV10 designs were similar; neither detected failures at 60-percent effectiveness, and both detected three out of four failures at 40-percent effectiveness. Isolation performance of the new PV10 design was better, in that it correctly isolated the three failures it detected at 40-percent effectiveness.

Table 31. Failure-Detection and Isolation Performance for New-Projection-Vector Design With No Turbulence

(a) Detection performance

Failed surface	Failure-detection time[a] as a function of percent surface effectiveness				
	0%	20%	40%	60%	80%
Right stabilizer			1.15	[b]ND	
Rudder			47.35	[b]ND	
Right elevator		1.35	ND	[b]ND	
Right aileron			6.60	[b]ND	

[a]Time of failure declaration relative to time of failure.

[b]See symbols list for definition.

(b) Isolation performance

Failed surface	Failure isolation as a function of percent surface effectiveness				
	0%	20%	40%	60%	80%
Right stabilizer			[a]CS (RS,RE)	[a]ND	
Rudder			Yes	↑	
Right elevator		[a]CS (RS,RE)	[a]ND	↓	
Right aileron			Yes		

[a]See symbol list for definition.

The performance of the three designs is summarized in table 32. The baseline system performed best with no turbulence, where it detected four out of four failures at 60-percent effectiveness; the other two designs detected none of those. In 10-ft/sec turbulence, however, the BL system was unusable as a result of false alarms, while the other two performed well; the new-threshold design was the best with respect to false alarms. The new TG design and the new PV10 design both performed well in detecting and isolating failures in turbulence, but the new PV10 design performed better. It detected three out of four failures at 80-percent effectiveness, and the new TG design detected none out of three. The new PV10 design is sufficiently superior to the new TG design to warrant using it as the basis for an adaptive design. In other words, an aircraft-path subsystem design that is adaptive to varying turbulence levels should include adaptive projection vectors as well as adaptive thresholds and gains.

67

Table 32. Summary of Performance of Baseline, New-Threshold, and
New-Projection-Vector Designs

(a) Detection and isolation of failures with no turbulence

Design	Number of failures/number detected/number correctly isolated[a] as a function of percent surface effectiveness				
	0%	20%	40%	60%	80%
Baseline				4/4/3	4/1/0
New TG	4/4/4	4/4/4	4/3/1	3/0/0	
New PV10		1/1/1	4/3/3	4/0/0	

[a]For stabilizer and elevator failures, isolated to horizontal tail (confusion set containing only stabilizer and elevator).

(b) Detection and isolation of failures with 10-ft/sec turbulence

Design	Number of failures/number detected/number correctly isolated[a] as a function of percent surface effectiveness				
	0%	20%	40%	60%	80%
Baseline					
New TG			3/3/3	4/3/1	3/0/0
New PV10			2/2/2	4/4/2	4/3/2

[a]For stabilizer and elevator failures, isolated to horizontal tail (confusion set containing only stabilizer and elevator).

(c) False-alarm performance (no failures) with 10-ft/sec turbulence

Design	Number of false triggers	Number of false alarms (false detections)	FDI active time,[a] sec
Baseline	11	7	22.5
New TG	2	0	168.0
New PV10	5	1	168.0

[a]Time aircraft-path subsystem is operational.

Adaptive Type Designs

Interpolated Design

Superior FDI performance is achieved when different projection vectors, gains, and thresholds are used in zero turbulence and in 10-ft/sec turbulence. In particular, the baseline (BL) design was superior at zero turbulence, and the new-projection-vector (PV10) design was superior at 10-ft/sec turbulence. In an operational FDI system, some technique must be incorporated into the system to switch between these two designs as the level of turbulence changes. For improved performance in other levels of turbulence, it seems logical that a smooth transition between the two designs as a function of the turbulence level would be preferred over an abrupt transition, or switch. Algorithms were implemented in the software to linearly interpolate between the

BL design values in zero turbulence and the new PV10 design values at 10-ft/sec turbulence for each of the trigger thresholds t_{T_i}, the trigger and verify projection vectors $\mathbf{P}_i$, the verify thresholds t_{V_i}, the isolate thresholds $t_{I_{i/j}}$, and the isolate projection vectors $\mathbf{P}_{i/j}$. Interpolation was performed as a function of the variable TURB, which represents the system's knowledge of the standard deviation of the turbulence, or gusts σ_G. In fact, the algorithms also extrapolated to levels higher than the 10-ft/sec level of the new PV10 design. After interpolation, the new trigger and isolate projection vectors were renormalized to unit length. The FDI system software did not use separate variables for the verify projection vectors and the verify gains, but combined them into one set of vectors $\mathbf{P}'_i$, where

$$\mathbf{P}'_i = G_{A_i} \mathbf{P}_i \tag{107}$$

The algorithms interpolated the vectors P'_i, and these were then used without normalization.

To perform the interpolation, the level of the turbulence σ_G must be known or estimated, and the limiting performance of the system would be when σ_G is known exactly. To evaluate this limiting performance, the algorithms in this design used the true value of turbulence by setting TURB = σ_G in the interpolation computations, and the system was called the interpolated design. Note that σ_G is the value specified for the simulation run, not the sample standard deviation of the actual sample sequence produced by the random-number generator.

To evaluate the false-alarm performance of the interpolated design at an intermediate turbulence level, three simulation runs were made while executing the CT4 climbing-turn maneuver in 5-ft/sec turbulence (TURB = σ_G = 5) with no failures. For comparison, similar runs were made with the BL and new PV10 designs. Results are summarized in table 33. Under these conditions, the BL design experienced 6 false alarms and 40 false triggers in 168 sec of operation. On the other hand, both the interpolated design and the new PV10 design experienced no false alarms and no false triggers in identical runs.

The performance of the interpolated design in detecting and isolating aircraft-path failures in 5-ft/sec turbulence was evaluated by simulating loss of surface effectiveness during the climbing-turn maneuver CT4; for comparison, similar runs were made with the new PV10 design. Results are shown as a function of the percent effectiveness of the failed surface for the new PV10 design in table 34 and for the interpolated design in table 35. With the surface at 60-percent effectiveness, all failures were detected by the interpolated design; however, only the rudder failure was detected by the new PV10 design. Furthermore, the interpolated design correctly isolated three of the four failures. At 80-percent effectiveness, the interpolated design detected and isolated the rudder failure, but not the stabilizer, elevator, and aileron failures. Thus, in 5-ft/sec turbulence the performance of the interpolated design was superior to that of the new PV10 design.

To assess false-alarm performance of the interpolated design in turbulence greater than the upper (PV10) design level of 10 ft/sec, three additional simulation runs with no failures were made in 15-ft/sec turbulence. The TURB was set equal to 15, so that the thresholds and projection vectors were extrapolated beyond the PV10 design level. Results of the runs with this extrapolated design are summarized in table 36. Nine false triggers and six false alarms were experienced in less than 82 sec. Thus, it appears that adjustment of the thresholds and projection vectors by linear extrapolation beyond the upper design level is not acceptable.

To obtain acceptable aircraft-path subsystem performance in turbulence significantly greater than 10 ft/sec, it appears that additional design points at higher turbulence levels must be obtained. Thresholds and projection vectors can then be calculated by interpolation between

Table 33. False-Alarm Performance Summary With 5-ft/sec Turbulence

(a) Baseline design

Run	Random-sequence set	Number of triggers	Number of false alarms	Isolated surface	FDI active time,[a] sec
1	1	11	3	[b]RT	56.00
2	2	12	1	[b]RT	56.00
3	3	17	2	[b]RT,[b]Ru	56.00

[a]Time aircraft-path subsystem is operational before being inhibited by a failure isolation.
[b]See symbol list for definition.

(b) New-projection-vector (PV10) design

Run	Random-sequence set	Number of triggers	Number of false alarms	Isolated surface	FDI active time,[a] sec
1	1	0	0		56.00
2	2	0	0		56.00
3	3	0	0		56.00

[a]Time aircraft-path subsystem is operational before being inhibited by a failure isolation.

(c) Interpolated design (TURB = 5 ft/sec)

Run	Random-sequence set	Number of triggers	Number of false alarms	Isolated surface	FDI active time,[a] sec
1	1	0	0		56.00
2	2	0	0		56.00
3	3	0	0		56.00

[a]Time aircraft-path subsystem is operational before being inhibited by a failure isolation.

Table 34. Failure-Detection and Isolation Performance for New-Projection-Vector Design With 5-ft/sec Turbulence

(a) Detection performance

Failed surface	Failure-detection time[a] as a function of percent surface effectiveness				
	0%	20%	40%	60%	80%
Right stabilizer			1.15	^bND	^bND
Rudder				34.45	
Right elevator			6.85	^bND	
Right aileron			6.40	^bND	

[a]Time of failure declaration relative to time of failure.
[b]See symbol list for definition.

(b) Isolation performance

Failed surface	Failure isolation as a function of percent surface effectiveness				
	0%	20%	40%	60%	80%
Right stabilizer			$^aCS\,(RS,RE)$	^aND	^aND
Rudder				Yes	
Right elevator			$^aCS\,(RS,RE)$	^aND	
Right aileron			Yes	^aND	

[a]See symbol list for definition.

(c) False-alarm performance

Run	Random-sequence set	Number of triggers	Number of false alarms	Isolated surface	FDI active time,[a] sec
1	1	0	0		56.00
2	2	0	0		56.00
3	3	0	0		56.00

[a]Time aircraft-path subsystem is operational before being inhibited by a failure isolation.

Table 35. Failure-Detection and Isolation Performance for Interpolated Design With 5-ft/sec Turbulence

(a) Detection performance

Failed surface	Failure-detection time[a] as a function of percent surface effectiveness				
	0%	20%	40%	60%	80%
Right stabilizer				1.15	^bND
Rudder				3.60	48.55
Right elevator			6.50	7.25	^bND
Right aileron				6.45	^bND

[a]Time of failure declaration relative to time of failure.
[b]See symbol list for definition.

(b) Isolation performance

Failed surface	Failure isolation as a function of percent surface effectiveness				
	0%	20%	40%	60%	80%
Right stabilizer	•			$^aCS\,(RS,RE)$	^aND
Rudder				Yes	Yes
Right elevator			$^aCS\,(RS,RE)$	$^aU\,(RA)$	^aND
Right aileron				Yes	^aND

[a]See symbol list for definition.

(c) False-alarm performance

Run	Random-sequence set	Number of triggers	Number of false alarms	Isolated surface	FDI active time,[a] sec
1	1	0	0		56.00
2	2	0	0		56.00
3	3	0	0		56.00

[a]Time aircraft-path subsystem is operational before being inhibited by a failure isolation.

Table 36. False-Alarm Performance of Extrapolated Design With 15-ft/sec Turbulence

Run	Random-sequence set	Number of triggers	Number of false alarms	Isolated surface	FDI active time,[a] sec
1	1	2	2	$^bU,^bRA$	14.20
2	2	2	2	$^bU,^bRS,^bRE$	12.50
3	3	5	2	$^bU,^bRA$	55.00

[a]Time aircraft-path subsystem is operational before being inhibited by a failure isolation.
[b]See symbol list for definition.

the appropriate design points. To this end, additional no-failure simulation runs were made in 20-ft/sec turbulence, and the residuals were processed to obtain new values for the diagonals of the white-noise and low-pass-noise covariance matrices, Σ_w and Σ_ℓ, respectively. These new values were input into the FDI design program to create another new-projection-vector design. When this design was evaluated in 20-ft/sec turbulence, six false triggers and four false alarms were experienced in 57.35 sec of operation during three simulation runs. To improve this performance, the trigger, verify, and isolate thresholds were increased by a factor of 1.5. With these new thresholds, no false alarms were encountered in three no-failure simulation runs in 20-ft/sec turbulence. The aircraft-path subsystem was then tested in 15-ft/sec turbulence. Thresholds and projection vectors were obtained by linearly interpolating (TURB = 15) between this latest design and the PV10 design. One false alarm was experienced in each of three no-failure simulation runs, again an unacceptable level of performance.

To improve system performance in the higher turbulence levels, the noise covariance matrices Σ_w and Σ_ℓ for 20-ft/sec turbulence were increased by a factor of 1.5, and these new values (shown in table 37) were used to create a new aircraft-path subsystem design (PV20). This procedure created new projection vectors, gains, and thresholds rather than just increasing the thresholds, and the resulting design values are summarized in tables 38 to 40. Nearly all the thresholds t_{T_i}, t_{V_i}, and $t_{I_{i/j}}$ increased relative to the PV10 design shown in tables 27 to 29, and some of the minimum detectable failure levels $\bar{f}_{s_{T_i}}$ and $\bar{s}_{i/j}$ increased dramatically because of the higher noise levels.

Table 37. Errors for Aircraft-Path Truth Model With PV20 Design

Residual	Standard deviation of white noise, $^a\sigma_w$	Low-frequency noise cutoff, rad/sec	Standard deviation of low-frequency noise, $^b\sigma_\ell$	HPF cutoff frequency, rad/sec	Standard deviation of total noise, $^c\sigma_f(20)$
x-acceleration, ν_x	0.599 ft/sec^2	2.0	1.31 ft/sec^2	0.5	16.5 ft/sec^2
y-acceleration, ν_y	.639 ft/sec^2		.768 ft/sec^2		9.92 ft/sec^2
z-acceleration, ν_z	2.64 ft/sec^2		5.33 ft/sec^2		67.3 ft/sec^2
P-acceleration, ν_P	.0599 rad/sec^2		.102 rad/sec^2		1.29 rad/sec^2
Q-acceleration, ν_Q	.0388 rad/sec^2		.0442 rad/sec^2		.573 rad/sec^2
R-acceleration, ν_R	.0236 rad/sec^2	↓	.030 rad/sec^2	↓	.386 rad/sec^2

^{a}Square root of diagonal terms of Σ_w.
^{b}Square root of diagonal terms of Σ_ℓ.
^{c}Square root of diagonal terms of Σ_f.

The PV20 design was tested in 20-ft/sec turbulence to evaluate false-alarm performance, and the results are shown in table 41. In three simulation runs with different random-number seeds, two false triggers and no false alarms were experienced in 168 sec of operation. When operated in 15-ft/sec turbulence (σ_G = TURB = 15), the system parameters were interpolated between the PV10 and PV20 values. For three no-failure runs, the results shown in table 42 were six false triggers and one false alarm in 131 sec of operation. While some improvement in false-alarm performance at the higher turbulence levels would be required for an operational system, it was decided to continue with the evaluation of the failure-detection performance of this design.

Table 38. PV20 Design Results for Aircraft-Path Trigger Test After
Projection-Vector Optimization

Design parameter	Left thrust	Right thrust	Left horizontal tail	Right horizontal tail	Rudder	Left aileron	Right aileron
P:							
(ν_x)	0.0151	0.0151	0	0	0	0	0
(ν_y)	0	0			.0176	0	0
(ν_z)					0	0	0
(ν_p)			↓	↓	0	.439	−.439
(ν_q)	↓	↓	−1.0	−1.0	0	−.899	−.899
(ν_r)	.9999	−.9999	0	0	−.9998	0	0
σ_{S_T}	.459	.459	.573	.573	.423	.767	.767
t_T	−8.577	−8.577	−8.224	−8.224	−8.687	−7.623	−7.623
$\bar{f}_{S_T}$	8.11	8.11	4.93	4.93	6.27	25.21	25.21

Table 39. PV20 Design Results for Aircraft-Path Verify Test After
Projection-Vector Optimization

Design parameter	Left thrust	Right thrust	Left horizontal tail	Right horizontal tail	Rudder	Left aileron	Right aileron
$\bar{s}$	0.142 lb × 10^3	0.142 lb × 10^3	0.178°	0.178°	0.131°	0.238°	0.238°
G_A	.142	.142	.178	.178	.131	.238	.238
G_D	.0101	.0101	.0158	.0158	.00862	.0282	.0282
k_T	2	2	2	2	2	2	2
t_V	.0203	.0203	.0315	.0315	.0172	.0565	.0565

The performance of the interpolated design in detecting and isolating failures in higher turbulence was evaluated by simulating loss of surface effectiveness. The results for turbulence levels of 20 ft/sec and 15 ft/sec are tabulated in tables 41 and 42, respectively. With TURB = σ_G = 20, no failures were detected at 60-percent effectiveness, and only the rudder and aileron failures were detected at 40 percent. At 0- and 20-percent effectiveness, all stabilizer, elevator, and rudder failures were detected; stabilizer and rudder detection occurred in less than 3 sec. The stabilizer and rudder failures were not isolated, but rather were undetermined failures. However, the resulting confusion set correctly contained the right stabilizer and elevator in the case of the stabilizer failure, and contained only the rudder in the case of the rudder failure. In the latter case, an undetermined failure was declared repeatedly during the run. Nevertheless, the fact that an isolation decision was not made in these cases indicates that perhaps the isolation thresholds are too high or that the isolation projection vectors need modification. The right-elevator failures, on the other hand, were isolated incorrectly to the right aileron. This performance was not nearly as good as the system performance in 10-ft/sec turbulence, where detection and isolation generally occurred with less severe failures.

With TURB = σ_G = 15 (table 42), stabilizer and elevator failures were detected at 40-percent surface effectiveness, aileron failures at 60 percent, and rudder failures at 80 percent. This

Table 40. PV20 Design Results for Aircraft-Path Isolate Test After
Projection-Vector Optimization

Design parameter	Left thrust	Right thrust	Left horizontal tail	Right horizontal tail	Rudder	Left aileron	Right aileron
$\sigma_{S_{i/j}}$:							
(LT)		1.007	0.546	0.546	1.96	0.830	0.857
(RT)			.546	.546	1.96	.857	.830
(LH)				1.757	.691	1.435	1.435
(RH)					.691	1.435	1.435
(Ru)						.833	.833
(LA)							1.014
(RA)							
$\bar{s}_{i/j}$:							
(LT)		0.156	0.0846	0.0846	0.304	0.129	0.133
(RT)			.0846	.0846	.304	.133	.129
(LH)				.272	.107	.222	.222
(RH)					.107	.222	.222
(Ru)						.129	.129
(LA)							.157
(RA)							
$k_{i/j}$:							
(LT)		2	2	2	2	2	2
(RT)			2	2	2	2	2
(LH)				2	2	2	2
(RH)					2	2	2
(Ru)						2	2
(LA)							2
(RA)							
$t_{I_{i/j}}$:							
(LT)		0.312	0.169	0.169	0.608	0.257	0.266
(RT)			.169	.169	.608	.266	.257
(LH)				.545	.214	.445	.445
(RH)					.214	.445	.445
(Ru)						.258	.258
(LA)							.315
(RA)							

performance is significantly better than at $\sigma_G = 20$ ft/sec, but not as good as at $\sigma_G = 10$ ft/sec. In this case, the rudder and aileron failures were correctly isolated, and the stabilizer and elevator failures were isolated to the proper confusion set.

The trigger and verify statistics and thresholds for each surface for a right-aileron failure are plotted in figures A11 and A12 for 20-ft/sec and 15-ft/sec turbulence, respectively. The statistics for the right aileron are repeated in figure 17. The thresholds in figure A11 are the values for the PV20 design. The thresholds in figure A12 are the values obtained by interpolating midway (TURB = 15) between the PV10 and PV20 designs and, of course, are lower (more negative) than those in figure A11 for TURB = 20. The verification/isolation process is initiated by a right-thrust trigger at 17.55 sec into the run. (See fig. A11.) All the right-aileron isolation tests passed in favor of the right aileron by 18.10 sec (not shown in fig. A11), but a failure/isolation is not declared until the right aileron verifies at 18.55 sec. No other verify tests passed.

Table 41. Failure-Detection and Isolation Performance for Interpolated Design With 20-ft/sec Turbulence

(a) Detection performance

Failed surface	Failure-detection time[a] as a function of percent surface effectiveness				
	0%	20%	40%	60%	80%
Right stabilizer	2.25	2.65	[b]ND	[b]ND	
Rudder	1.65	1.85	2.40		
Right elevator	14.40	14.45	[b]ND		
Right aileron			14.30		

[a]Time of failure declaration relative to time of failure.
[b]See symbol list for definition.

(b) Isolation performance

Failed surface	Failure isolation as a function of percent surface effectiveness				
	0%	20%	40%	60%	80%
Right stabilizer	[a]U (RS,RE)	[a]U (RS,RE)	[a]ND	[a]ND	
Rudder	[a]U (Ru)	[a]U (Ru)	[a]U (Ru)		
Right elevator	[a]RA	[a]RA	[a]ND		
Right aileron			Yes		

[a]See symbol list for definition.

(c) False-alarm performance

Run	Random-sequence set	Number of triggers	Number of false alarms	Isolated surface	FDI active time,[a] sec
1	1	1	0		56.00
2	2	0	0		56.00
3	3	1	0		56.00

[a]Time aircraft-path subsystem is operational before being inhibited by a failure isolation.

Table 42. Failure-Detection and Isolation Performance for Interpolated Design With 15-ft/sec Turbulence

(a) Detection performance

Failed surface	Failure-detection time[a] as a function of percent surface effectiveness				
	0%	20%	40%	60%	80%
Right stabilizer			7.70	^bND	
Rudder				4.10	13.20
Right elevator			38.55	^bND	
Right aileron				8.45	^bND

[a]Time of failure declaration relative to time of failure.
[b]See symbol list for definition.

(b) Isolation performance

Failed surface	Failure isolation as a function of percent surface effectiveness				
	0%	20%	40%	60%	80%
Right stabilizer			$^aCS\,(RS,RE)$	^aND	
Rudder				Yes	Yes
Right elevator			$^aCS\,(RS,RE)$	^aND	
Right aileron				Yes	^aND

[a]See symbol list for definition.

(c) False-alarm performance

Run	Random-sequence set	Number of triggers	Number of false alarms	Isolated surface	FDI active time,[a] sec
1	1	3	0		56.00
2	2	1	1	$^bRS,RE$	16.60
3	3	2	0		56.00

[a]Time aircraft-path subsystem is operational before being inhibited by a failure isolation.
[b]See symbol list for definition.
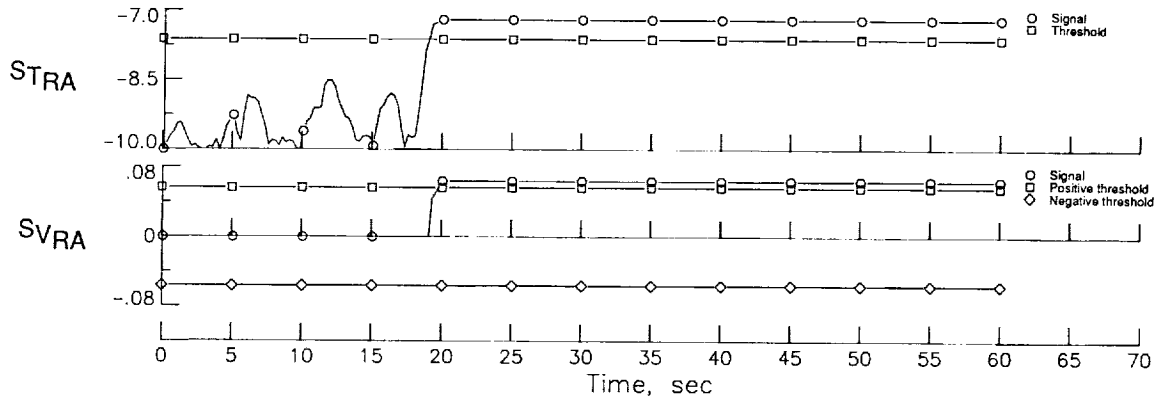
(a) 20-ft/sec turbulence.
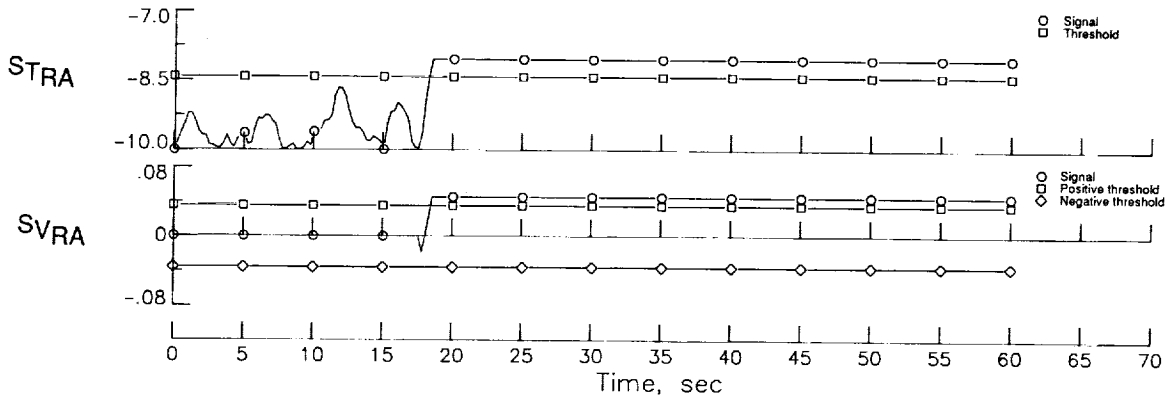
(b) 15-ft/sec turbulence.

Figure 17. Aircraft-path right-aileron trigger and verify statistics for right-aileron partially missing surface failure (40-percent effectiveness). Interpolated design.

The degradation in the performance of the aircraft-path subsystem in turbulence above 10 ft/sec, particularly the occurrence of false alarms that necessitated the increasing of the noise covariances above the measured values, indicates that some improvements in the design process are required. Perhaps some refinement of the design and truth models is necessary. The noise variances σ_w^2 and σ_ℓ^2 for the truth model in 20-ft/sec turbulence are far greater than those assumed for the baseline design (ref. 25), as can be seen by comparing the values in table 37 with those in table 6. Nevertheless, the process of linearly interpolating the projection vectors, gains, and thresholds worked well, as evidenced by the failure-detection and isolation performance in 15-ft/sec turbulence, where performance exceeded that at 20 ft/sec, and by the very good failure-detection/isolation performance and excellent false-alarm performance at 5-ft/sec turbulence.

Actuator-Path Subsystem

Because the aircraft-path subsystem is considerably more complex than the actuator-path subsystem, the emphasis when evaluating performance in turbulence has been placed on the aircraft path. However, turbulence did have some effect on the actuator-path subsystem. Table 43 summarizes the false-alarm performance of the actuator path during the three no-failure climbing-turn simulation runs in 20-ft/sec turbulence. There were a total of 29 false

78

triggers and 5 false alarms (false verifies or detections) in 168 sec of operation. Of the false alarms, two were rudder, two were right aileron, and one was left aileron. Obviously, this performance is unacceptable, and some redesign of the actuator-path subsystem is required. One facet of the design that should be examined is the determination of variances of the noise, or error, terms in the truth model. An adaptive system that adjusts thresholds as a function of the turbulence level may be necessary. Further work in this area has not been pursued, however, because it is believed that if an adaptive aircraft-path subsystem can be successfully developed, similar techniques can easily be applied to the actuator path.

Table 43. Actuator-Path Subsystem False-Alarm Performance With 20-ft/sec Turbulence

Run	Random-sequence set	Maneuver	Number of triggers	False alarms	FDI active time,[a] sec
1	1	CT4	16	$^aLA,^b RA$	56.00
2	2	CT4	5	^bRu	56.00
3	3	CT4	8	$^bR_u,^b RA$	56.00

[a]Time actuator-path subsystem is operational.
[b]See symbol list for definition.

Adaptive Design

As shown previously, improved aircraft-path subsystem performance in turbulence could be obtained by using the interpolated design that adjusts the gains, projection vectors, and thresholds as functions of the turbulence level TURB. In the interpolated design, the value of TURB is provided to the system a priori by setting it equal to σ_G, the standard deviation of the turbulence specified for the simulation run and input to the simulation for use by the random-number generator. In an operational system, this value is not known and must be determined in real time. Thus, the first step in evolving the interpolated design into a self-contained adaptive FDI system was the development of a turbulence estimator.

Turbulence estimator. Several different techniques were considered for obtaining an estimate of the standard deviation of the turbulence $\hat{\sigma}_G$, or wind gusts. Among those techniques briefly evaluated in simulation were averaging the squared, filtered output of the body-mounted accelerators and averaging the squared, filtered outputs of the angle-of-attack and angle-of-sideslip sensors. These methods proved inferior to a technique developed by Deckert et al. (ref. 34) for use in the NASA F-8 digital fly-by-wire program. This technique is discussed in more detail herein.

Consider the acceleration **a** of the aircraft at the center of gravity:

$$\mathbf{a} = \dot{\mathbf{V}} + \omega \times \mathbf{V} - \mathbf{g} \tag{108a}$$

or

$$\dot{\mathbf{V}} = \mathbf{a} - \omega \times \mathbf{V} + \mathbf{g} \tag{108b}$$

where the variables are inertial quantities in body axes. A discrete time approximation to equation (108b) is given in predictor-corrector form by equations (109) to (111) as follows:

$$\mathbf{V}^p(k) = \widehat{\mathbf{V}}(k-1) + \left[\mathbf{a}_m^*(k) + \mathbf{g}^*(k) - \omega_m^*(k) \times \mathbf{V}_m^*(k)\right] \Delta T \tag{109}$$

79

where $\mathbf{V}^p(k)$ is the predicted velocity at sample k, $\mathbf{V}(k-1)$ is the estimated velocity at sample $k-1$, and ΔT is the sample interval. The starred quantities are defined subsequently. Define a residual $\zeta(k)$ as

$$\zeta(k) = \mathbf{V}_m^*(k) - \mathbf{V}^p(k) \tag{110}$$

and let the estimated velocity $\widehat{\mathbf{V}}(k)$ be computed from

$$\widehat{\mathbf{V}}(k) = \mathbf{V}^p(k) + G_E\zeta(k) \tag{111}$$

To improve the accuracy of the integration of acceleration in equation (109), the measured accelerations, attitude rates, and velocities are averaged over the k and $k-1$ samples. Thus, the starred variables are defined as

$$\mathbf{a}_m^*(k) = \frac{1}{2}[\mathbf{a}_m(k) + \mathbf{a}_m(k-1)] \tag{112a}$$

$$\omega_m^*(k) = \frac{1}{2}[\omega_m(k) + \omega_m(k-1)] \tag{112b}$$

$$\mathbf{V}_m^*(k) = \frac{1}{2}[\mathbf{V}_m(k) + \mathbf{V}_m(k-1)] \tag{112c}$$

$$\mathbf{g}^*(k) = \frac{1}{2}[\mathbf{g}(k) + \mathbf{g}(k-1)] \tag{112d}$$

where

$$\mathbf{a}_m(k) = \begin{bmatrix} A_{m_x}^c(k) \\ A_{m_y}^c(k) \\ A_{m_z}^c(k) \end{bmatrix} \quad \begin{pmatrix} \text{outputs of body-mounted} \\ \text{accelerometers after compensation} \\ \text{for off-center-of-gravity effects} \end{pmatrix} \tag{113a}$$

$$\omega_m(k) = \begin{bmatrix} P_m(k) \\ Q_m(k) \\ R_m(k) \end{bmatrix} \quad (\text{attitude-rate gyro outputs}) \tag{113b}$$

$$\mathbf{V}_m(k) = \begin{bmatrix} \cos\beta_m(k)\cos\alpha_m(k) \\ \sin\beta_m(k) \\ \cos\beta_m(k)\sin\alpha_m(k) \end{bmatrix} V_{T_m}(k) \quad (\text{measured airspeeds}) \tag{113c}$$

$$\mathbf{g}(k) = \begin{bmatrix} -\sin\theta_m(k) \\ \cos\theta_m(k)\sin\Phi_m(k) \\ \cos\theta_m(k)\cos\Phi_m(k) \end{bmatrix} g \tag{113d}$$

The acceleration in equation (109) is inertial, but the velocity $\mathbf{V}_m$ is relative to the air. Therefore,

$$\mathbf{V}_m(k) = \mathbf{V}(k) - \mathbf{V}_w(k) + \epsilon(k) \tag{114}$$

where $\mathbf{V}(k)$ is inertial aircraft velocity, $\mathbf{V}_w(k)$ is wind velocity, and $\epsilon(k)$ is measurement error. If the measurements are perfect, the aircraft acceleration is constant or linearly changing, the gain G_E is small, and the wind velocity $\mathbf{V}_w(k)$ has zero mean and varies rapidly compared with the estimator response, then the estimated velocity $\widehat{\mathbf{V}}(k)$ tends toward the inertial velocity

$\mathbf{V}(k)$, and the residuals $\zeta(k)$ approach the wind velocity $\mathbf{V}_w(k)$. The residuals can then be used to estimate the level of the wind gusts, or turbulence.

Each channel (U, V, W, or x, y, z) of equations (109) to (111) should be included in a turbulence estimator, one channel of which is shown in figure 18. The residuals are high-pass filtered, to remove bias terms, and then squared. The squared output is then averaged in a low-pass filter to form an estimate of the variance of the turbulence in that channel. During the simulation evaluation, it was found that sensor noise in the residuals produced a significant nonzero value for the estimate when the actual turbulence was set to zero. To reduce this effect, a low-pass filter was implemented in the estimator preceding the high-pass filter.
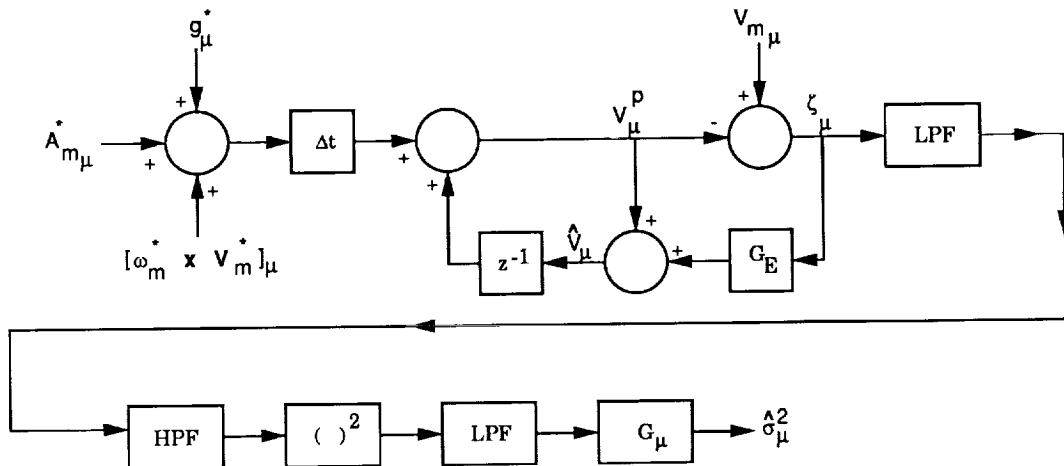
Figure 18. One channel of turbulence level estimator.

The estimator was evaluated by using the 737 nonlinear simulation over specified turbulence levels σ_G of 0 to 20 ft/sec. At $\sigma_G = 10$ ft/sec, three simulation runs were made during straight and level flight, with a different sample sequence from the random-number generator for each run. These three runs were repeated while executing the CT4 climbing-turn maneuver. Similar runs were made with $\sigma_G = 20$ ft/sec.

Results are shown in figure 19 for each of the three channels of the estimator. The horizontal axis is the sample standard deviation of the turbulence σ_T for the 60-sec run computed as the rms of the sample standard deviations of the simulated gusts σ_U, σ_V, and σ_W; that is,

$$\sigma_T = \left[\frac{1}{3} \left(\sigma_U^2 + \sigma_V^2 + \sigma_W^2 \right) \right]^{1/2} \tag{115}$$

The vertical axis is the mean value over the 60-sec run of the estimate $\hat{\sigma}_U$, $\hat{\sigma}_V$, or $\hat{\sigma}_W$. The average error in these estimates was -0.57, -0.98, and 1.1 ft/sec for $\hat{\sigma}_U$, $\hat{\sigma}_V$, and $\hat{\sigma}_W$, respectively. Simulation results showed that the accuracy of the estimator could be improved if the outputs of the three channels were combined in an rms fashion to form an estimate $\hat{\sigma}_T$, as shown in the final design (fig. 20). Mean values of $\hat{\sigma}_T$ are also plotted in figure 19, and these estimates are more accurate. A time-history plot of the estimate $\hat{\sigma}_T$ is shown in figure 21, together with a plot of the sample standard deviation (rms of the three components) of the most recent 100 samples (5 sec) of the simulated turbulence for a run where $\sigma_G = 10$ ft/sec. Although the estimate certainly does not track the sample standard deviation exactly, it is anticipated that the estimator will be sufficiently accurate to use in an adaptive FDI system. Parameter values for the final estimator design are listed in table 44.

81
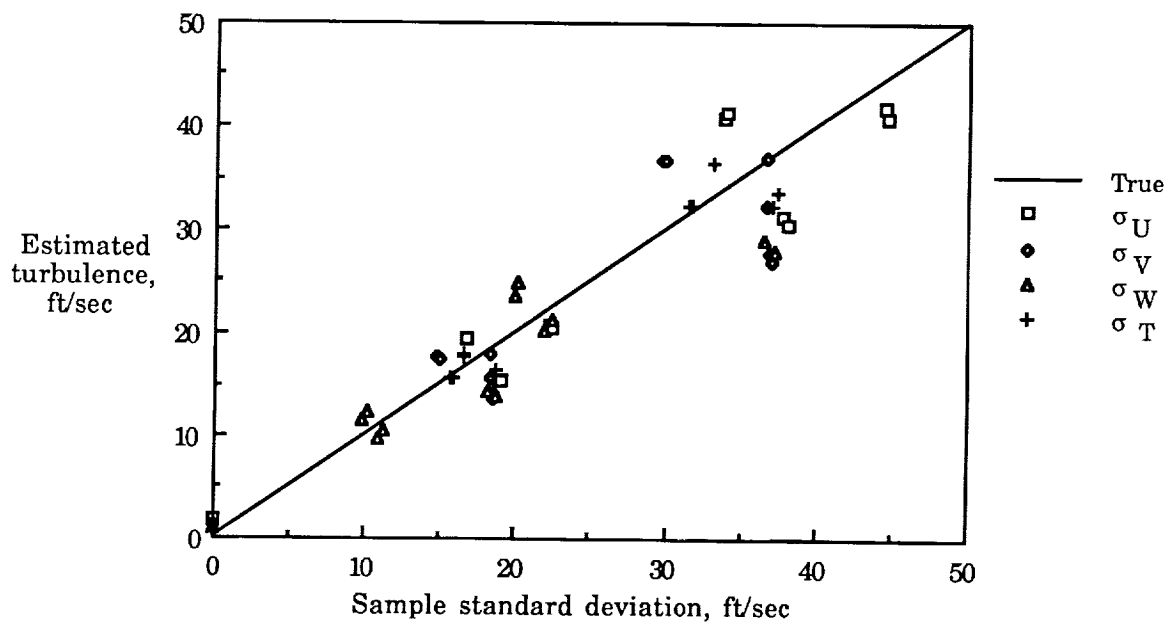
Figure 19. Results for turbulence level estimator.
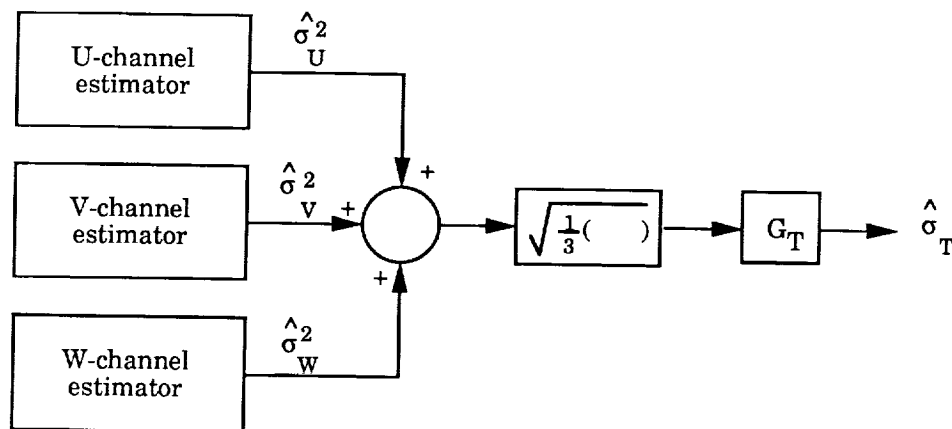
Figure 20. Turbulence level estimator final design.
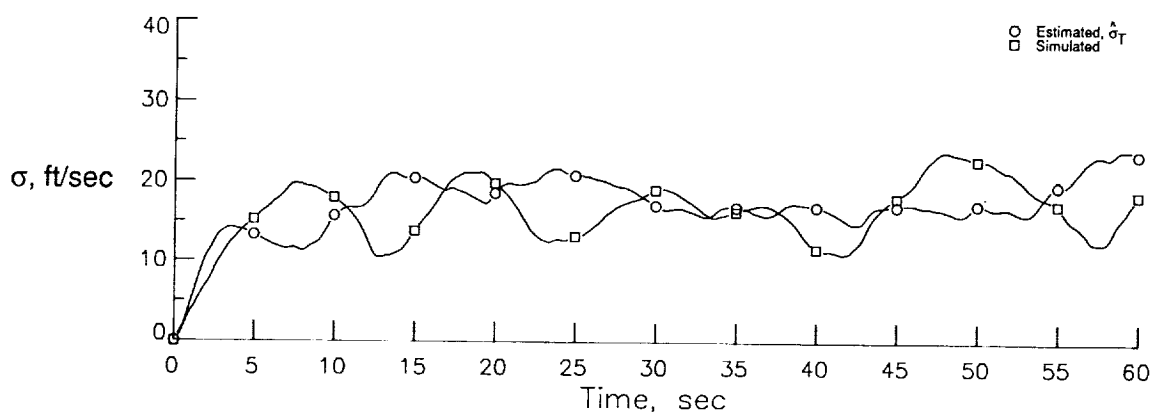
Figure 21. Time history of turbulence level estimator output.

82

Table 44. Parameter Values for Final Design of Turbulence Level Estimator

Parameter	Variable	Value
Estimator feedback gain	G_E	0.010
Low-pass noise filter time constant, sec	T_{NLP}	.200
High-pass-filter time constant, sec	T_{HP}	5.000
Low-pass averaging filter time constant, sec	T_{LP}	5.000
U-channel gain	G_U	2.110
V-channel gain	G_V	1.650
W-channel gain	G_W	1.400
Output gain	G_T	1.045

Design description. In the interpolated design previously discussed, the thresholds and projection vectors were determined by linear interpolation between two end points according to the independent variable TURB. Two sets of end points were used: the BL and the PV10 design values for TURB between 0 and 10, or the PV10 and the PV20 design values for TURB between 10 and 20, as selected before the simulation run. The value of TURB was set equal to the value of σ_G specified for the run; thus, the interpolated thresholds, gains, and vectors stayed constant throughout a run.

For the adaptive design, the turbulence estimator was implemented in the FDI software. At each sample interval, an estimate of the level of turbulence $\hat{\sigma}_T$ was computed, and TURB was set equal to this value before the aircraft-path subsystem computations were performed. The range of the independent variable TURB was divided into two regions, and linear interpolation was performed as shown in figure 22. For TURBL $\leq$ TURB $\leq$ TURBM, the dependent variables were interpolated between YL and YM, corresponding to the BL and PV10 design values, respectively. For TURB > TURBM, the dependent variables were interpolated between (or extrapolated above) YM and YH, corresponding to the PV10 and PV20 design values, respectively. Values of 0, 10, and 20 for TURBL, TURBM, and TURBH, as used in the interpolated design, were inappropriate for the adaptive design; these values were those specified for the turbulence standard deviation for a simulation run, but were not the actual sample standard deviations, which were generally larger. The turbulence estimator attempts to estimate the sample standard deviation of approximately the latest 5 sec of turbulence. Thus, nominal values of the sample standard deviation, not the specified σ_G, should be used. Values of 0, 17, and 34 were selected for TURBL, TURBM, and TURBH, respectively.
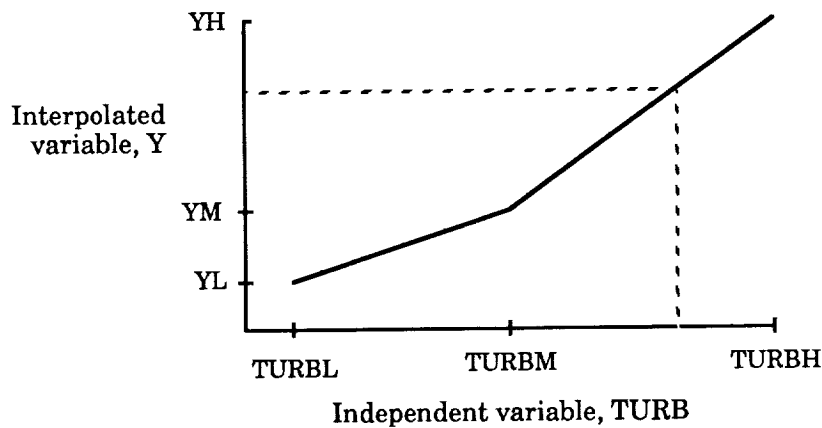
Figure 22. Linear interpolation scheme for adaptive design.

83

Simulation results. To evaluate the detection and isolation performance of the adaptive design in a turbulence environment, simulation runs were made at specified turbulence levels σ_G of 0, 5, 10, 15, and 20 ft/sec with aircraft-path failures simulating partial effectiveness of each of the four surfaces: right stabilizer, rudder, right elevator, and right aileron. To evaluate false-alarm performance, three no-failure runs with different sample sequences for the turbulence were made at each of the same turbulence levels except zero, where only one run was made. As in previous runs, the failures occurred at $t = 5$ sec, and the climbing-turn maneuver CT4 was initiated at $t = 10$ sec.

Results for the no-turbulence runs are tabulated in table 45. All four failures at 60-percent effectiveness were successfully detected, and the stabilizer and aileron failures were correctly isolated (the stabilizer to the right horizontal tail). The rudder and elevator failures at this failure level were isolated incorrectly. Failures at 80-percent effectiveness were not detected, but the two failures (rudder and elevator) at 40 percent were detected successfully and isolated correctly. Comparison with similar runs for the baseline design in table 13 shows that the BL design detected the rudder and aileron failures more quickly at 60-percent effectiveness, and the BL design detected one of four failures at 80-percent effectiveness. The BL design correctly isolated the rudder failure at 60-percent effectiveness. During the no-failure run, the adaptive design experienced no failures and only one false alarm, as did the baseline design. Thus, the adaptive design performed well in zero turbulence, although the baseline design was slightly better.

Results for 5-ft/sec turbulence are shown in table 46. At 60-percent effectiveness, the stabilizer, rudder, and elevator failures were detected, and the stabilizer and rudder failures were correctly isolated by the adaptive design. Failures at 80 percent were not detected, but at 40 percent the two failures were detected and isolated correctly. In three no-failure runs totaling 168 sec of operation, no false alarms and no false triggers were experienced. This is the same as the no-failure performance of the interpolated design shown in table 33.

Results for the adaptive design in 10-ft/sec turbulence are shown in table 47. All the failures at 40- and 60-percent effectiveness and two of the four at 80 percent were successfully detected. At 60 percent, the stabilizer and elevator failures resulted in undetermined failure declarations and were not isolated. The rudder failure was correctly isolated, even at 80-percent effectiveness. There were no false alarms and only two false triggers during three no-failure runs. Comparing the detection performance of the adaptive design with that of the PV10 design in table 30 shows that the adaptive design detected all the failures that were detected by the PV10 design, except the right stabilizer failure at 80-percent effectiveness; the adaptive design detected two of the failures significantly quicker. Isolation performance of the two designs was nearly equal. False-alarm performance of the adaptive design was superior to that of the PV10 design and vastly superior to that of the BL design in table 15.

As can be seen in table 48, in 15-ft/sec turbulence the adaptive system detected and isolated three out of three aircraft-path failures at 40-percent effectiveness, detected four of four and isolated two at 60 percent, but detected none at 80-percent effectiveness. In three no-failure runs, the system experienced two false triggers and one false alarm of the right horizontal tail in 128.6 sec of operation. This result is slightly better than the interpolated design (see table 42), which missed two detections at 60-percent effectiveness and experienced the same false alarm and five false triggers under the same conditions.

Table 49 contains results for the adaptive design for $\sigma_G = 20$ ft/sec. Again, the system detected all the failures at 60-percent effectiveness (and correctly isolated three of the four) and no failures at 80-percent effectiveness. No false alarms and only one false trigger occurred during

Table 45. Failure-Detection and Isolation Performance for Adaptive Design With No Turbulence

(a) Detection performance

Failed surface	Failure-detection time[a] as a function of percent surface effectiveness				
	0%	20%	40%	60%	80%
Right stabilizer				1.15	[b]ND
Rudder			1.85	8.90	
Right elevator			1.20	6.70	
Right aileron				22.20	

[a]Time of failure declaration relative to time of failure. [b]See symbol list for definition.

(b) Isolation performance

Failed surface	Failure isolation as a function of percent surface effectiveness				
	0%	20%	40%	60%	80%
Right stabilizer				[a]$CS(RS,RE)$	[a]ND
Rudder			Yes	[a]RT	
Right elevator			[a]$CS(RS,RE)$	[a]RA	
Right aileron				Yes	

[a]See symbol list for definition.

(c) False-alarm performance

Run	Random-sequence set	Number of triggers	Number of false alarms	Isolated surface	FDI active time,[a] sec
1	1	1	0		56.00

[a]Time aircraft-path subsystem is operational before being inhibited by a failure isolation.

Table 46. Failure-Detection and Isolation Performance for Adaptive Design With 5-ft/sec Turbulence

(a) Detection performance

Failed surface	Failure-detection time[a] as a function of percent surface effectiveness				
	0%	20%	40%	60%	80%
Right stabilizer				1.50	[b]*ND*
Rudder				24.05	[b]*ND*
Right elevator			1.50	7.25	[b]*ND*
Right aileron			6.30	[b]*ND*	

[a]Time of failure declaration relative to time of failure.
[b]See symbol list for definition.

(b) Isolation performance

Failed surface	Failure isolation as a function of percent surface effectiveness				
	0%	20%	40%	60%	80%
Right stabilizer				[a]*CS*(*RS,RE*)	[a]*ND*
Rudder				Yes	[a]*ND*
Right elevator			[a]*CS*(*RS,RE*)	[a]*U*(*RA*)	[a]*ND*
Right aileron			Yes	*ND*	

[a]See symbol list for definition.

(c) False-alarm performance

Run	Random-sequence set	Number of triggers	Number of false alarms	Isolated surface	FDI active time,[a] sec
1	1	0	0		56.00
2	2	0	0		56.00
3	3	0	0		56.00

[a]Time aircraft-path subsystem is operational before being inhibited by a failure isolation.

Table 47. Failure-Detection and Isolation Performance for Adaptive Design With 10-ft/sec Turbulence

(a) Detection performance

Failed surface	Failure-detection time[a] as a function of percent surface effectiveness				
	0%	20%	40%	60%	80%
Right stabilizer			1.00	1.75	[b]ND
Rudder				3.55	40.20
Right elevator			1.50	7.35	[b]ND
Right aileron				6.75	13.90

[a]Time of failure declaration relative to time of failure.
[b]See symbol list for definition.

(b) Isolation performance

Failed surface	Failure isolation as a function of percent surface effectiveness				
	0%	20%	40%	60%	80%
Right stabilizer			[a]$CS\,(RS, RE)$	[a]$U\,(LS, RS, LE, RE)$	[a]ND
Rudder				Yes	Yes
Right elevator			[a]$CS\,(RS, RE)$	[a]$U\,(RA)$	[a]ND
Right aileron				Yes	[a]$U\,(LT)$

[a]See symbol list for definition.

(c) False-alarm performance

Run	Random-sequence set	Number of triggers	Number of false alarms	Isolated surface	FDI active time,[a] sec
1	1	1	0		56.00
2	2	1	0		56.00
3	3	0	0		56.00

[a]Time aircraft-path subsystem is operational before being inhibited by a failure isolation.

87

Table 48. Failure-Detection and Isolation Performance for Adaptive Design With 15-ft/sec Turbulence

(a) Detection performance

Failed surface	Failure-detection time[a] as a function of percent surface effectiveness				
	0%	20%	40%	60%	80%
Right stabilizer			1.15	2.20	[b]ND
Rudder				1.85	
Right elevator			1.40	38.70	
Right aileron			1.55	39.70	

[a]Time of failure declaration relative to time of failure.
[b]See symbol list for definition.

(b) Isolation performance

Failed surface	Failure isolation as a function of percent surface effectiveness				
	0%	20%	40%	60%	80%
Right stabilizer			[a]CS(RS, RE)	[a]CS(LS, LE)	[a]ND
Rudder				Yes	
Right elevator			[a]CS(RS, RE)	[a]CS(RS, RE)	
Right aileron			Yes	[a]U(LA, RA)	

[a]See symbol list for definition.

(c) False-alarm performance

Run	Random-sequence set	Number of triggers	Number of false alarms	Isolated surface	FDI active time,[a] sec
1	1	1	0		56.00
2	2	1	1	[b]RS, [b]RE	16.60
3	3	0	0		56.00

[a]Time aircraft-path subsystem is operational before being inhibited by a failure isolation.
[b]See symbol list for definition.

Table 49. Failure-Detection and Isolation Performance for Adaptive Design With 20-ft/sec Turbulence

(a) Detection performance

Failed surface	Failure-detection time[a] as a function of percent surface effectiveness				
	0%	20%	40%	60%	80%
Right stabilizer				2.40	[b]ND
Rudder				1.25	
Right elevator			1.15	1.60	
Right aileron				1.60	

[a]Time of failure declaration relative to time of failure.
[b]See symbol list for definition.

(b) Isolation performance

Failed surface	Failure isolation as a function of percent surface effectiveness				
	0%	20%	40%	60%	80%
Right stabilizer				[a]$CS\,(RS,RE)$	[a]ND
Rudder				Yes	
Right elevator			[a]$CS\,(RS,RE)$	[a]RA	
Right aileron				Yes	

[a]See symbol list for definition.

(c) False-alarm performance

Run	Random-sequence set	Number of triggers	Number of false alarms	Isolated surface	FDI active time,[a] sec
1	1	1	0		56.00
2	2	0	0		56.00
3	3	0	0		56.00

[a]Time aircraft-path subsystem is operational before being inhibited by a failure isolation.

the no-failure runs. This performance is considerably superior to that of the interpolated design (table 41), which missed four out of four detections at 60-percent effectiveness and two out of four at 40 percent in 20-ft/sec turbulence. Time histories of the trigger and verify statistics and thresholds for one of the no-failure runs are plotted in figure 23. Contrary to previous time-history plots, the thresholds in this case are not constant but vary as a function of the estimate of the turbulence level plotted in figure 23. Note the false trigger in the left-horizontal-tail channel at $t \approx 6$ sec. The verify tests for the left thrust, right thrust, left horizontal tail, right horizontal tail, and left aileron all fail (verify no failure) within 1 sec. The rudder and right aileron exceed the time limit at the end of 1 sec without making a decision. At that time, a false trigger is declared, and the aircraft-path subsystem resets and continues to operate. Thus, no false alarm occurred.

Performance of the adaptive design is summarized in tables 50 and 51. In 688 sec of operation in turbulence from 0 to 20 ft/sec, the system experienced one false alarm and six false triggers. All partially missing surface failures at 40-percent effectiveness were detected and correctly isolated. At 60-percent effectiveness, 19 out of 20 were detected, and of these 11 were correctly isolated. When the surfaces failed at 80-percent effectiveness, the system performance degraded severely, as only 2 out of 19 failures were detected. The adaptive system performed well in turbulence levels where the baseline was completely unusable because of false alarms. Furthermore, previous simulation experience (ref. 26) has shown that this airplane and flight control system design are very robust to control-surface failures, and many smaller failures, such as those at 80-percent effectiveness, produce effects that are hardly noticeable (thus, difficult to detect), let alone catastrophic. Therefore, missed detections at this level do not necessarily make the FDI system unusable. Also, it should be kept in mind that the turbulence levels referred to in the discussion were the specified levels, and the actual wind-gust sample sequences in most cases exhibited a sample standard deviation larger than the specified value.

Summary of Results

A procedure for designing a decentralized failure-detection and identification (FDI) system to detect and isolate control-element failures in aircraft control systems has been developed by Weiss and Hsu (NASA CR-178213). Using this procedure, Weiss designed a baseline FDI system, consisting of an actuator-path subsystem and an aircraft-path subsystem, for a modified Boeing 737 airplane. In the current report, this design was evaluated in detail by using a six-degree-of-freedom simulation of the airplane, including atmospheric turbulence based on the Dryden model. The design procedure was extended to improve performance of the system in turbulence. This extension resulted in the development of an adaptive FDI system, which was also evaluated in detail.

Evaluation of the baseline design showed that when operated in a no-turbulence environment, the actuator-path subsystem performed very well. All actuator-path failures—stuck at neutral, stuck at current position, and hardover—were detected in a timely manner; in the no-failure simulation runs, there were no actuator-path false alarms. The aircraft-path subsystem also performed well in zero turbulence. There were no false alarms, and partially missing surface failures of the stabilizer, rudder, elevator, and aileron were all detected when the remaining surface effectiveness was 60 percent. The right-stabilizer failure was isolated to the fictitious right horizontal tail, since the system cannot distinguish between stabilizer and elevator failures because of their identical effects.
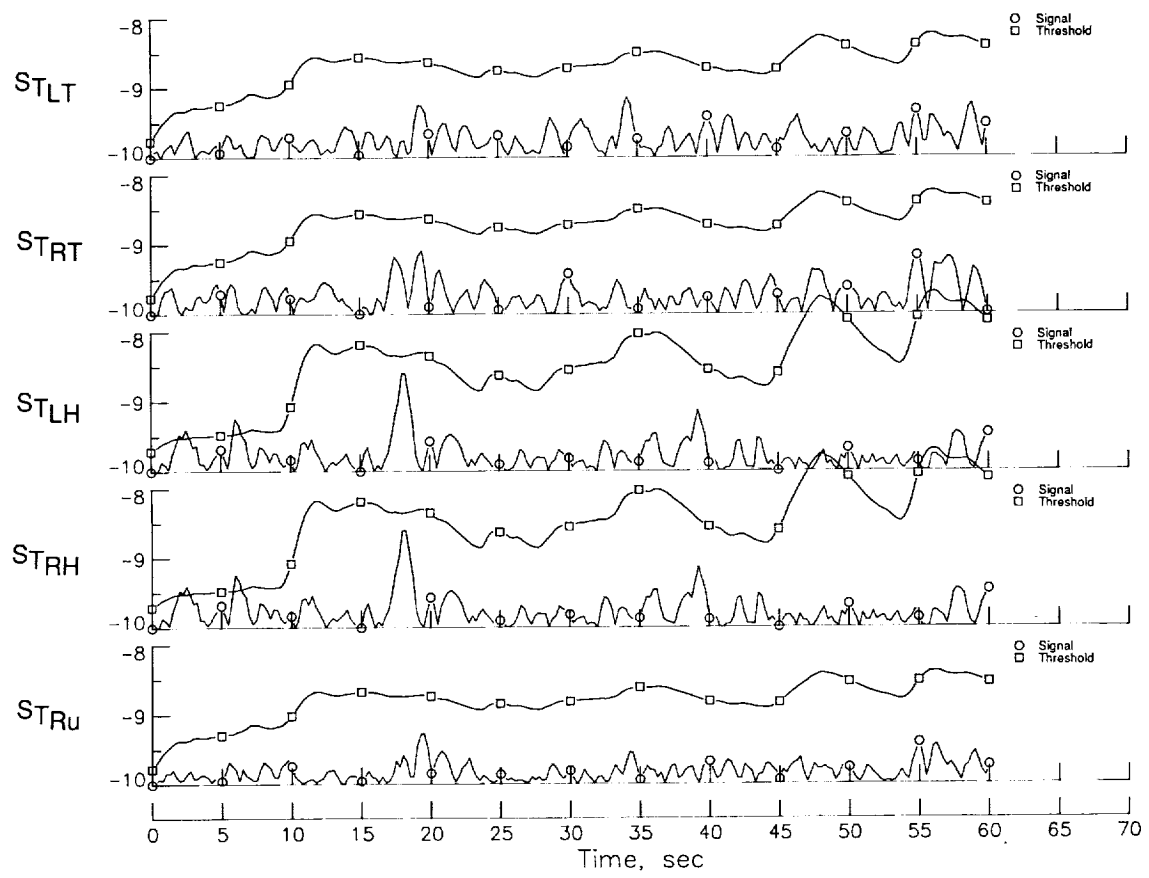
Figure 23. Aircraft-path trigger and verify statistics and turbulence level estimate. Adaptive design; no failure; 20-ft/sec turbulence.
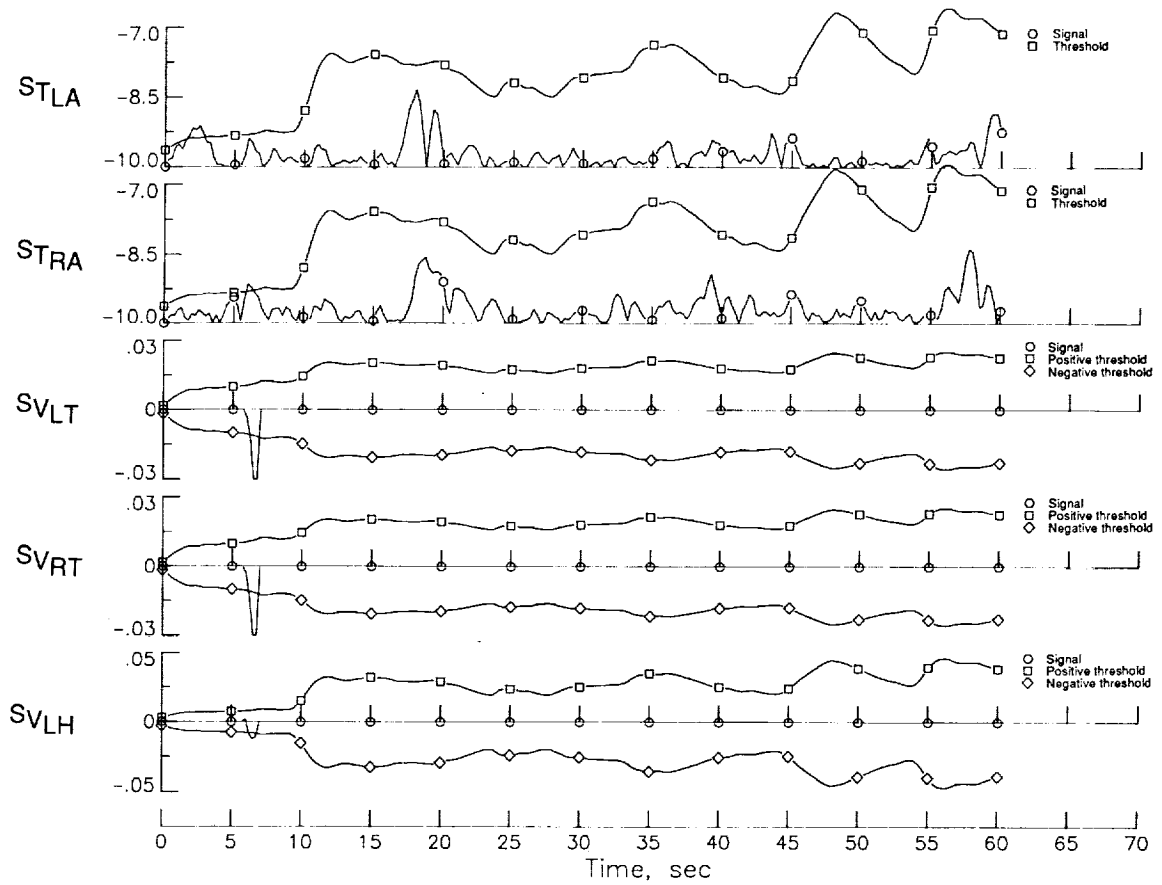
Figure 23. Continued.
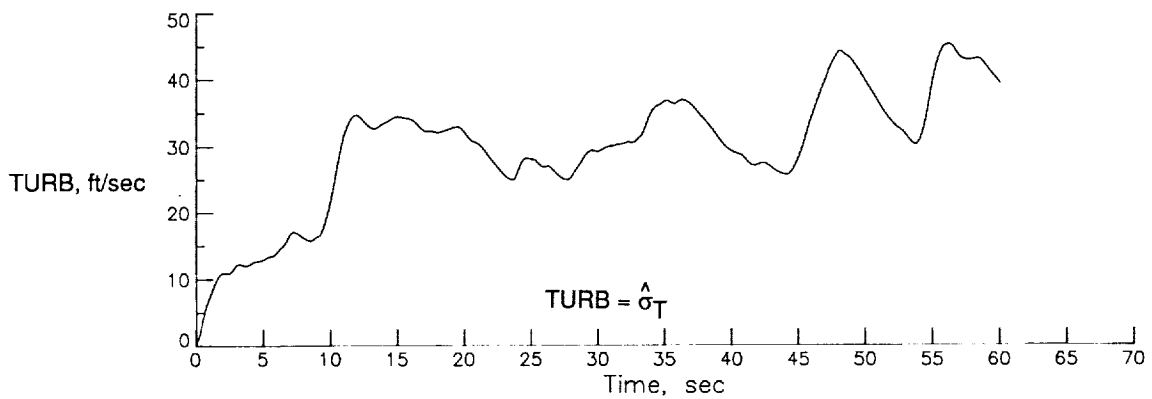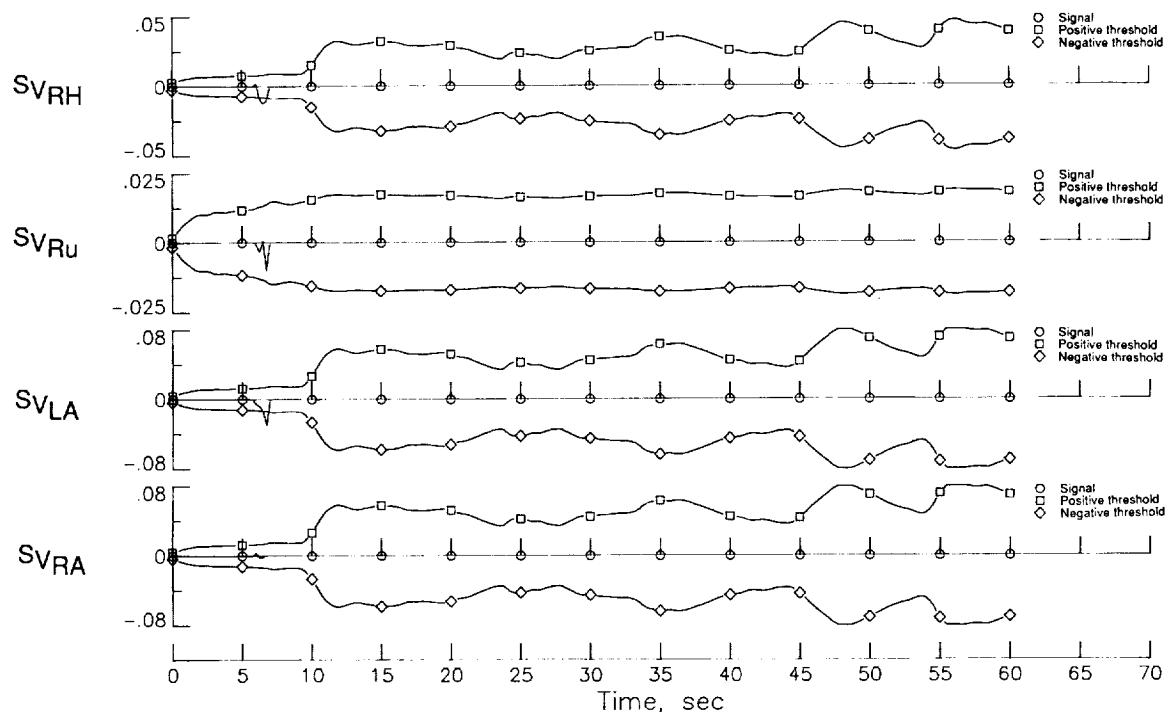
Figure 23. Concluded.

C-2

Table 50. False-Alarm Performance of Adaptive Design

(a) No turbulence

Run	Random-sequence set	Number of triggers	Number of false alarms	Isolated surface	FDI active time,[a] sec
1	1	1	0		56.00

[a]Time aircraft-path subsystem is operational before being inhibited by a failure isolation.

(b) 5-ft/sec turbulence

Run	Random-sequence set	Number of triggers	Number of false alarms	Isolated surface	FDI active time,[a] sec
1	1	0	0		56.00
2	2	0	0		56.00
3	3	0	0		56.00

[a]Time aircraft-path subsystem is operational before being inhibited by a failure isolation.

(c) 10-ft/sec turbulence

Run	Random-sequence set	Number of triggers	Number of false alarms	Isolated surface	FDI active time,[a] sec
1	1	1	0		56.00
2	2	1	0		56.00
3	3	0	0		56.00

[a]Time aircraft-path subsystem is operational before being inhibited by a failure isolation.

Table 50. Concluded.

(d) 15-ft/sec turbulence

Run	Random-sequence set	Number of triggers	Number of false alarms	Isolated surface	FDI active time,[a] sec
1	1	1	0		56.00
2	2	1	1	[b]RS, [b]RE	16.60
3	3	0	0		56.00

[a]Time aircraft-path subsystem is operational before being inhibited by a failure isolation.
[b]See symbol list for definition.

(e) 20-ft/sec turbulence

Run	Random-sequence set	Number of triggers	Number of false alarms	Isolated surface	FDI active time,[a] sec
1	1	1	0		56.00
2	2	0	0		56.00
3	3	0	0		56.00

[a]Time aircraft-path subsystem is operational before being inhibited by a failure isolation.

(f) Summary

Number of triggers	Number of false alarms	FDI active time,[a] sec
6	1	688.60

[a]Time aircraft-path subsystem is operational before being inhibited by a failure isolation.

Table 51. Summary of Detection and Isolation Performance of Adaptive Design

(a) Detection performance

Failed surface	Number of failures/number detected as a function of percent surface effectiveness				
	0%	20%	40%	60%	80%
Right stabilizer			2/2	5/5	5/0
Rudder			1/1	5/5	5/1
Right elevator			5/5	5/5	5/0
Right aileron			2/2	5/4	4/1
All			10/10	20/19	19/2

(b) Isolation performance

Failed surface	Number of failures detected/number isolated[a] as a function of percent surface effectiveness				
	0%	20%	40%	60%	80%
Right stabilizer			2/2	5/3	0/0
Rudder			1/1	5/4	1/1
Right elevator			5/5	5/1	0/0
Right aileron			2/2	4/3	1/0
All			10/10	19/11	2/1

[a]For stabilizer and elevator failures, isolated to horizontal tail (confusion set containing only stabilizer and elevator).

When the actuator-path subsystem was evaluated with model errors in the range of 5 to 15 percent, stuck-at-current-position failures were reliably detected without false alarms. With larger model errors (12.5 to 37.5 percent), the same failures were still detected, but some false alarms were experienced. When the aircraft-path subsystem was operated at trim points in the vicinity of the design point, aircraft-path failures were reliably detected with no false alarms, but isolation performance was slightly degraded. At a trim point farther away (cruise instead of terminal area), the system was unusable because of false alarms. When moderate random errors were added to the aircraft-path model, the system was still able to detect failures at 60-percent effectiveness, although two false alarms occurred.

In 10-ft/sec turbulence, the actuator-path subsystem continued to perform well. Again, all actuator-path failures were detected with no false alarms. On the other hand, the baseline aircraft-path subsystem was completely unusable in 10-ft/sec and higher turbulence because of the large number of false alarms. This result, plus examination of the residuals, indicated that many of the baseline values used in the truth model for the standard deviations of the errors in the residuals were too small. New values for the truth model in 10-ft/sec turbulence were obtained, and two new aircraft-path subsystem designs were produced. One of these, called new-threshold (TG) design, retained the old projection vectors but computed new gains and thresholds. The other, called new-projection-vector (PV10) design, was a totally new design. Both of these new designs performed well in 10-ft/sec turbulence and were far superior to the baseline design in false-alarm performance. There was a small edge in performance to the new-projection-vector design. However, performance of the new designs in zero turbulence was not

nearly as good as that of the baseline design, which indicated that some type of adaptive design was necessary for operation in atmospheric turbulence and that the adaptive process probably should include adaptation of the projection vectors as well as the gains and thresholds.

When a new aircraft-path subsystem (PV20) was designed for operation in 20-ft/sec turbulence, the standard deviations of the errors obtained at 20-ft/sec wind gusts for the truth model were not large enough and had to be increased to obtain adequate false-alarm performance at that turbulence level. Thus, the design procedure at the higher turbulence levels needs refinement or the method of obtaining parameter values for the truth model needs improvement. Nevertheless, after the truth model was adjusted, the PV20 design performed well in 20-ft/sec gusts. At these higher gust levels, the baseline actuator-path subsystem also experienced some false alarms. Redesign of the actuator-path subsystem was not pursued because it was felt that if an adaptive aircraft-path subsystem could be successfully developed, similar techniques could be easily applied to the less complex actuator path.

The design procedure was extended to produce an interpolated design for operation over a range of turbulence levels. This design was accomplished by linearly interpolating the thresholds, gains, and projection vectors between their baseline, PV10, and PV20 design values based on the FDI system's knowledge of the turbulence level. In the interpolated design, this knowledge was supplied by the simulation user before each run as the specified value of the turbulence standard deviation for that run. The interpolated design performed well over the turbulence range of 0 to 20 ft/sec, but the design was impractical, or incomplete, in that the required knowledge of the turbulence magnitude is unknown in flight operation.

A turbulence estimator was developed based on the technique used in the NASA F-8 digital fly-by-wire program. This technique estimates the sample standard deviation of the latest 5 sec of turbulence. This estimator was combined with the interpolated design to produce an adaptive aircraft-path subsystem. This adaptive design was evaluated in 0-, 5-, 10-, 15-, and 20-ft/sec turbulence and performed well over the entire range. It successfully detected and isolated all partially missing surface failures at 40-percent effectiveness, and it detected 19 out of 20 failures at 60-percent effectiveness. Only at the smallest failure magnitude (80-percent effectiveness) did performance degrade. Furthermore, in 688 sec of simulation time with no failures, there was only one false alarm.

Although the decentralized FDI technique is robust to small model errors, and the extension of the technique to an adaptive system allows the system to operate in atmospheric turbulence, problems remain to be solved in the development of an operational FDI system. The two most urgent needs are (1) the continuation of the work reported in NASA CR-181664 to extend the system from a single operating point to operation over the entire operating envelope of the aircraft, and (2) flight testing to provide more realistic noise, or error, values for the truth models and to provide reliable false-alarm evaluation.

NASA Langley Research Center
Hampton, VA 23665-5225
January 4, 1991

Appendix

Time-History Plots From the Simulation
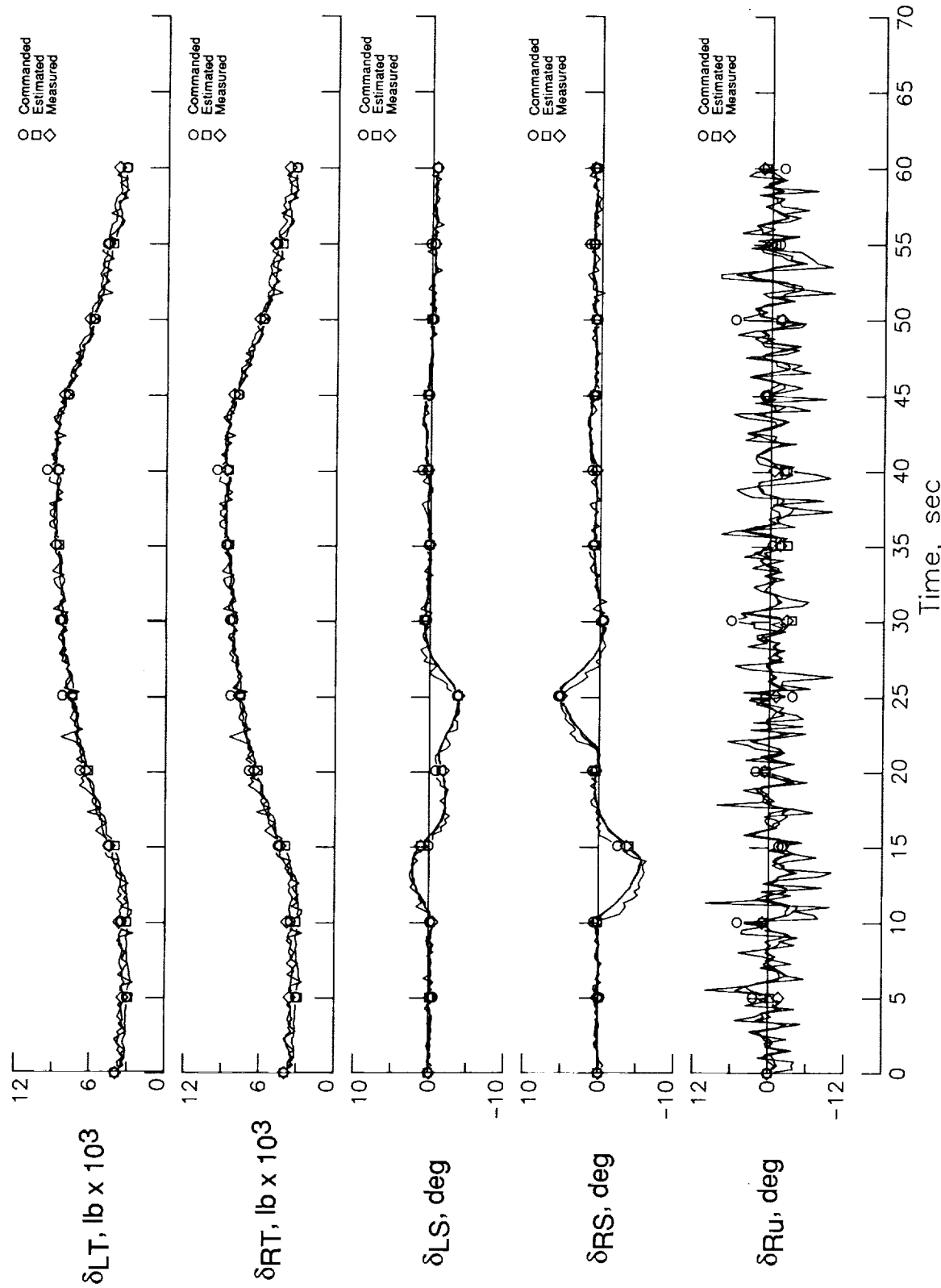
Figure A1. Actuator positions and residuals for stuck right-aileron failure with no turbulence.

98

Figure A1. Continued.

99

Figure A1. Continued.

100
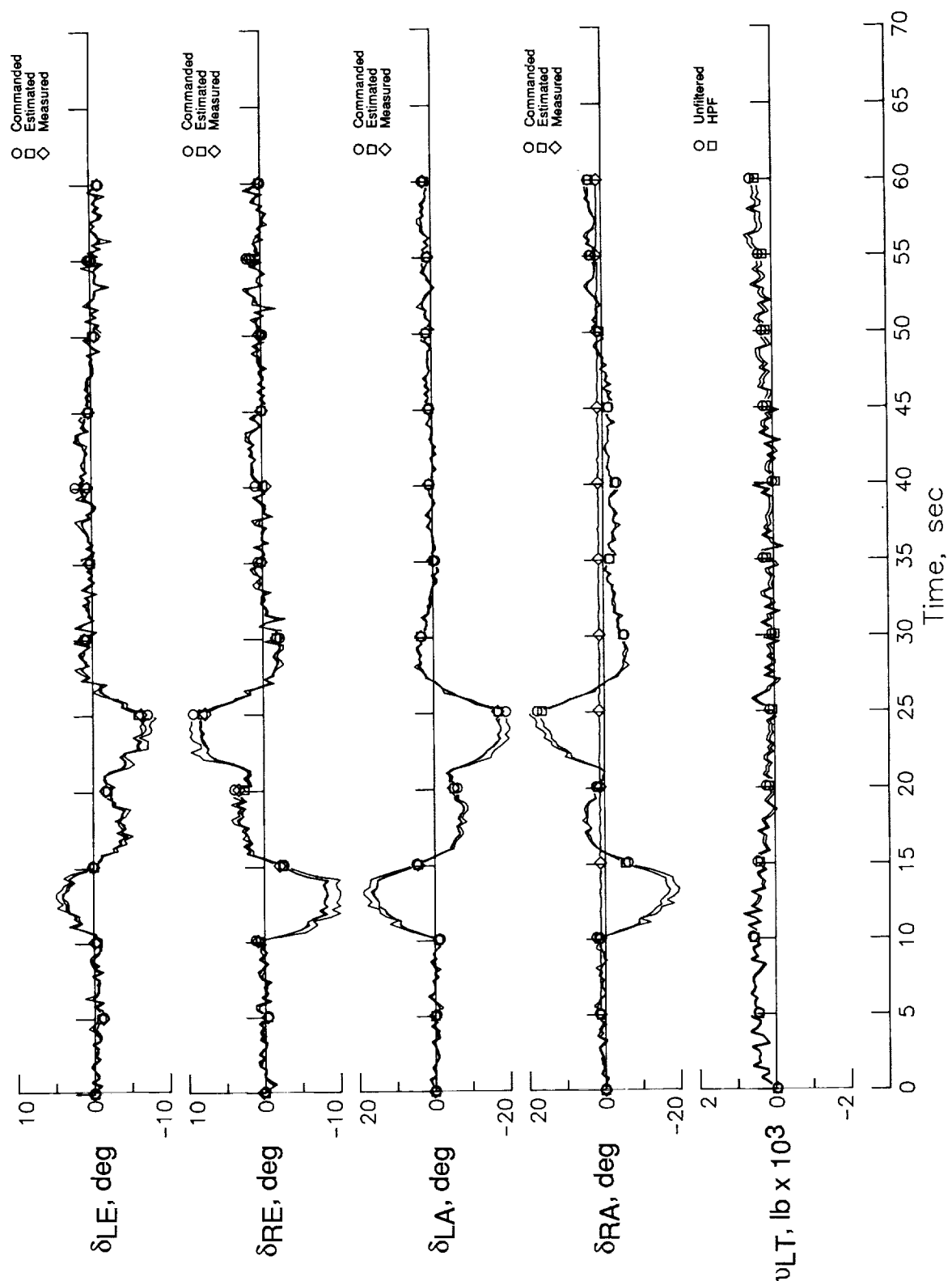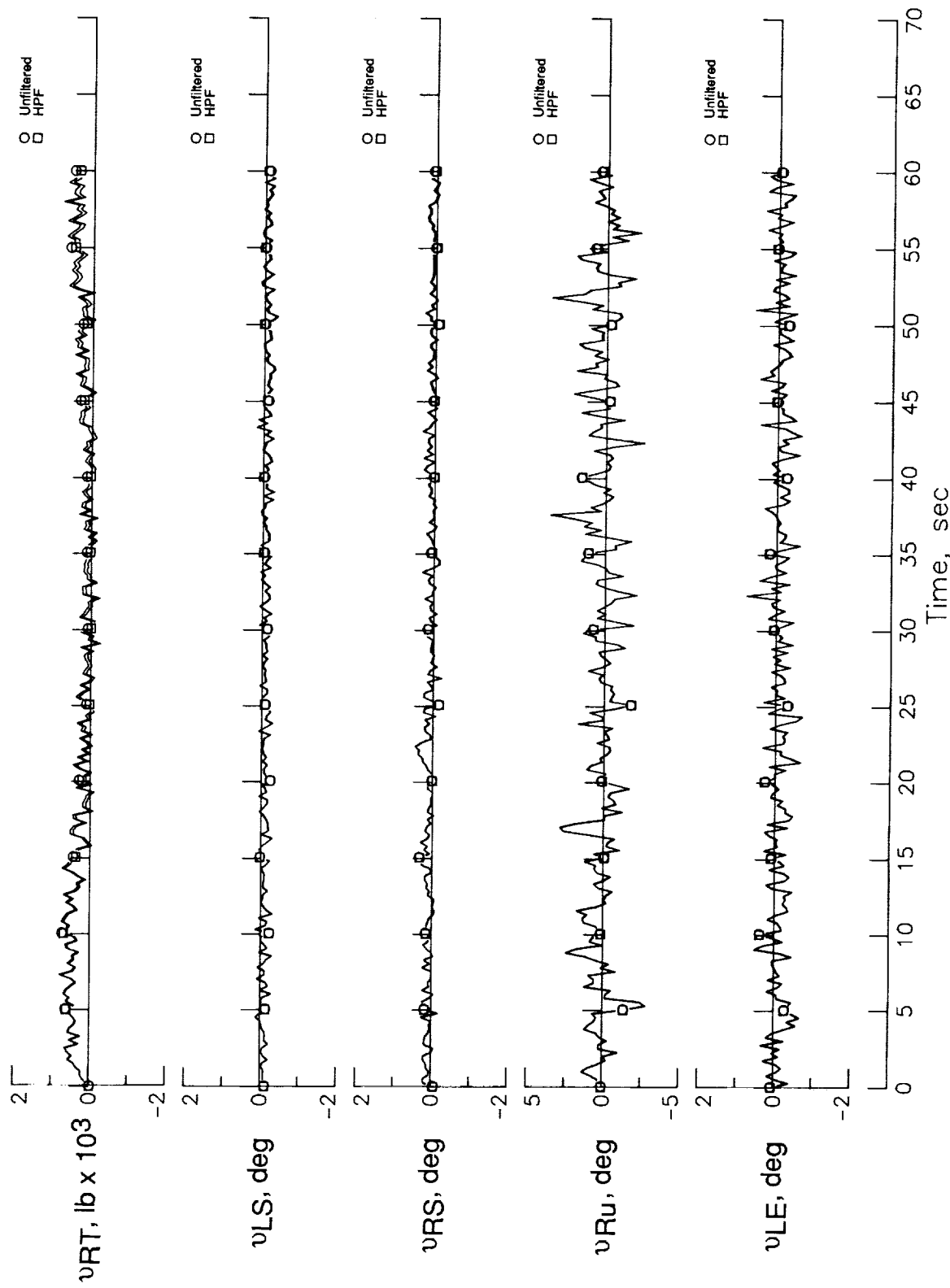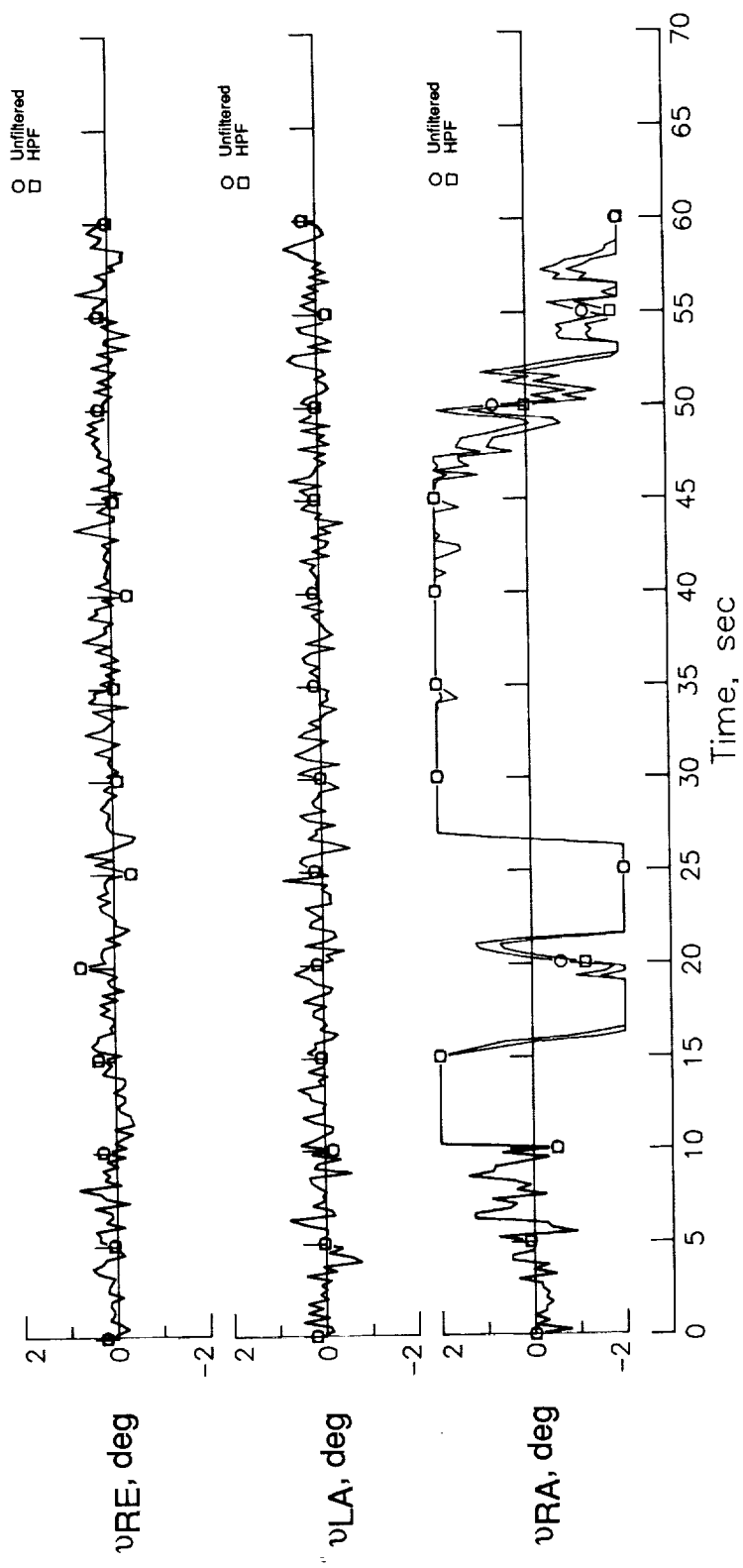
Figure A1. Concluded.

101
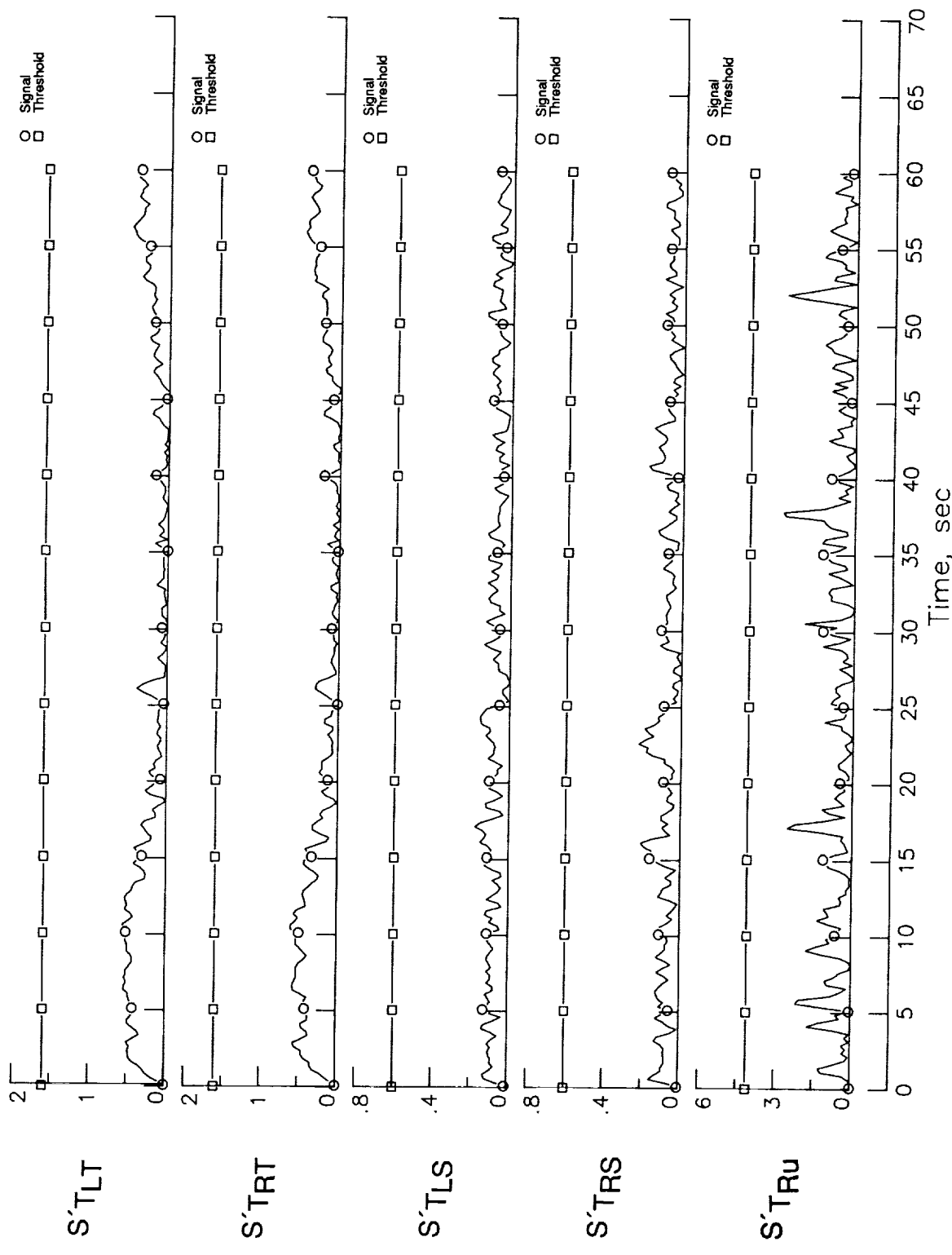
Figure A2. Actuator-path trigger and verify statistics for stuck right-aileron failure with no turbulence.
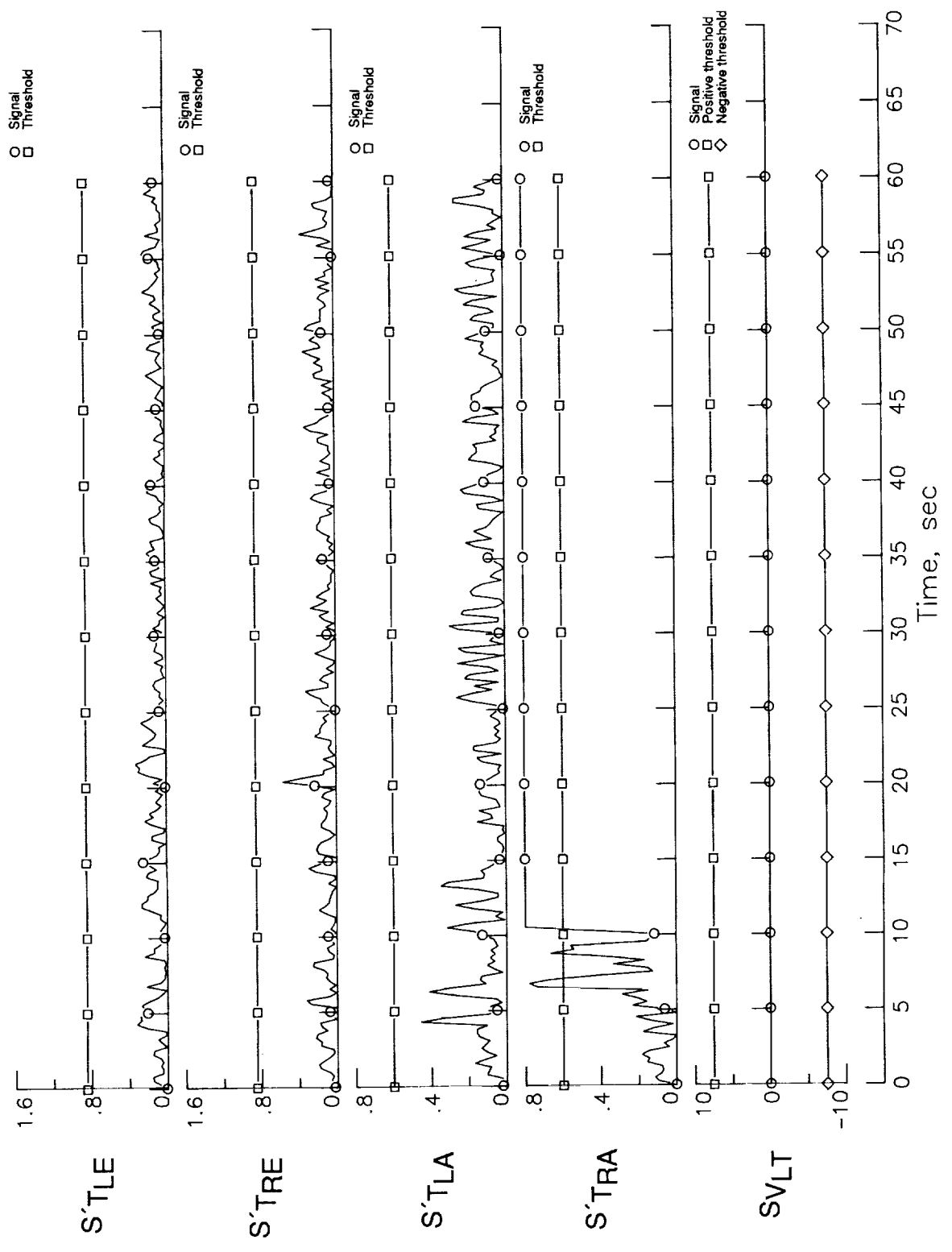
Figure A2. Continued.
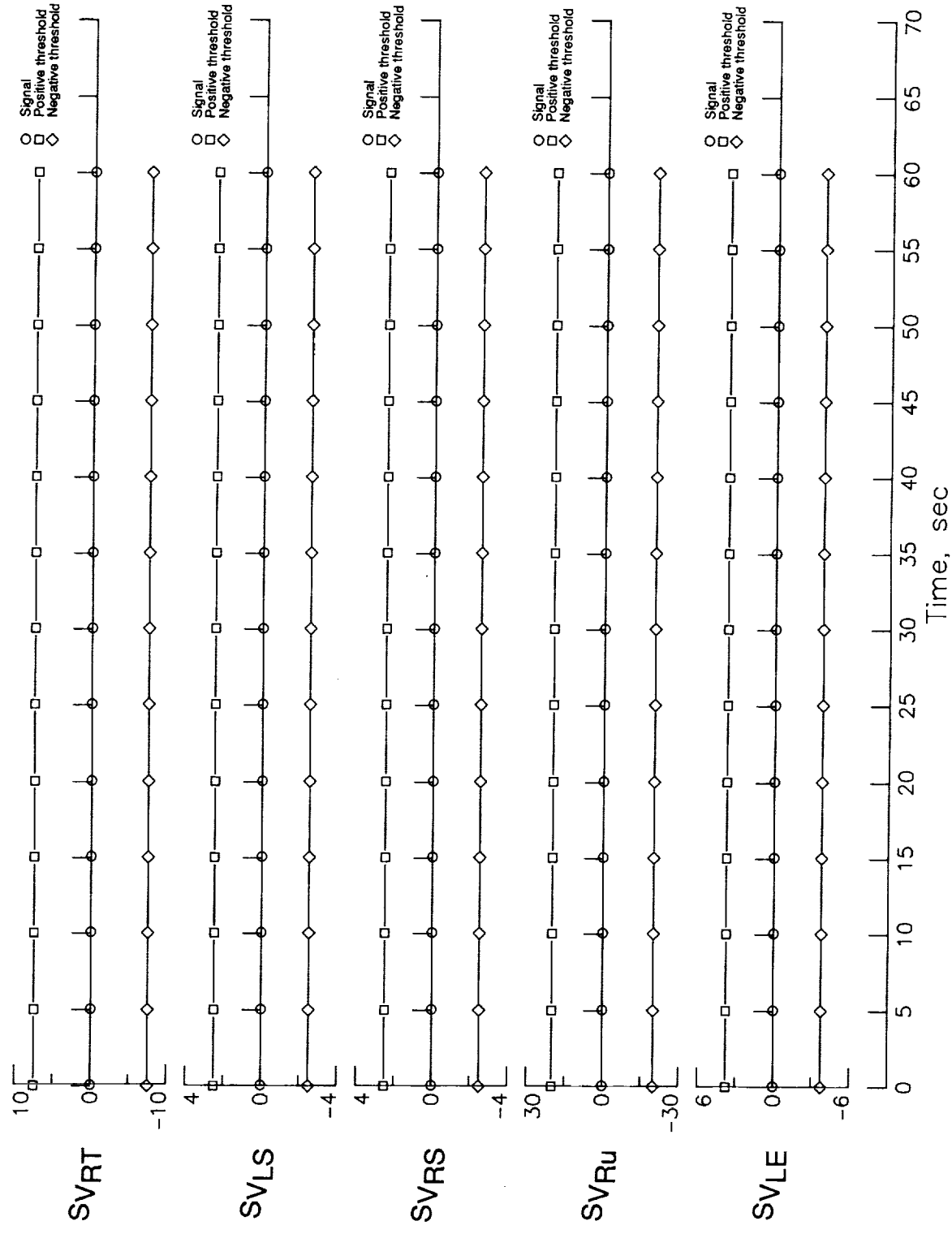
Figure A2. Continued.
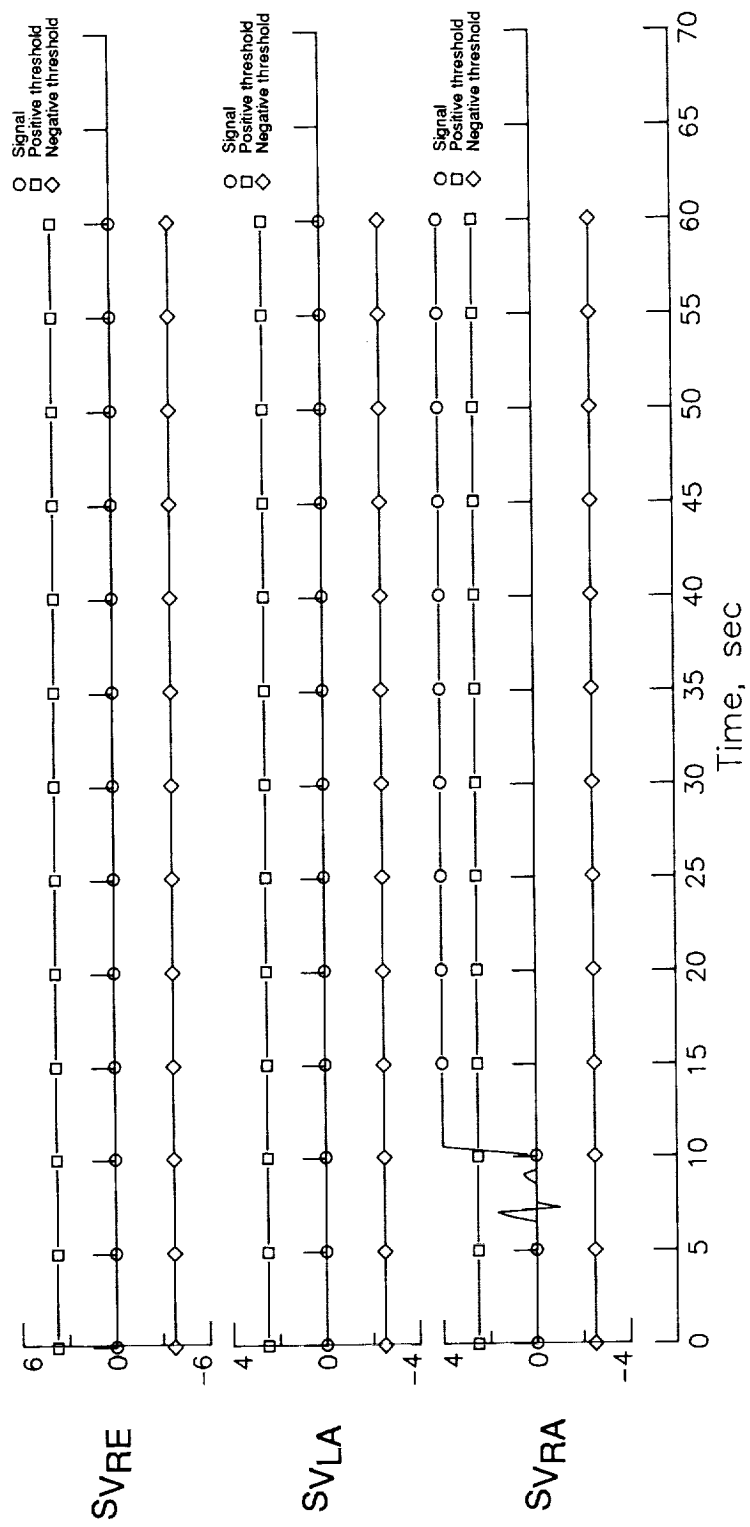
Figure A2. Concluded.

105
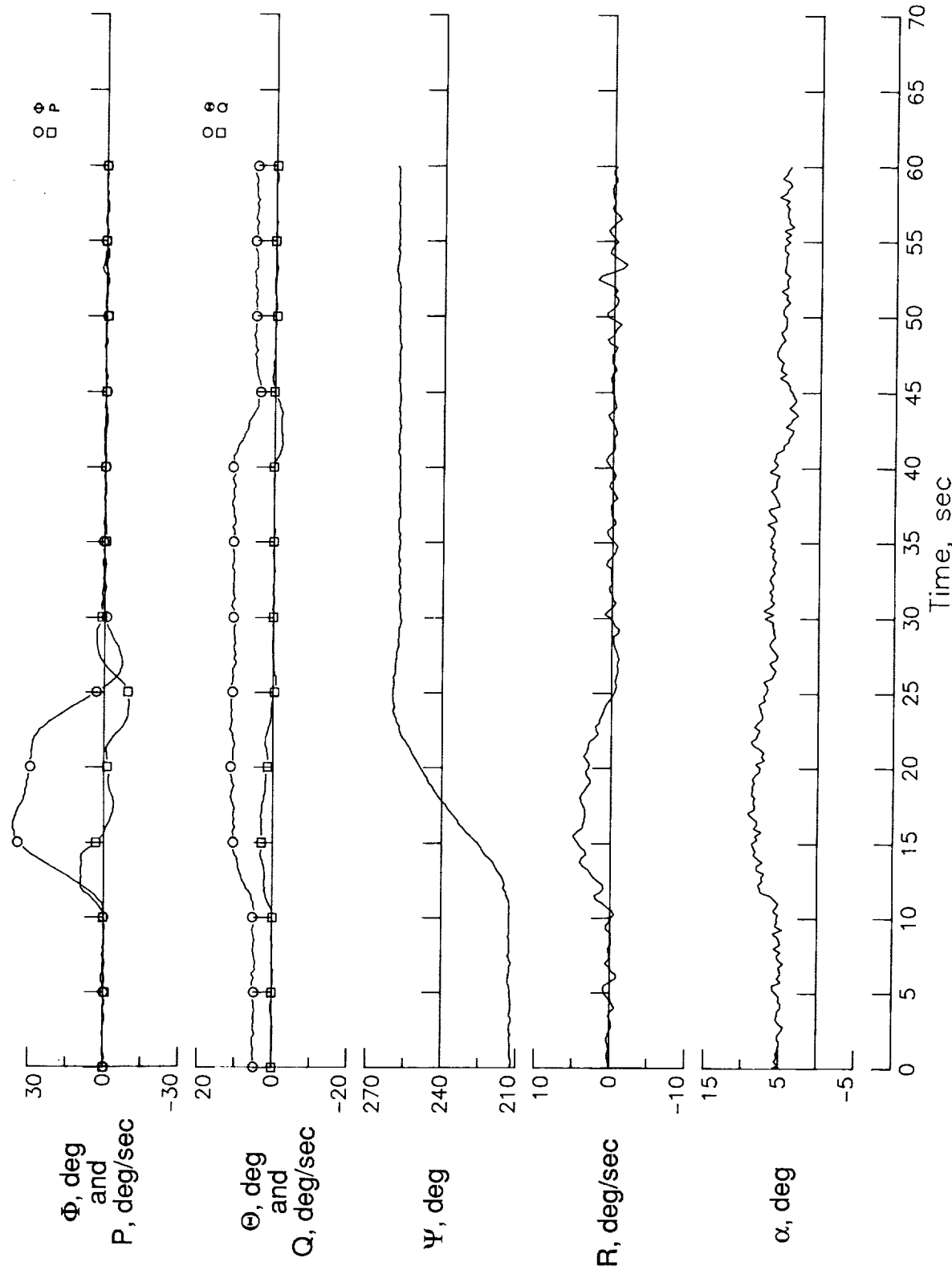
Figure A3. Aircraft sensor outputs for right-aileron partially missing surface failure (60-percent effectiveness) with no turbulence.
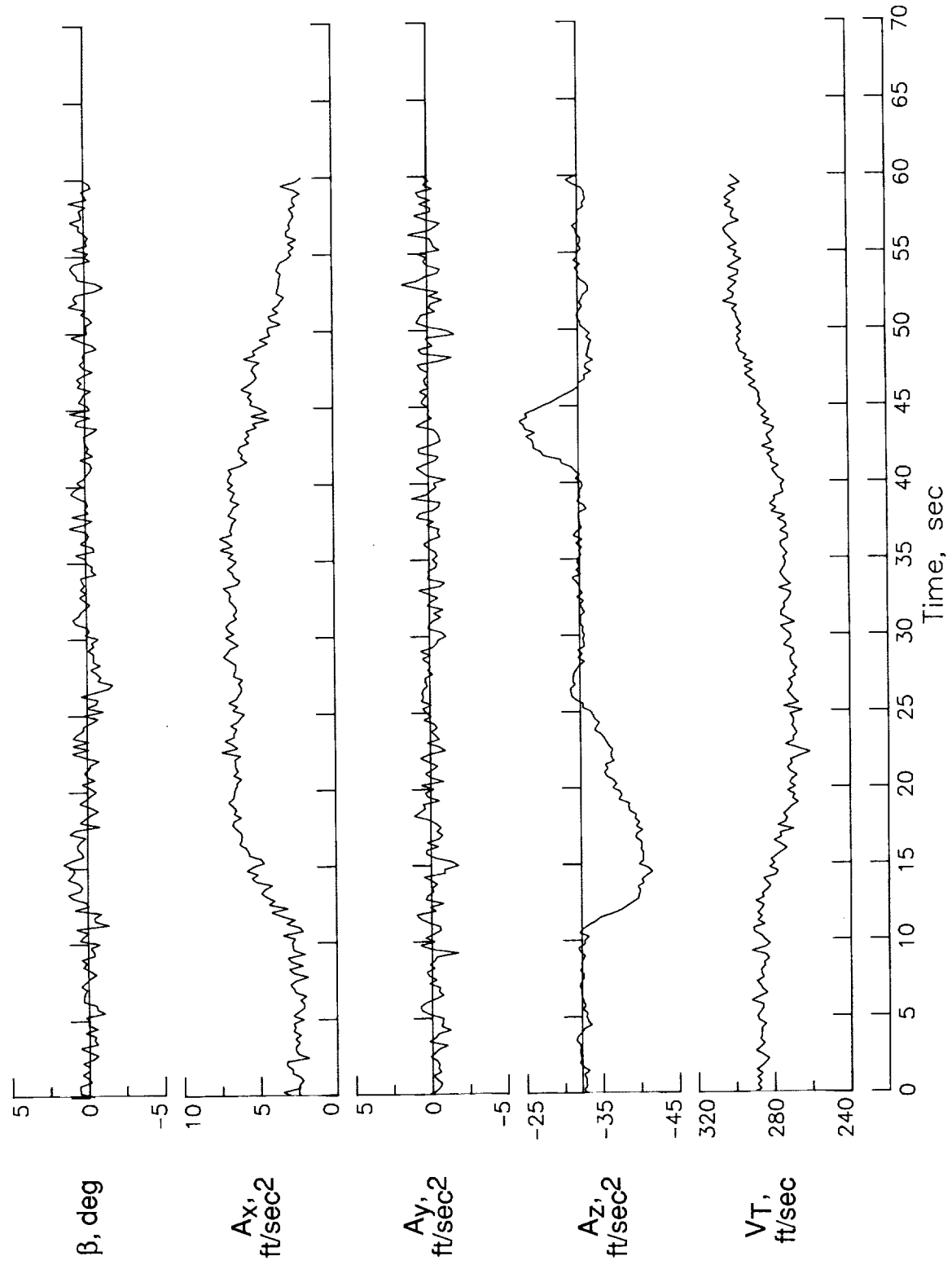
Figure A3. Continued.

107

Figure A3. Continued.

108

Figure A3. Continued.

109

Figure A3. Continued.

110
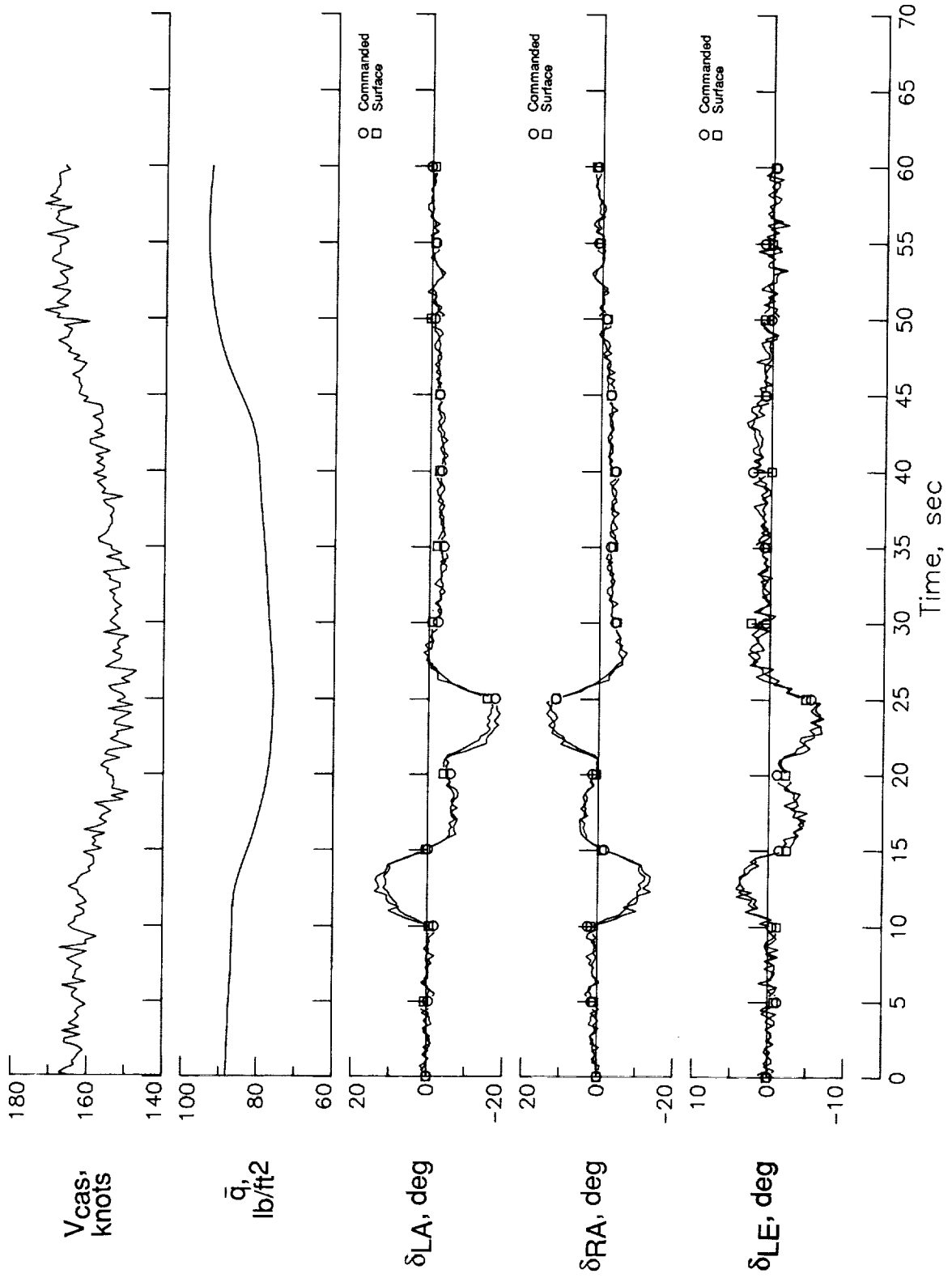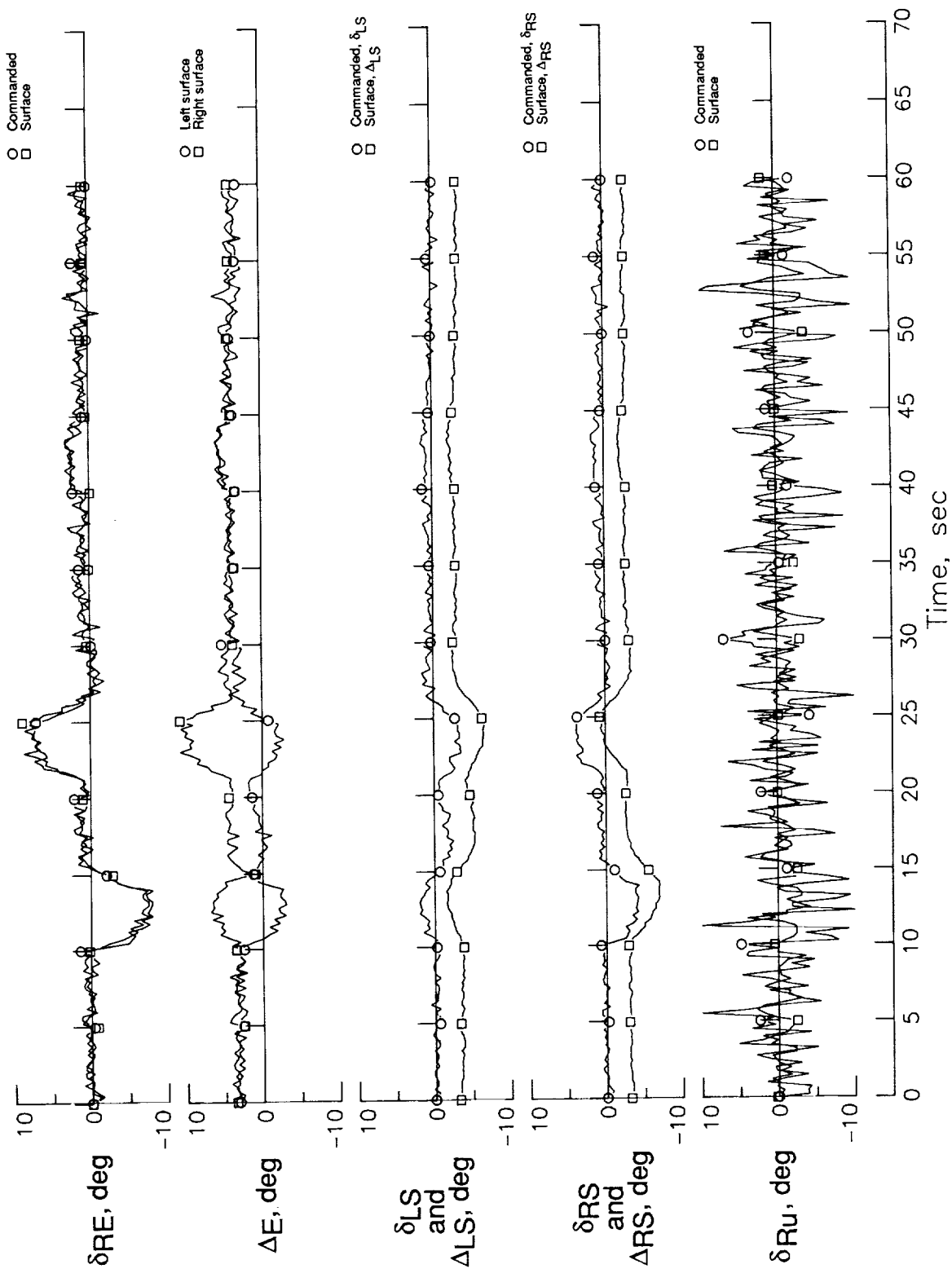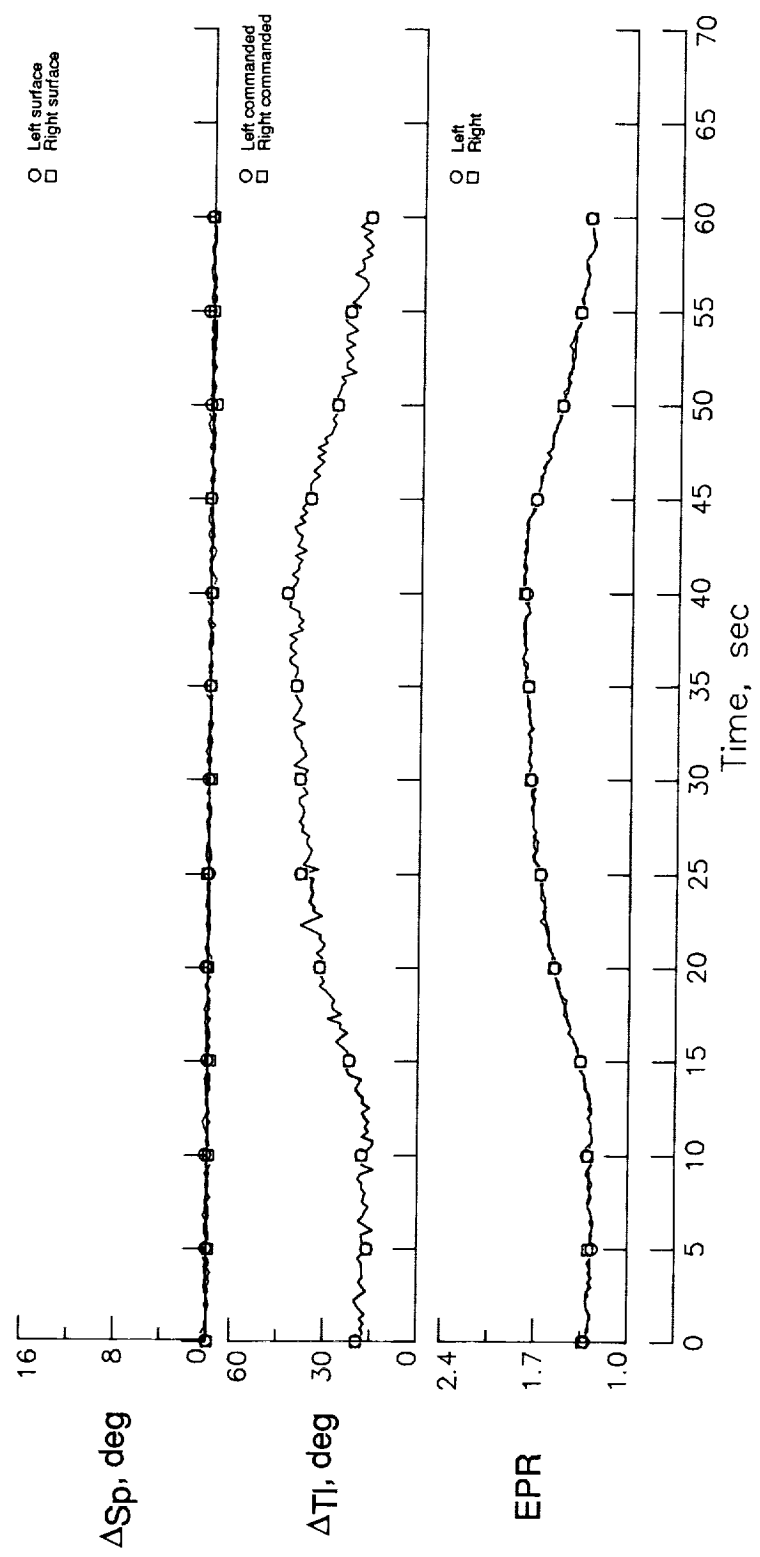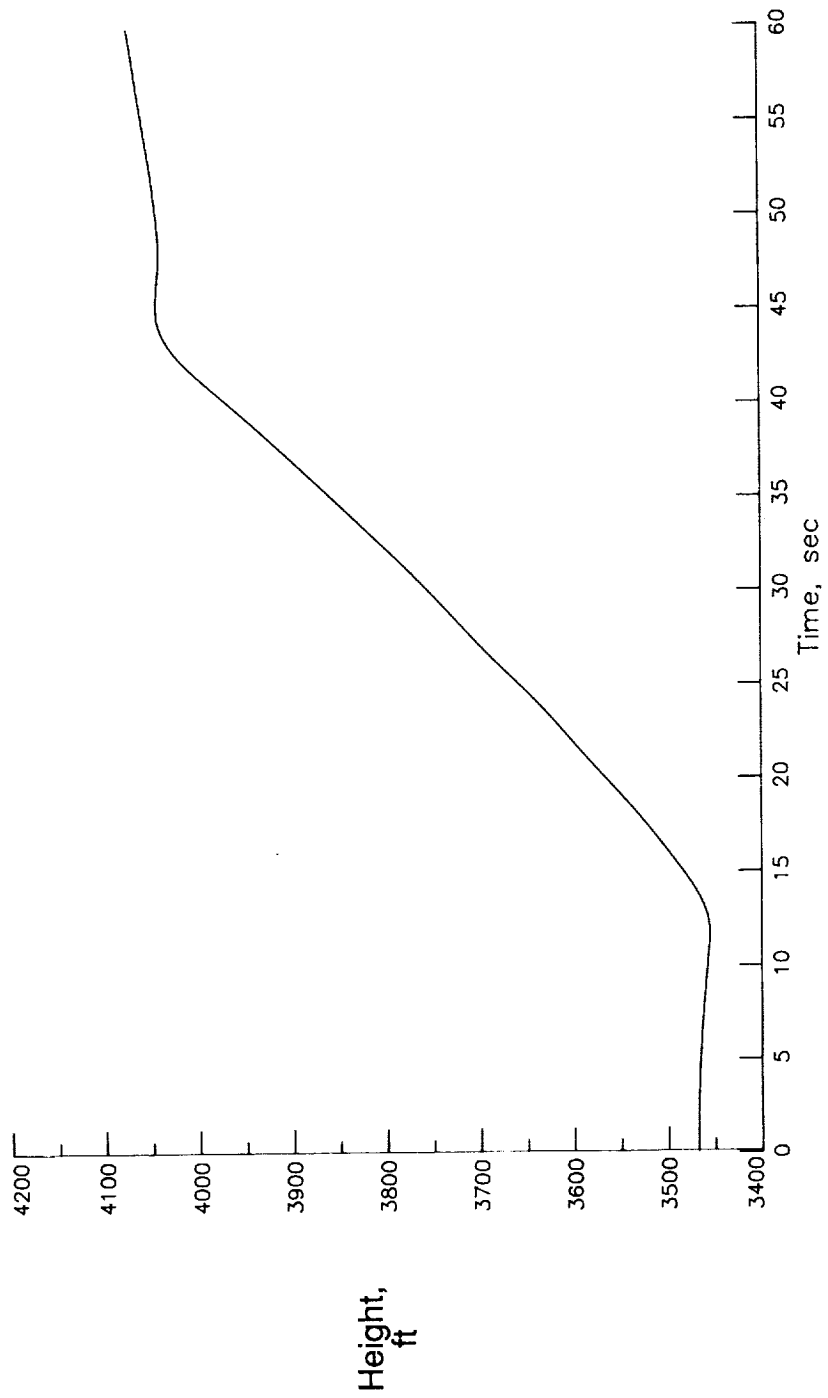
Figure A3. Concluded.

111
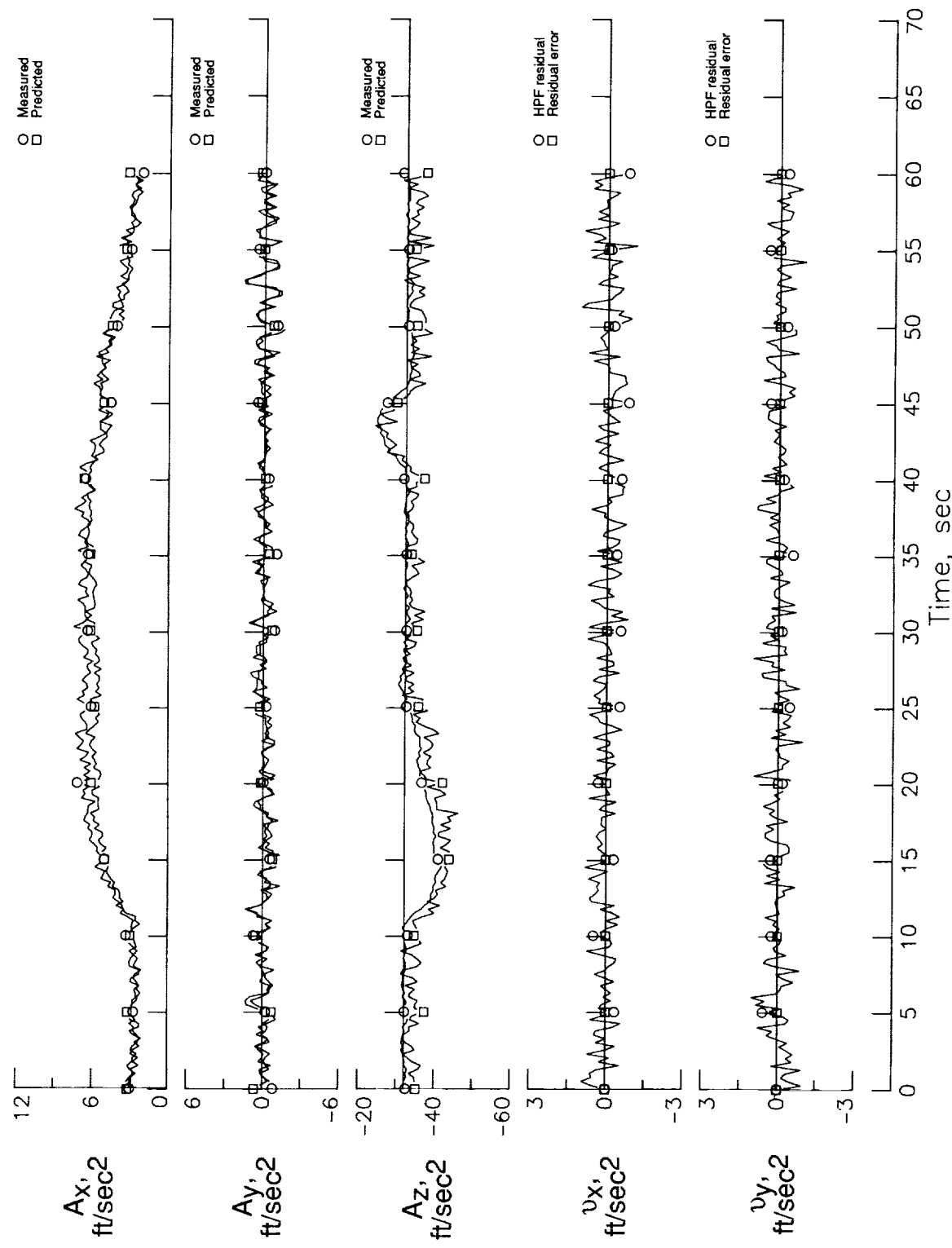
Figure A4. Aircraft-path measurements and residuals for right-aileron partially missing surface failure (60-percent effectiveness). Baseline design; no turbulence.

112
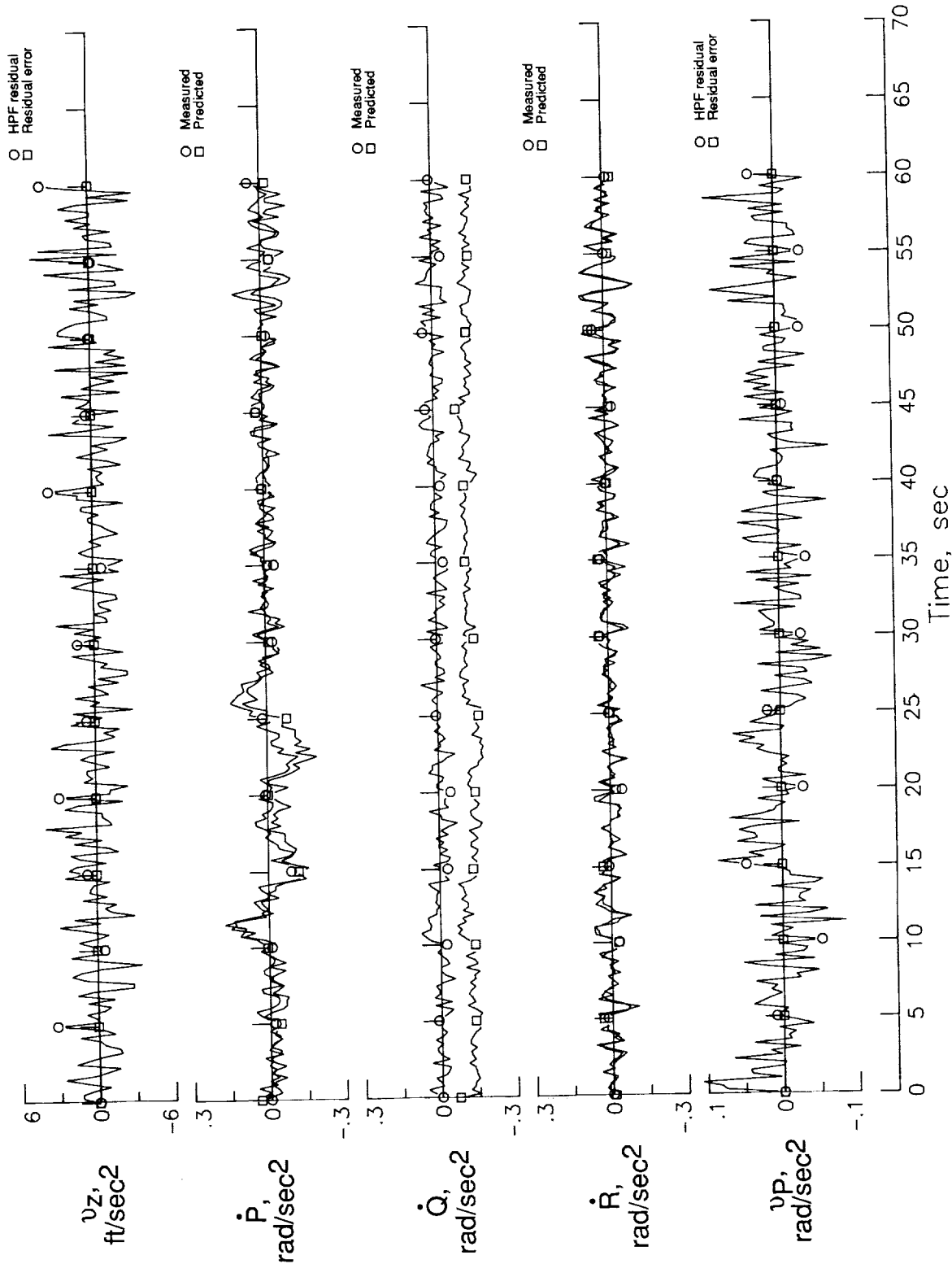
Figure A4. Continued.

113
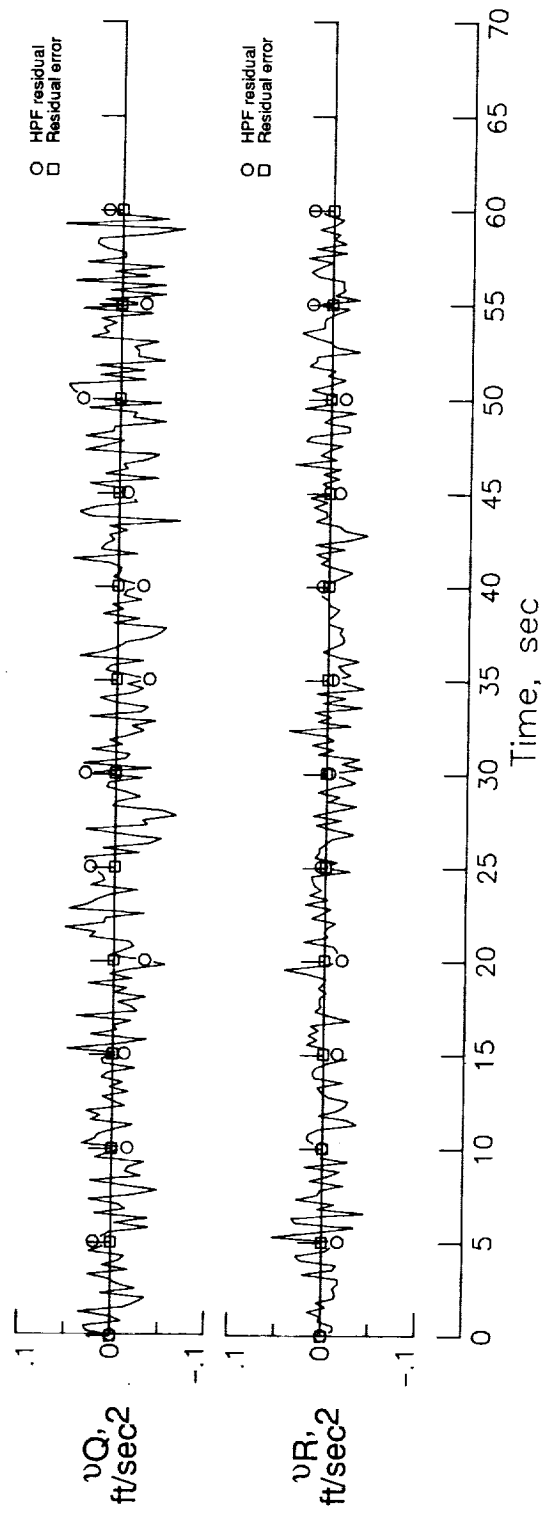
Figure A4. Concluded.

114
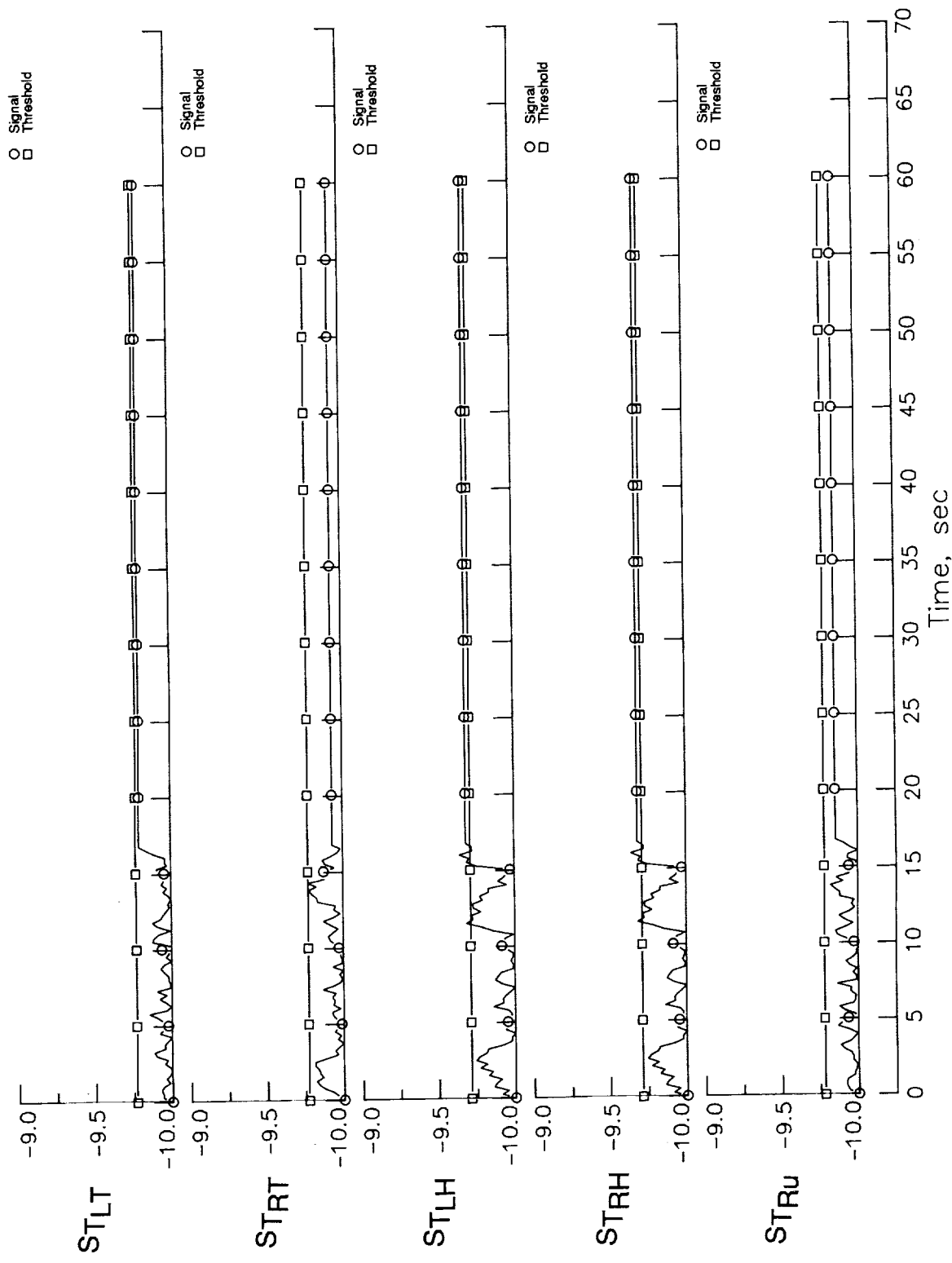
Figure A5. Aircraft-path trigger and verify statistics for right-aileron partially missing surface failure (60-percent effectiveness). Baseline design; no turbulence.
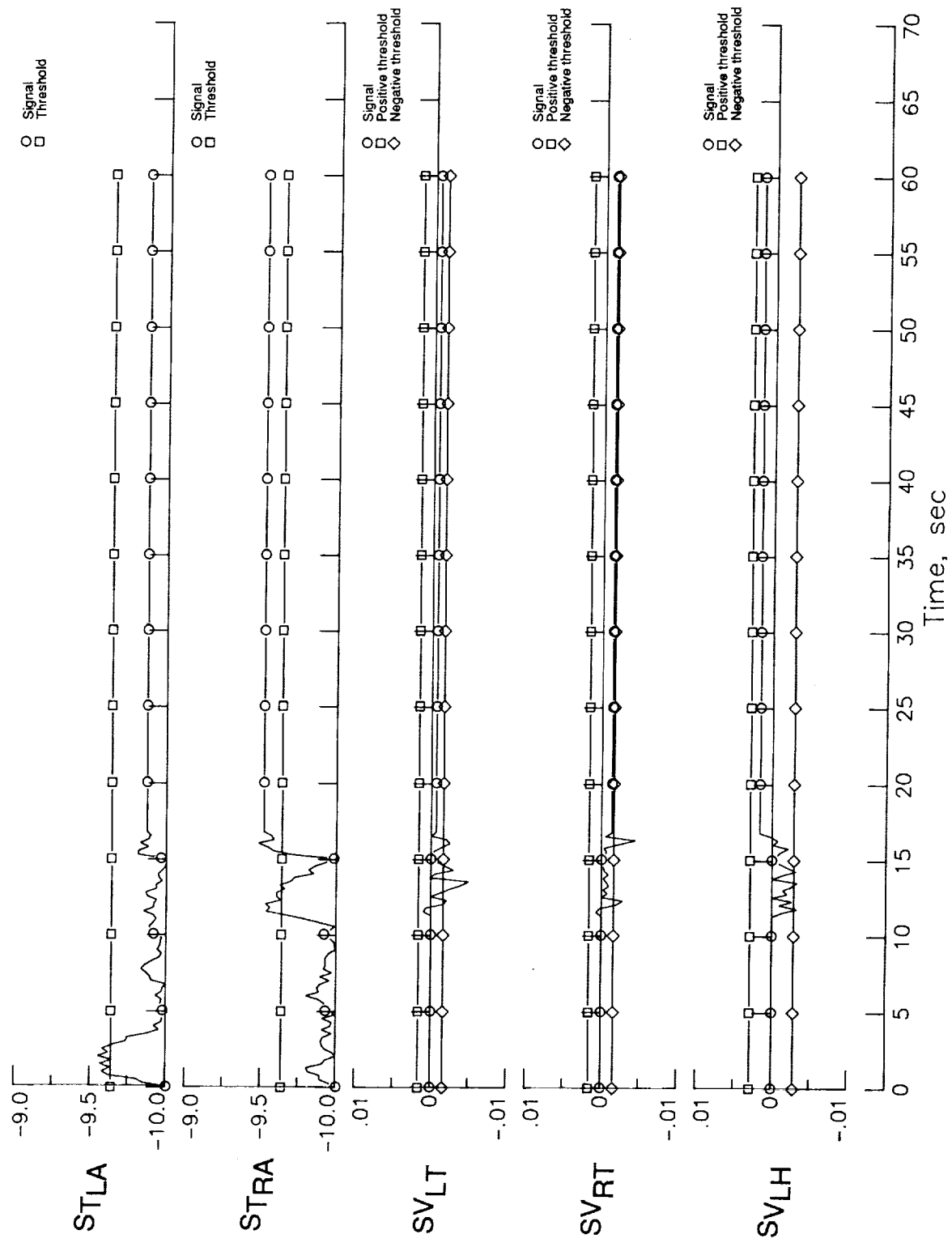
Figure A5. Continued.

116
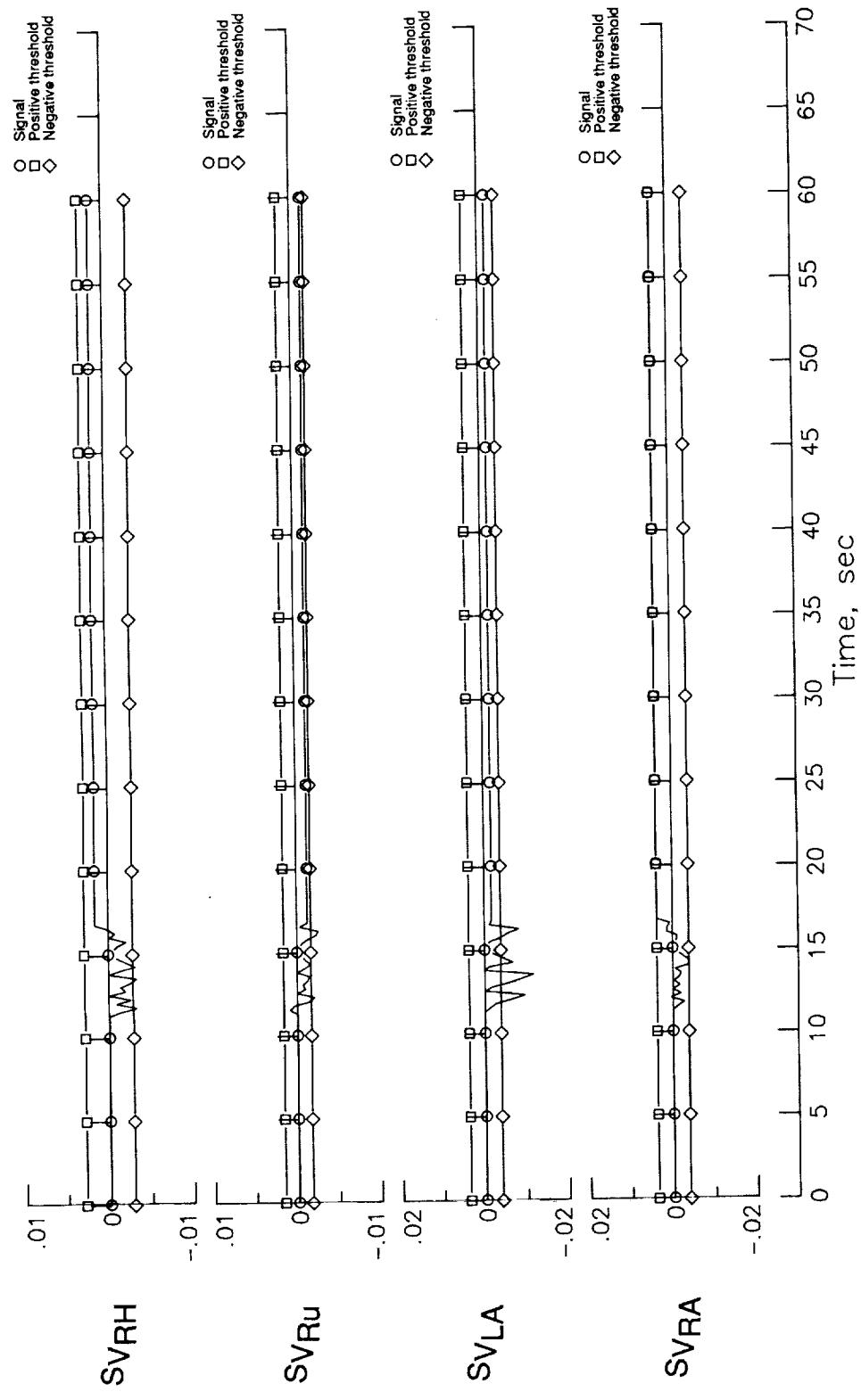
Figure A5. Concluded.

117
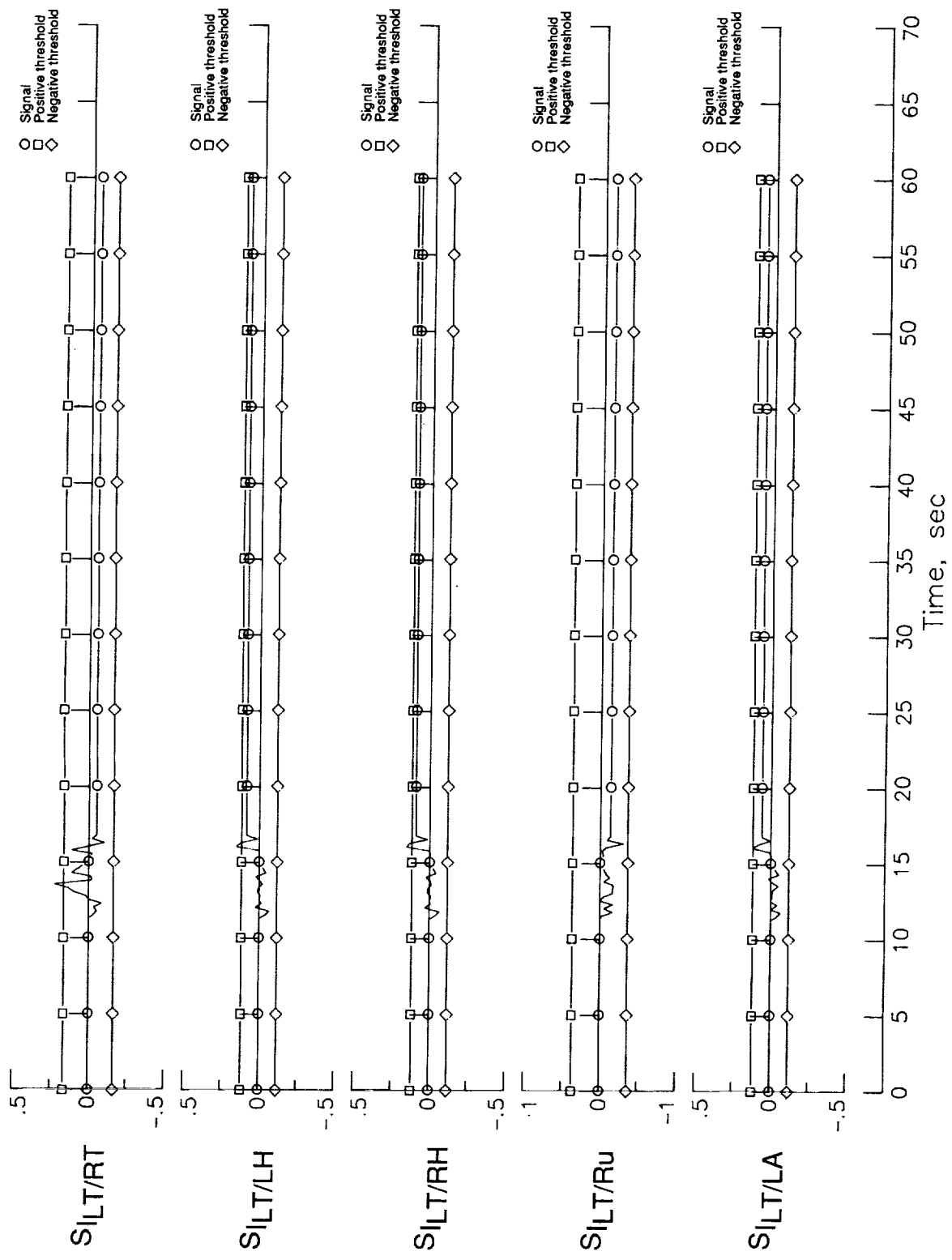
Figure A6. Aircraft-path isolate statistics for right-aileron partially missing surface failure (60-percent effectiveness). Baseline design; no turbulence.

118

Figure A6. Continued.

119
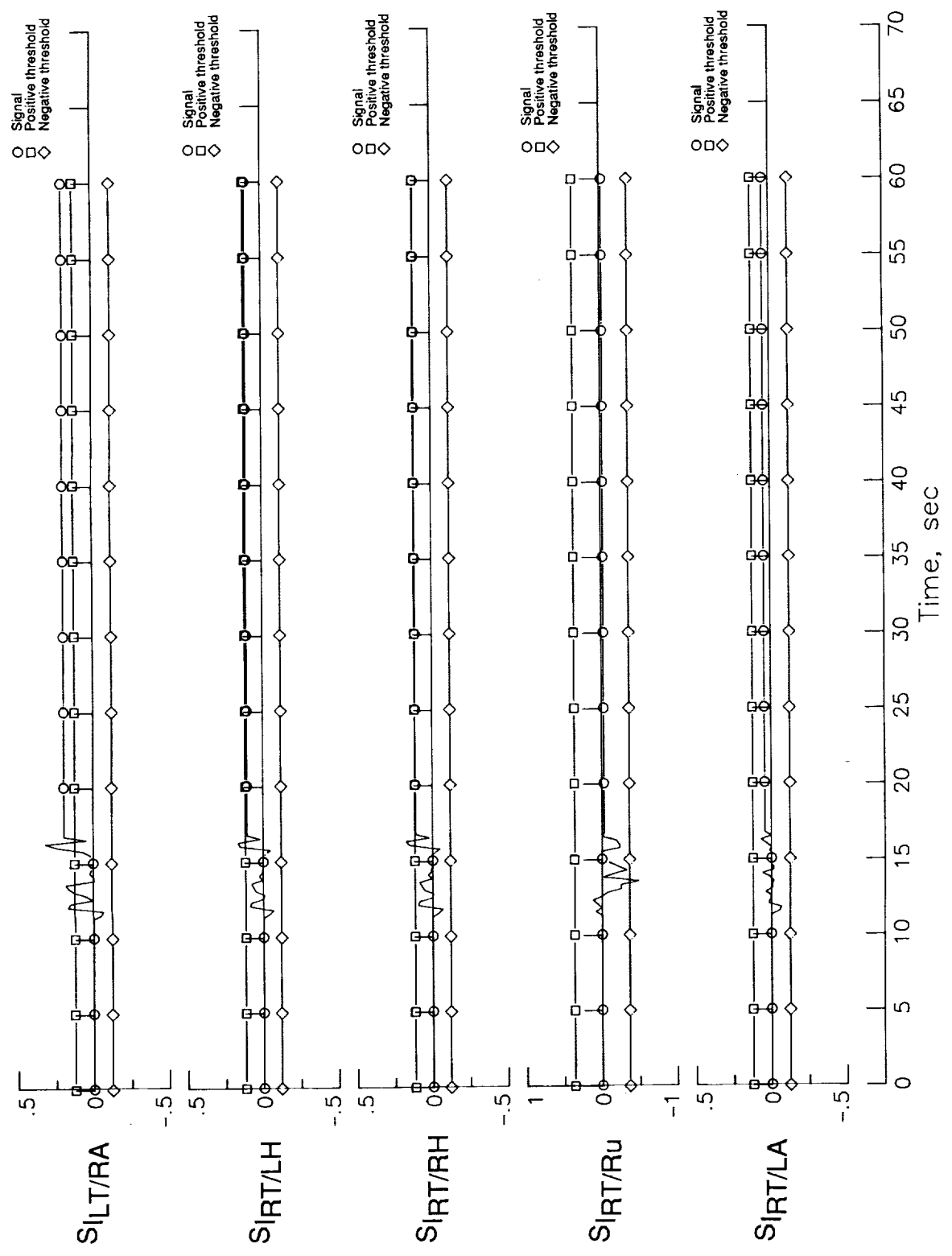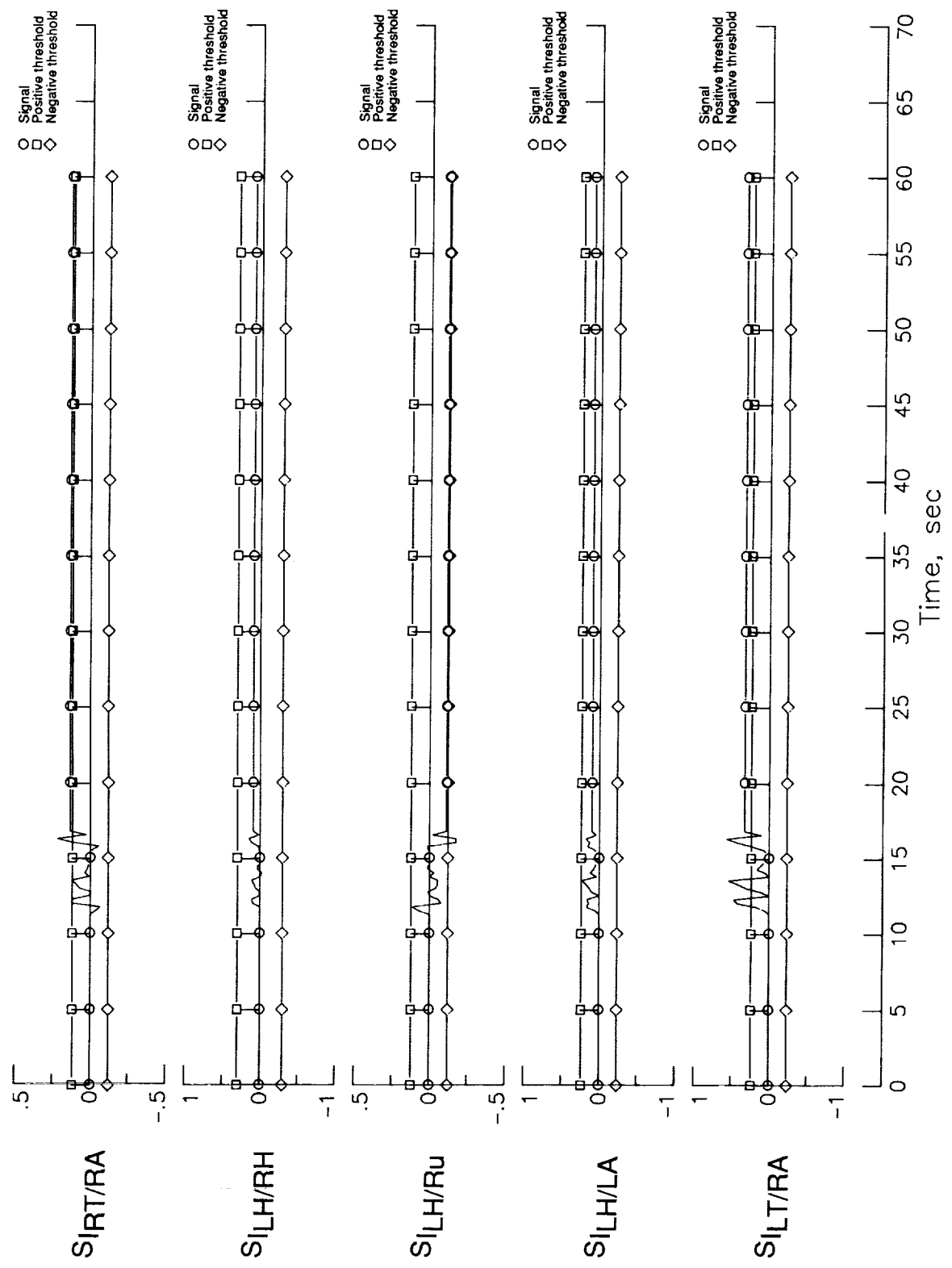
Figure A6. Continued.

Figure A6. Continued.

121
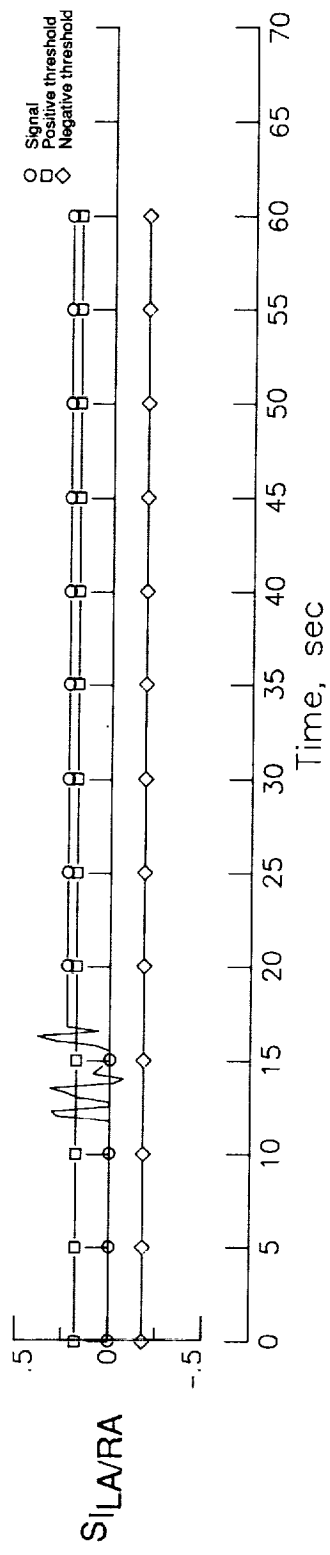
Figure A6. Concluded.

122
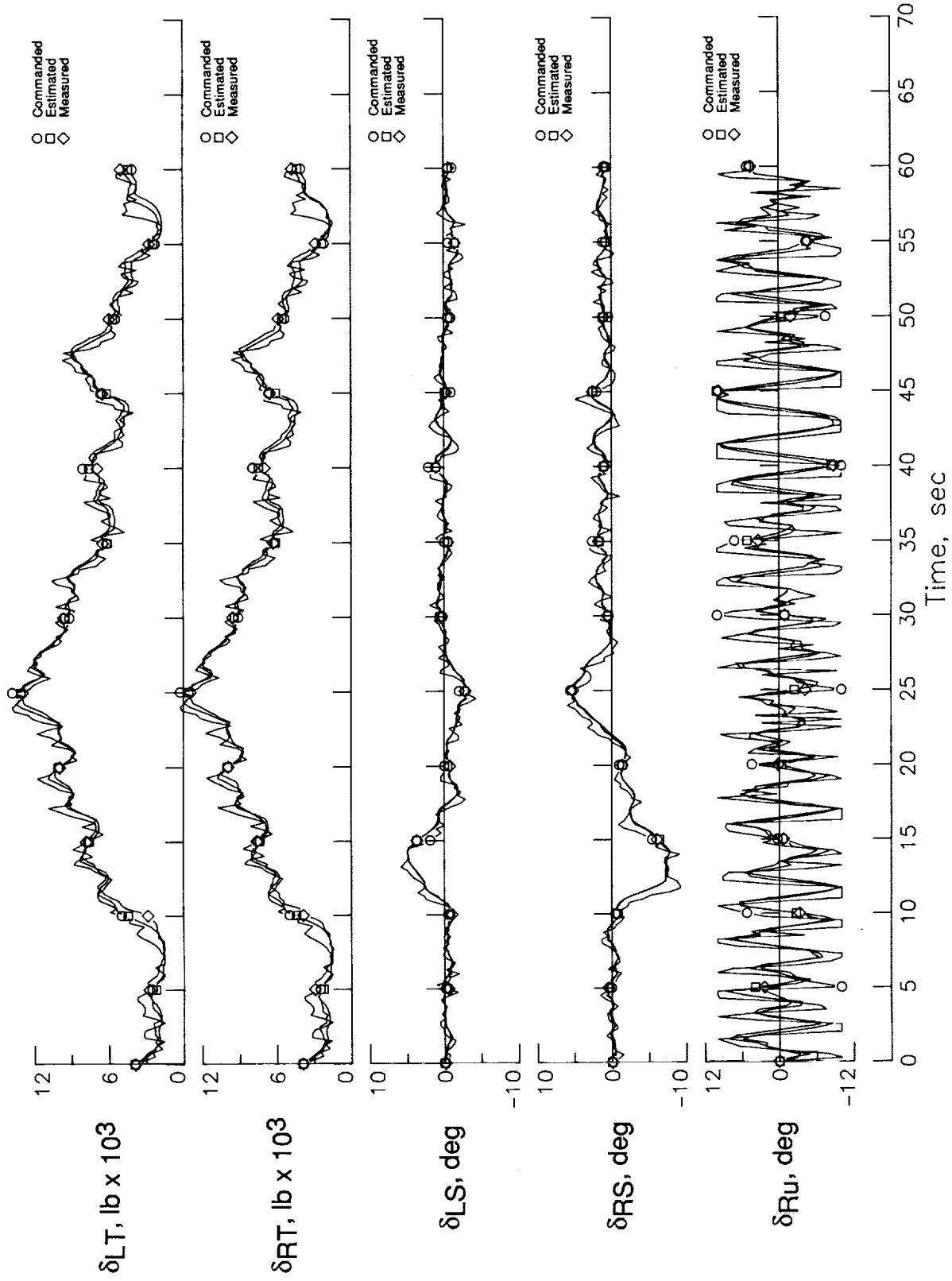
Figure A7. Actuator positions and residuals for stuck right-aileron failure with 10-ft/sec turbulence.

123

Figure A7. Continued.

124

Figure A7. Continued.

125
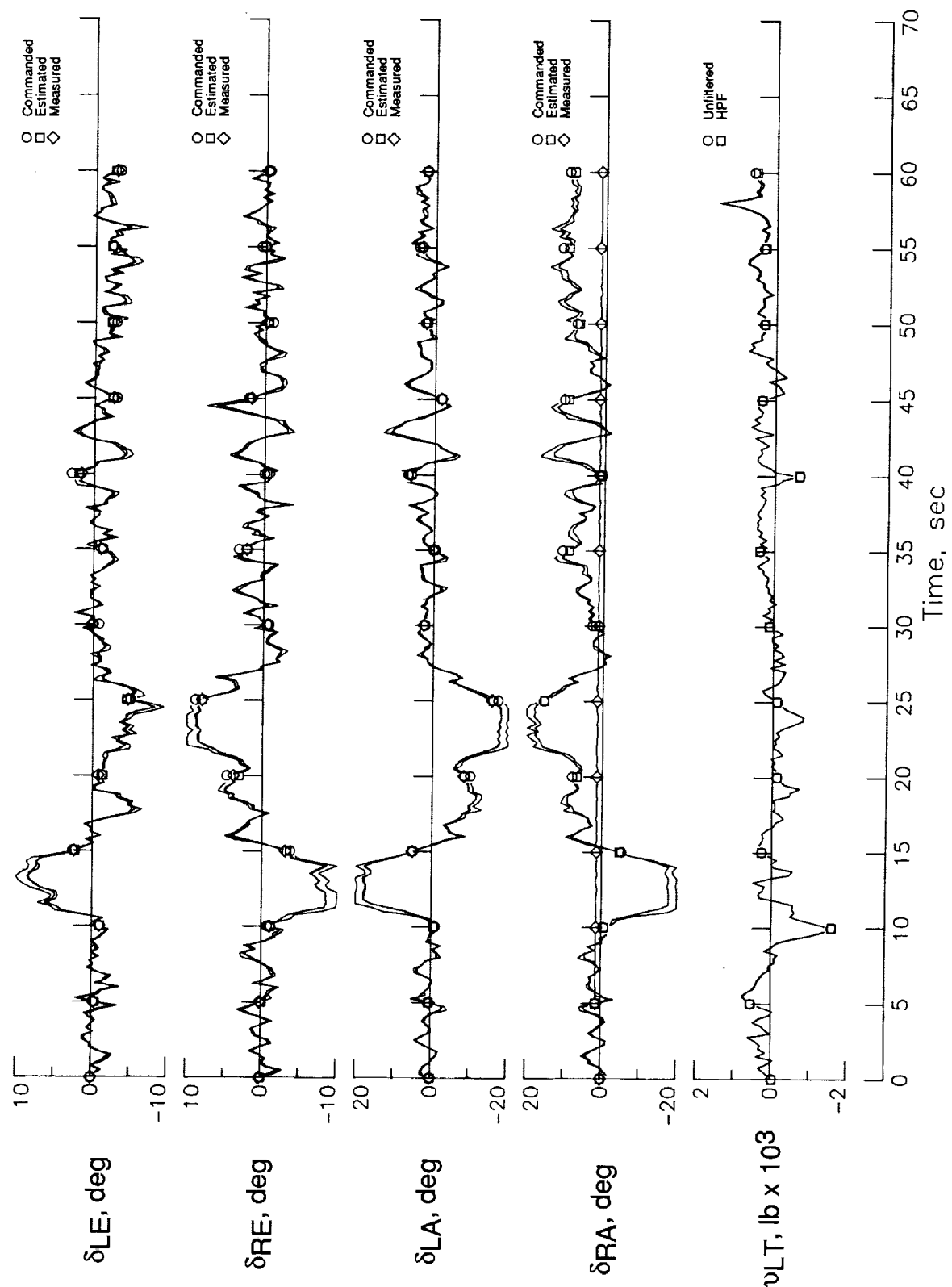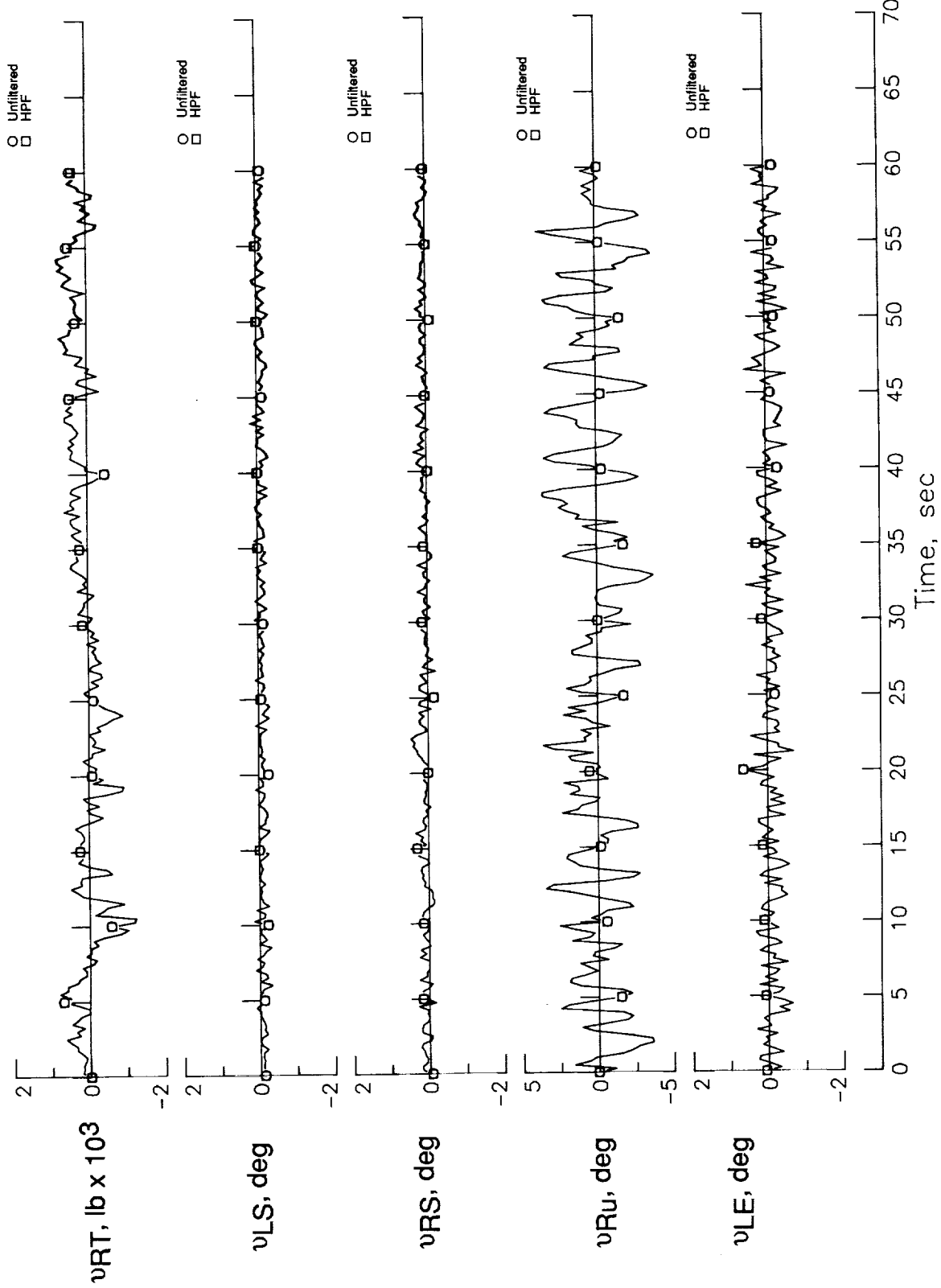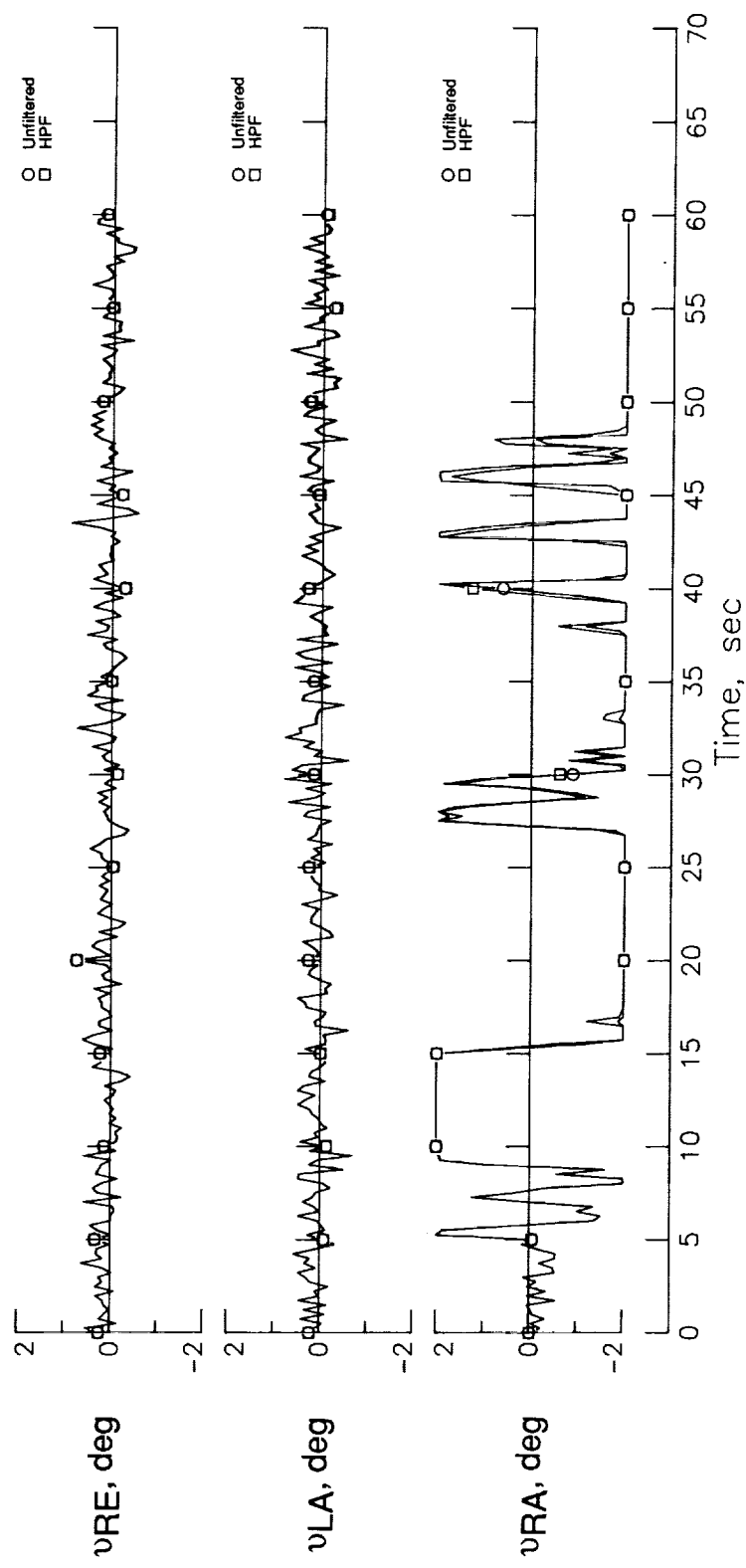
Figure A7. Concluded.

126
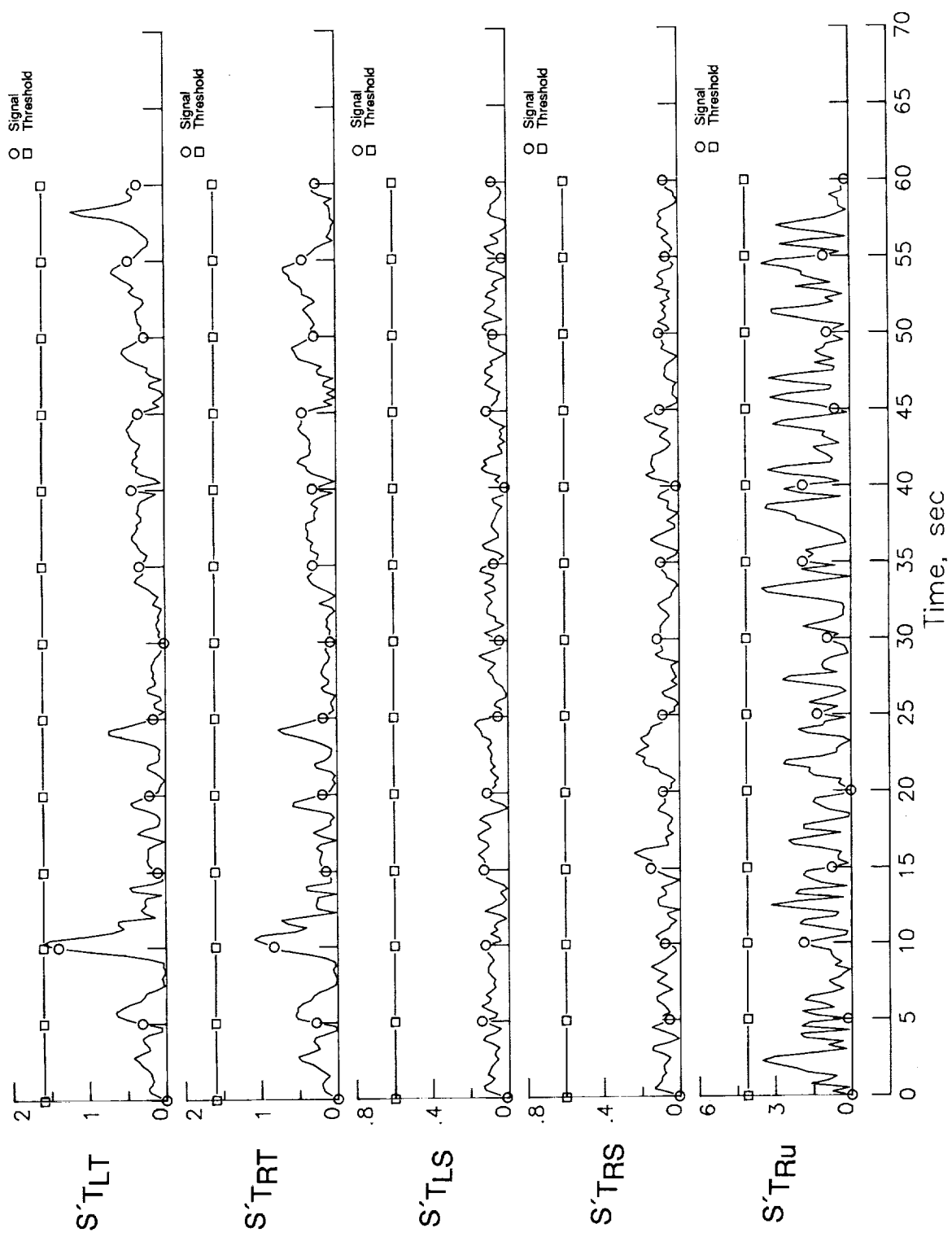
Figure A8. Actuator-path trigger and verify statistics for stuck right-aileron failure with 10-ft/sec turbulence.

127

Figure A8. Continued.

128
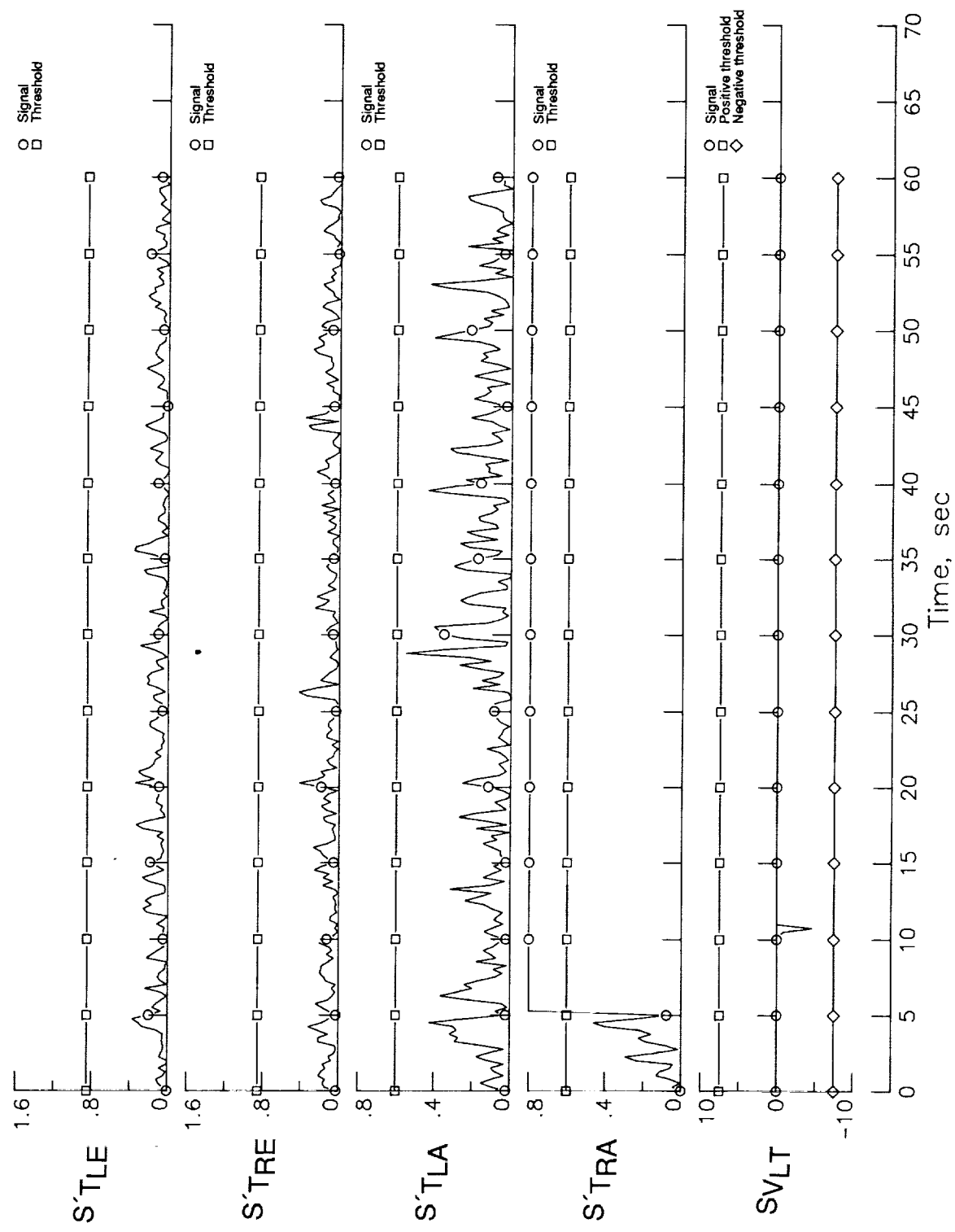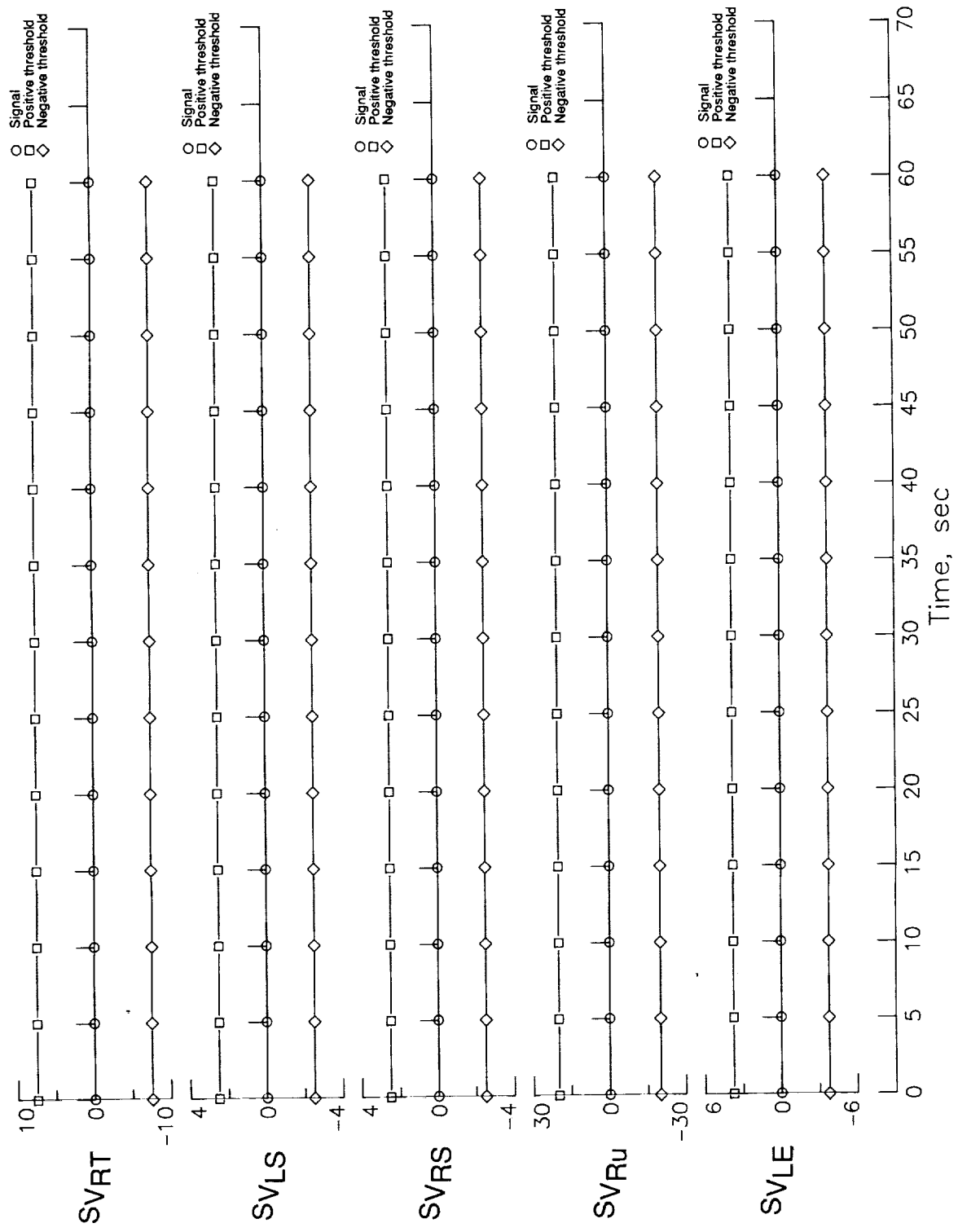
Figure A8. Continued.
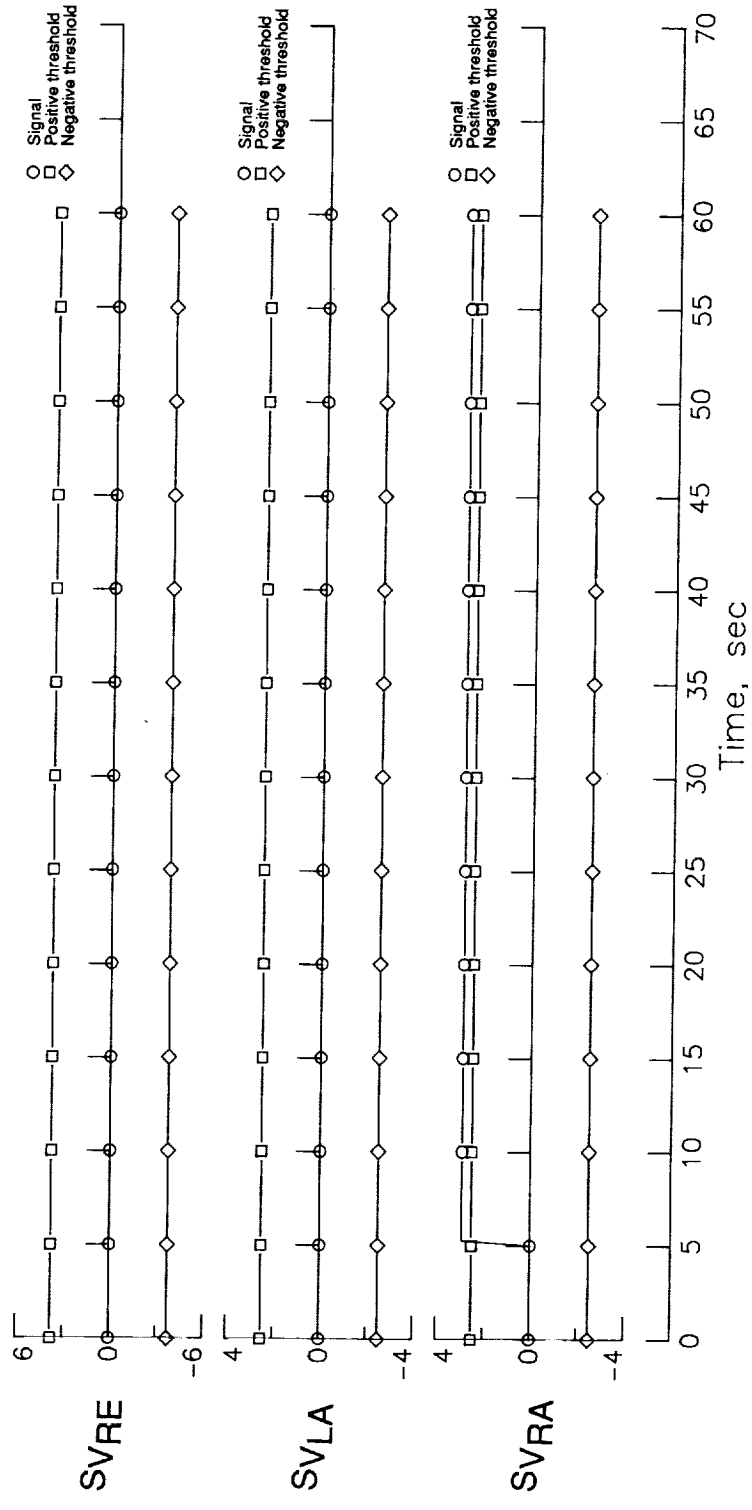
Figure A8. Concluded.

130
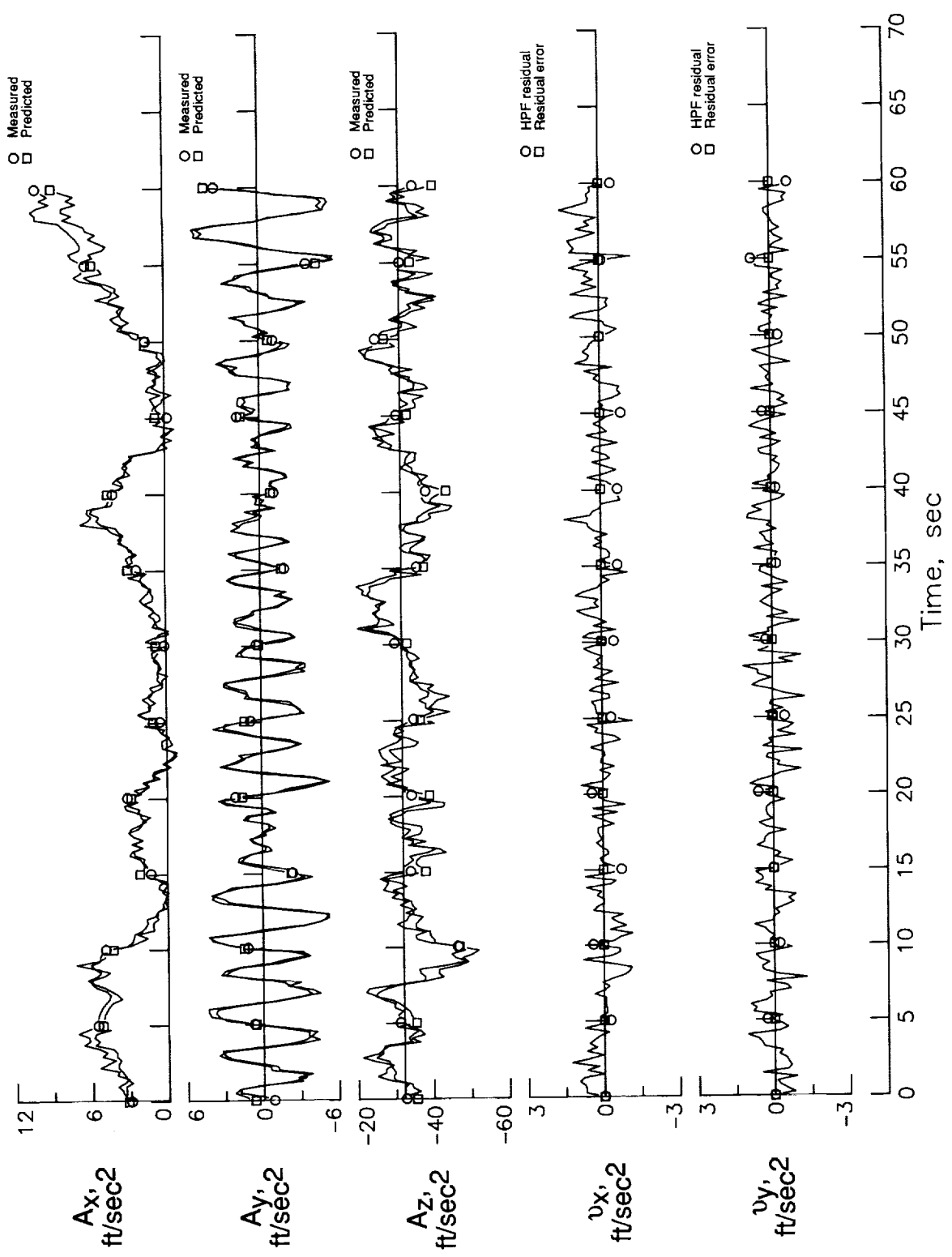
Figure A9. Aircraft-path measurements and residuals for baseline design with no failure, no maneuver, and 10-ft/sec turbulence.

131
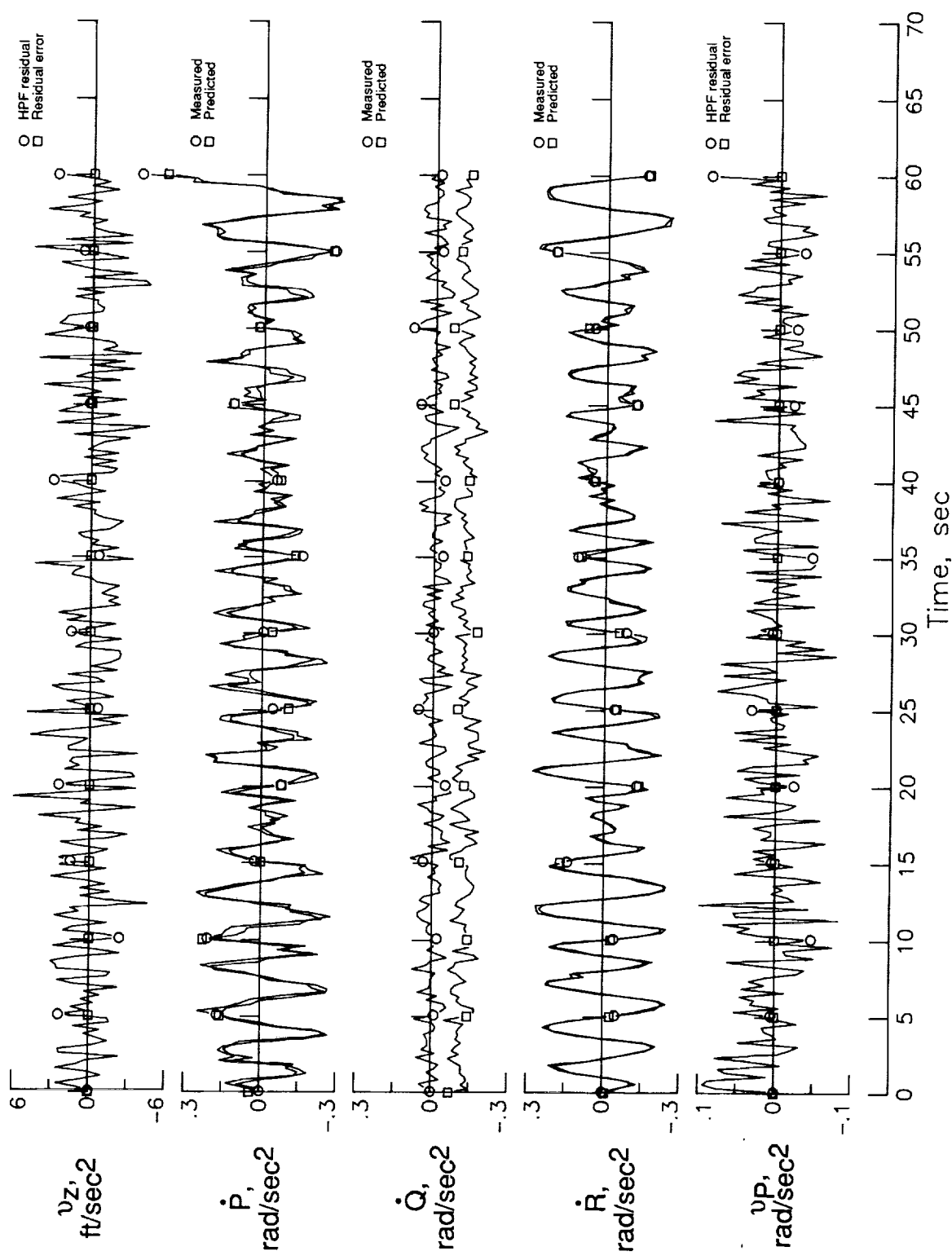
Figure A9. Continued.

132
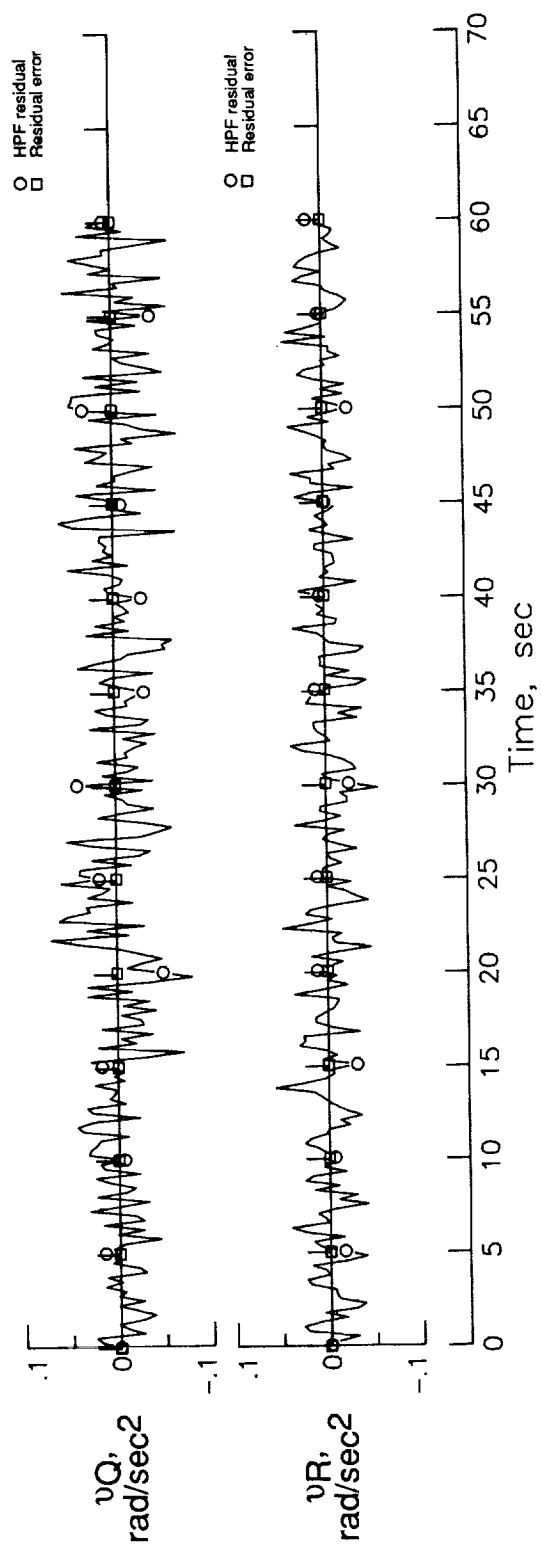
Figure A9. Concluded.

133
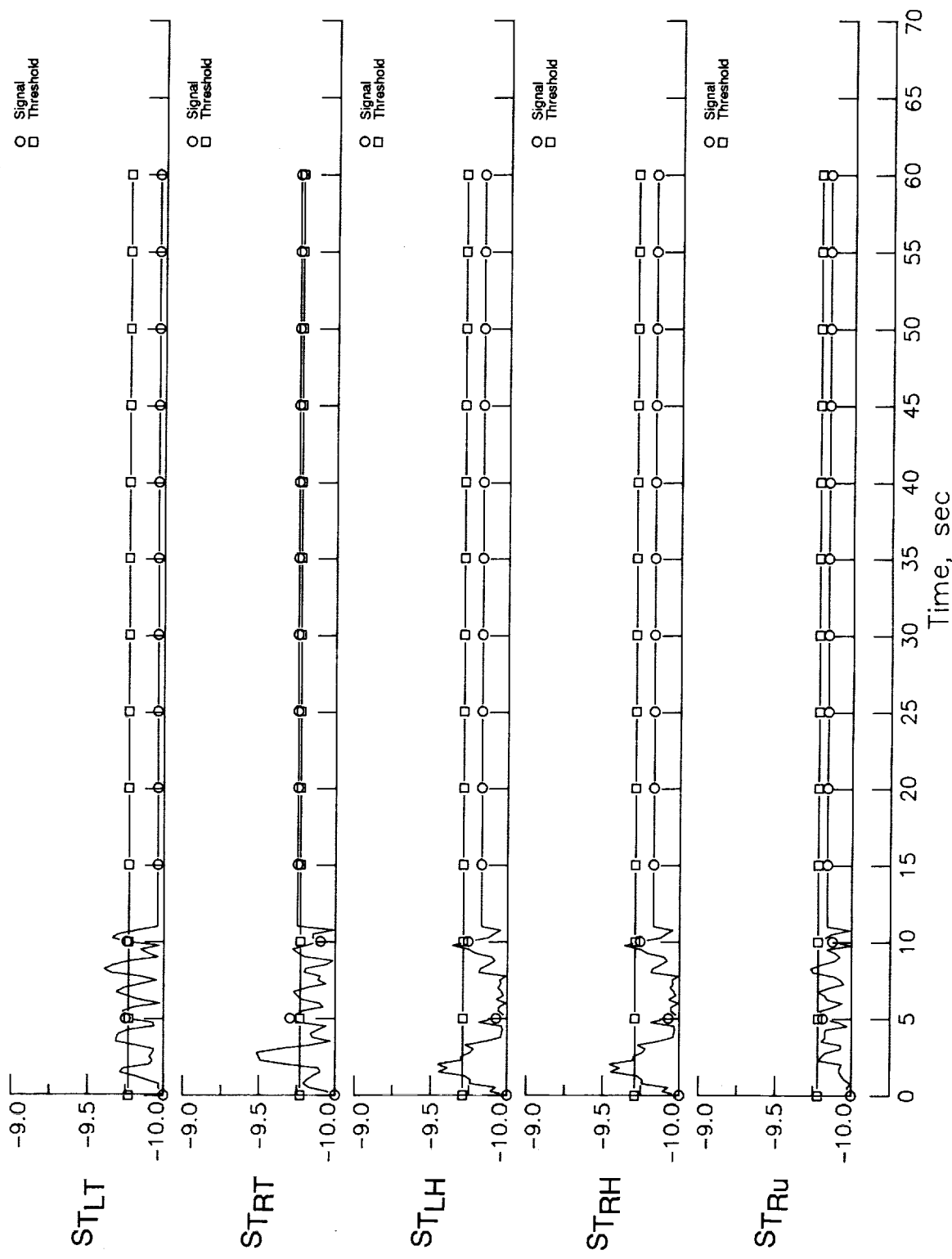
Figure A10. Aircraft-path trigger and verify statistics for baseline design with no failure, no maneuver, and 10-ft/sec turbulence.
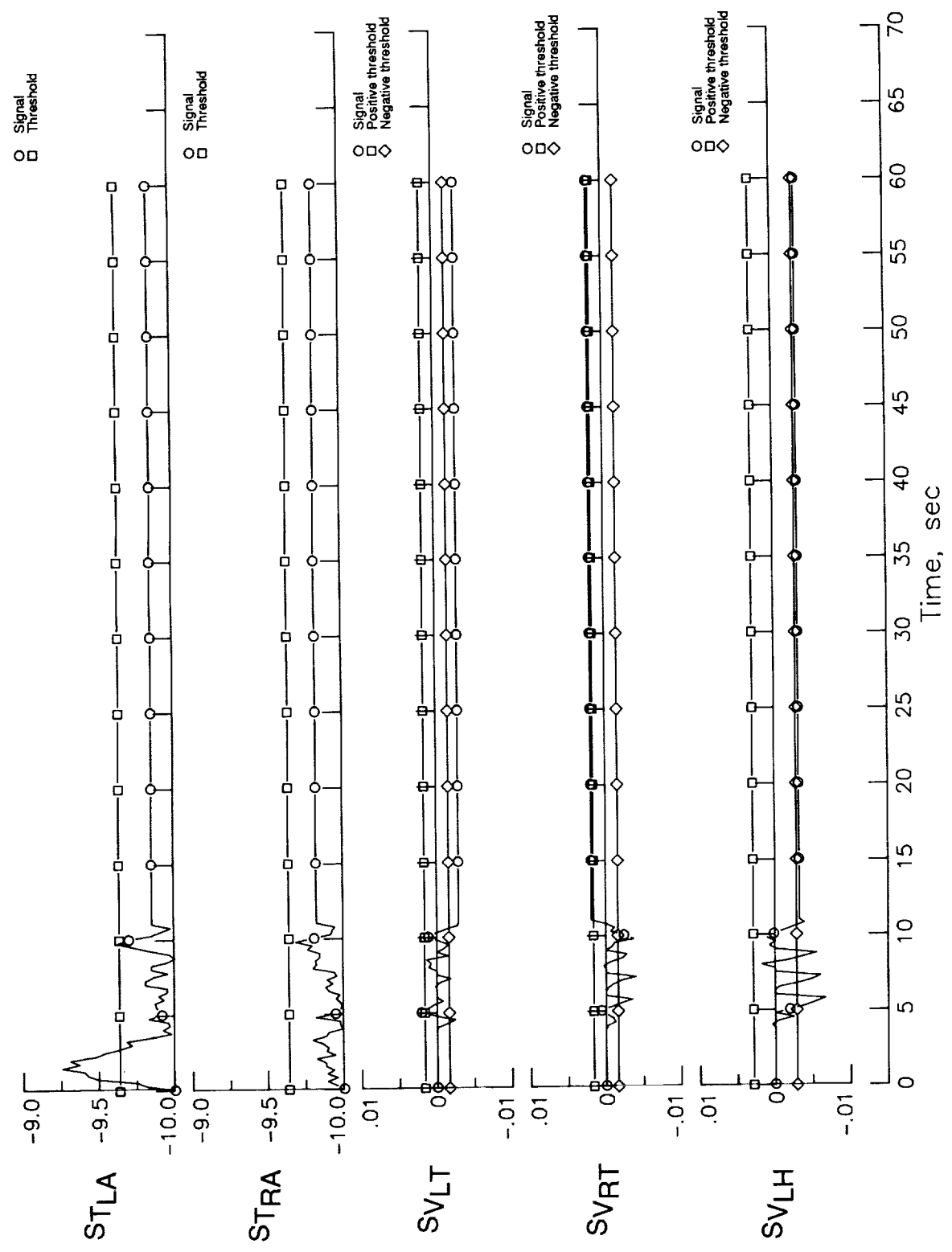
Figure A10. Continued.

135
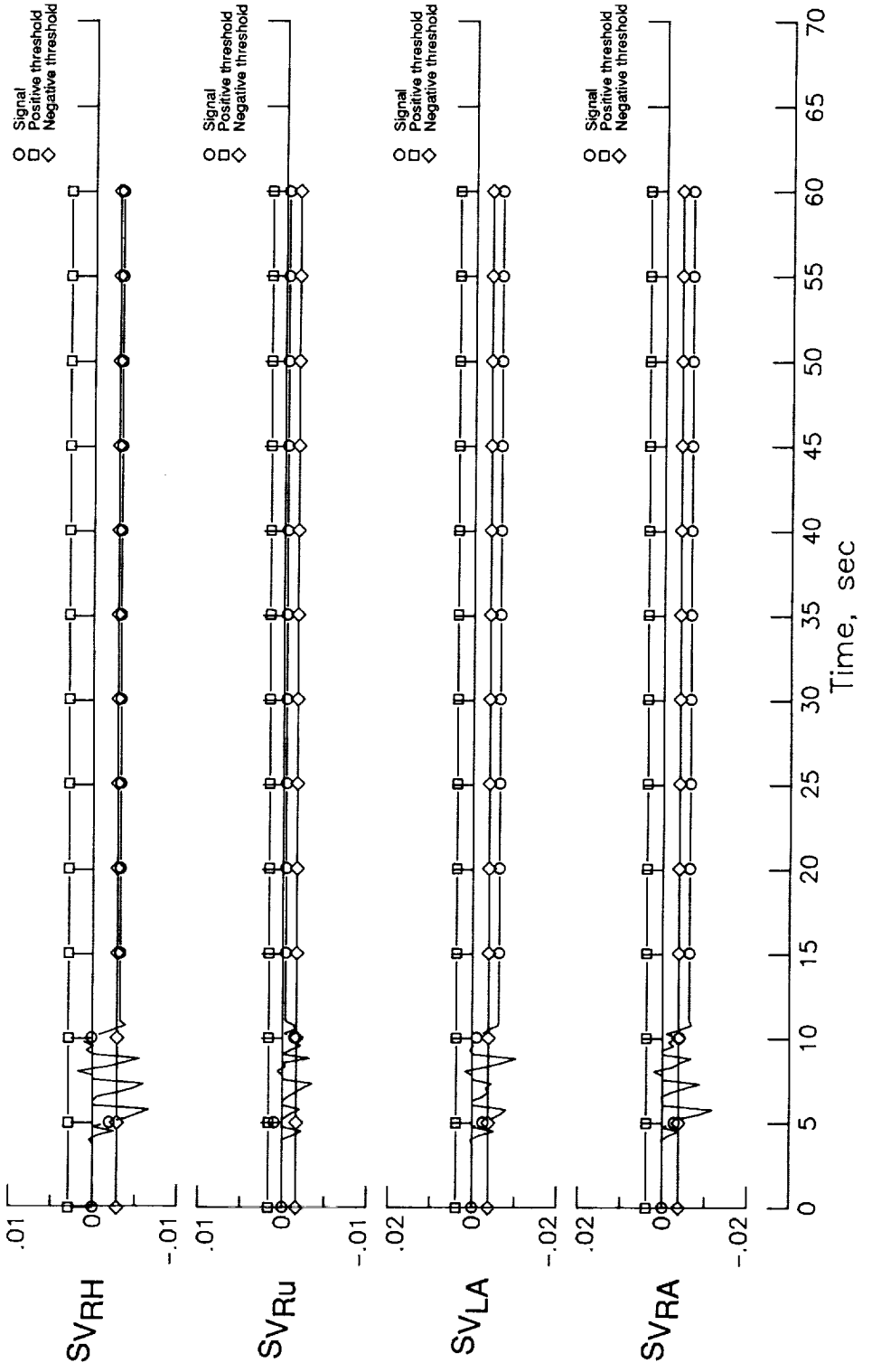
Figure A10. Concluded.
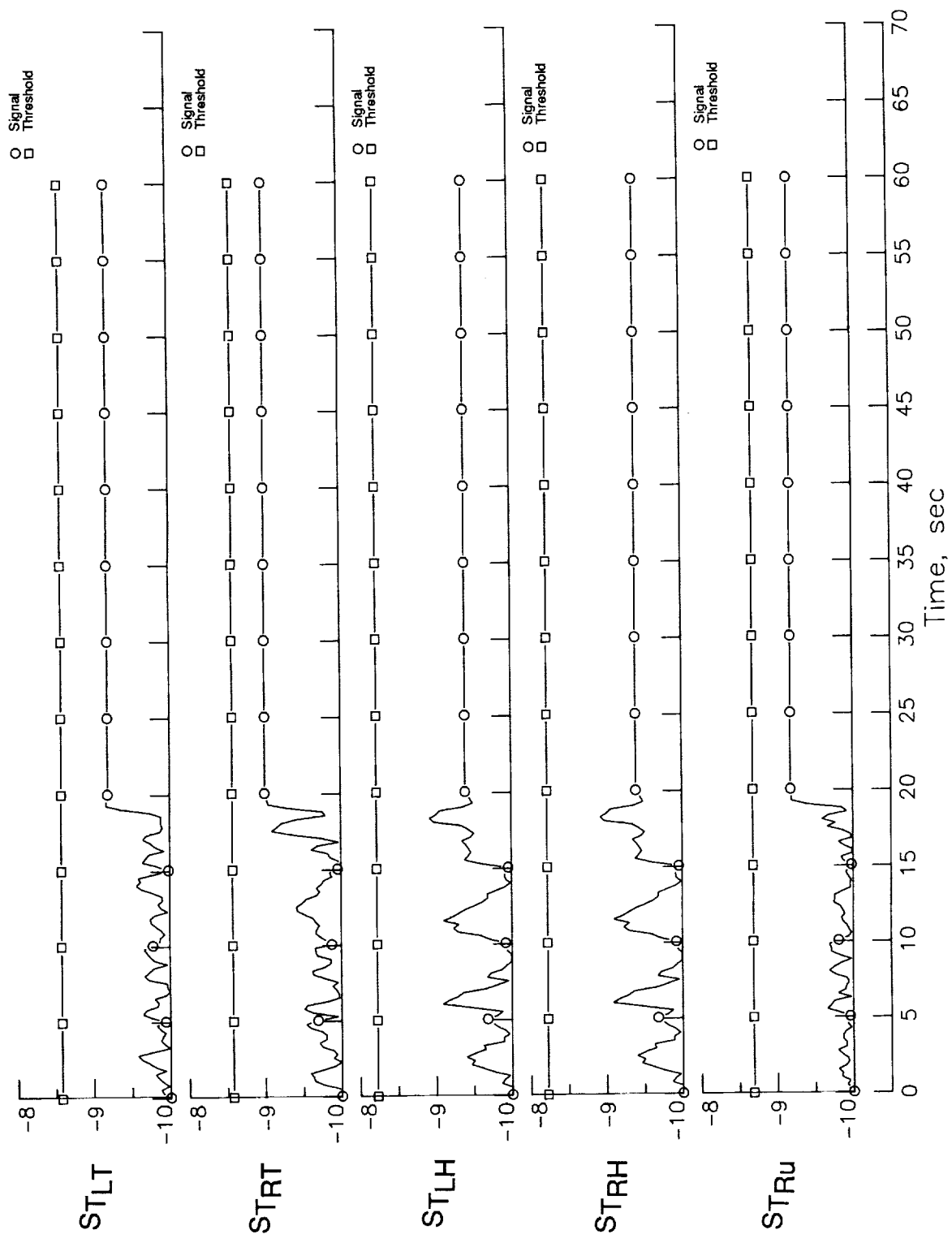
Figure A11. Aircraft-path trigger and verify statistics for right-aileron partially missing surface failure (40-percent effectiveness). Interpolated design; 20-ft/sec turbulence.

137
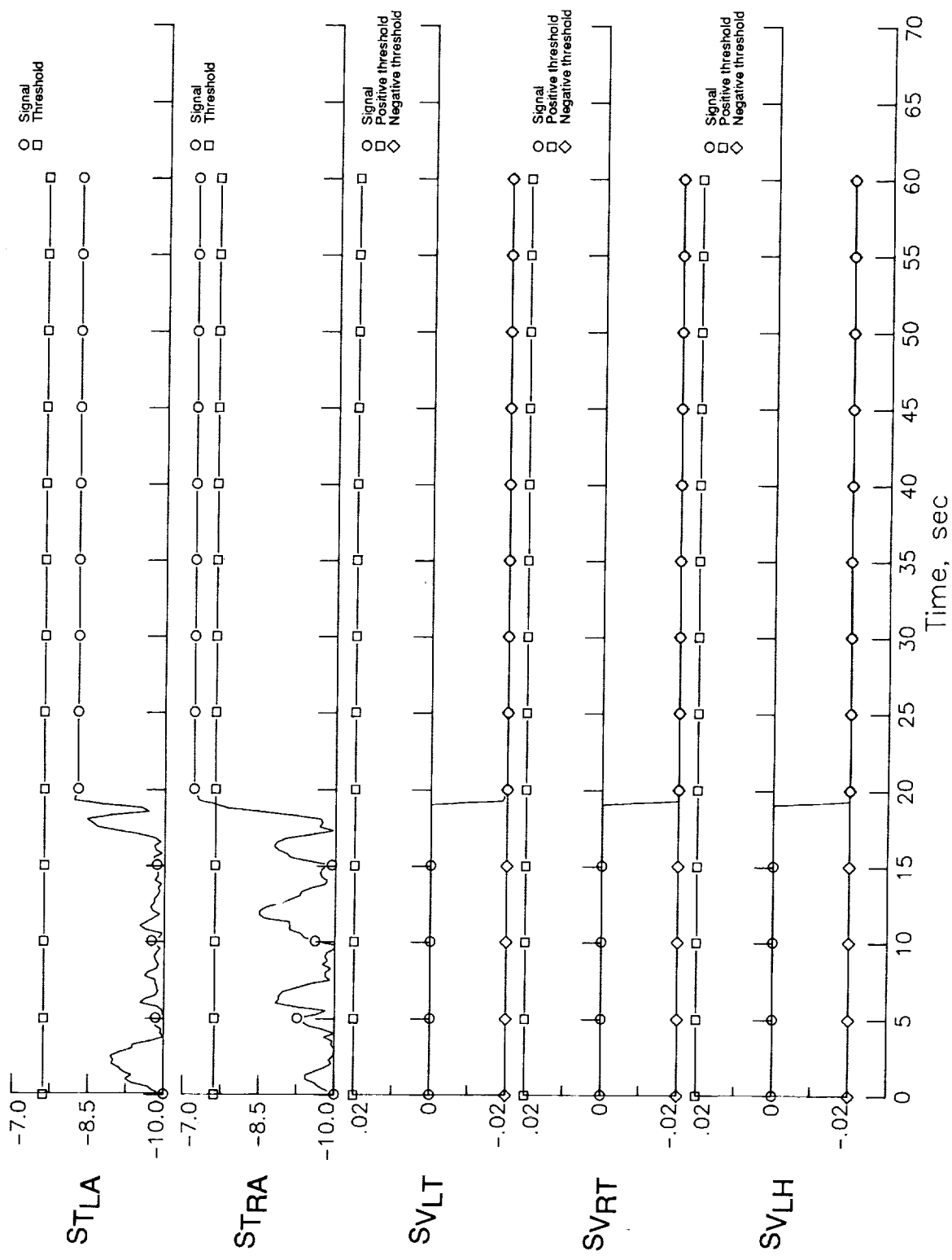
Figure A11. Continued.

138
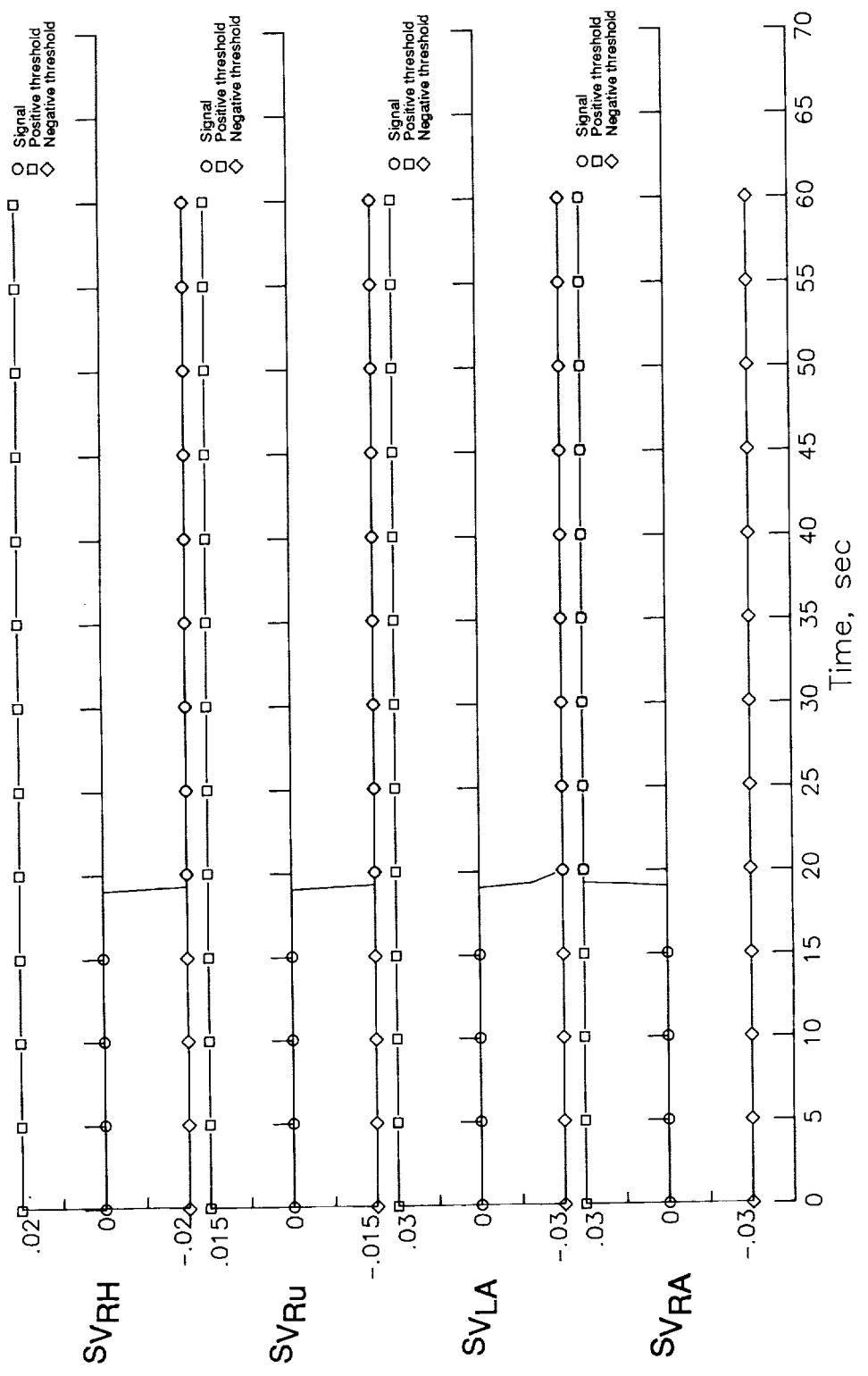
Figure A11. Concluded.
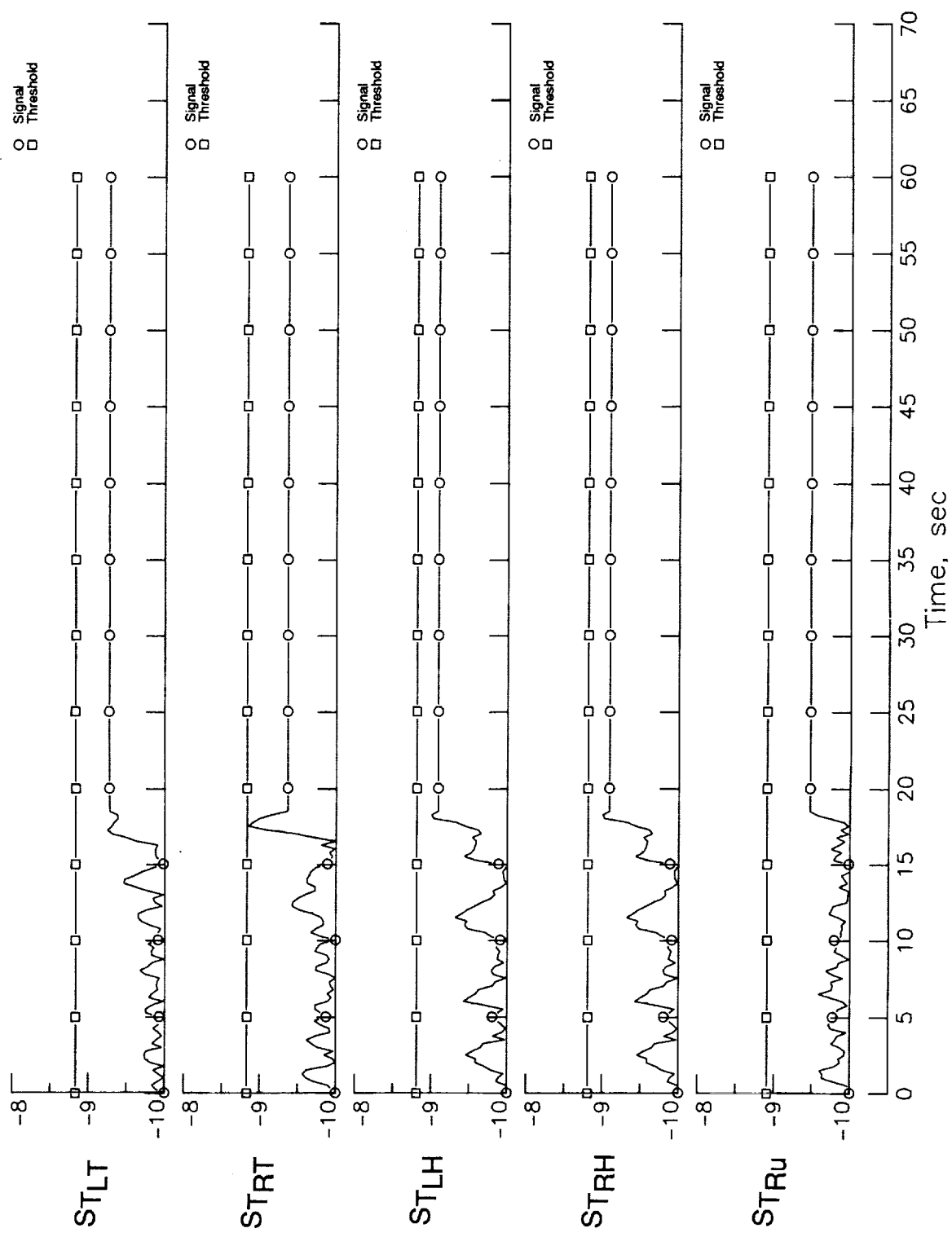
Figure A12. Aircraft-path trigger and verify statistics for right-aileron partially missing surface failure (60-percent effectiveness). Interpolated design; 15-ft/sec turbulence.

140
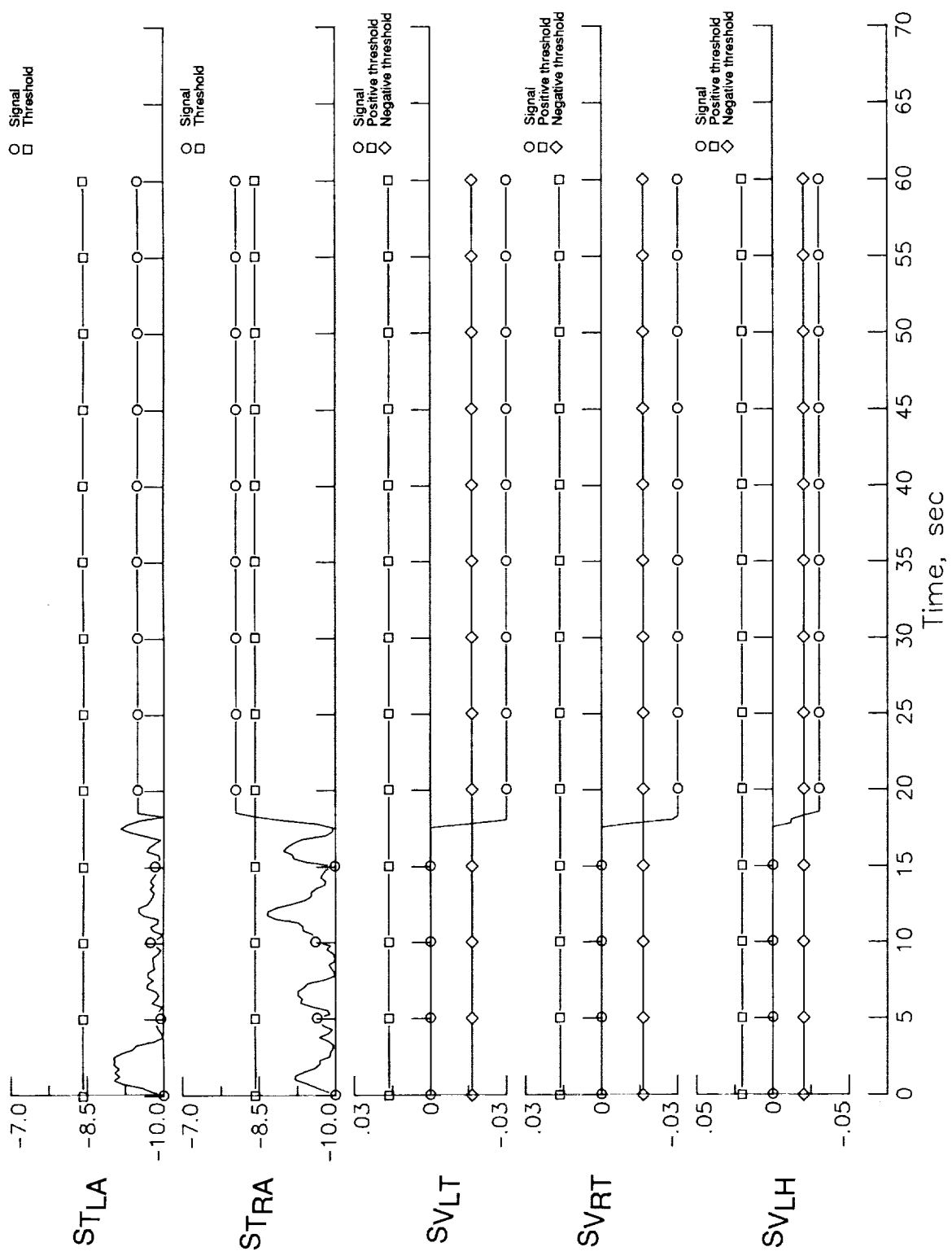
Figure A12. Continued.

141
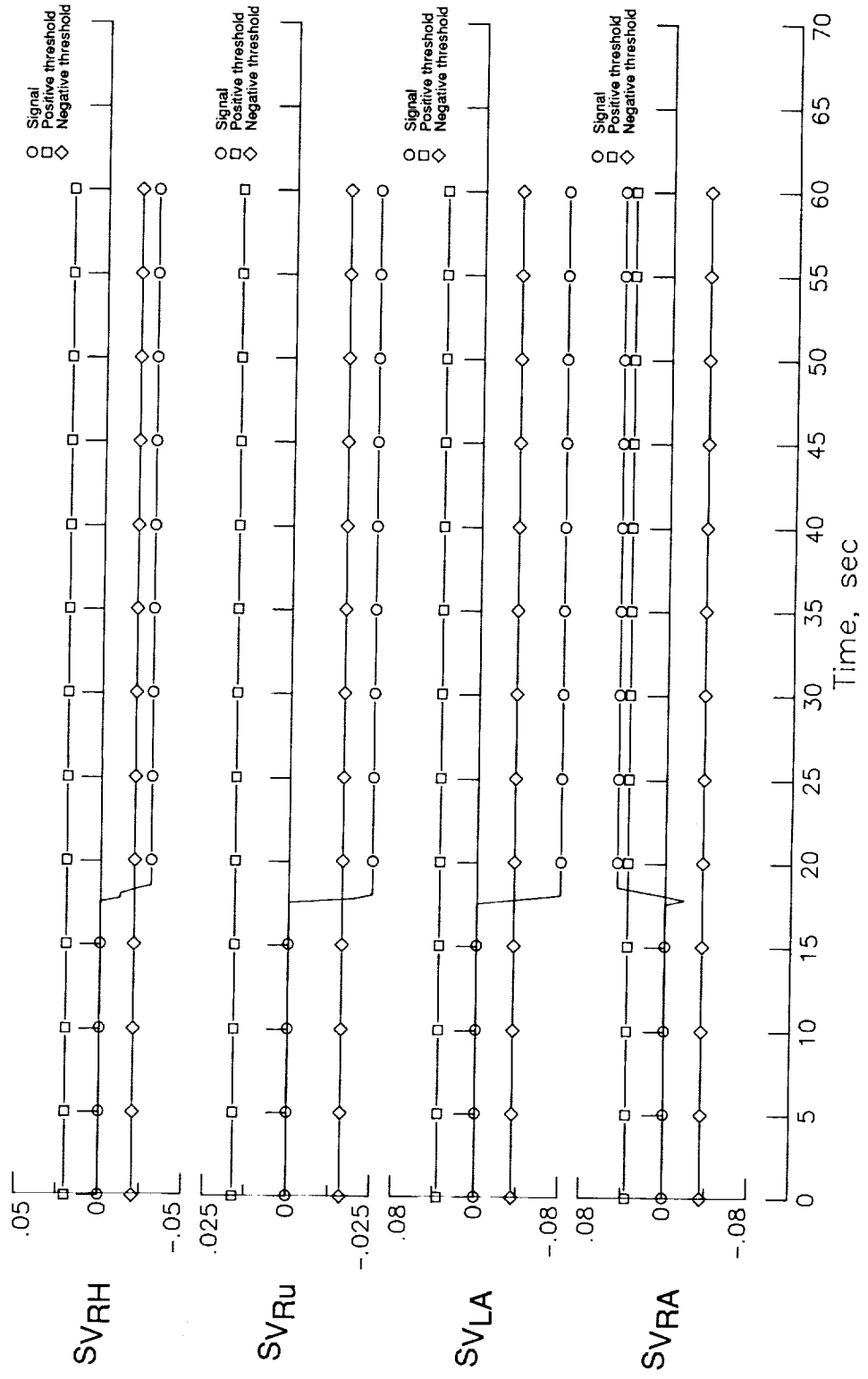
Figure A12. Concluded.

References

1. Willsky, Alan S.: A Survey of Design Methods for Failure Detection in Dynamic Systems. *Automatica*, vol. 12, no. 6, Nov. 1976, pp. 601–611.
2. Chow, Edward Y.: *Failure Detection System Design Methodology.* NASA CR-163792, 1980.
3. Chow, Edward Y.; and Willsky, Alan S.: Issues in the Development of a General Design Algorithm for Reliable Failure Detection. *Proceedings of the 19th IEEE Conference on Decision & Control Including the Symposium on Adaptive Processes, Volume 2*, 80CH1563-6, Inst. of Electrical and Electronics Engineers, Inc., 1980, pp. 1006–1012.
4. Motyka, P.; Landey, M.; and McKern, R.: *Failure Detection and Isolation Analysis of a Redundant Strapdown Inertial Measurement Unit.* NASA CR-165658, 1981.
5. Deyst, J.; Deckert, J.; Desai, M.; and Willsky, A.: Development and Testing of Advanced Redundancy Management Methods for the F-8 DFBW Aircraft. *Proceedings of the 1977 IEEE Conference on Decision & Control Including the 16th Symposium on Adaptive Processes and a Special Symposium on Fuzzy Set Theory and Applications, Volume 1*, 77CH1269-OCS, Inst. of Electrical and Electronics Engineers, Inc., 1977, pp. 309–315.
6. Caglayan, Alper K.; and Lancraft, Roy E.: *An Aircraft Sensor Fault Tolerant System.* NASA CR-165876, 1982.
7. Friedland, Bernard: Maximum Likelihood Failure Detection of Aircraft Flight Control Sensors. *J. Guid., Control & Dyn.*, vol. 5, no. 5, Sept.–Oct. 1982, pp. 498–503.
8. Willsky, Alan S.; and Jones, Harold L.: A Generalized Likelihood Ratio Approach to State Estimation in Linear Systems Subject to Abrupt Changes. *Proceedings of the 1974 IEEE Conference on Decision and Control Including 13th Symposium on Adaptive Processes*, Inst. of Electrical and Electronics Engineers, Inc., 1974, pp. 846–853.
9. Chow, Edward; Dunn, Keh-Ping; and Willsky, Alan S.: *A Dual-Model Generalized Likelihood Ratio Approach to Self-Reorganizing Digital Flight Control System Design.* Res. Status Rep. #1 (NASA Grant NSG-1112), Electronic Systems Lab., Massachusetts Inst. of Technology, Apr. 14, 1975.
10. Bueno, Ramon; Chow, Edward; Gershwin, Stanley B.; and Willsky, Alan S.: *A Dual-Mode Generalized Likelihood Ratio Approach to Self-Reorganizing Digital Flight Control System Design.* NASA CR-146386, 1975.
11. Bueno, Ramon A.: *Performance and Sensitivity Analysis of the Generalized Likelihood Ratio Method for Failure Detection.* NASA CR-149272, 1977.
12. Electronic Systems Lab., Dep. of Electrical Engineering and Computer Science, Massachusetts Inst. of Technology: *A Dual-Mode Generalized Likelihood Ratio Approach to Self-Reorganizing Digital Flight Control System Design.* NASA CR-149317, 1976.
13. Liu, Jack S.; and Jones, Harold L.: Linear Manifold Constrained GLR. *IEEE Trans. Autom. Control*, vol. AC-22, no. 6, Dec. 1977, pp. 988–989.
14. Chang, C. B.; and Dunn, K. P.: On GLR Detection and Estimation of Unexpected Inputs in Linear Discrete Systems. *IEEE Trans. Autom. Control*, vol. AC-24, no. 3, June 1979, pp. 499–501.
15. Motyka, P.; Bonnice, W.; Hall, S.; and Wagner, E.: *The Evaluation of Failure Detection and Isolation Algorithms for Restructurable Control.* NASA CR-177983, 1985.
16. Hall, Steven Ray: A Failure Detection Algorithm for Linear Dynamic Systems. D.Sci. Thesis, Massachusetts Inst. of Technology, June 1985.
17. Bonnice, W.; Wagner, E.; Hall, S.; and Motyka, P.: *The Evaluation of the OSGLR Algorithm for Restructurable Control.* NASA CR-178083, 1986.
18. Bundick, W. Thomas: *A Preliminary Evaluation of the Generalized Likelihood Ratio for Detecting and Identifying Control Element Failures in a Transport Aircraft.* NASA TM-87620, 1985.
19. Beard, Richard Vernon: Failure Accommodation in Linear Systems Through Self-Reorganization. Ph.D. Thesis, Massachusetts Inst. of Technology, Feb. 1971.
20. Jones, Harold Lee: Failure Detection in Linear Systems. Ph.D. Thesis, Massachusetts Inst. of Technology, Aug. 1973.
21. Meserole, Jere Schenck, Jr.: Detection Filters for Fault-Tolerant Control of Turbofan Engines. Ph.D. Thesis, Massachusetts Inst. of Technology, June 1981.
22. Bundick, W. Thomas: *A Preliminary Evaluation of a Failure Detection Filter for Detecting and Identifying Control Element Failures in a Transport Aircraft.* NASA TM-87576, 1985.
23. Boudreau, Jean A.; and Berman, Howard L.: *Dispersed and Reconfigurable Digital Flight Control System Study. Volume I—Sections 1 Through 10, Appendixes A, B, C.* AFFDL-TR-79-3125, Vol. 1, U.S. Air Force, Dec. 1979. (Available from DTIC as AD B051 452L.)
24. Caglayan, A. K.; Rahnamai, K.; Moerder, D. D.; and Halyo, N.: *A Hierarchical Reconfiguration Strategy for Aircraft Subjected to Actuator Failure/Surface Damage.* AFWAL-TR-87-3024, U.S. Air Force, May 1987. (Available from DTIC as AD B113 556L.)
25. Weiss, Jerold L.; and Hsu, John Y.: *Design and Evaluation of a Failure Detection and Isolation Algorithm for Restructurable Control Systems.* NASA CR-178213, 1987.

26. Weiss, Jerold L.; and Hsu, John Y.: *Integrated Restructurable Flight Control System Demonstration Results.* NASA CR-178305, 1987.

27. Weiss, Jerold L.; and Hsu, John Y.: *Expanded Envelope Concepts for Aircraft Control-Element Failure Detection and Identification.* NASA CR-181664, 1988.

28. Eterno, John S.; Weiss, Jerold L.; Looze, Douglas P.; and Willsky, Alan: Design Issues for Fault Tolerant-Restructurable Aircraft Control. *Proceedings of the 24th IEEE Conference on Decision & Control, Volume 2,* 85CH2245-9, IEEE Control Systems Soc., 1985, pp. 900–905.

29. Weiss, Jerold L.; Eterno, John S.; and Hsu, John Y.: Evaluation of Detectability and Distinguishability of Aircraft Control Element Failures Using Flight Test Data. *Proceedings of the 1986 American Control Conference, Volume 3,* 86CH2336-6, American Automatic Control Council, 1986, pp. 1551–1557.

30. Weiss, Jerold L.; Willsky, Alan S.; Looze, Douglas P.; Crawford, John T.; and Huber, Robert R.: Detection and Isolation of Control Surface Effectiveness Failures in High Performance Aircraft. *Proceedings of the IEEE 1985 National Aerospace and Electronics Conference—NAECON 1985, Volume 1,* 85CH2189-9, Inst. of Electrical and Electronics Engineers, Inc., 1985, pp. 552–559.

31. Weiss, Jerold L.; Stifel, J. Mark; and Govindaraj, K. S.: Flight Test Results of a Control Element Failure Detection and Isolation Algorithm. *Proceedings of the IEEE 1986 National Aerospace and Electronics Conference—NAECON 1986, Volume 4,* 86CH2307-7, Inst. of Electrical and Electronics Engineers, Inc., 1986, pp. 1393–1399.

32. Weiss, J. L.; Willsky, A. S.; Pattipati, K. R.; and Eterno, J. S.: Application of FDI Metrics to Detection and Isolation of Sensor Failures in Turbine Engines. *Proceedings of the 1985 American Control Conference, Volume 2,* 85CH2119-6, American Automatic Control Council, 1985, pp. 1114–1120.

33. Weiss, Jerold L.; Pattipati, Krishna R.; Willsky, Alan S.; Eterno, John S.; and Crawford, John T.: *Robust Detection/Isolation Accommodation for Sensor Failures.* NASA CR-174797, 1985.

34. Deckert, James C.; Desai, Mukund N.; Deyst, John J., Jr.; and Willsky, Alan S.: *Reliable Dual-Redundant Sensor Failure Detection and Identification for the NASA F-8 DFBW Aircraft.* NASA CR-2944, 1978.

35. Sage, Andrew P.; and Melsa, James L.: *Estimation Theory With Applications to Communications and Control.* McGraw-Hill, Inc., c.1971.

36. Etkin, Bernard: *Dynamics of Atmospheric Flight.* John Wiley & Sons, Inc., c.1972.

37. Looze, D. P.; Krolewski, S.; Weiss, J. L.; Barrett, N. M.; and Eterno, J. S.: *Automatic Control Design Procedures for Restructurable Aircraft Control.* NASA CR-172489, 1985.

38. Weiss, Jerold L.; Looze, Douglas P.; Eterno, John S.; and Grunberg, Daniel B.: *Initial Design and Evaluation of Automatic Restructurable Flight Control System Concepts.* NASA CR-178064, 1986.

39. Roskam, Jan: *Airplane Flight Dynamics and Automatic Flight Controls. Part I: Chapters 1 Through 6 —Rigid Airplane Flight Dynamics (Open Loop).* Roskam Aviation and Engineering Corp., 1979.

NASA	Report Documentation Page	
National Aeronautics and Space Administration		

1. Report No. NASA TP-3051	2. Government Accession No.	3. Recipient's Catalog No.
4. Title and Subtitle Development of an Adaptive Failure-Detection and Identification System for Detecting Aircraft Control-Element Failures		5. Report Date May 1991
		6. Performing Organization Code
7. Author(s) W. Thomas Bundick		8. Performing Organization Report No. L-16801
9. Performing Organization Name and Address NASA Langley Research Center Hampton, VA 23665-5225		10. Work Unit No. 505-66-41-04
		11. Contract or Grant No.
12. Sponsoring Agency Name and Address National Aeronautics and Space Administration Washington, DC 20546-0001		13. Type of Report and Period Covered Technical Paper
		14. Sponsoring Agency Code

15. Supplementary Notes

Programming support was provided by Jessie Yeager of Planning Research Corporation, Hampton, Virginia.

16. Abstract

A methodology for designing a failure-detection and identification (FDI) system to detect and isolate control-element failures in aircraft control systems is reviewed. An FDI system design for a modified Boeing 737 aircraft is also reviewed, and the results of evaluating this system via simulation are presented. The FDI system performed well in a no-turbulence environment, but it experienced an unacceptable number of false alarms in atmospheric turbulence. An adaptive FDI system, which adjusts thresholds and other system parameters based on the estimated turbulence level, was developed and evaluated. The adaptive system performed well over all turbulence levels that were simulated and reliably detected all but the smallest magnitude, partially missing, surface failures.

17. Key Words (Suggested by Author(s)) Failure detection Fault detection Analytical redundancy Fault tolerant	18. Distribution Statement Unclassified—Unlimited Subject Category 08
19. Security Classif. (of this report) Unclassified	20. Security Classif. (of this page) Unclassified	21. No. of Pages 147	22. Price A07

NASA FORM 1626 OCT 86